

## Crystallographic texture control in a non-oriented electrical steel by plastic deformation and recrystallization

Nguyen-Minh, T.

**DOI**

[10.4233/uuid:cff86e71-055e-47d3-bb5d-c0b73c0b3b5c](https://doi.org/10.4233/uuid:cff86e71-055e-47d3-bb5d-c0b73c0b3b5c)

**Publication date**

2021

**Document Version**

Final published version

**Citation (APA)**

Nguyen-Minh, T. (2021). *Crystallographic texture control in a non-oriented electrical steel by plastic deformation and recrystallization*. [Dissertation (TU Delft), Delft University of Technology]. <https://doi.org/10.4233/uuid:cff86e71-055e-47d3-bb5d-c0b73c0b3b5c>

**Important note**

To cite this publication, please use the final published version (if applicable). Please check the document version above.

**Copyright**

Other than for strictly personal use, it is not permitted to download, forward or distribute the text or part of it, without the consent of the author(s) and/or copyright holder(s), unless the work is under an open content license such as Creative Commons.

**Takedown policy**

Please contact us and provide details if you believe this document breaches copyrights. We will remove access to the work immediately and investigate your claim.

**Crystallographic texture control  
in a non-oriented electrical steel  
by plastic deformation and recrystallization**

Dissertation

for the purpose of obtaining the degree of doctor  
at Delft University of Technology  
by the authority of the Rector Magnificus, Prof.dr.ir. T.H.J.J. van der Hagen,  
chair of the Board for Doctorates  
to be defended publicly on  
Friday 29 January 2021 at 12:30 o'clock

by

Tuan NGUYEN-MINH

Master of Science in Materials Science and Engineering,  
Delft University of Technology, the Netherlands  
born in Hanoi, Vietnam

Composition of the doctoral committee:

Rector Magnificus,	Chairperson
Prof.dr.ir. L.A.I. Kestens	Delft University of Technology, promotor
Prof.dr.ir. R.H. Petrov	TU Delft/Ghent University, Belgium, promotor

Independent members:

Prof.dr.ir. J. Sietsma	Delft University of Technology
Prof.dr.ir. A. Van Bael	Catholic University of Leuven, Belgium
Prof.dr.ir. J.J. Sidor	Eotvos Lorand University, Hungary
Prof.dr. F.J.G. Landgraf	University of Sao Paulo, Brazil
Dr. K. Ushioda	Osaka University, Japan
Prof.dr. M.J. Santofimia Navarro	Delft University of Technology, reserve member

This research was funded by the European Commission through the Research Fund for Coal and Steel (RFCS) Programme.

Keywords: crystallographic texture, crystal plasticity, recrystallization, shear banding, electrical steels

Printed in the Netherlands

Copyright © 2020 by Tuan NGUYEN-MINH

All rights reserved. No part of this book may be reproduced, stored in a retrieval system, or transmitted, in any form or by any means, without prior permission from the copyright owner.

ISBN 978-94-6423-120-5

# Contents

1 Introduction.....	1
2 Quantitative texture analysis .....	7
2.1 Descriptions of crystallographic orientation.....	7
2.1.1 Transformation matrix .....	8
2.1.2 Miller indices .....	10
2.1.3 Pole figure and Inverse pole figure .....	11
2.1.4 Euler angles.....	14
2.2 Representation of orientation distribution function.....	18
2.3 Measurement of crystallographic orientations by EBSD .....	23
2.4 Summary.....	27
2.5 References.....	27
3 Electrical steels.....	29
3.1 Introduction to electrical steels.....	29
3.1.1 Alloying elements.....	29
3.1.2 Impurities.....	31
3.1.3 Grain size.....	31
3.1.4 Texture .....	32
3.2 Histories of electrical steels .....	34
3.2.1 Grain-oriented (GO) electrical steels.....	34
3.2.2 Non-oriented (NO) electrical steels.....	36
3.3 Processing of electrical steels.....	37
3.3.1 Processing of GO electrical steels .....	37
3.3.2 Processing of NO electrical steels .....	38

3.4	Advanced techniques for texture control in NO electrical steels .....	39
3.4.1	Surface textures.....	40
3.4.2	Multi-stage cold rolling and annealing .....	43
3.4.3	Cross rolling.....	46
3.4.4	Thin strip casting .....	48
3.5	References.....	50
4	Plastic deformation and recrystallization.....	53
4.1	Theory of single crystal plasticity.....	54
4.2	Polycrystal plasticity models.....	60
4.2.1	Full constraints Taylor model.....	60
4.2.2	Relaxed constraints models.....	63
4.3	Physical phenomenon of static recrystallization.....	67
4.4	Statistical models for recrystallization texture prediction.....	73
4.4.1	Bunge-Kohler model.....	75
4.4.2	Kestens-Jonas model .....	79
4.5	Summary.....	85
4.6	References.....	86
5	Material and manufacturing.....	89
5.1	Introduction .....	89
5.2	Material .....	90
5.3	Manufacturing procedures .....	90
5.3.1	Warm rolling.....	92
5.3.2	Hot band annealing .....	93
5.3.3	Cold rolling .....	93
5.3.4	Final annealing.....	93
5.4	Initial samples .....	93

6 Deformation textures of the Fe-1.2 wt.% Si alloy after rolling .....	97
6.1 Hot-rolled samples.....	98
6.1.1 Symmetrically hot-rolled samples.....	98
6.1.2 Asymmetrically hot-rolled samples.....	103
6.2 Cold-rolled samples.....	109
6.2.1 Symmetrically cold-rolled samples.....	109
6.2.2 Asymmetrically cold-rolled samples.....	111
6.3 Deformation condition of rolling.....	113
6.3.1 Geometrical approach.....	114
6.3.2 Finite element (FE) simulation.....	118
6.4 Simulation of deformation textures.....	123
6.4.1 Persistent features.....	123
6.4.2 Homogeneous development of deformation textures.....	133
6.4.3 Heterogeneity of the deformation textures .....	135
6.5 Conclusions.....	140
6.6 References.....	141
7 Recrystallization textures of the Fe-1.2 wt.% Si alloy after annealing .....	143
7.1 Evolutions of recrystallization textures .....	144
7.1.1 Hot band annealing textures .....	144
7.1.2 Annealing textures after cold rolling and annealing.....	148
7.2 Simulations of recrystallization textures .....	151
7.2.1 The stored energy of deformed crystals .....	151
7.2.2 Recrystallization textures of rough rolled samples.....	157
7.2.3 Recrystallization textures of warm rolled samples .....	163
7.2.4 Final annealing textures .....	169
7.3 Conclusions.....	174

7.4 References.....	175
8 Locally oriented crystals in cold rolled samples .....	179
8.1 The roles of local orientations in deformed samples on developments of recrystallization texture.....	179
8.2 Local texture developments in microscopic shear bands of the {111}<112> and the {110}<110> oriented crystals .....	183
8.2.1 Crystal plasticity simulations for shear banding in the {111}<112> oriented grains.....	184
8.2.2 Shear banding in the {110}<110> oriented grains .....	190
8.3 The development of the $\alpha$ -fiber texture by local deformations .....	199
8.4 Conclusions.....	212
8.5 References.....	214
9 General conclusions.....	217
Summary.....	223
Samenvatting .....	229
List of publications.....	235
Acknowledgements .....	237
Curriculum Vitae.....	239

# 1

## Introduction

Metals and metallic alloys are highly ordered structural materials. These materials are composed of primitive units, which are characterized by short range, intermediate range and long range order corresponding to the microscopic, mesoscopic and macroscopic scale respectively.

At the microscopic level, a metallic material is composed of atoms associated with the main, substitute, and interstitial elements. The crystallographic structure of a material is formed by the short range and long range periodic arrangement of these atoms. Among all seven possible crystal systems, hexagonal and cubic crystals are the most energetically favorable for metals and their solid solutions. These two crystal structures consist of densely packed atoms. One of the most peculiar aspects of the crystallographic lattice is the fact that the distribution of atoms in space is not isotropic. In any crystallographic structure, there are always differences of atomic



density along various spatial directions. This difference, though small, is enough to have a profound impact on the properties of these crystals, and more precisely on the anisotropy of these properties.

At the macroscopic scale, metallic materials are composed of many crystals with different orientations. A random arrangement of these crystals in an aggregate yields (on averaged) equal behaviors in all directions of the polycrystal, and therefore isotropic material properties. However, a random arrangement of grains is hardly achieved in bulk materials. During processing, materials are always constrained in some specific directions by mechanical forces and/or thermal boundary conditions. Grains exhibiting the best ability to accommodate external constraints (compared with other grains) will constitute higher fractions of the aggregate. Processing conditions amplify the difference in the volume fractions of differently oriented grains in the polycrystal. In general, polycrystalline materials are composed of non-randomly oriented grains.

The orientation preference of grains in a polycrystalline is referred to as the *crystallographic texture*. Texture results from the structural character of crystals and has significant effects on the anisotropy of the material properties. Response of crystal grains to external constraints, lead to the formation of a *new* texture. Understanding the relationship between textures and material behaviors is a two-fold issue. On the one hand, this relationship accounts for material behaviors, based on the crystallographic structure of materials. Consequently, properties can be improved via texture optimization. On the other hand, understanding the responses of crystallites to external constraints provides insight into texture development during material processing. Therefore, texture and material property control can be achieved by manipulating the processing parameters.

Texture control in *electrical steels* represents one of the most extensively investigated issues in both steel manufacturing and materials research. In fact, the relationship between the texture and the properties of these materials has been investigated already since the first decades of the 20<sup>th</sup> century. Electrical steels are primarily employed as magnetic flux carrier in rotating electrical devices (electrical

machines) or tension transformers. Conventionally, the sheets are piled up in lamellar stacks, which configure the so-called *iron core* of the magnetic device. The optimum performance of such iron core requires high magnetic induction and low energy core loss. From the crystallographic point of view, the high magnetic induction of electrical steels involves a large number of crystal grains with the easy (spontaneous) magnetization axes parallel to the external magnetic field direction. For transformer cores, the direction of the magnetic flux vector is fixed in space, whereas for rotating parts of electrical machines, the direction permanently rotate in the plane of the sheet. Therefore, two different types of electrical steels exist with very different types of textures. For transformer cores, grain-oriented (GO) steels are employed, whereas for rotating machines, non-oriented (NO) grades are needed. In GO steels the crystallographic texture is such that the large majority of the grains have the  $\langle 100 \rangle$  direction parallel to the rolling direction of the sheet, and thus fixed in space according to the requirements of the flux distribution in a transformer core. For the NO oriented steel it is required that the  $\langle 100 \rangle$  directions are arbitrarily distributed in the plane of the sheet, as are the flux lines in the soft core of the rotating electrical device. For both types of materials, texture formation during material processing and appropriate methods to obtain the desired textures for electrical steels are permanently challenging questions.

In manufacturing, the texture of electrical steels is controlled by thermo-mechanical processes. These processes primarily include hot rolling, cold rolling and annealing. The standardization of the thermo-mechanical processes helps to increase productivity and the consistency of obtaining high quality materials. However, optimum textures for electrical steels are hardly achieved through standard processes. Conventional thermo-mechanical processes provide limited opportunities for the texture modification of materials. Therefore, many innovative processes aimed at changing the textures of electrical steels have been proposed. Compared with the conventional processes, these new processes yield greater variety of textures. These new textures hold significant potential for improving the properties of electrical steels. However, employing the new processes in the industrial production of

materials requires a thorough understanding of texture formation and impacts of processing parameters to texture developments.

The aim of this study is to investigate the *texture evolution during deformation and recrystallization in body centered cubic crystal materials*. There is a particular focus on asymmetric rolling, which is an innovative sheet rolling processing, on formation of deformation and recrystallization textures. Although the material of choice in this study is a typical NO grade of electrical steel with 1.2 wt.% of Si addition, the physical phenomena under consideration here are similar to all different materials of the same crystallographic structure. The study includes both an experimental and theoretical component. Microstructure and texture of materials after each processing steps are measured by orientation contrast microscopy by electron backscattered diffraction. Evolution of texture during deformation and recrystallization is modeled with physically based crystal plasticity simulations. Differences in textures of conventional and asymmetrical rolling are compared and the potential application of asymmetric rolling for texture control of electrical steels are then discussed. Experimental results and theoretical arguments for the texture evolution observed in this study are presented in chapters of this thesis, given as follows.

**Chapter 2** provides the theoretical background and introduces the methods employed for measuring the crystallographic texture. Various types of representations of crystallographic orientations by means of pole figures (PFs), inverse pole figures (IPFs) and in Euler angle space are considered. The method developed by H.J. Bunge using spherical harmonic expansions to calculate the orientation distribution function (ODF) from a discrete orientation dataset is briefly reviewed. Fundamentals of electron backscatter diffraction (EBSD), a powerful technique for instantaneous characterization of the microstructure and texture of materials are also described.

**Chapter 3** provides a general overview of electrical steels. The categories, history, quality improvement and production of electrical steels are reviewed. In addition, the chemical composition, grain size, impurity and particularly texture requirements for

these materials are mentioned. The texture developments after conventional and innovative processing routes is summarized.

**Chapter 4** presents the theories that describe texture development during deformation and recrystallization. These physical phenomena are described by mathematical models that are employed for texture predictions. Texture development during plastic deformation is considered by various crystal plasticity models. Among those, the full constraints Taylor (FCT) and the ALAMEL models, which are extensively used in this study, are completely described. The evolution of crystallographic orientations during recrystallization is investigated through statistical models on the orientation spaces. Specifically, the Bunge-Kohler model and the Kestens-Jonas model are investigated.

**Chapter 5** provides full description of the materials and processing procedures used in this study. Chemical composition and manufacturing conditions of the initial samples are given. In addition, the initial microstructure and texture of the material are investigated via EBSD measurements. Manufacturing schedules, specified in terms of the parameters of the subsequent processing steps, including hot rolling, hot band annealing, cold rolling and final annealing are provided. A combination of symmetric and asymmetric rolling, both at high and room temperatures, defines different processing routes for the material. These different processing routes are expected to yield a various type of textures.

**Chapter 6** describes microstructure and texture evolution after deformation. The results of EBSD measurements are presented for samples subjected to symmetrical and asymmetrical rolling at both room and high temperatures. Comparisons of samples subjected to different deformation conditions reveal the influence of rolling configuration and rolling temperature on microstructure and texture formation. The evolution of the deformation textures is subsequently evaluated via crystal plasticity models. Impact of processing parameters, such as thickness reduction and friction condition on texture development, is also predicted.

**Chapter 7** focuses on the developments of the recrystallization textures after annealing. Textures and microstructures on continuous and interrupted annealed samples are determined by EBSD measurements. The developments of different recrystallization textures is discussed. Moreover, the evolutions of macroscopic recrystallization textures is illustrated via simulation results of the Kestens-Jonas model.

**Chapter 8** describes a cross-link investigation on texture evolution at the local scale. Formation of recrystallization texture components is linked to their evolution during deformation. The formation of local texture components, which are hardly observed in macroscopic deformation texture, plays an important roles in the formation of recrystallization textures. Furthermore, the orientation preferences in shear bands and deformation bands of major texture components can be predicted by applying crystal plasticity models at the microscopic scale. The formation of these local textures accounts for the occurrence of corresponding orientations in recrystallization textures.

In **Chapter 9**, general conclusions on microstructure and texture developments after thermo-mechanical processes are given. The most important processing parameters which have impacts on evolution of microstructure and texture during deformation and annealing are indicated. Mechanisms in which these parameters affect developments of microstructure and texture on materials are summarized. Suggestions on optimizing microstructure and texture of materials by controlling processing parameters are also given.

# 2

## Quantitative texture analysis

### *2.1 Descriptions of crystallographic orientation*

A crystallite in three-dimensional space is described by its position and orientation. For an aggregate of millions or billions of grains, the spatial positions of single crystals are less important than their crystallographic orientations. A representation of crystallographic orientation requires two orthogonal coordinate systems. One of these reference systems is attached to the sample, whereas the other is determined for each individual crystallites in the aggregate and thus attached to the axes of the crystal reference system.

The *sample reference system*, in principle, can be selected arbitrarily. However, geometrical directions of the material manufacturing process are conventionally chosen as sample reference systems. For rolled and subsequently annealed materials, the sample reference axes (X, Y and Z) are usually chosen to coincide with the rolling

direction (RD), the transverse direction (TD) and the normal direction (ND) of the rolled sheet. For extruded or drawn materials, the Z-axis of the sample reference system is commonly set parallel to the extrusion direction or the wire drawing axis, whereas the other two axes (X and Y) are chosen arbitrarily in the plane perpendicular to Z-axis. The *crystal reference system* is defined by three orthogonal vectors attached to the lattice of the crystal structure, and this system is kept identical for all grains in the polycrystalline aggregate. In BCC structured materials, because of the orthonormal lattice, the crystallographic axes [100], [010] and [001] are respectively chosen as X, Y and Z directions of the crystal reference system.

Having specified the sample and crystal reference systems, an *orientation* is then defined by specifying the directions of the crystal coordinate vectors with respect to the sample coordinate system [1]. Mathematically, an orientation is represented by a rotation operation ( $g$ ) which transforms the sample coordinate system ( $K_S$ ) into the crystal coordinate system ( $K_C$ ):

$$K_C = g \cdot K_S \quad (2.1)$$

### 2.1.1 Transformation matrix

The most fundamental way to represent an orientation is by a *transformation matrix*. For a three dimensional orientation, this matrix is squared, orthonormal and includes nine real elements. The values of these elements are the direction cosines of the angles between crystal reference axes and sample reference axes. For instance, the first row of the transformation matrix contains the cosines of angles between the [100] crystal axis and each of the three sample reference axes (X, Y, Z), respectively, as given in Figure 2.1. The corresponding three angles are denoted as  $\alpha_1$ ,  $\beta_1$  and  $\gamma_1$ . A transformation matrix is given as following:

$$g = \begin{pmatrix} g_{11} & g_{12} & g_{13} \\ g_{21} & g_{22} & g_{23} \\ g_{31} & g_{32} & g_{33} \end{pmatrix} = \begin{pmatrix} \cos \alpha_1 & \cos \beta_1 & \cos \gamma_1 \\ \cos \alpha_2 & \cos \beta_2 & \cos \gamma_2 \\ \cos \alpha_3 & \cos \beta_3 & \cos \gamma_3 \end{pmatrix} \quad (2.2)$$

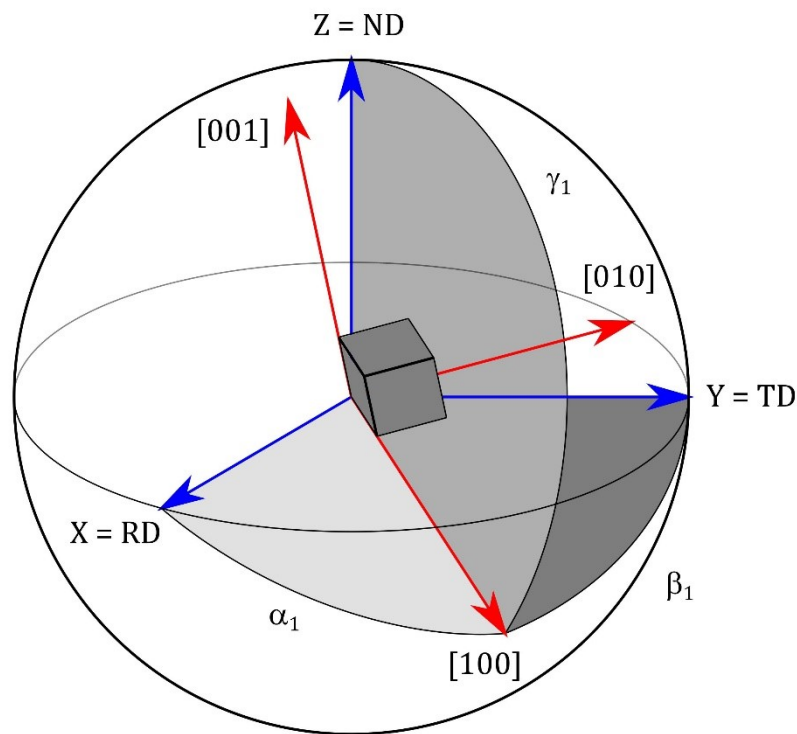


**Figure 2.1** The transformation of sample coordinate system (X, Y, Z) to crystal coordinate system ([100], [001], [010]) in form of a transformation matrix.

Representation of orientations by transformation matrices, though very powerful for calculations, has two practical disadvantages. The first disadvantage comes from the over-determination of the orientation. In fact, a three dimensional rotation of an entity only requires three independent parameters, instead of nine elements as given by the transformation matrix. Storing crystallographic orientations in the form of transformation matrices in computer programs requires a memory space that is three times larger than actual necessity. To avoid this problem, three independent components among nine components of a transformation matrix can be deduced, based on its characteristics. For a transformation matrix, the cross product of any two rows or columns gives the third one, and for any row or column the sum of the squares of the three components is equal to unity. The second disadvantage of using transformation matrices is their poor quality in terms of visualization and interpretation of orientations. Neither with all nine components nor with three independent components of a transformation matrix, it is easy to spatially visualize the corresponding orientation. Graphical representation for transformation matrices



requires at least three dimensional space. Moreover, physical information of orientations (i.e. rotation angles and rotation axis) is hidden by cosine functions, which is not convenient for human perception. Because of these disadvantages, the description of orientation by transformation matrix is only applicable in mathematical calculations.

### 2.1.2 Miller indices

A comprehensive way to describe an orientation is via *Miller indices*. In this representation, positions of crystallographic plane and direction with respect to the sample reference system are denoted by rational digits. These numbers are derived from the direction cosines in the first and the third columns of the transformation matrix, meaning coordinates of the X and Z sample directions in the crystal reference frame.

Practically, the Miller indices are obtained by first multiplying the direction cosines in each column by a suitable factor, so as to obtain whole numbers. Then these whole numbers are divided by the lowest common denominator and written as  $(hkl)[uvw]$  or  $\{hkl\}\langle uvw \rangle$ . The indices of  $(hkl)[uvw]$  are used for a specific planes and directions, while the indices  $\{hkl\}\langle uvw \rangle$  denote a family of all symmetry equivalent orientations. The first set of these Miller indices (i.e.  $(hkl)$  or  $\{hkl\}$ ) represent crystallographic planes, which are normal to the sample Z direction. The second set (i.e.  $(uvw)$  or  $[uvw]$ ) represent crystallographic directions which are parallel to the sample X direction, whilst laying in the  $(hkl)$  or  $\{hkl\}$  planes. Miller indices of arbitrary orientations are complicated, since they are represented by multi digit numbers. Multiplying the direction cosines by factors of hundreds or thousands and rounding off to the nearest low index partially solves the problem. In this way, arbitrary crystallographic orientations are associated with ideal ones, which have single digit Miller indices. However, by grouping orientations, the angular resolution of orientation representation decreases.

The representation of orientations by Miller indices is very familiar to metallurgists. The main advantage of this orientation description is its emphasis on important reference crystallographic planes and directions, which are parallel to

principal directions of samples. This is very helpful for texture analysis, since particular orientations are quickly visualized by their Miller indices, rather than by their transformation matrices. For example, one of the preferred orientations in BCC structural materials after the conventional rolling is given in form of transformation matrix as following:

$$g = \begin{pmatrix} 0.707 & 0.408 & 0.577 \\ -0.707 & 0.408 & 0.577 \\ 0.000 & -0.817 & 0.577 \end{pmatrix} \quad (2.3)$$

It is rather difficult to visualize the orientation of the crystal from this transformation matrix. Instead of that, if the Miller indices ( $\{111\}\langle 110\rangle$ ) are used, orientations of  $\langle 110\rangle//RD$  and  $\{111\}\perp ND$  can be readily recognized.

### 2.1.3 Pole figure and Inverse pole figure

Any direction in space can be described by the spherical coordinates of a point on a unit spherical surface. *Spherical coordinates* on a unit sphere, therefore, can be used to represent crystallographic orientations. According to this representation, coordinates of two nonlinear vectors define an orientation of a crystal. These vectors can be chosen freely, but they should contain physical information of crystals, e.g. normal directions of (hkl) crystal planes. The point, which is the intersection of the crystal axis ([hkl]) and the surface of unit sphere, is called the (hkl) pole. Providing the unit sphere is attached to an external frame, position of a pole is defined by two angular coordinates,  $\alpha_{hkl}$  and  $\beta_{hkl}$ . In general, geological terminologies of the North and South, meaning upper and lower parts of a vertical axis, are used to determine the external frame of the unit sphere. Accordingly, the coordinate  $\alpha_{hkl}$  of a pole is defined as a deviation angle from the North Pole of the sphere, while the coordinate  $\beta_{hkl}$  is the azimuth angle from a fixed direction, which is perpendicular to the North direction and lays in the equatorial plane (Figure 2.2). In the case of rolled samples, the North direction of the sphere is commonly chosen to be parallel to the normal direction (ND) of the sheet, while the reference direction on the equatorial plane is chosen parallel to the rolling direction (RD) of the sheet. Apparently, the spherical coordinates of one pole do not define any specific crystallographic orientation. It is because

crystallographic orientations require three independent parameters, whereas a pole is represented by only two coordinates. To identify crystallographic orientations, the third parameter of spherical coordinates is required. This coordinate can be chosen as the rotation angle  $\gamma_{hkl}$  of the crystal rotation around the pole axis. Alternatively, the ambiguity in orientation description can be solved by using spherical coordinates of at least two poles.

The description of a crystallographic orientation by spherical coordinates is not convenient for visualization, since most of practical analyses are carried on a two dimensional workspace. To transform the information from a two dimensional spherical surface to a two dimensional plane, a projection method is required. In crystallography, the *stereographic projection* is commonly used. The equatorial plane of the unit sphere is used as the plane of projection. For any pole (P) in the North hemisphere, the projection image (p) is the intersection point of the projection plane and a projection line, connecting the pole (P) and the South Pole. For poles in the southern hemisphere, the determination of projection images is similar, but the projection lines in these situations are started from the North Pole. By this projection method, images of crystallographic poles, from both North and South hemispheres are all observable inside the equator, i.e. the so called primitive circle of the unit sphere.

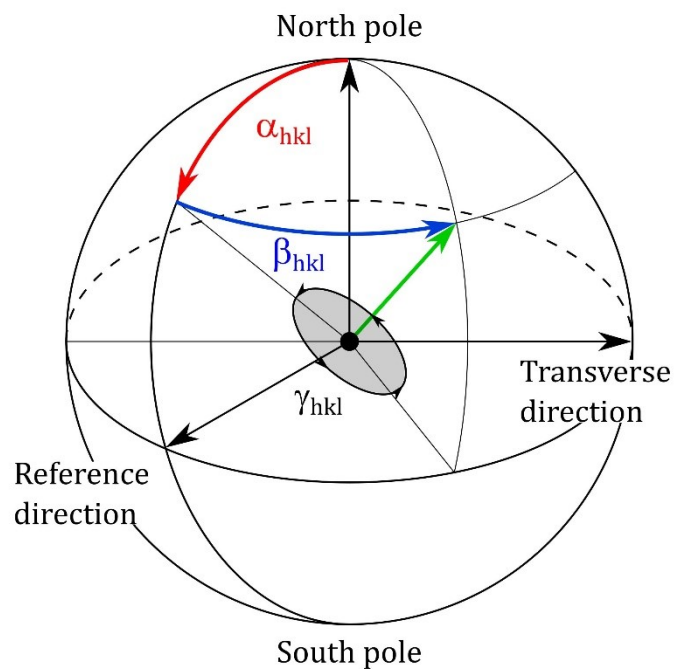


**Figure 2.2 Spherical coordinates of a (hkl) plane in cubic crystals.**

An attractive property of the stereographic projection is the preservation of angular relationships in the crystal. The angle between two poles can be measured

directly as a distance along the projection image of an arc of the great circle connecting the 2 poles. However, because projection images of great circles are not straight lines, in general, the measurement of an angular distance requires the aid of a coordinate grid, the so called the *Wulff net*.

A special type of stereographic projections, which contains the projection images of a specific plane family ( $\{hkl\}$ ), is the *pole figure* (PF). This type of stereographic projection is intensively used in investigations of crystallographic orientations and texture, because the representation of different plane families in a crystal on separated pole figures makes the crystallographic orientations much easier to be observed. Furthermore, representation of orientations on pole figures is very comprehensive as pole figure can be measured experimentally by X-ray or neutron diffraction.

Instead of representing spherical coordinates of crystallographic poles in a fixed sample frame, coordinates of specific sample directions, referred to a fixed crystal system, can be used to describe an orientation. In this representation, the roles of crystal and sample directions are reversed. An orthogonal crystal system is chosen as a fixed frame of the unit sphere. For materials with cubic crystal systems crystallographic directions  $[100]$ ,  $[010]$ , and  $[001]$  are usually used to define the crystal reference system. The orientation is then defined by polar coordinates of sample directions on the crystal reference system. For rolled samples, they are two among the three sample directions (RD, TD and ND) of material sheets. The stereographic projection of sample poles on crystal reference frame configures the so called *inverse pole figure* (IPF). Accordingly, crystallographic orientations of rolled samples can be given in RD-, TD-, and ND-IPFs.

To identify the position of a projection image on pole figure/inverse pole figure, two mathematical steps are described as following. First, spherical coordinates of the pole for a crystal given by a transformation matrix is calculated. Assuming a crystallographic pole of interest with Miller indices  $(hkl)$ , its two angular coordinates ( $\alpha_{hkl}$  and  $\beta_{hkl}$ ) on a fixed sample reference frame are defined by:

$$\begin{pmatrix} \sin \alpha_{hkl} \cos \beta_{hkl} \\ \sin \alpha_{hkl} \sin \beta_{hkl} \\ \cos \alpha_{hkl} \end{pmatrix} = \frac{1}{N} \cdot (g)^{-1} \cdot \begin{pmatrix} h \\ k \\ l \end{pmatrix} \quad (2.4)$$

in which,  $N$  is the normal value of the vector  $[hkl]$ :  $N = \sqrt{h^2 + k^2 + l^2}$ ,  $(g)^{-1}$  is the inverse of transformation matrix. The presence of the inverse of transformation matrix in the above equation implies the rotation of the crystal direction  $[hkl]$  to align with the predefined sample direction. In the second step, position of the projection image on the pole figure is calculated from the spherical coordinates ( $\alpha_{hkl}$  and  $\beta_{hkl}$ ). The angular coordinate ( $\beta_{hkl}$ ) of the projection image on the pole figure is identical to the corresponding coordinate of the pole on the unit sphere, whereas the radial coordinate ( $\Phi_{hkl}$ ) is given by:

$$\Phi_{hkl} = R \cdot \tan\left(\frac{\alpha_{hkl}}{2}\right) \quad (2.5)$$

with  $R$  the radius of the unit sphere ( $R = 1$ ). In a similar way, the position of a projection on the inverse pole figure can also be determined. To account for the rotation of sample direction in a fixed crystal reference frame of the inverse pole figure, the transformation matrix is replaced by its inverse in equation 2.2.

#### 2.1.4 Euler angles

*Euler angles* refer to a set of three consecutive rotations which transforms a coordinate system from the sample position to the one of a crystal. The rotations of Euler angles can be implemented in various ways, but the most common method is formulated by H.J. Bunge [2]. In Bunge notation, a coordinate system, initially coinciding with the sample reference system, is first rotated around its Z-axis of the angle  $\varphi_1$ . Due to this rotation, the X- and Y-axes of the coordinate system transforms to the X'- and Y'-axes. The second rotation of the angle  $\Phi$  around the X'-axis then transforms the Z- and Y'-axes to Z'- and Y''-axes. Finally, the rotation of angle  $\varphi_2$  around the Z'-axis brings the coordinate system to the position of the crystal (Figure 2.3). Analytically, the three rotations of Euler angles are represented by transformation matrices:

$$g_{\varphi_1}^Z = \begin{pmatrix} \cos \varphi_1 & \sin \varphi_1 & 0 \\ -\sin \varphi_1 & \cos \varphi_1 & 0 \\ 0 & 0 & 1 \end{pmatrix}$$

$$g_{\Phi}^{X'} = \begin{pmatrix} 1 & 0 & 0 \\ 0 & \cos \Phi & \sin \Phi \\ 0 & -\sin \Phi & \cos \Phi \end{pmatrix} \quad (2.6)$$

$$g_{\varphi_2}^{Z''} = \begin{pmatrix} \cos \varphi_2 & \sin \varphi_2 & 0 \\ -\sin \varphi_2 & \cos \varphi_2 & 1 \\ 0 & 0 & 1 \end{pmatrix}$$

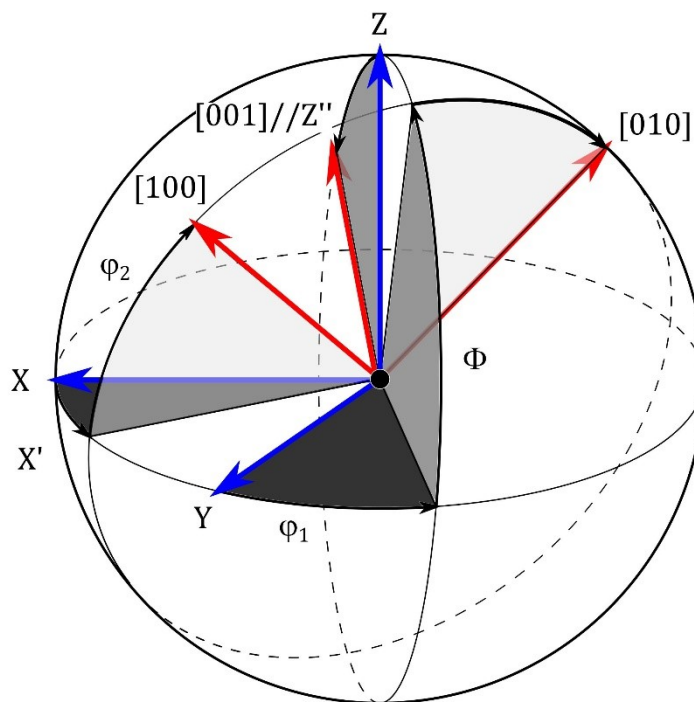


**Figure 2.3 Rotations through the Euler angles ( $\varphi_1, \Phi, \varphi_2$ ) in order to bring the sample reference system to the position of the crystal reference system.**

The transformation matrix of an orientation is thus composed by the multiplication of these transformation matrices corresponding to the three Euler rotations:

$$g = g_{\varphi_2}^{Z''} \cdot g_{\Phi}^{X'} \cdot g_{\varphi_1}^Z \quad (2.7)$$

Following its definition, any orientation can be represented by a set of three Euler angles of  $(\varphi_1, \Phi, \varphi_2)$ . This representation is convenient for the expression of an orientation by a point in a three dimensional Cartesian space, specifically named the Euler space. Because the Euler angles are periodic with the interval of  $2\pi$ , the span of Euler space is from 0 to  $2\pi$  in all three dimensions  $(\varphi_1, \Phi, \varphi_2)$ . However, for any orientation of the coordinates  $(\varphi_1, \Phi, \varphi_2)$ , there always exists an equivalent orientation of the coordinates  $(\pi+\varphi_1, 2\pi-\Phi, \pi+\varphi_2)$ . This relationship can be easily recognized from the identity of corresponding transformation matrices. Because of this equivalence, an Euler space of  $0 \leq \varphi_1, \varphi_2 \leq 2\pi$  and  $0 \leq \Phi \leq \pi$ , is enough to represent all crystallographic orientations in general.

Depending on the crystal and the sample symmetries, orientations have more equivalent positions in Euler space. The multi-position of an orientation in the Euler space can be reduced by limiting the range of Euler angles so that each orientation has a unique coordinate representation in the space. The reduced Euler space is called the fundamental zone or asymmetric domain, and can be derived for specific sample and crystal symmetry classes. For cubic crystals, the effect of various sample symmetries on the span of Euler space was investigated by Popiech [3]. As the sample symmetry changes from triclinic (no symmetry) to monoclinic and orthotropic, the maximum value of the  $\varphi_1$ -angle is reduced from  $2\pi$  to  $\pi$  and  $\pi/2$ , whereby the ranges of  $\varphi_1$ - and  $\Phi$ -angles are kept fixed from 0 to  $\pi/2$ . These reduced Euler spaces are obtained by considering only the two- and four-fold symmetries of cubic crystals. In fact, a smaller range of the  $\Phi$ -angle can be derived by taking into account the threefold rotation axis along the  $\langle 111 \rangle$  direction of the cubic crystal. However, by including the threefold symmetry, the fundamental zones of Euler space will have irregular shapes which is rather difficult for graphic representations and visualization. Therefore, the threefold symmetry of cubic crystal is commonly suppressed in the determination of fundamental zones, making an orientation appear three times in reduced Euler spaces.

For better visualization, texture and crystallographic orientations are usually shown in two-dimensional sections, instead of the three dimensional volume, of the Euler space. Sections of constant  $\varphi_1$  or  $\varphi_2$ -Euler angle are intensively used. Among those, the section of  $\varphi_2 = 45^\circ$  is of particularly interest for texture analyses of BCC structural material. As can be seen in the Figure 2.4, most of the important orientations and texture fibers in BCC structural materials are represented in this section. Their exact Euler coordinates and also the equivalent Miller indices are given in Table 2.1.

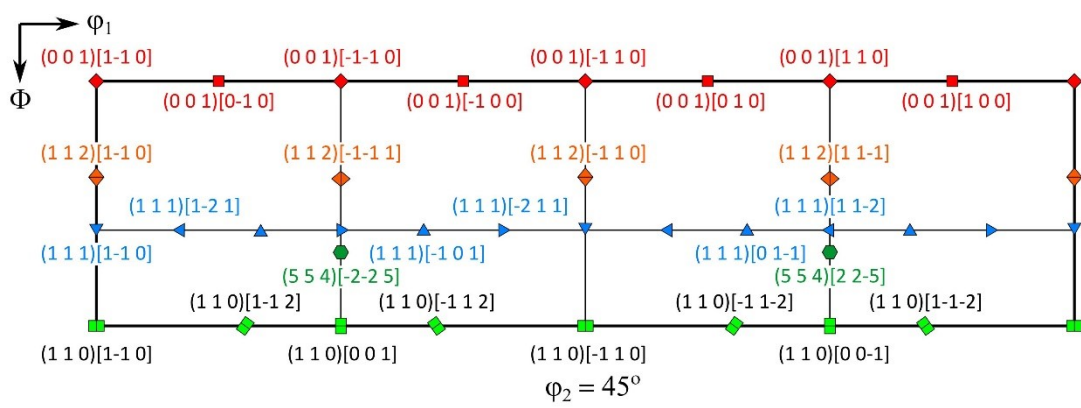


**Figure 2.4** The  $\varphi_2 = 45^\circ$  section of Euler space representing important orientations and texture fibers of BCC structural materials with cubic crystal and triclinic sample symmetries.

The representation of orientation by coordinates of a point in Euler space is very comprehensive. However, orientation distances are not comparable in the Euler space. That is because the Euler space is a curved space; i.e. volumes of orientation elements ( $d\varphi_1 d\Phi d\varphi_2$ ) are not identical across Euler space. They are different by a sine function of the  $\Phi$ -angle, the volume element is defined by  $\sin\Phi (d\varphi_1 d\Phi d\varphi_2)$ . Only orientation distances, lying in the plane  $\Phi = \text{constant}$  of the Euler space, can be directly compared from the difference in Euler coordinates ( $d\varphi_1$  and  $d\varphi_2$ ). The curvature of Euler space even becomes a singularity in the plane  $\Phi = 0$ , where an orientation is represented by a line of  $\varphi_1 + \varphi_2 = \text{constant}$ , instead of a point. In the plane  $\Phi = 0$ , orientation distances are defined by the difference in either  $\varphi_1$ - or  $\varphi_2$ - coordinates, but not in both.



Designation	Euler angles ( $\phi_1, \phi, \phi_2$ )	Miller indices (hkl)[uvw]
H	(0, 0, 45)	{001}<110>
C	(45, 0, 45)	{001}<100>
J	(0, 19.27, 45)	{113}<110>
I	(0, 35.26, 45)	{112}<110>
E	(0, 54.74, 45)	{111}<110>
F	(30, 54.74, 45)	{111}<112>
G	(90, 90, 45)	{110}<001>
L	(0, 90, 45)	{110}<110>
Cu	(90, 35.26, 45)	{112}<111>
Br	(35.26, 90, 45)	{110}<112>
$\alpha$ -fiber		<110> // RD
$\gamma$ -fiber		<111> // ND
$\theta$ -fiber		<001> // ND
$\tau$ -fiber		<110> // TD

**Table 2.1 Orientations and texture fibers in the  $\phi_2 = 45^\circ$  section of BCC structural materials.**

Beyond representations which are mentioned here, crystallographic orientations can also be described by axis/angle pairs, Rodrigues vectors and unit quaternions. In general, each representations have their unique properties, which, if purposely applied, can bring a lot of convenience to investigations of crystallographic orientation and texture. However, they also contain ineligible disadvantages. Conclusively, there is no superior representation for crystallographic orientation and texture. For quantitative texture analysis, the most popular representation are Euler angles, which is partly due to the full development of mathematical operations in Euler space [2]. In the section below, the use of generalized spherical harmonics to express an orientation distribution function (ODF) in Euler space is briefly described. A similar method in unit quaternion space, which has recently been developed, can be referred from elsewhere [4;5].

## 2.2 Representation of orientation distribution function

Microstructures of polycrystalline materials in general are characterized by grains of various sizes, shapes and crystallographic orientations. Phase and chemical compositions also play crucial roles on the formation of microstructure. Although a concept of generalized microstructure function has been proposed [6], a detailed representation of microstructure is very complicate for mathematical descriptions. For texture analyses, the focus is on crystallographic orientations and their volume

fractions, while other microstructure features are not concurrently considered. In this section, the representation of crystallographic orientation density by orientation distribution function is described.

For an orientation  $g$ , enclosed by an element of orientation  $dg$  in the orientation space, occupies the volume  $dV$  in the microstructure. If  $V$  is the total volume of all orientations in the microstructure, the volume fraction of the orientation ( $g$ ) is defined by:

$$\frac{dV}{V} = f(g)dg \quad (2.8)$$

In this equation,  $f(g)$  is the *orientation distribution function* (ODF), which represents the statistical dispersion in an infinitesimal element around orientation  $g$  in the orientation space. The higher the value of  $f(g)$ , the larger volume fraction of the orientation ( $g \pm dg$ ) in the microstructure.

By a series of generalized spherical harmonics, any ODF is constructed as:

$$f(g) = \sum_{l=0}^{\infty} \sum_{m=-l}^{+l} \sum_{n=-l}^{+l} C_l^{mn} T_l^{mn}(g) \quad (2.9)$$

in which,  $C_l^{mn}$  are series expansion coefficients corresponding to the terms of the generalized spherical harmonic functions  $T_l^{mn}(g)$ . As the orientation  $g$  is denoted by three Euler angles  $(\varphi_1, \Phi, \varphi_2)$ , the generalized spherical harmonics can be written as:

$$T_l^{mn}(g) = e^{im\varphi_2} P_l^{mn}(\cos \Phi) e^{in\varphi_2} \quad (2.10)$$

where  $P_l^{mn}(\cos \Phi)$  is the generalized form of the associated Legendre functions. It can be expressed by a Fourier series:

$$P_l^{mn}(\cos \Phi) = \sum_{s=-l}^{+l} Q_l^{ms} Q_l^{ns} e^{is\Phi} \quad (2.11)$$

with  $Q_l^{ms}$  are real coefficients, which are commonly given in form of tables of input data for each  $l$ -indices, as in [7]. In principles, the value of  $Q_l^{ms}$ -coefficient is defined

for each  $m$ - and  $s$ -index, ranging from  $-l$  to  $+l$  value. However, the number of independent values is massively reduced, because of the relationships between  $Q_l^{ms}$ -coefficients:

$$\begin{aligned} Q_l^{ms} &= (-1)^{l+s} Q_l^{-ms} \\ Q_l^{ms} &= Q_l^{sm} \end{aligned} \quad (2.12)$$

From these relationships, it can be concluded that the value of function  $P_l^{mn}(\cos\Phi)$  is either real or purely imaginary, uniquely depending on whether the sum of  $m$ - and  $n$ -indices are even or odd.

Since an orientation can be described by a rotation matrix and if two rotations ( $g_1$  and  $g_2$ ) are carried out successively, the final orientation is represented by a multiplication of corresponding matrices ( $g_2 \cdot g_1$ ). Following to this rule, the addition theorem of generalized spherical harmonics, which is nothing than the rule of matrix multiplication, is given as:

$$T_l^{mn}(g_2 \cdot g_1) = \sum_{s=-l}^{+l} T_l^{ms}(g_2) T_l^{sn}(g_1) \quad (2.13)$$

Generally, the values of  $C_l^{mn}$ -coefficients can be chosen freely without any constraint. They can be real or complex values. However, because the ODF is representative for a statistical distribution of orientations, the function  $f(g)$  must be a real and positive quantity. This condition, indeed, implies a relationship between the ODF and its conjugate function:

$$f(g) = f^*(g) \quad (2.14)$$

Providing that the changes in sign of both  $m$  and  $n$ -indices are imposed simultaneous, values of associated Legendre functions are invariant ( $P_l^{mn}(\cos\Phi) = P_l^{m-n}(\cos\Phi)$ ). Applying this relationship to equation of 2.14 leads to the constraint of  $C_l^{mn}$ -coefficients:

$$C_l^{*mn} = (-1)^{m+n} C_l^{-m-n} \quad (2.15)$$

Furthermore, the value of the ODF at any orientation ( $g$ ) is expected to be identical when crystal ( $g_B$ ) and sample ( $g_A$ ) symmetric rotation transformations are applied:

$$f(g) = f(g_B \cdot g \cdot g_A) \quad (2.16)$$

The selection of  $C_l^{mn}$ -coefficients, in fact, is limited by the presence of crystal and sample symmetries. Taking into account the condition of symmetries, specific relations between coefficients can be derived [8]. Among the series expansion coefficients of the ODF, only some ( $C_l^{sn}$ ) are independent quantities. The rest  $C_l^{mn}$ -coefficients must follow certain relations of the symmetry groups:

$$C_l^{mn} = \sum_{s=-l}^{+l} T_l^{ms}(g_B) C_l^{sn} \quad (2.17)$$

which are simply linear combinations of independent  $C_l^{ns}$ -coefficients, with the pre-factors being generalized spherical harmonics of particular symmetry operation ( $g_B$ ). Differently, the condition of symmetries can be incorporated by the method of symmetrically invariant functions [3]. Instead of the functions ( $T_l^{mn}(g)$ ), symmetric generalized spherical harmonic functions ( $T_l^{\mu\nu}(g)$ ) can be defined as:

$$T_l^{\mu\nu}(g) = \sum_{m=-l}^{+l} \sum_{n=-l}^{+l} A_l^{\mu m} A_l^{\nu n} T_l^{mn}(g) \quad (2.18)$$

where  $A_l^{\mu m}$  and  $A_l^{\nu n}$  are symmetry coefficients of the left (crystal) and right (sample) symmetry groups, respectively. Values of  $A_l^{\mu m}$  and  $A_l^{\nu n}$ , in principle, are solutions of the system of equations:

$$T_l^{\mu\nu}(g) = T_l^{\mu\nu}(g_B \cdot g \cdot g_A) \quad (2.19)$$

Depending on the symmetry group, solutions of symmetry coefficients are different. For most of the crystallographic symmetry groups, the expression of the

symmetry coefficients is rather simple. For instance, the  $A_l^{\mu m}$  coefficients of the orthorhombic group ( $D_2$ ) can be written as:

$$A_l^{\mu m} = \frac{\varepsilon_m}{\sqrt{2}} [\delta_{m'm} + (-1)^{m'} \delta_{-m'm}]$$

$$m' = 2(\mu - 1)$$
(2.20)

$$\varepsilon_m = \begin{cases} \frac{1}{\sqrt{2}} & \text{if } \mu = 1 \\ 1 & \text{if } \mu \neq 1 \end{cases}$$

However, this is not the case for the cubic symmetry groups (T and O), whereby the diagonal threefold axis is coexistent to the two- and fourfold axes. There is no simple analytical expression for the  $A_l^{\mu m}$  coefficient of cubic symmetry groups. They need to be derived numerically by solving the system of equations 2.19 with ( $g_B$ ) being an element of the cubic group and ( $g_A$ ) being an element of the triclinic group, as suggested by Bunge [2]. Alternatively, they can be calculated by using mathematical operators called projectors and their associated matrices, as proposed by Esling et al [9]. In current practice of quantitative texture analysis, the symmetry coefficients of cubic symmetry groups are calculated once and stored as input data of texture analysis software. Once the  $A_l^{\mu m}$  and  $Q^{ms}$ -coefficients are known, the symmetric ODF can be written as:

$$f(g) = \sum_{l=0}^{\infty} \sum_{\mu=1}^{M(l)} \sum_{\nu=1}^{N(l)} C_l^{\mu\nu} T_l^{\mu\nu}(g)$$
(2.21)

whereby  $C_l^{\mu\nu}$  are the coefficients of the symmetric generalized spherical harmonics,  $M(l)$  and  $N(l)$  are the numbers of linearly independent solutions of  $A_l^{\mu m}$  and  $A_l^{\nu n}$  coefficients.

Like the functions  $T_l^{mn}(g)$ , the symmetric generalized spherical harmonics  $T_l^{\mu\nu}(g)$  form a systems of orthonormal functions:

$$\int_{\Omega} T_l^{\mu\nu}(g) T_l^{*\mu'\nu'}(g) dg = \frac{1}{2l+1} \delta_{ll} \delta_{\mu\mu'} \delta_{\nu\nu'} \quad (2.22)$$

with  $T_l^{*\mu\nu}(g)$  being the complex conjugate quantity of  $T_l^{\mu\nu}(g)$  function,  $\Omega$  represents the set of all orientations in the reduced Euler space. If both sides of the equation 2.21 are multiplied with the quantity of  $T_l^{*\mu\nu}(g)$  and integrated over the orientation space, the orthonormal relationship of symmetric generalized spherical harmonics leads to:

$$C_l^{\mu\nu} = (2l+1) \int_{\Omega} f(g) T_l^{*\mu\nu}(g) dg \quad (2.23)$$

This equation can serve for the determination of the  $C_l^{\mu\nu}$ -coefficients from a set of discrete orientations obtained by EBSD measurements or texture simulations. Providing that the volume fractions of discrete orientations are known, the  $C_l^{\mu\nu}$ -coefficients can be determined by substituting equation 2.8 into the right part of equation of 2.23 and changing the integral operator to sum over all orientations in the set:

$$C_l^{\mu\nu} = (2l+1) \sum_i T_l^{*\mu\nu}(g_i) \left( \frac{dV_i}{V} \right) \quad (2.24)$$

In the next section, the EBSD technique and orientation determination from EBSD patterns are described. For the derivation of crystallographic pole density functions (PDFs) by X-ray or neutron diffractions, and the calculation of  $C_l^{\mu\nu}$ -coefficients from these functions the reader is referred to [1;2].

### 2.3 Measurement of crystallographic orientations by EBSD

Electron backscatter diffraction (EBSD) is one of the most powerful characterization methods, which can directly link microstructure and crystallographic texture of materials. In this technique, diffraction patterns of backscattered electrons are collected and used for the local determination of crystallographic orientation. The physical phenomenon and geometrical set-up of the EBSD technique are briefly explained hereunder.

Because of the wave-particle duality, electron beams also can be considered as waves of radiation. Like electromagnetic radiations, electrons are diffracted by elastic scattering of the incident waves at the atoms of the sample material. The difference of electron diffraction from other types of diffraction (i.e. X-rays, neutron ...) is in the interaction with the diffracting substance. Electrons interact with both the shell electrons and the nucleus of the scattering atoms, while X-rays only interact with the former and neutrons with the latter. The wavelength of electron radiations is in a range of  $10^{-6}$  to  $10^{-5}$   $\mu\text{m}$ , which is several orders of magnitude smaller than those of common neutron and X-ray radiations. Obviously, this statement excludes synchrotron radiations which have similar or even smaller wavelengths of electrons, but require large and much more sophisticated particle accelerators. The scattering amplitude of electron radiation, which describes the efficiency of an atom in scattering radiation, decreases with  $\sin\theta/\lambda$ , which is similar to that of X-rays, but more rapidly from a much higher initial value. Therefore, the intensity of electron diffraction patterns exhibits a strong contrast, and electron radiation is better suited to apply for high resolution investigations than other types of radiations.

For crystalline materials in which atoms are arranged periodically, scattered waves of electron radiations interfere to form a secondary wave. In most of the cases, the reflected intensity is annihilated to zero, because of the destructive interference of the diffracted waves. Only at specific angles will the wave fronts be in phase, and is the reflected intensity enhanced. The condition for reinforcement of reflected beams can be described by the Bragg law of diffraction:

$$n\lambda = 2d \sin \theta \quad (2.25)$$

whereby  $n$  represents the order of reflection,  $d$  is the spacing of atomic planes,  $\lambda$  is the wavelength of the incident beam and  $\theta$  is the so called Bragg angle, i.e. half of the angle between the transmitted and diffracted beams. Although Bragg's law of diffraction is simply a geometrical relationship of lattice spacing, the wavelength of the incident radiation and the diffraction angle, it is equally obeyed by an incident electron beam, illustrating perfectly the wave-particle duality of elementary particles.

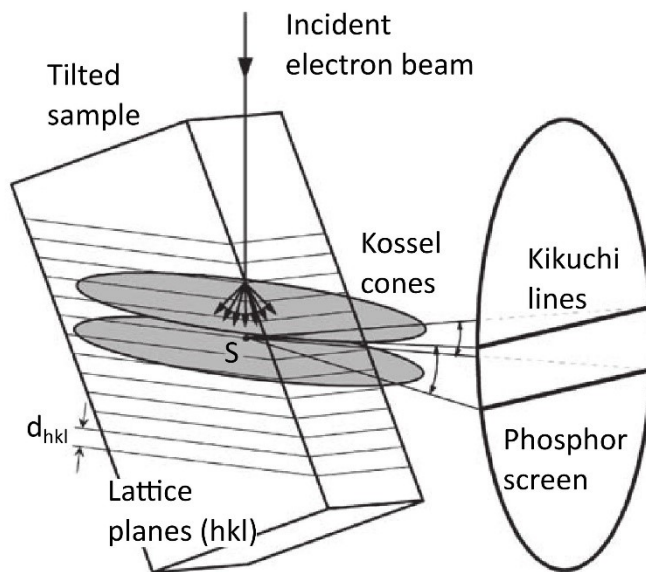


**Figure 2.5 Diffraction of diffracted electrons when incident electrons interact with crystal forms Kossel cones and Kikuchi lines [1]**

A remarkable feature of electron diffraction is the *diffused scattering*, occurring when an electron beam enters a crystalline sample. For a given lattice plane, elastic scattered radiations come from all directions of space, i.e. not solely from the direction of incident beam. The diffraction of scattered electrons, therefore, occurs in all directions which incline to the crystal plane of the same Bragg angle ( $\theta$ ), Figure 2.5.

The loci of diffracted radiations are circular conical surfaces. These cones, so called Kossel cones, symmetrically extend about the normal axis of the crystal plane in both positive and negative directions with the half apex angle of  $90^\circ - \theta$ .

To obtain electron diffraction patterns, planar detector systems (e.g. phosphor screen and CCD camera) are employed. Because of the detector geometry, electron diffraction patterns, in principle, appear as the intersection of a plane with a conic surface, thus producing a conic section. However, for typical values of electron wavelength and lattice spacing, the Bragg angle of electron diffraction is approximately  $0.5^\circ$  to  $1.0^\circ$ . The half apex angle of diffraction cones is close to  $90^\circ$ , and these cones are almost flat. Consequently, the intersection of the detector plane and diffraction cones can be considered as a pair of parallel lines. These pairs of lines, called Kikuchi bands, are distinctive for each crystal plane. The angular distance between lines of a Kikuchi band ( $2\theta$ ) is dependent on the lattice spacing ( $d$ ) of the diffracting plane, according to Bragg's law. The intersections of various Kikuchi bands define projections of zone axes in the electron diffraction patterns. The distance between two projected points is proportional to the angles of the two zone axes.



By calculating angular relationships between zone axes of a diffraction pattern and comparing them to those of a standard pattern, crystallographic orientations of diffracted volumes can be determined. The orientation determination of electron backscatter diffraction pattern is, theoretically, straightforward. However, the geometrical setup of EBSD measurements is usually complicated and has a huge impact on the accuracy of orientation determination. Generally, investigated samples are tilted  $60^\circ$  to  $80^\circ$  respectively to the beam axis, while the camera is set vertically in the working chamber of microscopes. The purpose of this geometrical setup is to maximize the intensity of backscattered radiations with the penalty of spatial resolution which deteriorates with increasing tilting angle of the sample. In addition, the angular range of the measured pattern is sensitive to the distance between the diffracting spot and the detector. For a longer distance, the angular range of the measured pattern is smaller, the number of captured Kikuchi bands is less and the contrast of the diffraction pattern become weaker. If the detector is moved closer to the sample, the number of Kikuchi bands is more abundant, but the resolution of patterns is also reduced. In both extreme positions, the confidence of orientation determination is low. Therefore, the distance between sample and detector is always optimized and calibrated for each microscope-EBSD detector systems.

The orientation determination or indexation is tedious and time consuming for manual implementation. Alternatively, it can be speed up by using computational algorithms. One of the most effective algorithms uses the Radon transform to convert the measured diffraction pattern to a Hough image [10]. Since the Radon transform converts a straight line to a point, Kikuchi bands of the measured diffraction pattern are represented by points in the Hough image. The comparison of the measured and standard diffraction patterns is easier and more robust with the image transformation. Nowadays, the fully automated procedure can bring the maximum indexing speed of 100 to 200 patterns per second. It means a million of crystallographic orientations can be measured within a couple of hours. Combining with appropriate scanning step size and the moving of sample stage, EBSD can be used for investigations of both large sample areas (e.g. several millimeters square) and high resolution (e.g.  $\sim 20$ -100 nanometers). Orientation information, collected by EBSD

measurements under appropriate conditions, is statistically significant for the determination of the material texture and comparable to the ones observed in texture measurements by X-ray diffraction.

## *2.4 Summary*

Polycrystalline materials are composed by an aggregate of crystal grains. The microstructure of these materials is characterized by many parameters, liked shape, size and orientation of grains. The crystallographic orientation can be represented by various mathematical entities. Among these, the transformation matrix, Miller indices, spherical coordination projection (i.e. pole figure and inverse pole figure) and Euler angles are described in this chapter. Each of these representations has its own advantages and disadvantages. However, there is no perfect description for all applications. For texture analysis, the Euler angles are wider used than other notations. In this chapter, mathematical methods, based on spherical harmonic expansions, for quantitative texture analyses in Euler space were reviewed in detail. These methods help to construct the orientation distribution function of materials from pole density measurements and discrete orientation collections. Electron backscatter diffraction, a powerful experimental method to collect discrete orientations in combination with microstructural observation, is also described in this chapter.

## *2.5 References*

- [1] Engler O, Randle V. Introduction to Texture Analysis - Macrotecture, Microtexture, and Orientation Mapping, Second ed.; 2010.
- [2] Bunge HJ. Texture Analysis in Materials Science - Mathematical Methods, First ed. Berlin: Butterworth & Co; 1982.
- [3] Bunge HJ, Esling C. Quantitative Texture Analysis, First ed. Germany: Deutsche Gesellschaft fur Metalkunde; 1982.
- [4] Mason JK, Schuh CA. Hyperspherical harmonics for the representation of crystallographic texture. *Acta Mater.* 2008;56:6141.

- [5] Mason JK, Schuh CA. Expressing crystallographic textures through the orientation distribution function: Conversion between generalized spherical harmonic and hyperspherical harmonic expansions. *Metal Mat Trans A Phys Metall Mat Sci.* 2009;40:2590.
- [6] Fullwood DT, Niezgoda SR, Adams BL, Kalidindi SR. Microstructure sensitive design for performance optimization. *Prog Mater Sci.* 2010;55:477.
- [7] Bunge HJ. Calculation of the Fourier Coefficients of the Generalized Spherical Functions. *Krist. Tech.* 1974;9:939.
- [8] Roe RJ. Inversion of pole figures for materials having cubic crystal symmetry. *Journal of Applied Physics.* 1966;37:2069.
- [9] Kyōkai NT. Proceedings: The sixth international conference on Texture of Materials (ICOTOM6) September 28/October 3, 1981, Tokyo, Japan: Iron and Steel Institute of Japan; 1981.
- [10] Lassen NK. Automated determination of crystal orientations from electron backscattering patterns. Department of Mathematical Modelling, vol. PhD: Technical University of Denmark, 1994.

# 3

## Electrical steels

### *3.1 Introduction to electrical steels*

Electrical steel is a common name for one group of iron and silicon alloys [1]. These alloys are also known as silicon (Si) steels, although they usually contain a very small amount of carbon (C) to be considered as steels. As discussed in the following sections, the magnetic properties of electrical steels are influenced by the chemical composition, microstructure, and texture of the material.

#### *3.1.1 Alloying elements*

The main alloying element of electrical steels is silicon (Si), which is intentionally added to materials with the aim to modify electric and magnetic properties the pure iron. In Figure 3.1, dependences of several electric and magnetic properties on silicon content of electrical steels are summarized. Adding more silicon to pure iron produces

iron-silicon alloys of higher electrical resistivity but lower magnetic saturation induction. Similarly, crystal anisotropy and mechanical ductility (represented by total elongation) of materials decrease with the increasing of the silicon content. For a good balance among various properties, commercial electrical steels typically contain 1.0 to 3.5 wt.% Si. Higher silicon contents make materials too brittle to be cold rolled into sheet [2]. However, materials containing up to 6.5 wt.% Si have been produced in laboratory scale. The main aim for these high silicon alloys is to further increase electrical resistivity and decrease magnetic anisotropy at the price of lower magnetic saturation, as compared to conventional materials. The high-silicon alloys have been considered promising materials for high-frequency applications. Nevertheless, none of the current manufacturing methods for high silicon steels is applied successfully to commercial production.

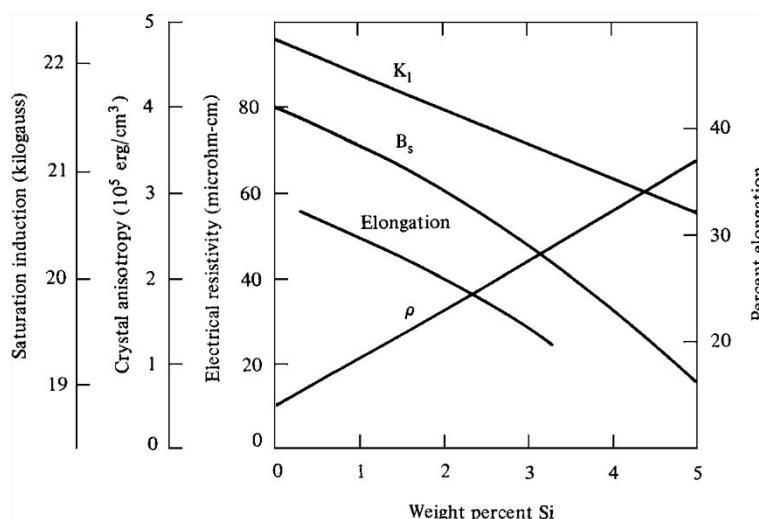


**Figure 3.1 Dependence of magnetocrystalline anisotropy constant  $K_1$ , saturation induction  $B_s$ , electrical resistivity  $\rho$  and total elongation for non-oriented polycrystalline sheet 0.47 mm thick [2].**

Besides Silicon, Aluminum (Al) is also popularly used as an alloying element for electrical steels. Aluminum, in general, have similar effects as Silicon on magnetic induction, magnetostriction and electrical resistivity of electrical steels. Influences of Al on electrical steels, however, are far less than those of Si. The alloy of  $Fe_{1-x-y}Si_xAl_y$  with optimum composition of  $x=0.1$  and  $y=0.05$  in weight fraction has very special properties of nearly zero anisotropy, zero magnetostriction and very low core loss [1]. It is widely produced in the commercial name of Sendust. Nevertheless, because of the high amount of alloying elements (Silicon and Aluminum), the formation of ordered phases ( $Fe_3Si$  and  $Fe_3Al$ ) increases remarkably. These DO3 ordered phases result in

very brittle materials so that the materials are mostly provided in powder or dust form.

### *3.1.2 Impurities*

The occurrence of other elements in the form of impurities may have a negative effect on the magnetic properties of electrical steels. Concentrations of nitrogen (N), oxygen (O), and sulfur (S) exceeding 20 ppm may be detrimental to the permeability and lead to increased energy losses of steels [1]. In solution, these elements have negligible effect on the magnetic properties, except for a small reduction in the saturation magnetization. However, in precipitated inclusions (especially those with sizes of  $\sim 0.1 \mu\text{m}$ ), impurities induce magnetic aging, i.e., a slow deterioration of magnetic properties with time [3]. Additionally, inclusions have a significant impact on the grain size and crystallographic orientation of the polycrystal. Nevertheless, the presence of impurities in electrical steels must be well controlled rather than completely eliminated [3]. This is attributed to the fact that inclusions can be used for microstructure and texture modification of steels. In fact, during primary and secondary recrystallization, manganese sulfide (MnS) and aluminum nitride (AlN) are frequently used to inhibit the growth of magnetically unfavorable crystallographic orientations. Inclusion-induced retardation of domain wall motion is then minimized by subsequent heat treatments (e.g., desulfurization).

### *3.1.3 Grain size*

The magnetic properties of electrical steels are also influenced by the grain size. In fact, the magnetic losses increase with increasing grain size of the polycrystal, owing to the increased width of the magnetic domains and distance that the walls must move during magnetization. In contrast, the total grain boundary length in the microstructures increases with decreasing grain size. Most of the boundaries act as magnetic obstacles and are overcome only with additional energy, thereby leading to an increase in the hysteresis loss of the steels. The effects of grain size on the magnetic

properties are usually balanced by optimizing the microstructure of the steels [4]. The desired grain size (ranging from a hundred micrometers to ten millimeters) of the material depends on the application of the material.

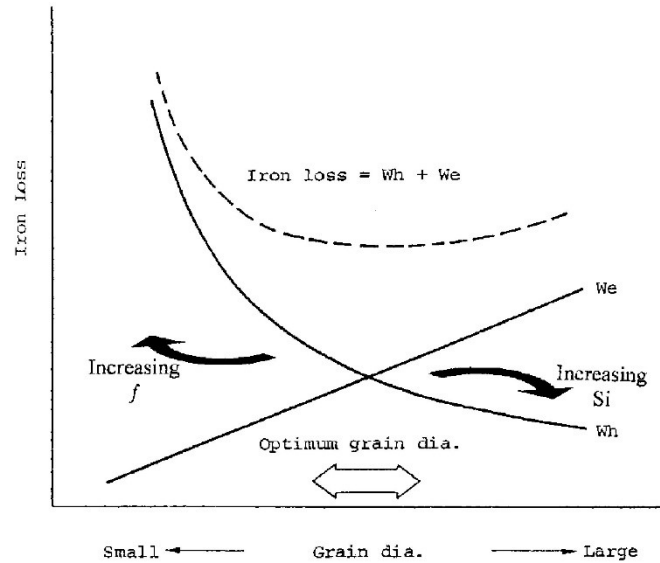


**Figure 3.2 Grain-size dependence of core losses in electrical steels [4].**

### 3.1.4 Texture

Electrical steels are used in magnetic flux-carrying cores and, hence, magnetic anisotropy

constitutes one of the most important properties of these materials. The anisotropy of steels results from the structural arrangement of atoms in each crystal grain and preferred orientations of grains in the polycrystal.

At room temperature, crystallites of iron and silicon alloys have a body-centered cubic (BCC) structure. Like those of other BCC-structured materials, under low applied fields, the saturation magnetizations of electrical steels are achieved when the

$\langle 100 \rangle$  axes of the crystallites are aligned parallel to the field direction (Figure 3.3). This indicates that the saturation magnetization along  $\langle 100 \rangle$  axes (i.e., the easy directions of magnetization) is realized only through domain wall motion (Figure 3.4). In contrast to the saturation

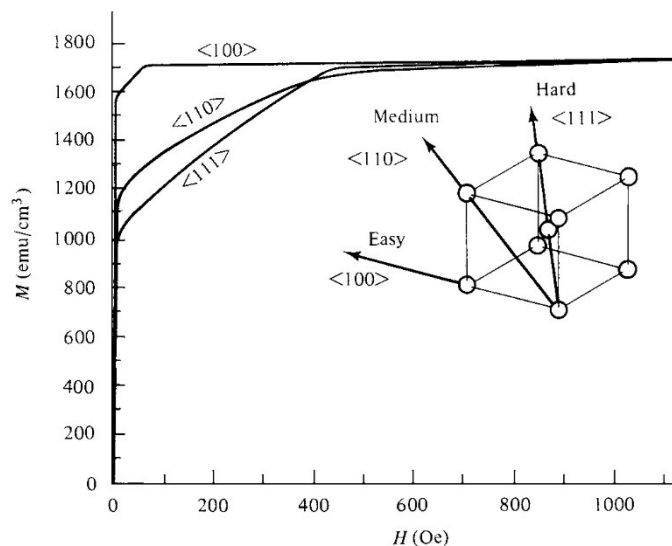


**Figure 3.3 Magnetization curves for single crystals of iron [2].**

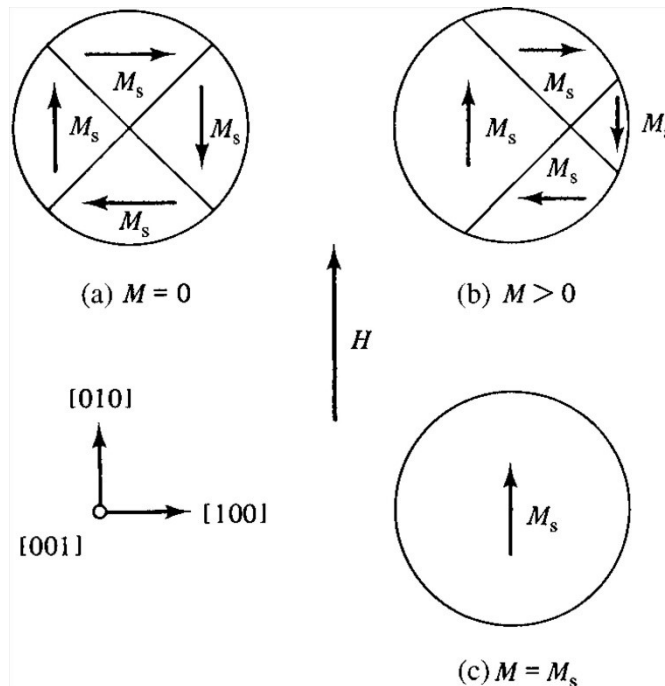


**Figure 3.4 Magnetization along the [010] direction of an iron single crystal. The saturation of magnetization occurs via domain wall motion at relatively low applied fields [2].**

magnetization along the  $\langle 100 \rangle$  axes, the magnetization along other crystal axes (e.g.,  $\langle 110 \rangle$  or  $\langle 111 \rangle$ ) occurs (i) only under relatively high fields and (ii) via both domain wall motion and domain rotation (Figure 3.5). During domain rotation, the net magnetic moment of each atom, rather than the domain (i.e., groups of atoms), is rotated. The net magnetic moment is very strong and, therefore, magnetization fields of several hundred oersteds (rather than a few tens of oersteds as in the case of  $\langle 100 \rangle$  axes) are required.

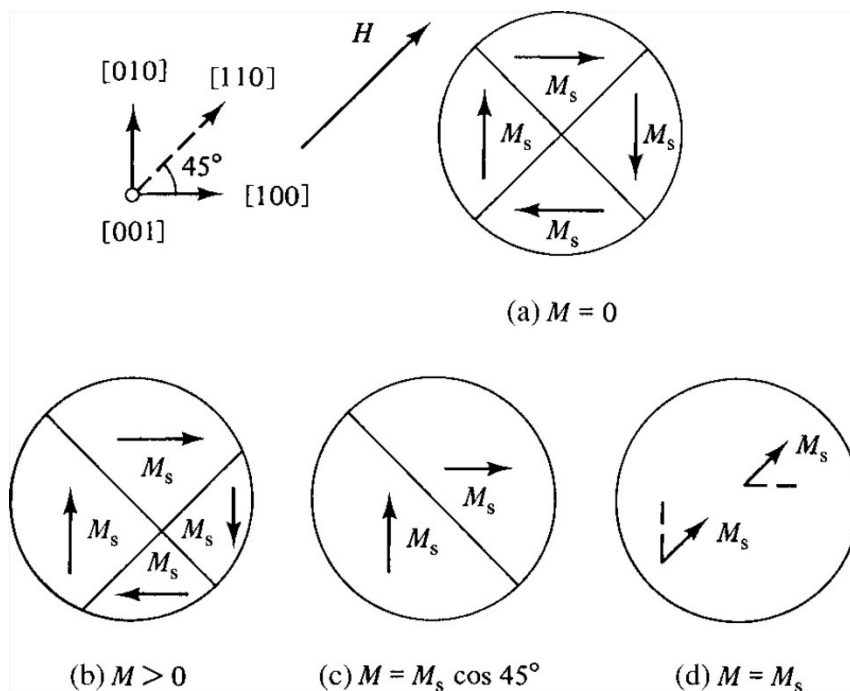


**Figure 3.5 Magnetization along the [110] direction of an iron single crystal. The saturation magnetization is realized after domain wall rotation at high applied fields [2].**



In an aggregate, magnetic anisotropy is maintained and magnified by the preferred orientations of the crystallites (i.e., texture). Furthermore, different electromagnetic devices require specific magnetization fields. The orientations comprising the optimum textures that yield excellent magnetic properties of various electrical steels, therefore, vary with the intended application of the steel.

For transformers, magnetization fields are applied along a unique direction. Suitable textures for GO electrical steels contain a high fraction of  $\langle 100 \rangle$  crystal axes that are parallel to a certain direction in the sheet plane. In reality, only the well-known Goss texture (after N.P. Goss [5] who developed the complex cold rolling and annealing processing route that yields the  $\{110\}\langle 001 \rangle$  orientation) is technically feasible. In a rolled sheet, the  $\{110\}$  planes and  $\langle 001 \rangle$  axes of Goss-oriented grains are parallel to the rolling plane and the rolling direction, respectively.

For rotating devices, magnetization fields operate in all directions of the sheet plane. Therefore, textures with an isotropic distribution of easy magnetization directions ( $\langle 100 \rangle$  crystal axes) on the same plane are considered ideal for the materials. This condition is best fulfilled by the  $\theta$ -fiber texture or the so-called Cube fiber texture. From a crystallographic point of view, the Cube fiber texture is characterized by all grains with a (i)  $\{100\}$  plane parallel to the plane of the sheet and (ii) homogeneous distribution of two  $\langle 100 \rangle$  axes on this plane.

### *3.2 Histories of electrical steels*

By their application, electrical steels are divided into two main classes namely, grain-oriented (GO) steels and non-oriented (NO) steels, which are used for transformers and rotating devices (i.e., motors and generators), respectively.

#### *3.2.1 Grain-oriented (GO) electrical steels*

The application of GO electrical steels is traced back to the 1880s when wrought iron was first used as magnetic cores of transformers. Despite the abundance and availability of the material at that time, the corresponding magnetic properties were poor. Improvements in these properties started with the work of Hadfield et al. in 1900. The results of that work showed that adding small amounts of Si to iron yielded

an increase in the resistivity of the cores and, consequently, a decrease in the eddy current loss. Moreover, the harmful effect of impurities in steels was identified and avoided by refining the processes. Although further improvement (i.e., the replacement of the solid core by lamellae-stacked cores) required an additional rolling stage, this replacement helped to reduce the effect of eddy currents. A stacked core of 100 lamellae required  $\sim 50$  times less energy than a solid core with the same dimensions [6].

By the 1920s, the anisotropic nature of the magnetic properties was well understood. This knowledge assisted N.P. Goss in developing a processing route that combines cold rolling and annealing for the production of highly oriented electrical steels [5]. In 1939, production based on this route yielded a reduction (to 1.5 W/kg at 1.5 T and 50 Hz) in the core losses. The Goss-developed process remains the basis of present-day production processes. The formation mechanism of the Goss texture, which has been considered in numerous scientific studies, remains debatable. In 1965, the first-ever high-permeability GO electrical steel was produced by Nippon Steel Corporation.

By the early 1970s, the important role of stress coating was understood, i.e., the stress sensitivity of power loss and magnetostriction is reduced by introducing a high tensile stress during coating. Stress coating is more beneficial for steels with higher

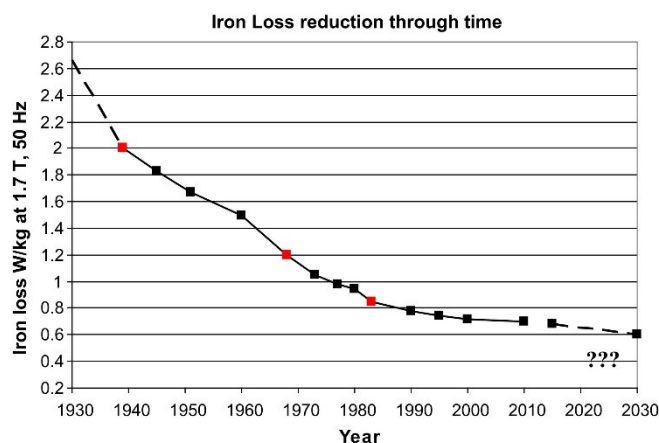


**Figure 3.6** Losses at 1.7T-50Hz in the highest available grades of commercial electrical steels [7].

anisotropy (than for those with lower anisotropy), particularly high-permeability steels. Magnetic properties of the steels have improved steadily with optimization of the production process. In the 1980s, laser scribing in the transverse direction of the rolled strips was used as a loss-reduction strategy for high-permeability steels.

Owing to the domain refinement, laser-scribed steels (separation: 5 mm) suffer 5.0 to 10.0% lower losses than the untreated steels.

Most present-day GO electrical steels, with optimum Si content of 2.9–3.2 wt.%, suffer core losses of 0.74–0.89 W/kg at 1.5 T and 50 Hz. Commercial GO electrical steels include conventional/regular grades (CGO) and high permeability grades (HGO). The strength of the Goss texture and, hence, the magnetic quality constitute the main difference between these grades. In addition, coarse-grained microstructures (grain diameter: 10 mm) are considered ideal for minimizing the influence of grain boundaries on magnetization. The steels are usually produced as coiled strips with thickness and width of 0.23–0.35 mm and up to 1200 mm, respectively.

### *3.2.2 Non-oriented (NO) electrical steels*

The performance of electrical steels for magnetic flux-carrying cores of rotating devices has been gradually improved. Owing to the progressive elimination of impurities, losses at 1.5 T and 50 Hz have been reduced from 7.0 W/kg, in the first Si-containing steels, to <2.0 W/kg, in the best present-day grades {Moses, 1990 #336}. Until the 1930s, strips were produced mainly via hot rolling directly from the slab to the final shape. This process was then replaced by a combination of hot and cold rolling, which (compared with only hot rolling) improved the flatness and uniformity of hot rolled slab. The corresponding magnetic properties of the steels improved, owing to the consistency of the production line. However, cold rolling of the steel usually generates magnetically unfavorable textures, leading to a reduction in the permeability and an increase in the core losses. This negative effect has been minimized and high-quality steels have been obtained by applying a two-stage cold rolling with an intermediate annealing (IA) step. In addition, since the 1960s, coating of the steels has been widely employed as a loss-prevention strategy. Various coating techniques have helped to (i) improve the punching and welding performance during manufacture and (ii) insulate eddy currents between lamella in the steels. Up to the 1980s, electrical steels for rotating devices suffered from magnetic aging (i.e., a slow deterioration of magnetic properties with time) induced mainly by carbide

precipitation. To avoid this effect, decarburization in moist hydrogen ( $H_2$ ) was used to reduce the C content of the steels to a harmless level (i.e., ~20 ppm). The decarburization parameters were selected to ensure that excellent magnetic properties were realized through growth of the microstructure. The standard grain size of NO electrical steels is strongly dependent on the magnetizing frequency, operating flux density, resistivity, Si content, and texture. However, the grain size of 100  $\mu m$  is popularly desired.

NO electrical steels are more versatile than GO electrical steels. The criteria for specific applications and the processing routes employed for achieving the desired properties differ between these steels. The Si content of NO electrical steels (which are classified as either full-processed grades or semi-processed grades) ranges from 0 to 3.0 wt.%. After final annealing, the full-processed grades exhibit high permeability and low hysteresis loss. However, owing to the low material hardness, size and shape control of the stamped products is difficult. Semi-processed grades have gained widespread acceptance in the last few years. These steels are sent to the customer in the partly annealed state with a suitable hardness for stamping. Although requiring a customer heat treatment after punching, semi-processed NO electrical steels have homogeneous magnetic properties. Strips with thicknesses of 0.35 to 0.8 mm are typically produced for both grades of NO steels.

### *3.3 Processing of electrical steels*

#### *3.3.1 Processing of GO electrical steels*

The processing of GO electrical steels is relatively standardized. The Goss process, though developed in the 1930s, still forms the basis of various production routes for GO electrical steels. In a conventional Goss process, the hot-rolled strip is pickled to remove surface oxides. The pickled strip is then cold rolled (to a thickness of ~0.6 mm from an initial hot band thickness of 2.0–2.5 mm), annealed, and subsequently cold rolled to the final thickness (0.2–0.3 mm). Afterward, the carbon content of the material is reduced (to <0.003%) via decarburization and the decarburized strip is then coated with a thin magnesium oxide (MgO) layer. During the key stage of the

Goss process, i.e., a batch annealing performed at 1200 °C for 24 h, the steel undergoes grain growth, which transits to discontinuous growth of {110}<001> grains. The presence of manganese sulfide (MnS) particles, as selective grain growth inhibitors, has a significant effect on the abnormal growth (i.e., secondary recrystallization) of Goss-oriented grains. Moreover, a thin magnesium silicate layer (referred to as the glass film or forsterite layer) is formed from the reaction of magnesium oxide in the surface of the strips. The excessive magnesium oxide is then removed during the flattening of the strips. A thin phosphate layer, applied during the subsequent tension coating, reacts with the magnesium silicate to form a strong, highly insulating coating. At the end of conventional Goss process, the strip has a strong texture, which is 6°-deviated from the {110}<001> orientation.

The first-ever HGO electrical steels were manufactured by Nippon Steel Corporation in 1965. Compared with the conventional Goss process, this manufacturing process eliminated the cold rolling stages, employed aluminum nitride (AlN) as the grain growth inhibitor, and yielded better texture control. Owing to this better control, the permeability and hysteresis of HGO electrical steels were (three-fold) higher and (30–40%) lower, respectively, than those of the CGO electrical steels.

### *3.3.2 Processing of NO electrical steels*

In general, NO electrical steels are processed via casting, hot rolling, cold rolling, and annealing. Although the manufacturing of these steels seems straightforward, the combination of processing stages for controlling the chemical composition, microstructure, and texture of specific steel grades is truly state-of-the-art. Typically, the strip processing of NO electrical steels begins with continuous casting of slabs from steel liquid (in an electrical furnace) or basic oxygen melting in a vacuum degassing chamber. Carbon, nitrogen, and sulfur concentration levels in this stage are kept low, thereby minimizing the negative effect of these impurities on the magnetic properties of the steel. The slabs are then hot-rolled to coils (i.e., hot bands) with thicknesses ranging from 2 to 4 mm. Hot bands with thicknesses of 0.7 to 1.0 mm are sometimes produced, but control of the thickness homogeneity and surface quality is extremely challenging. In fact, the standard (0.35 to 0.8 mm) is typically realized by

cold rolling the steel strips. Prior to cold rolling, shot-blasting, side-trimming, and pickling processes are usually performed to remove scale and improve the surface quality of the strips. The cold rolling is performed with tandem or reversing mills. In the tandem mill, the strip is passed from roll-stand to roll-stand and the thickness is progressively reduced. In contrast, in the reversing mill, the strip is passed from left to right through one mill stand, then back again, and after several such passes the final desired thickness is attained. Relatively small rolls are used to ensure that the strips undergo considerable reduction. These small-diameter rolls are usually installed in multi-high rolling mills to minimize the effect of roll bending on the strip profile.

In addition to hot and cold rolling, the processing route of NO electrical steels also includes several types of heat treatments, which are typically applied between the rolling stages and after lamination punching. These treatments combined with rolling stages, are aimed mainly at modifying the chemical composition, microstructure, and texture of steels. Furthermore, IA is applied between cold rolling stages to ensure that the softness of the steel strips is retained before a further thickness reduction is implemented. However, the final annealing is used to control grain growth and texture development in the steels. NO electrical steels are usually annealed in decarburization atmospheres, with the aim of reducing the C concentration of the steel to levels that have negligible effect on the magnetic properties. In addition, decarburization annealing plays a key role in the development of suitable textures in these steels.

### *3.4 Advanced techniques for texture control in NO electrical steels*

Electrical steels with excellent magnetic properties have been obtained via optimization of the processing routes. Feasible progressive improvements have been realized, owing to significant advances in the manipulation and control of the chemical composition, coating layers, grain size, impurities, and thickness of steels. However, texture optimization (particularly at the industrial scale) for good magnetic properties remains elusive. The desired texture is only well-controlled in exceptional cases. In most situations, optimum textures are only applicable at the laboratory scale. Various techniques have been developed for texture control of NO electrical steels. The occurrence of the Cube orientation and Cube fiber textures in either the surface

or the bulk of the material may be stimulated by the annealing atmosphere and chemical composition of the material. In fact, the surface texture of electrical steels may (i) differ significantly from the bulk texture and (ii), as discussed below, have considerable impact on the magnetic properties of these materials.

### *3.4.1 Surface textures*

Texture control for electrical steels is commonly aimed at imposing suitable crystal orientations that yield good magnetic properties for the bulk of the material. However, owing to the thin sheet geometry, many of the grains are exposed to the external atmosphere. In general, the interaction between crystal grains and the external atmosphere leads to differences in the surface and bulk textures. This results from the lack of neighboring atoms in the sub-surface grains, which, in turn, leads to a relatively high energy of the solid-vapor interface (i.e. the so-called surface energy). The number of missing atoms differs from plane to plane and, hence, the surface energy is strongly dependent on the grain orientation. In addition, interactions of interfacial atoms with various gas molecules lead to changes in the surface energy of the grains. Walter [8] determined the effect of surface energy variations on texture development. Under vacuum conditions, the {011} planes of grains, which are parallel to the sheet plane, have the minimum surface energy of the planes comprising the Fe-3wt.%Si alloy considered in this work. However, in oxygen- or sulfur-containing annealing atmospheres, grains with <001> axes parallel to the ND have the lowest surface energy. Differences in the surface energy induce grain boundary migration in the sub-surface layer of samples annealed at 1200 °C for 1 h under controlled atmospheres. The grains with the lowest surface energy then become the dominant grains in the sub-surface microstructure.

By controlling the annealing atmosphere, a favorable surface texture can be obtained via the surface-energy-induced grain boundary migration mechanism. However, texture variation across the sheet thickness is a major drawback for all surface texture control method. Different metallurgical processes have been proposed for stimulating the growth of surface grains into the bulk [9-14]. Most of these processes are based on a local phase transformation where decarburization plays a

key role. Moreover, these heat treatments are characterized by the inward growth of surface grains that yields a columnar microstructure, which spans the entire sheet thickness. Manganese removal and decarburization (for e.g., by an oxide separator) are typical methods to induce this type of microstructure.

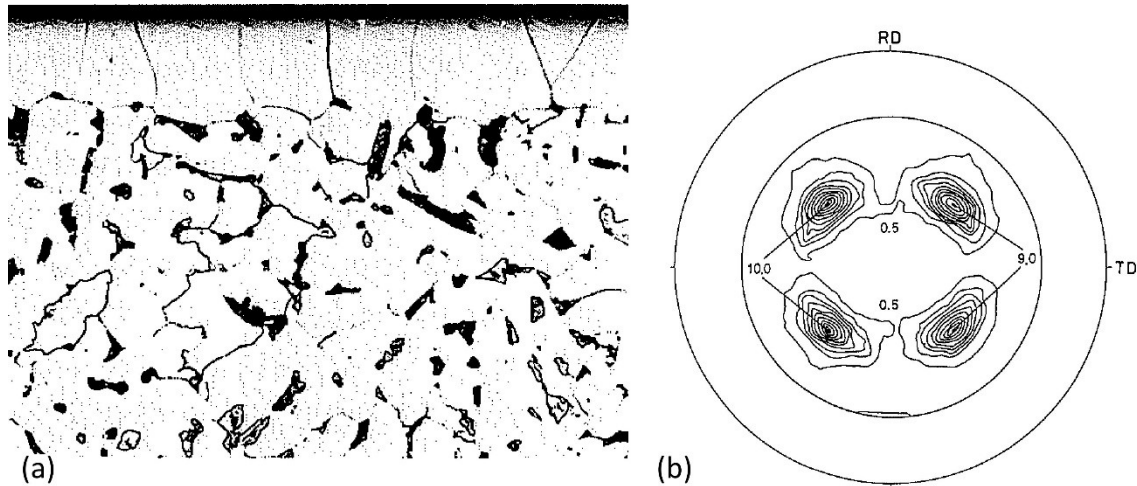
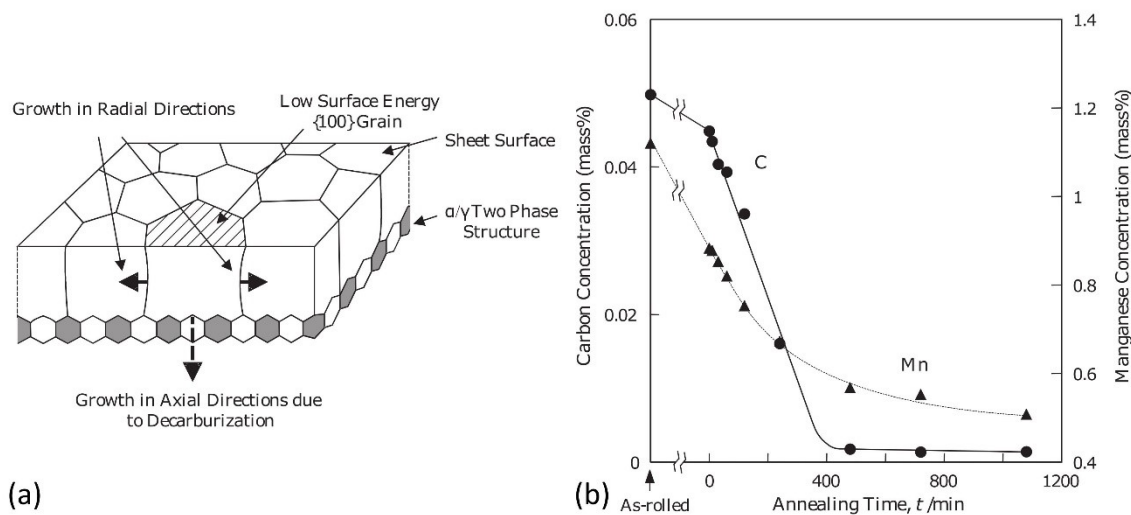


Figure 3.7(a) Microstructure and (b) (110) pole figure of the investigated material after 9 h of vacuum annealing at 950 °C [15].

**Manganese removal and decarburization:** Tomida et al. [10;11;15] proposed a two-stage annealing treatment for texture control of a cold-rolled and recrystallized NO electrical steel with the following chemical composition: 0.095 wt.% C, 2.06 wt.% Si, 1.01 wt.% Mn, 0.11 wt.% Al, and 0.001 wt.% P, and S. For gradual manganese diffusion from the sheet, the first annealing stage (duration: 10 min to 9 h, temperature: 800–1100 °C) of this treatment was performed under a vacuum ( $10^{-3}$  Pa). These annealing temperatures were chosen to ensure ferrite-austenite or full austenite formation in the steel. Manganese is a strong austenite-stabilizing element and, hence, manganese removal stimulated an austenite-to-ferrite phase transformation in the sub-surface layers. Ferrite grains with  $\langle 001 \rangle // ND$  orientations have the lowest surface energy and therefore are the most dominant of the newly formed grain. In the second stage of the two-stage treatment, samples were annealed at 850 °C in a decarburization atmosphere to promote the growth of surface ferrite grains. This treatment yielded a columnar microstructure with a sharp  $\{001\} \langle 110 \rangle$  texture, as shown in Figure 3.7.



**Decarburization by oxide separator:** In a different study, a strong  $\{001\}\langle 210 \rangle$  texture developed in silicon steel sheets decarburized via annealing with oxide separator layers [12-14]. After cold rolling and annealing, steel sheets (thickness: 0.35 mm) containing 0.051 wt.% C, 3.02 wt.% Si, and 1.12 wt.% Mn, were laminated with different oxide separator layers. Each of these layers was a fibrous mixture of 52%  $\text{SiO}_2$  and 48%  $\text{Al}_2\text{O}_3$ . In some cases,  $\text{TiO}_2$  powder was also added to the layers. The samples were annealed for 12 h in a vacuum furnace at temperatures ranging from 900 to 1100 °C. Owing to the decarburization occurring during this annealing, the carbon concentration of the steel sheets decreased to 0.001 wt.%. The decarburization was induced by a thermo-chemical reaction of carbon (C) with silicon dioxide ( $\text{SiO}_2$ ), which resulted in the formation of silicon (Si) and carbon monoxide (CO). In addition, the Si concentration of the steel increased, owing to the deposition of Si on the sheet surfaces. However, the manganese content of the sub-surface layers decreased, because of the vaporization. These changes in the chemical composition across the sheet thickness resulted in growth (via phase transformation) of the surface ferrite grains toward the center of the sheets (Figure 3.8). The columnar microstructure, resulting from the heat treatment, was characterized by a strong  $\{001\}\langle 210 \rangle$  texture.



**Figure 3.8 Schematic of decarburization-induced columnar grain growth [12].**

**Two-step decarburization:** Decarburization is typically achieved via prolonged high-temperature annealing treatments performed under very well-controlled atmospheres. From an industrial application viewpoint, these required processing conditions represent a major disadvantage of decarburization processes. Recently, Kovac et al. [9] proposed a two-step decarburization process, which is highly compatible with a continuous production line. With this heat treatment, steels are annealed in the two-phase ferrite-austenite region, with samples being subjected to a stepped temperature schedule and a decarburization atmosphere. A fine primary recrystallized microstructure and a thin decarburized ferrite region on the steel surface are obtained via high-temperature annealing of the samples in the first step of the process. In the second step, the annealing temperature is lowered and the holding time is extended to promote decarburization and the growth of columnar grains. Recrystallization occurs in the first period and, hence, cold-rolled steels can be directly heat-treated without a preliminary annealing step. However, to support the directional growth that competes with the equiaxial development of grains during

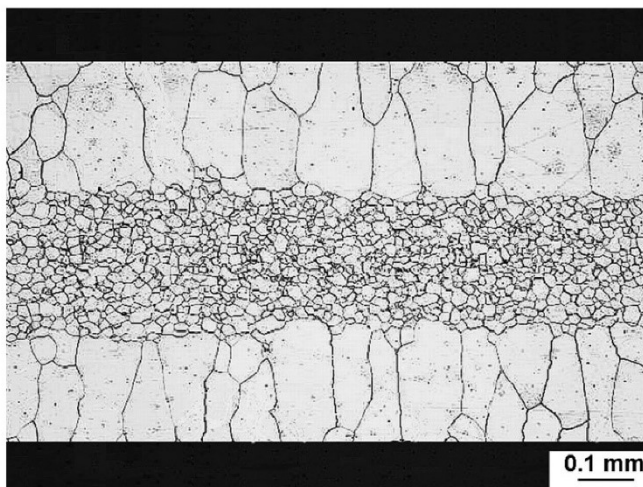


**Figure 3.9** Columnar-grained microstructure of an electrical steel after annealing (duration: 3.5 min, heating rate: 10 °C/s) in a wet atmosphere of cracking ammonia [16].

primary recrystallization, a high thermal gradient must be maintained across the sheet thickness. This is achieved by employing a fast heating rate and a short holding time during the first period of annealing [16]. Two-step decarburization of a semi-processed NO electrical steel yields a columnar-grained microstructure with a strong  $\{001\}\langle 110 \rangle$  texture, as given in Figure 3.9.

### 3.4.2 Multi-stage cold rolling and annealing

In conventional processing routes, cold rolling constitutes an essential step for realizing the desired thickness (0.5 mm) of material strips. The deformation that

results in 70–80% thickness reduction generates both strong  $\alpha$ - and  $\gamma$ -fiber textures, which are detrimental to the magnetic properties of the steels. In addition, preferred nucleation and selective growth during primary recrystallization lead to increased intensities of these fibers. However, more magnetically favorable orientations, than those comprising the  $\alpha$ - and  $\gamma$ -fibers, can be obtained by carefully redesigning the cold rolling and annealing steps of the processing routes.

An investigation on the effect of cold rolling reduction on the recrystallization texture showed that the  $\{001\}\langle 210 \rangle$  orientation (rather than the  $\alpha$ - $\gamma$  fiber) dominated the annealing texture of one-stage severely cold-rolled (reduction: 97.5%) samples [17]. This orientation ( $\{001\}\langle 210 \rangle$ ), although yielding non-optimum magnetic properties, is still more magnetically favorable than the  $\alpha$ - $\gamma$  fiber texture. In addition, Nakamura et al. [18] found that two-stage cold rolling with IA yielded increased intensity of  $\{001\}\langle 210 \rangle$  orientations in the final recrystallization textures.

The occurrence of the  $\{001\}\langle 210 \rangle$  orientation in recrystallization textures of steel with 0.0024 wt.% C, 0.13 wt.% Si, 0.22 wt.% Mn, and 0.072 wt.% P was also investigated [19]. The investigated samples were subjected to (i) hot rolling at 1200 °C to a thickness of 2.2 mm, (ii) the first cold rolling stage (thickness reduction: 77%), (iii) IA (duration: 30 s, temperatures: 540–700 °C, atmosphere: argon (Ar)), (iv) the second cold rolling stage (thickness reduction: 12%), and (v) final annealing at 800 °C for 30 s under Ar atmosphere. Although different annealing temperatures were employed, similar EBSD results were obtained for the IA samples. Grains with the  $\langle 111 \rangle // \text{ND}$  orientation and  $\langle 110 \rangle // \text{RD}$  orientation constituted most of the recrystallized grains and the deformed grains, respectively. Grains with  $\{001\}\langle 210 \rangle$  orientations constituted only a minor fraction of the microstructure. However, the IA temperature had a significant impact on the texture formed after final annealing. For example, an IA temperature of 640 °C yielded the highest intensities of the  $\{001\}\langle 210 \rangle$  orientations in final annealed sample, accounting for 60% of the recrystallized grains. The occurrence of this orientation in the final annealing texture was attributed to heterogeneous nucleation in deformed grains of the first rolling stage and the growth by strain-induced boundary migration (SIBM) of recrystallized grains during IA and final annealing.

During both IA and final annealing, strain-induced boundary migration (SIBM) plays a key role in the occurrence of  $\{001\}\langle 210 \rangle$ -orientation in the recrystallization texture. During SIBM (i.e., a nucleation mechanism) part of a pre-existing grain boundary bulges out, leaving behind a region with lower dislocation content than the pre-migration content [19]. Therefore, compared with their higher-stored energy counterparts, crystallites with low stored energy are more stable and more likely to grow as recrystallized grains in the final annealing microstructure. This mechanism, i.e., SIBM, represents just one of various nucleation mechanisms for recrystallization. In fact, SIBM is the dominant mechanism only in cases of relatively small plastic deformation (for e.g., during a second rolling stage where the thickness of the material is reduced 12% [19]).

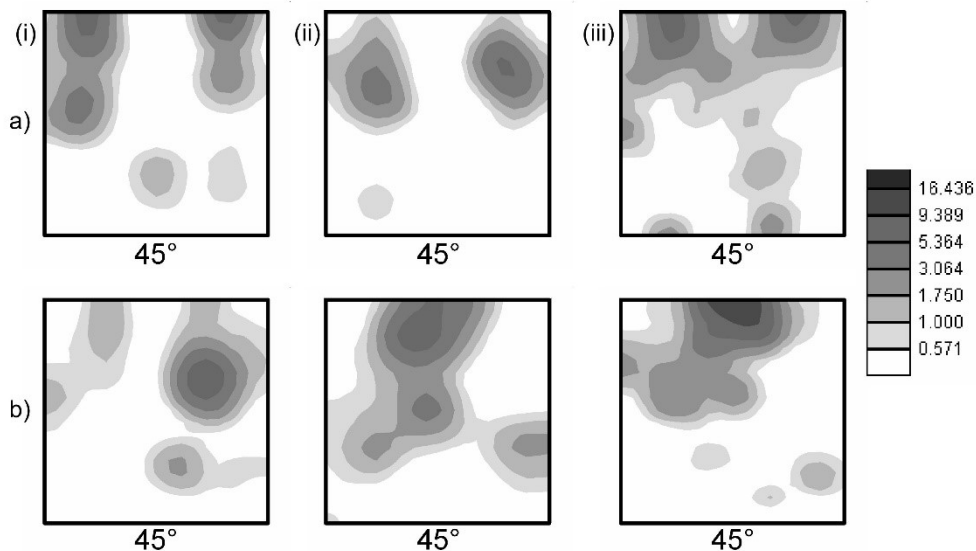


**Figure 3.10**  $\varphi_2 = 45^\circ$  ODF sections showing the recrystallization textures corresponding to the (a) sub-surface and (b) mid-plane of an iron-silicon alloy subjected to three-stage rolling (first (i), second (ii), and third stages (iii): 90%, 10%, and 10% thickness reductions, respectively) and annealing [20].

Texture control via multi-stage cold rolling and annealing has also yielded a  $\langle 001 \rangle // \text{ND}$  fiber texture in a columnar-structured iron-silicon-aluminum alloy [20;21]. In this study, a three-stage cold rolling (thickness reduction: 90% in the first stage; 10% in each of the other two stages) was implemented. Recrystallization was induced by annealing the samples for 1 h at 760–800 °C, between each rolling stage.

After the second and the third rolling passes, SIBM during the annealing step resulted in texture strengthening of the  $\langle 001 \rangle // \text{ND}$  fiber (see Figure 3.10).

### 3.4.3 Cross rolling

During cross rolling, the rolling direction of the subsequent pass is rotated  $90^\circ$  with respect to the direction of the previous pass. This rotation leads to changes in the orientation stability and crystallites rotate continuously toward new stable positions. In BCC-structured materials, orientations of the  $\alpha$ -fiber ( $\langle 110 \rangle // \text{RD}$ ) are extremely stable under the plane strain compression associated with uni-directional rolling. However, when the rolling direction is rotated by  $90^\circ$ , the  $\alpha$ -fiber texture transforms into the  $\tau$ -fiber ( $\langle 110 \rangle // \text{TD}$ ) texture. Most of the  $\tau$ -fiber fiber texture components are meta-stable and unstable orientations and, hence, cross rolling results in deformation texture of decreased volume fraction of these orientations. The rotated Cube ( $\{001\} \langle 110 \rangle$ ) component, however, is the only orientation with both a zero rotation rate and an invariant position during cross rolling. Therefore, the texture intensity of this orientation enhances during cross rolling.

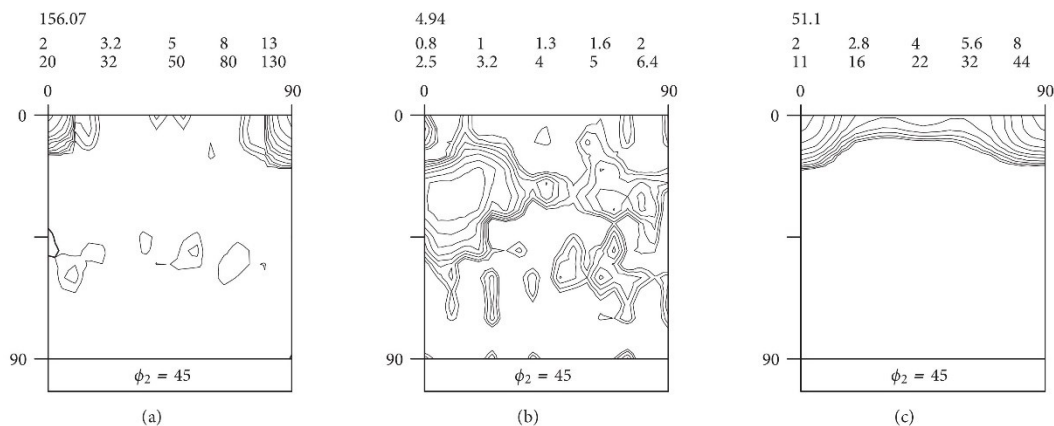


**Figure 3.11** Texture evolution in a NO electrical steel subjected to (a) cross rolling, (b) primary recrystallization, and (c) additional deformation (4–8% thickness reduction) and heat treatment [23].

Using cross rolling, Kestens et al. [22] developed a sharp rotated Cube ( $\{001\} \langle 110 \rangle$ ) texture in a typical low-grade NO electrical steel with the following composition: 0.036 wt.% C, 0.153 wt.% Mn, 0.575 wt.% Si, 0.292 wt.% Al, and traces of P, S, and N. The texture of the initial hot-rolled material was characterized by a high-

intensity (26 times random) rotated Cube component with a small spread in the transverse direction. The material was subjected to 70% thickness reduction via three different cold cross-rolling routes (A, B, and C) and annealing at 730 °C for 180 s in a salt bath. In deformation routes A and C, the direction of each cold-rolling pass was kept perpendicular to the direction of hot rolling and was 90°-rotated with respect to the direction of the previous pass, respectively. The resulting textures were, nevertheless, similar, i.e., each consisted of an extremely strong rotated Cube component (maximum intensity: over 150 times and 133 times the random level for routes A and C, respectively). In route B, the material was cold rolled in two stages of equal accumulated true strain, but different alignment of the cold rolling direction with respect to the initial hot rolling direction. Parallel and perpendicular alignments

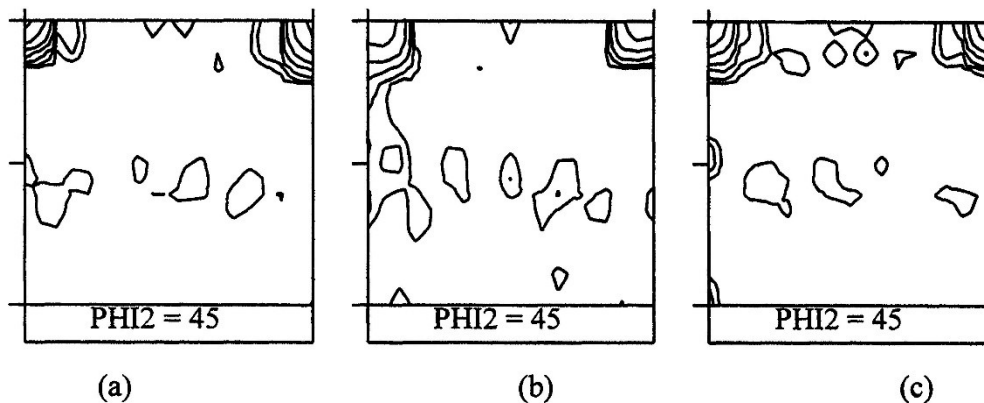


**Figure 3.12  $\varphi_2 = 45^\circ$  ODF sections showing the cross-rolling textures of an NO electrical steel subjected to various deformation routes [22].**

were employed in the first and second stages, respectively. This deformation route yielded a high-intensity rotated Cube component, but the intensity was lower than the intensities resulting from the other routes. Although the deformation textures resulting from routes A, B, and C were characterized by differing intensities, the corresponding recrystallization textures exhibited almost the same intensities. The texture of the annealed samples consisted mainly of the  $\{311\}\langle 136 \rangle$  orientation (maximum intensities: 5.0–7.0 times the random level), which yields only mediocre magnetic properties. However, additional treatment of this material via light cold rolling (4–8% thickness reduction) and subsequent annealing, generated a  $\theta$ -fiber texture with maximum intensity at the rotated Cube component [23]. Calculation results of the same study [23] show that this texture yields outstanding magnetic

properties, although the incorporation of cross rolling and additional treatment into a continuous processing line remains unrealized.

### *3.4.4 Thin strip casting*

Through thin strip casting, steel strips with the same thickness and width as those of the hot rolling stage are produced directly from the melt, i.e., the hot rolling stages are eliminated. Electrical steel production via thin strip casting is therefore simpler than production via conventional routes. Furthermore, directional dendritic growth (which occurs during casting) yields columnar grains with  $\theta$ -fiber orientations. Laboratory-scale casting is usually performed by a vertical twin-roll caster. In this process, the steel is melted in an induction furnace and then poured into a tundish. The molten steel then flows through a nozzle under the Ar shield into the internal water cooled casting rollers [24].

The microstructure of the steel strips in the roll gap is formed from three sequential processes: rapid solidification, cooling, and hot rolling [25]. Crystal nucleation and growth occur in the first stage of casting, when the melt contacts the roll surfaces. Owing to the roughness of the roll, this contact occurs mainly at the micro-peak positions of the surfaces. High and stable heat removal at these peaks leads to the nucleation and growth of crystals and the formation of a thin shell. In the second stage, cooling and thermal contraction of this shell result in further crystal growth and shell lift-off from the roll surface. In the final stage, the two shells grow toward each other, and are then welded as well as slightly deformed by hot rolling. The solid micro-inclusions and broken dendrite arms and tips, resulting from the solidification process, are all pushed by the solidification front into the thin residual semi-solid layer. This layer is then filled with small crystals and micro-inclusions, and compressed between the two growing shells.

The influence of processing parameters on the texture evolution of strip cast steels is complex and remains only partly understood. Park et al. [26;27] determined the effect of super heating on the microstructure and texture of an alloy of iron and 4.5 wt.% Si. The through-thickness microstructure of the as-cast steel strip (width 100 mm, thickness: 1.5 mm) was divided into three regions. Regions 1, 2, and 3 (**Error! R**

reference source not found.) correspond to the rapidly solidified thin layer near the surface of the strip, equiaxed dendritic layer, and columnar dendritic layer in the center of the strip, respectively. The thickness of each region varies with the super heat of the melt. Strips experiencing to a super heat of 20 °C consisted mainly of

equiaxed dendritic grains with weak Goss ( $\{110\}\langle 001\rangle$ ) and Copper ( $\{112\}\langle 111\rangle$ ) orientations. The  $\theta$ -fiber texture components featured prominently in both regions 1 and 3, but occurred with a higher intensity in region 3 (i.e., in the center of the strip). A weak  $\gamma$ -fiber texture also occurred in this region. At a super heat of 30 °C, columnar dendritic grains spanned the thickness of the strip, with a few Goss grains occurring in the sub-surface layer. However, most of the grains lying in the region spanning the surface to the center of the strip had  $\theta$ -fiber orientations (Figure 3.13).

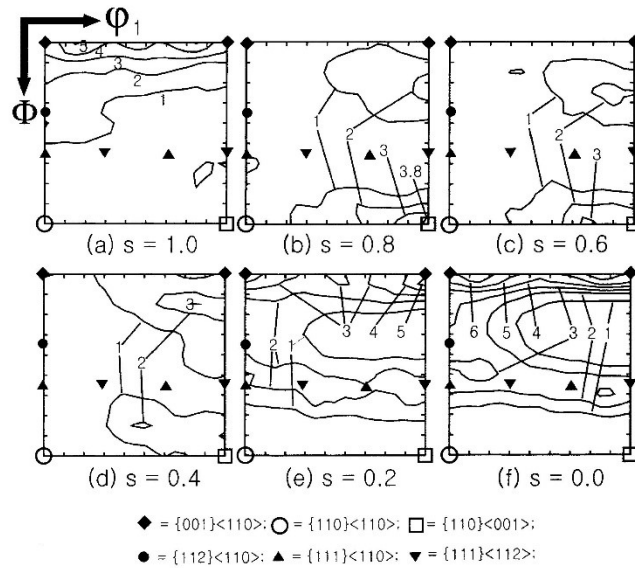


**Figure 3.13**  $\phi_2 = 45^\circ$  ODF sections showing textures measured at various thicknesses, i.e., from sub-surface ( $s = 1.0$ ) to center layer ( $s = 0$ ), of a strip-cast 4.5 wt.% Si steel sheet [26].

Zhang et al. [24] also considered the effect of the super heat on texture evolution. In that work, a NO electrical steel, containing 1.3 wt.% Si, was strip cast using a vertical twin roll caster. The super heat of the melt ranged from 20 to 60 °C, and 2.6-mm-thick as-cast steel strips were obtained. After pickling, the strips were cold rolled to a thickness of 0.5 mm, and recrystallization annealed for 5 min at 950 °C in a 30%-70%  $H_2-N_2$  atmosphere. As-cast strips with coarse-grained microstructures (average grain size:  $\sim 98 \mu\text{m}$ – $395 \mu\text{m}$ ) were obtained when the super heat was increased from 20 °C to 60 °C. Moreover, compared with 20 °C, 60 °C yielded a sharper orientation preference, as a relatively random distribution of grains was replaced by a strong Cube ( $\{001\}\langle 100\rangle$ ) orientation. After cold rolling and final annealing, this preferred



Cube orientation was (for the most part) replaced by the  $\eta$ -(<100>//RD) fiber texture with maximum intensity at the Goss orientation.

### 3.5 References

- [1] McHenry ME. Silicon Steels, Buschow KHJ, Robert WC, Merton CF, Bernard I, Edward JK, Subhash M, Patrick V, (eds.) in. Encyclopedia of Materials: Science and Technology (Second Edition). Oxford: Elsevier; 2001. p.8584.
- [2] Cullity BD, Graham CD. Introduction to magnetic materials: John Wiley & Sons; 2011.
- [3] Beckley P, Engineers IoE. Electrical Steels for Rotating Machines: Institution of Engineering and Technology; 2002.
- [4] Moses T. Opportunities for exploitation of magnetic materials in an energy conscious world. Interdiscip. Sci. Rev. 2002;27:100.
- [5] Goss NP. Electrical sheet and method and apparatus for its manufacture and test. U.S.Patent. 1934; 1,965,559.
- [6] Beckley P. Steels, Silicon Iron-based: Magnetic Properties, Buschow KHJ, Robert WC, Merton CF, Bernard I, Edward JK, Subhash M, Patrick V, (eds.) in. Encyclopedia of Materials: Science and Technology (Second Edition). Oxford: Elsevier; 2001. p.8847.
- [7] Moses AJ. Energy efficient electrical steels: Magnetic performance prediction and optimization. Scripta Materialia. 2012;67:560.
- [8] Walter JL. Control of texture in magnetic material by surface energy. Journal of Applied Physics. 1965;36:1213.
- [9] Kovác F, Dzubinský M, Sidor Y. Columnar grain growth in non-oriented electrical steels. J Magn Magn Mater. 2004;269:333.
- [10] Tomida T. A new process to develop (100) texture in silicon steel sheets. J Mater Eng Perform. 1996;5:316.

- [11] Tomida T. (100)-textured 3% silicon steel sheets by manganese removal and decarburization. *Journal of Applied Physics*. 1996;79:5443.
- [12] Tomida T. Decarburization of 3%Si-1.1%Mn-0.05%C steel sheets by silicon dioxide and development of {100}<012> texture. *Mater. Trans*. 2003;44:1096.
- [13] Tomida T, Uenoya S, Sano N. Fine-grained doubly oriented silicon steel sheets and mechanism of cube texture development. *Mater. Trans*. 2003;44:1106.
- [14] Tomida T, Sano N, Ueda K, Fujiwara K, Takahashi N. Cube-textured Si-steel sheets by oxide-separator-induced decarburization and growth mechanism of cube grains. *J Magn Magn Mater*. 2003;254–255:315.
- [15] Tomida T, Tanaka T. Development of (100) Texture in Silicon Steel Sheets by Removal of Manganese and Decarburization. *ISIJ Int*. 1995;35:548.
- [16] Sidor Y, Kovac F, Kvackaj T. Grain growth phenomena and heat transport in non-oriented electrical steels. *Acta Mater*. 2007;55:1711.
- [17] Heyer RH, McCabe DE, Elias JA. *Flat Rolled Products*. 1962;3:29.
- [18] Nakamura H, Matsumura K. Manufacture of electromagnetic steel sheet having small anisotropy. Japanese Patent 1986; 61003838.
- [19] Humphreys FJ, Hatherly M. *Recrystallization and related annealing phenomena*, Second ed. New York: Elsevier Science; 2004.
- [20] Doherty RD, Stojakovic D, Landgraf FJG, Kalidindi SR. Retention of the <001> fiber texture for Fe-Si electric motor steels. *Mater Sci Forum*. 2007;550:497.
- [21] Stojakovic D, Doherty RD, Kalidindi SR, Landgraf FJG. Thermomechanical processing for recovery of desired <001> fiber texture in electric motor steels. *Metall Mat Trans A Phys Metall Mat Sci*. 2008;39:1738.

[22] Kestens L, Jonas JJ, Van Houtte P, Aernoudt E. Orientation selection during static recrystallization of cross rolled nonoriented electrical steels. *Texture Stress Microstruct.* 1996;26-27:321.

[23] Kestens L, Jacobs S. Texture control during the manufacturing of nonoriented electrical steels. *Texture Stress Microstruct.* 2008;2008.

[24] Zhang Y, Xu Y, Liu H, Li C, Cao G, Liu Z, Wang G. Microstructure, texture and magnetic properties of strip-cast 1.3% Si non-oriented electrical steels. *J Magn Magn Mater.* 2012;324:3328.

[25] Zapuskalov N. Effect of coiling operation on strip quality of 4.5% Si steel in twin-roll casting process. *ISIJ Int.* 1999;39:463.

[26] Park JY, Oh KH, Ra HY. Texture and deformation behavior through thickness direction in strip-cast 4.5wt% Si steel sheet. *ISIJ Int.* 2000;40:1210.

[27] Park JY, Oh KH, Ra HY. Effects of superheating on texture and microstructure of Fe-4.5wt%Si steel strip by twin-roll strip casting. *ISIJ Int.* 2001;41:70.

# 4

## *Plastic deformation and recrystallization*

Texture evolution during deformation and recrystallization in polycrystalline materials are intricate phenomena. They are sensitive to both manufacture and material parameters. In general, these texture developments are understood as material responses to external constraints. During deformation, geometrical constraints lead to elastic lattice distortion, mechanical twinning and dislocation glides in grains. During recrystallization, re-arrangements of dislocation and migrations of grain boundaries, which are activated by thermal energy, lead to reductions of internally stored energy of the polycrystalline aggregate. In this chapter, fundamental mechanisms of crystal plasticity and recrystallization are described.

Physical models to predict texture evolutions during plastic deformation and recrystallization are then discussed.

#### 4.1 Theory of single crystal plasticity

Most metallic materials for structural applications are polycrystal. Plasticity of polycrystalline material is a collective behavior of single crystals in the aggregate responding to the mechanical boundary conditions. In this section, theory of elasto-plastic deformation for single crystals is introduced. The up-scaling from single- to poly-crystal behavior will be presented in the next section which contains various homogenization assumptions.

In the approach of continuum mechanics, deformation in a single crystal is represented by the so called *deformation gradient tensor* ( $\mathbf{F}$ ). This tensor measures the change in direction and magnitude of infinitesimal vectors from un-deformed (reference) stage to the deformed (current) stage:

$$\mathbf{F} = \frac{\partial \mathbf{x}}{\partial \mathbf{X}} \quad (4.1)$$

in which  $\mathbf{x}$  and  $\mathbf{X}$  are coordinates in deformed and un-deformed stages of the same vectors. Conventionally, the total deformation of a crystallite ( $\mathbf{F}$ ) can be divided into elastic and plastic parts. The multiplicative decomposition of this total deformation, therefore, can be expressed as following:

$$\mathbf{F} = \mathbf{F}^{el} \mathbf{F}^p = \mathbf{R}^* \mathbf{U}^{el} \mathbf{F}^p \quad (4.2)$$

where  $\mathbf{F}^{el}$  is the elastic deformation gradient tensor which is composed by a rigid body rotation ( $\mathbf{R}^*$ ) and an elastic stretch ( $\mathbf{U}^{el}$ ) of the crystal lattice;  $\mathbf{F}^p$  is the plastic deformation gradient tensor.

The total deformation can be imagined to occur in two steps (c.f. Figure 4.1). First, the crystallite is plastically deformed from a reference to a fictitious intermediate stage. During plastic deformation, this crystallite is sheared by lattice motions, but its lattice structure is unaffected and the crystal volume is preserved. Second, elastic stretch and rigid body rotation bring the crystallite from the intermediate to the

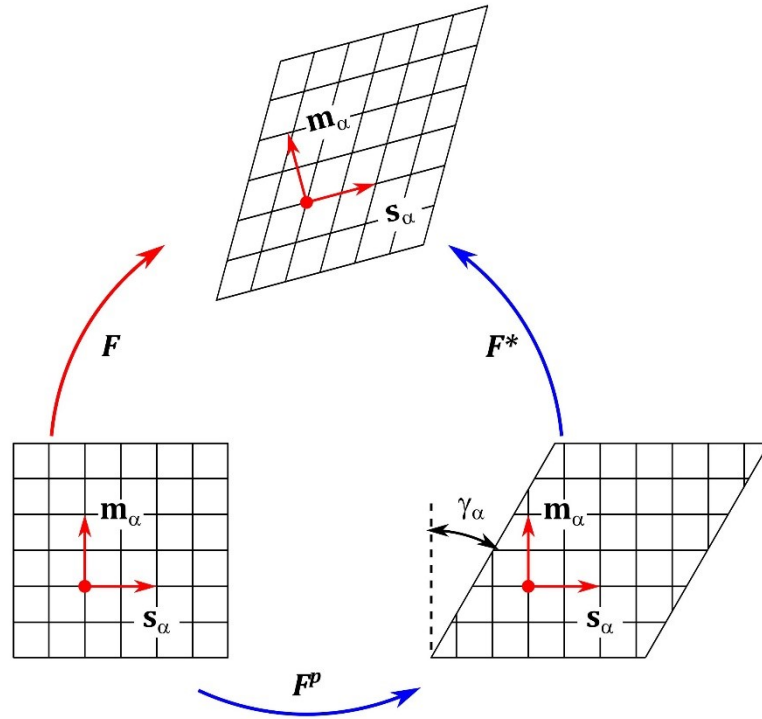


**Figure 4.1 Kinematic model of elasto-plastic deformation for single crystals.**

current stage. The elastic stretch causes a distortion of the crystal lattice and changes the crystal volume, while the rigid body rotation changes the orientation of the crystallite to fit its prescribed position.

In most metallic materials, elastic deformation is rather small. The magnitude of the elastic deformation is about two orders lower than that of plastic deformation. Nevertheless, effects of the elastic deformation on crystallites can be represented by a Green strain tensor ( $\mathbf{E}$ ), which is measured at the intermediate stage, and does not interfere with rigid body rotation of the crystallite:

$$\mathbf{E} = \frac{1}{2}(\mathbf{F}^{elT} \mathbf{F}^{el} - \mathbf{I}) = \frac{1}{2}(\mathbf{U}^{elT} \mathbf{U}^{el} - \mathbf{I}) \quad (4.3)$$

The work conjugate to the Green strain ( $\mathbf{E}$ ) is the second Piola-Kirchhoff stress ( $\mathbf{S}$ ) which is proportional to the Green strain ( $\mathbf{E}$ ) by the fourth order elasticity stiffness tensor ( $\mathbf{C}$ ) of the crystallite:

$$\mathbf{S} = \mathbf{C} : \mathbf{E} \quad (4.4)$$

In addition, the second Piola-Kirchhoff stress ( $\mathbf{S}$ ) can be derived from the Cauchy stress ( $\boldsymbol{\sigma}$ ) of the crystallite, measured at the current stage as:

$$\mathbf{S} = \det(\mathbf{F}^{el}) \mathbf{F}^{el^{-1}} \boldsymbol{\sigma} \mathbf{F}^{el^{-T}} = \det(\mathbf{U}^{el}) \mathbf{U}^{el^{-1}} \mathbf{R}^{*T} \boldsymbol{\sigma} \mathbf{R}^* \mathbf{U}^{el^{-1}} \quad (4.5)$$

Contrary to the negligible effects of elastic deformation, plastic deformation has a major contribution to the shape change and re-orientation of crystallites. Plastic deformation of crystallites is carried by dislocation slips, mechanical twinning or both. As the main focus of this study is the texture evolution in BCC structural materials, plasticity induced by mechanical twinning is not further considered. That is because, in reality, mechanical twinning does not frequently occur during deformation of metals with high stacking fault energy. Only after large deformation with high strain rates or at very low temperatures, mechanical twinning might be observed in BCC structural materials. However, crystal plasticity in such severe conditions is not the scope of the current study.

Dislocation slip, as the main mechanism to carry plasticity in crystallites, is a discrete response rather than a continuum behavior. Interruption of dislocation slip can be clearly recognized from the features of this phenomenon (c.f. Figure 4.2). Slip, in fact, is a collective consequence of many dislocation gliding in conjunction. Glide does not occur in arbitrary directions as it is restricted to certain crystallographic planes, along well-defined crystallographic directions. Planes of dislocation glide, so

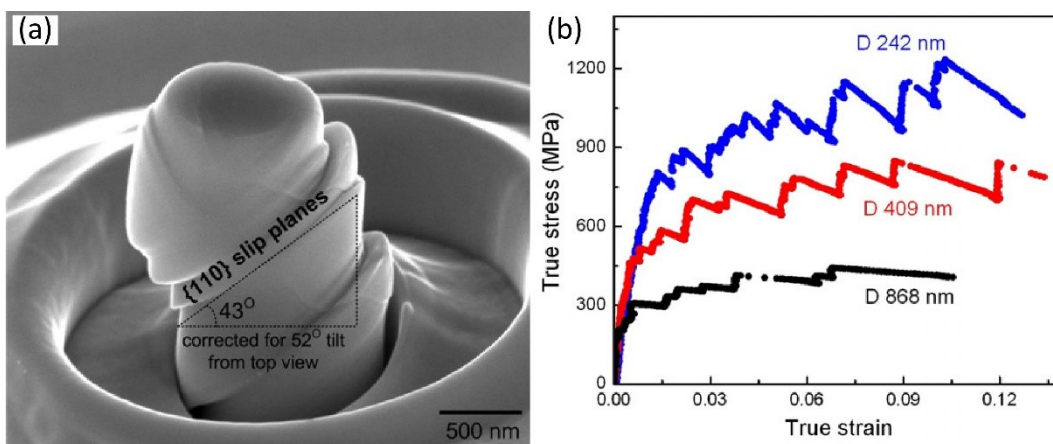
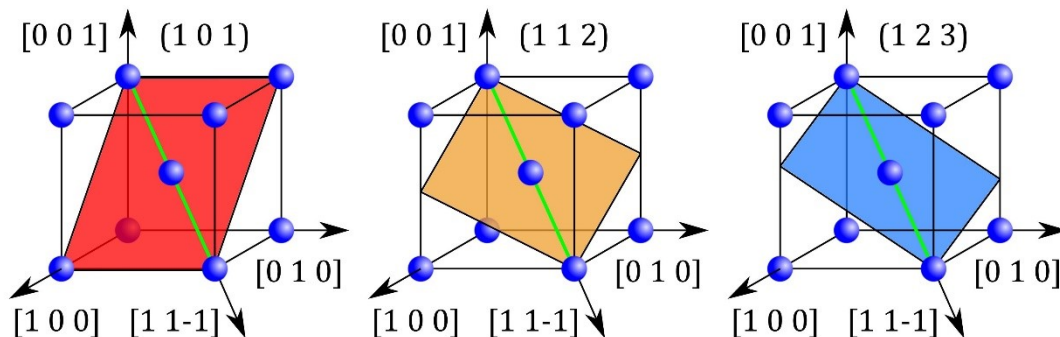


Figure 4.2 Micro-pillar compressive test of a Niobium crystal [1].

called *slip planes*, usually are the ones having the highest atomic density, whereas directions which contain the most closely spaced atoms are *slip directions*. A pair of a slip plane and a slip direction in that plane constitutes a *slip system*.

BCC crystallites have the highest linear atomic density along the  $\langle 111 \rangle$ -crystallographic axes, and thus dislocations glide along the four  $\langle 111 \rangle$  directions. The magnitude of a glide, associated with a single dislocation, is half the distance of the BCC lattice diagonal. Conversely, slip planes of BCC structural metals are not clearly determined. Because of the wavy slip lines, observed in studies aiming to determine the active slip systems, the  $\{112\}$ - and  $\{123\}$ -planes are also considered as slip planes in BCC crystals, besides the highest density  $\{110\}$ -planes. This phenomenon, called *pencil glide*, is not yet fully understood. However, it has been proposed to be a result of non-planar cores of screw dislocations in non-closely packed structural materials [2]. For an exhaustive explanation for the non-planar structure of the dislocation core the reader is referred to the work of Vitek et al. [2].

Regarding the intricate behavior of BCC structural materials, pencil glide is also considered in this study. For calculations of crystal plasticity at room temperature, two families of slip systems, namely the  $\{110\}\langle 111 \rangle$  and the  $\{112\}\langle 111 \rangle$  slip systems, are considered (c.f. Figure 4.3). Glide on the third slip system of the  $\{123\}\langle 111 \rangle$  is taken into account, whenever crystal plasticity calculations at high temperature are carried out. Additionally, because of crystal symmetry, there are multi-variants for each available slip families. For BCC structured materials, the slip families of



**Figure 4.3** Various slip systems of BCC structural materials which are taken into account by this study.



{110}<111> and {112}<111> produce 12 variants each, while the number of variants for the {123}<111> slip family is 24. Among these slip systems, not all are activated during plastic deformation. Slip only occurs when the applied shear stress on the slip plane in the slip direction reaches a critical value. This is the conclusion, first pointed out by Taylor et al. [3;4] from studies on the plastic extension of aluminum crystals. The criterion for selection of slip systems was then generalized and is now better known as the *Schmid law* [5] of critical resolved shear stress for crystal plasticity. Mathematically, the Schmid law is expressed as:

$$\dot{\gamma}^{\alpha} = \begin{cases} 0 & \text{if } \tau^{\alpha} < \tau_c^{\alpha} \\ \dot{\gamma} & \text{if } \tau^{\alpha} = \tau_c^{\alpha} \end{cases} \quad (4.6)$$

where  $\dot{\gamma}^{\alpha}$  is the shear rate of a slip system ( $\alpha$ );  $\tau^{\alpha}$  and  $\tau_c^{\alpha}$  are the applied shear stress and the critical resolved shear stress of the same slip system. The shear stress ( $\tau^{\alpha}$ ) acting on a slip system ( $\alpha$ ) is determined by the second Piola-Kirchhoff stress ( $\mathbf{S}$ ) as following:

$$\tau^{\alpha} = \mathbf{S} : \mathbf{M}^{\alpha} \quad (4.7)$$

in which,  $\mathbf{M}^{\alpha}$  is the Schmid tensor of a slip system ( $\alpha$ ). This Schmid tensor can be derived from the dyadic production ( $\otimes$ ) of a unit vector ( $\vec{b}^{\alpha}$ ) along the slip direction and another unit vector ( $\vec{m}^{\alpha}$ ) normal to the slip plane:

$$\mathbf{M}^{\alpha} = \frac{1}{2} (\vec{b}^{\alpha} \otimes \vec{m}^{\alpha} + \vec{m}^{\alpha} \otimes \vec{b}^{\alpha}) \quad (4.8)$$

According to equation 4.6, there will be no slip activity until the applied shear stress  $\tau^{\alpha}$  reaches the value of the resolved shear stress  $\tau_c^{\alpha}$  on one or more slip systems. Progressive deformation will lead to generation, accumulation and interaction of dislocations. Because of these dislocation activities, the *free path* for dislocation glides in latter deformation stages is shortened, shear rates gradually decrease and require higher applied stress to be maintained. This phenomenon is called the *work hardening* of crystallites during plastic deformation.

The hardening law for a crystallite, in a simple form, can be described by a linear increment of resolved shear stress ( $\tau_c^\alpha$ ) to slips ( $\gamma_\beta$ ) of all slip systems. Instantaneous increment of resolved shear stress corresponding to the accumulation rate of dislocation glides is given as following:

$$\dot{\tau}_c^\alpha = \sum_{\beta} h_{\alpha\beta} \dot{\gamma}_\beta \quad (4.9)$$

In this equation, the hardening parameters ( $h_{\alpha\beta}$ ) represent for effects of total glides on the slip system  $\beta$  on the resolved shear stress of the slip system  $\alpha$ . For linear hardening behavior, values of  $h_{\alpha\beta}$  are constant during the crystal plasticity. Differently, the rate sensitivity of slip activities can be taken into account by imposing a power function to the hardening law:

$$\tau_c^\alpha = \tau_0 \left| \frac{\dot{\gamma}_\alpha}{\dot{\gamma}_0} \right|^m \text{sign}(\dot{\gamma}_\alpha) \quad (4.10)$$

where  $m$  is the strain rate sensitivity parameter,  $\dot{\gamma}_0$  is the reference strain rate and  $\tau_0$  is the resistance of crystal. The choice of hardening law generally depends on the phenomenon or material behavior, which is targeted to be the subject of investigation. Specifically, for texture evolution studies, the hardening law may have influences on rotation paths of individual crystallites grains. However, the preferred texture components and the rotation toward them of all grains in an aggregate are not severely impacted by the choice of hardening law.

The velocity gradient tensor of crystal plasticity at intermediate stage ( $L^p$ ), therefore, is fully depended on shear rates ( $\dot{\gamma}^\alpha$ ) of slip systems in crystallites:

$$L^p = \dot{F}^p F^{p-1} = \sum_{\alpha} M^{\alpha} \dot{\gamma}^{\alpha} \quad (4.11)$$

The total velocity gradient tensor ( $L$ ) is:

$$L = \dot{F} F^{-1} \quad (4.12)$$

$$L = \dot{R}^* R^{*-1} + R^* (\dot{U}^{el} U^{el-1}) R^{*T} + R^* U^{el} (\dot{F}^p F^{p-1}) U^{el-1} R^{*T} \quad (4.13)$$

In the equation 4.13, the first term on the right-hand side ( $\dot{R}^* R^{*-1}$ ) is better known as the lattice spin, which is proportional to the rotation rate ( $\dot{R}^*$ ) of crystallites. These lattice spin and rotation rate are used to update the crystal orientation after each deformation step imposed on the crystallites. The second term in the equation 4.13 represents the rate of elastic stretch, while the last one is the rate of plastic deformation. Both are measured at the current stage. To simplify situations in which texture evolution is more interested, the stretch tensor ( $U^{el}$ ) of elastic deformation is always pre-estimated or even completely removed from calculation models. In these cases, crystallites are assumed to be fully plastic.

## 4.2 Polycrystal plasticity models

The plastic deformation of a polycrystalline aggregate is the collective behavior of single crystals responding to mechanical constraints. However, this behavior is not simply the sum of all single crystal responses. Interactions among grains in an aggregate lead to stress equilibrium and strain compatibility. The up-scaling from microscopic to macroscopic deformation requires assumptions about grain interactions. Individual responses of crystallites need to be compatible to the common behavior of the aggregate, which is commonly described by a homogenization hypothesis. In the sections below, various assumptions of grain interaction are described. The consequences of these hypotheses are then shown in the results of various calculation models.

### 4.2.1 Full constraints Taylor model

As one of the pioneering researchers on crystal plasticity, G.I. Taylor observed effects of dislocation glides on various metallic single crystals during uniaxial compression and extension [3;4;6-9]. These data helped him to develop the first calculation model of crystal plasticity, which is now widely known as the *full constraints Taylor* (FCT) model [10]. The initial purpose of this model is to account for mechanical properties of polycrystalline aggregates from the single crystal behavior. However, because of the complication and difficulty to analyze stress and strain in

polycrystal, the FCT model can only be applied to several special cases of multi-grain deformation, such as e.g. materials with a columnar microstructure subjected to uniaxial tension or compression along the columnar axis. According to Taylor, that is because each grain in these situations suffers exactly the same strain as the bulk material. This condition ensures the strain compatibility among neighboring grains, but it put each grains into extremely strict constraints. In a presumed Taylor-like aggregate, grains respond independently and directly to the macroscopic deformation conditions without interaction with their neighbors.

Although grain interaction was not appropriately incorporated and polycrystal deformation simulations were limited, the FCT model does capture some essential features of single crystal plasticity. In this model, any prescribed strain for a crystallite can be resolved into multi-slip activities. Because elasticity of the crystallite is small and negligible, whereas plasticity conserves the volume, the total strain can be accounted for by linear combinations of shears on a set of 5 *basic slip systems*. A slip system is basic if and only if its activities cannot be resolved by linear combinations of the others on the same set. Accordingly, multi-slip activities during crystal plasticity, no matter how complicated, produce a net effect similar to the one of basic slip sets. However, not all basic sets of slip systems provide crystal plasticity solutions for the externally imposed boundary conditions. The principle of virtual work requires the least energy dissipation of activated slips systems among all possible solutions. Therefore, the number of solutions for a crystal plasticity problem are usually small and finite.

A fast and robust procedure to solve Taylor crystal plasticity problems is provided by linear programming with simplex algorithm [11]. An optimum solution for the crystal plasticity problem is obtained by optimizing basic slip rates to strain and internal energy rate conditions:

$$\left\{ \begin{array}{l} \dot{\gamma}^\alpha \neq 0 \\ \sum_{\alpha} \dot{\gamma}^\alpha \mathbf{M}^\alpha = \text{sym}(\mathbf{L}^p) \\ P = \sum_{\alpha} \tau_c^\alpha |\dot{\gamma}^\alpha| = \min \end{array} \right. \quad (4.14)$$

in which,  $\dot{\gamma}^\alpha$  is the shear rate of a basic slip system ( $\alpha$ ),  $\text{sym}(\mathbf{L}^p)$  is the symmetric part of plastic velocity gradient tensor (i.e. the plastic strain rate tensor) and  $P$  is the dissipated rate of internal work. In most of the situations, solution for the crystal plasticity problem is unique. However, there are cases in which more than one set of slip systems can satisfy conditions 4.14. In the absence of a unique solution to equations 4.14, one refers to the so called *Taylor ambiguity* in slip system determination.

The Taylor ambiguity in slip system determination is caused by two main reasons. First, it is due to the critical resolved shear stresses of slip systems. In crystal plasticity simulation, they are usually assumed to have the same value, particularly at the beginning of deformation. If the prescribed strain can be solved by various basic slip sets, internal energy rates of these sets are only distinguished by the total magnitude of slip rates. The chance for more than one slip set to exhibit the minimum internal energy rate increases and hence equations 4.14 may have multi-solutions. The second reason for the Taylor ambiguity is the assumption of full constraint, implemented by the model. Since the FCT model only takes into account the strain compatibility, the stress equilibrium among grains, in general, is not satisfied. The ambiguity in the stress state of a crystallite, the so called *Taylor degeneracy*, has no influence on the shear rates of slip systems, and brings no clue for selection of solution in the case of Taylor ambiguity. On the contrary, if only part of the crystal stress state is known, the Taylor ambiguity can be solved easily. For instance, activities on 5 basic slip systems are required, since crystal plasticity generally contains 5 independent strain components. Nevertheless, if the number of non-zero strain components is less than the number of activated slip systems, there will be more activated slip systems than necessary. Obviously, a slip system is activated when it fulfills the Schmid law, but not because it belongs to a basic set. Any basic slip set, formed by activated slip systems,

can be a potential solution. However, the true solution for the crystal plasticity is the one, constructing the known stress state.

For the reasons listed above, the Taylor ambiguity is most problematic when the FCT model is applied to simulate the plastic deformation of materials with cubic crystal structure, particularly at the beginning of deformation. To avoid the first source of Taylor ambiguity, the critical resolved shear stresses of various slip systems need to be distinguished. However, there is no real reason to make them different, especially for slip systems of the same family. In addition, the hardening behavior of a crystal is complicated and not fully understood. Temporarily, a phenomenological strain rate sensitive hardening law can be used to decrease the impact of the Taylor ambiguity to simulation results. For the second source of the Taylor ambiguity, the FCT model is not able to solve it without violating the basic assumptions of the model. Modifications of the Taylor model, which relaxes the Taylor constraint and bring simulation results closer to reality, will be discussed in the next section.

#### *4.2.2 Relaxed constraints models*

The assumption of total uniform strain in the full constraints Taylor model indeed is too strict. Except in uniaxial tension and compression of columnar crystal materials, in all other cases of polycrystal plasticity, grain interaction cannot be neglected. This interaction leads to stress equilibrium and strain partitioning among neighboring grains. The strain applied to each individual grains, therefore, is very different from the macroscopic strain.

#### **Classical relaxed constraints models**

To improve performance of the Taylor model, the full constraint of Taylor theory needs to be “relaxed”. It requires to take into account variations of plastic deformation from grain to grain in the polycrystalline aggregate. Different assumptions have been proposed to break the uniformity of applied strain to each crystals [12;13]. Calculation models based on these assumption are called *classical relaxed constraints models*. They all assume that the geometrical shape of grains changes with each increment of the deformation, whereby it is allowed that some components are

differentiated with respect to neighboring grains. Some components of the deformation tensor have more influence on crystal behaviors than the others. By incorporating in the model the difference of these deformation components from grain to grain, the plastic accommodation of the polycrystalline aggregate would more accurately predicted. Specifically, during conventional rolling, all grains in an aggregate are compressed in the normal direction and elongated in the rolling direction. The expansion of grains in the transverse direction can be neglected, if the widening in this direction of the material sheet is small. Thus, as the strain increases, crystal grains becomes flattened and elongated. A large portion of grain boundaries is parallel to the RD-TD plane. If there are differences in the deformation configurations between crystal grains, the most significant variation are in the strain components, lying on the RD-TD plane (c.f. Figure 4.4). Instead of having the same values as the macroscopic strain, these strain components should be left free to vary so as to minimize or *relax* the shear stresses in the RD-TD plane. Physically, it implies that grains are allowed shear freely over each other along the boundary plane, i.e. the RD-TD plane in cases of conventional rolling.

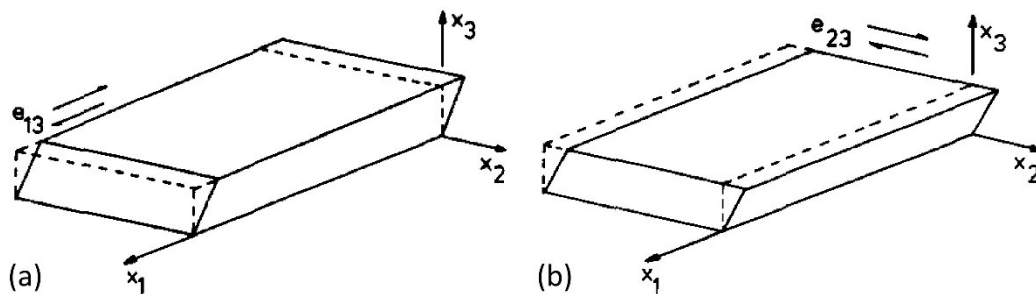


Figure 4.4 Shears in RD-ND (a) and TD-ND of a flat grain, deformed by plane strain compression of rolling [13].

### Grain cluster models

As the strain heterogeneity is taken into account, the predicted textures are improved [13;14]. However, the simulated textures, even from the classical relaxed constraint models, still exhibit important discrepancies compared to the experimental counterparts. Classical relaxed constraints models have several shortcomings. (i) The response of crystal will minimize the (shear) stress components, but the effect of neighboring grains is not taken into account. (ii) Relaxation leads to a strain misfit

between grains in an aggregate. (iii) The extent of the relaxations are self-defined by each crystal grains, but the relaxation directions in models are uniformly prescribed. Such strict imposition of the relaxation is not realistic and consequently limits the application of relaxed constraints crystal plasticity model. Relaxations on RD-TD plane are significant only for the plane strain compression mode (rolling) but cannot be universally applied to arbitrary strain modes. Even for plane strain compression, the textures of mildly rolled materials are not well captured by classical relaxed constraints models. Simulation results may even overshoot texture developments after different deformations rather than the conventional rolling.

The strain misfit in the classical relaxed constraints models is due to the fact that no grain interaction is taken into account. Since the grain interaction includes both stress equilibrium and strain compatibility at grain boundaries, one method to consider the grain interaction is by full field calculations. It means that crystal grains must be investigated in very specific conditions of shape, size, orientation, while taking into account the precise topology of the microstructure. Such calculation can be carried out by crystal plasticity finite element (CPFE) simulations. However, the need to define a specific microstructure will cause the loss of statistical representation of texture calculations, unless a massive simulation is implemented. While the price for a full field calculation is not always affordable, texture developments, simulated by crystal plasticity finite element (CPFE) or crystal plasticity fast Fourier transform (CPFFT) models, are local rather than global results.

In the LAMEL [14] and GIA [16] models, the microstructure of materials is considered to be a set of grain clusters. Each cluster includes a small number of crystal points or nodes. In the LAMEL model, a cluster consists of a pair of crystals stacked one on top of the other, whereas in the GIA model, there are eight crystal points, arranged together in two rows and two columns. The full constraints condition is applied to the grain cluster, but within a cluster relaxations are allowed. The LAMEL model considers three types of relaxations, corresponding to three shears of a grain pair (c.f. Figure 4.5). Type I and II are shears on boundary plane of the pair. They leave the boundary plane invariant (i.e. there is no rotation and distortion of the plane). On the contrary, the Type III is a homogeneous shear across the grain pair, and it causes



a distortion of the grain boundary. This type of relaxation can be imagined as boundary sliding (classical relaxation) of lateral clusters. The relaxation of grain cluster models is quite similar to the one of classical relaxed constraints models. However, in a grain cluster, both stress equilibrium and strain compatible are imposed. It means relaxations in the LAMEL Type I and II have the same magnitude and opposite direction, whereas in Type III they are both equal for a grain pair.

### Advanced LAMEL model

The strain misfit problem is solved by grain cluster models, but the definition of grain clusters still raises problems. It is not evident to describe materials by a bimodal structure of grains and their clusters. There is no criterion to differentiate between grain boundary and cluster boundary. The number of crystal points in a cluster remains ambiguous as it could be any number from one till all grains included in the observed microstructure. Like the full constraints and classical relaxed constraints Taylor models, grain cluster models cannot explain the strain heterogeneity within crystal grains. These problems have motivated Van Houtte et al. [15] to develop the *advanced LAMEL model (ALAMEL)*. As its name accounts for, the ALAMEL model shares the same mathematical foundation with the LAMEL model. However, the physical arguments of the ALAMEL model are very different from the previous ones.

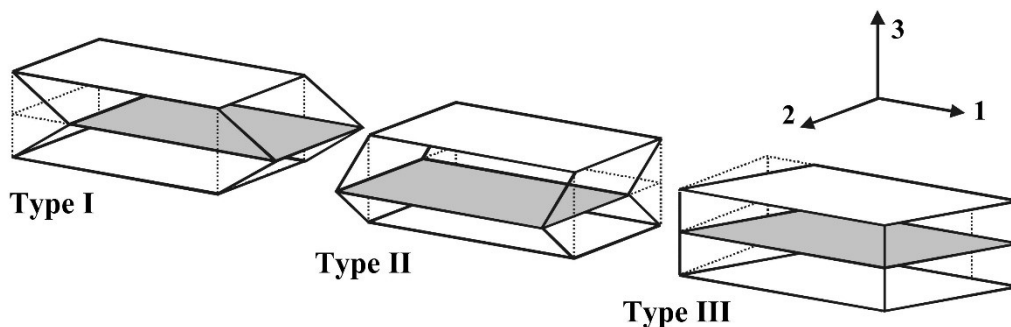


**Figure 4.5** Three types of relaxation considered in the LAMEL models. Type I corresponds to RD-ND shear, Type II to TD-ND shear and Type III to RD-TD shear [15].

In the ALAMEL model, there is no grain cluster, but each grain is subdivided into smaller parts, so called affected zones associated with grain boundary segments. The grain subdivision is argued on the principle of in-grain strain heterogeneity and grain fragmentation, which are usually observed in the microstructure of plastically

deformed metals. Each grain zone corresponds to one grain boundary segment and is only influenced by another zone of a different grain at the opposite side of the boundary segment (c.f. Figure 4.6). Interaction between zones of the same grain is assumed to be small and negligible. For a pair of grain zones, the interaction is regulated by stress equilibrium and strain compatible conditions, which in turn control relaxations on the grain boundary.

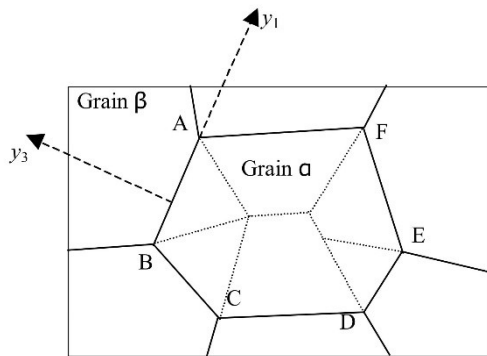


**Figure 4.6 Schematic illustration for grain subdivision in ALAMEL model in which grains are subdivided in influence zones of boundary segments [15]. The grain might be subdivided in influences of grain boundary segments AB, BC, CD, DE, EF, FA (Pseudo-2D case)**

The grain boundary in the ALAMEL model is more general and natural than in the LAMEL model. It is not limited to flat and orthonormal grain boundaries. Any plane which is defined by its normal vector can be considered as a boundary segment. Enclosing by many boundary segments, grains exhibit a more realistic geometry than a brick-shape. From sphere to polygon, grain shapes can be quantified by many discretized boundary segments. Not only flat and elongated but round and equi-axial grains can be incorporated in the ALAMEL model. Without any ambiguity, the ALAMEL model is able to investigate crystal plasticity behavior in much more complex deformation configurations, and not exclusively the plane strain compression of conventional rolling.

### 4.3 Physical phenomenon of static recrystallization

During plastic deformation, crystal defects (mainly dislocations) are generated and trapped inside the material. The internal energy of the deformed materials, therefore, increases and this creates a thermo-dynamical instable or metastable condition. Among others, the recrystallization process is a microstructural stabilization process in which a “new” microstructure is formed in the deformed matrix by the formation and migration of high angle grain boundaries [17]. The high

angle criteria of grain boundaries in this definition implies the misorientation angle between neighboring grains higher than  $10^\circ$  to  $15^\circ$ . The driving force for recrystallization is the plastically stored energy in materials. Formation and migration of grain boundaries during recrystallization are carried by atomic and vacancy diffusions, as similar to reconstructive phase transformations. In this section, mechanisms of recrystallization are described. The main focus is on influences and evolution of crystallographic textures during recrystallization.

In general, a stable state of microstructures can be achieved by various solid state reactions, i.e. phase transformation, recovery, recrystallization and grain growth. It is worthwhile to distinguish recrystallization among the others. The first difference among solid state transformation processes is the driving force of each processes. Phase transformations normally have the largest driving forces, whereas recovery and grain growth have the smallest ones. The driving force for phase transformation is about 1 kJ/mol, for recrystallization it varies from 10 to 100 J/mol, while for recovery and grain growth it is about 2 orders of magnitude smaller than for recrystallization [18]. Secondly, solid state reactions are distinguished by their physical mechanisms. During phase transformation a microstructure stabilization occurs by changing the crystallographic structure. In a reconstructive or displacive phase transformation atoms move by diffusing or shuffling, respectively, across the interphase boundaries to construct a new phase of lower Gibbs free energy. Recovery and recrystallization reduce the internal energy of the deformed state by re-arrangements and annihilations of lattice defects. However, there is no formation and migration of high angle boundaries during recovery. As a result, the grain morphology after recovery is very similar to the one of the deformation state, though orientation gradients in grains are partially reduced. Grain growth is another microstructure stabilization process during which high angle boundaries migrate under the pressure of reducing grain boundary area energy. The growth is labeled as *normal* when the grain size distribution remains self-similar during the entire growth process, while it is qualified abnormal when a bimodal grain size distribution appears in the process, meaning that a few grains grow at the expense of the remaining matrix grains.

Although they clearly can be distinguished in terms of driving force, solid state reactions may occur concurrently in a material. Very frequently, a material is deformed at high temperature, closed to the critical point of phase transformation. Not only phase transformation but also recovery and recrystallization can occur during deformation. The situation is less complicated when the material is deformed at low temperature and then undergoes an annealing heat treatment at elevated temperature. In this case, unless annealing time and temperature are very strictly controlled, recovery and recrystallization are expected to occur in overlapping mode. On one hand, the occurrence of various processes leads to a competition, which is particularly the case for thermally activated recovery mechanism that are driven by the stored energy of plastic deformation. On the other hand, these processes competing for the same energy source also interact with each other. For example, recovery is considered as a necessary step in the nucleation stage of recrystallization. Rearrangements of dislocations and migrations of sub-grain boundaries during recovery can lead to abnormal sub-grain growth, which is an essential nucleation mechanism of recrystallization. Therefore, it is not evident to separate or isolate recrystallization from recovery.

Recrystallization, similar to other thermal activated processes, can be divided in two subsequent stages: nucleation and growth. In the nucleation stage, small crystal volumes with low densities of lattice defects are formed in existing deformed (and recovered) microstructure. During nucleation, dislocations are rearranged and annihilated, high angle boundaries are also created by diffusion assisted mechanisms such as the climb of dislocations. The formation of high angle boundaries is an essential step for the mutation of defect-free crystal volumes to recrystallization nuclei. At least, parts of the crystal volumes need to be surrounded by high angle boundaries for further growth. Rearrangement of dislocations and formation of high angle boundaries, on the one hand, reduces orientation gradients and thus the internal energy of crystal volumes. On the other hand, they increase surface energy of crystal volumes by introducing new grain-grain interfaces. The increase in surface energy, therefore, must be compensated by a reduction in volumetric part of the energy so that the formation of the nucleus provides a net energy gain. In general,

nuclei should exhibit a critical size and surrounded by high angle boundaries. The role of high angle boundaries on recrystallization will be further discussed particularly during growth, as below mentioned.

In the second stage of recrystallization, nuclei grow into the deformed matrix and form a new microstructure. This growth is characterized by the migration of high angle boundaries sweeping through the deformed grains. The rate in which a nuclei grows is controlled by two factors: the stored energy of deformed grains and the mobility of grain boundary. For the same nucleus, the growth will be faster if the difference of stored energy across the grain boundary is larger and with increasing mobility of the GB. The stored energy of the deformed crystals is dependent on dislocation structures, which in turn are variants of the crystallographic orientations and the applied deformation mode. Boundary mobility, in general, is a function of grain misorientation. Normally, boundaries having the misorientation angles higher than  $10^\circ$  to  $15^\circ$  migrate faster than low angle boundaries. Their migration rates are about 100 to 1000 times faster than those of low angle boundaries [18]. The mobility of low angle boundaries, including dislocation walls, is controlled by the diffusion rate of vacancies. On the contrary, the rate determining step of high angle grain boundaries is the jump frequency of atoms from shrinking to growing grains. Because in polycrystal, atoms are much more abundant than vacancies, the mobility of high angle boundaries, therefore, is faster than that of low angle ones.

The migration rate of grain boundary is dependent on the misorientation between grains. However, it is not simply a linear relationship. Ultimately, the mobility of grain boundaries is dependent on their atomic density, meaning the free volume of the boundaries. Structure and chemistry are the two factors which have large impact on grain boundary mobility. In solid solutions of multi component alloys, differences in atomic sizes lead to segregation of alloying elements toward grain boundaries. Atomic densities of grain boundaries in multi component alloys are higher, and thus migration rates of boundaries are slower than those in pure materials. Even if atomic sizes of elements in alloys are compatible or materials are pure, there still may be a variation in the migration rate of high angle grain boundaries. Grain boundaries,

according to current perception, is considered as a structural entity, rather than a defect or a disorder feature of crystalline materials.

Structure or atomic arrangement of grain boundaries apparently defines the atomic density of the boundaries, and hence has impact on their mobility. The structure of grain boundaries can be characterized by five parameters [19]. Three parameters represent the crystallographic misorientation between neighboring grains, while two additional parameters are required to determine the inclination angles of the boundary plane with reference to a reference system. The crystallographic misorientation, similar to the crystallographic orientation, can be described by a triplet of Euler angles, a transformation matrix, a rotation axis-angle pair or a Rodrigues vectors. Among these, the axis-angle pair is the most comprehensive notation and intensively used to represent misorientation. This notation directly links the physical features of grain boundaries to the mathematical quantities. The axis of rotation is the normal vector to a common crystal plane for the two grains, whereas the angle of rotation is the deviation between similar vectors lying in that common plane. Because crystallites are 3-dimensional objects, there are numerous ways to define an axis-angle pair for a grain pair. Regardless the rotation axis, the crystallographic misorientation is conventionally defined by the smallest rotation angle between two crystals. For cubic structural materials, this disorientation angle has the range from  $0^\circ$  to  $62.8^\circ$  [20;21], of which a value from  $10^\circ$  to  $15^\circ$  is normally selected as a criterion for the transition from low to high angle boundaries. The boundary mobility of low and high angle grain boundaries, indeed, is very different. However, the variation of mobility on high angle grain boundaries is not exclusively dependent on disorientation angles. The structure of grain boundaries is more completely described by including both misorientation angle and axis. Special properties of grain boundaries are able to recognized by the *axis angle pair* because of the connection between this misorientation representation and structure of grain boundaries. If the misorientation axis can be described by a low Miller index crystallographic direction, there will be a common atomic plane between the two crystals. This atomic plane is perpendicular to the misorientation axis, and it implies the atomic arrangements of both neighboring crystals. As such a superstructure exists

which is continuous across the grain boundary, implying that a boundary lattice cell is defined by the so called coincident site lattice (CSL) of the two crystallographic planes [22]. The periodicity of the boundary lattice is characterized by the number of lattices between two coincident lattice sites. These boundaries are called CSL boundaries and denoted by  $\Sigma n$ , in which  $n$  is the periodicity of the coincident lattice sites. E.g. the  $\Sigma 3$  or  $\langle 111 \rangle 60^\circ$  boundary is the coherent twinning boundary of FCC cubic crystals. One of every three lattice sites on the boundary plane of a crystal is coincident with the one of the opposite crystal. The atomic density of the  $\Sigma 3$  boundary is high, and hence the mobility of this boundary is one of the lowest. In a deeper analysis, the grain boundary structure can be classified in different dimensions: tilt and twist, special and random, symmetric and asymmetric. However, those boundary structure analyses are beyond the scope of this study, and they will not be discussed here. Exhaustive references of boundary structure and impact of boundary migration on recrystallization and grain growth can be found elsewhere [18;23]. Within this work, the  $\langle 110 \rangle 26.5^\circ$  ( $\Sigma 19$ ) boundary is considered to have the highest mobility among all grain boundaries of BCC structured materials. This hypothesis is a result of previous studies on nucleation and growth of BCC structured materials during recrystallization [24]. Specifically, Ibe and Lucke studied growth selection during recrystallization of the Fe-3.0 wt.%Si alloy [25]. They observed the fast growth rate of grains having the  $\langle 110 \rangle 26.5^\circ$  boundary and attributed it to the selective growth. This selective growth in the Fe-3.0 wt.% Si alloy is less frequently observed than the high migration rate of the  $\langle 111 \rangle 40^\circ$  boundary in FCC structured materials. However, they are both accounted for by the misorientation dependence of mobility and activation energy for high angle boundary migrations. Furthermore, it has been observed that the difference in migration rate among various high angle boundaries is decreased as the temperature is increased. Hence, the high mobility of the  $\langle 110 \rangle 26.5^\circ$  boundary will be integrated into simulation models for calculations of texture evolution during recrystallization whenever difference in migration rate of high angle grain boundaries is expected. Particularly, the high migration rate of the  $\langle 110 \rangle 26.5^\circ$  boundaries should be more prominent in recrystallization of cold rolled materials rather than of warm rolled materials.

#### *4.4 Statistical models for recrystallization texture prediction*

Many calculation models have been proposed to simulate the recrystallization texture of metallic materials after annealing. Depending on relevant aspects, the recrystallization texture models can be categorized into two main groups: microstructural and statistical based models.

Microstructural models for recrystallization texture simulate the phenomenon considering changes of geometry and topological features of the microstructure. The deformation microstructure is considered as the initial state at the onset of recrystallization. In cellular automata or Monte Carlo models, the topology of the deformed state is discretized in a set of representative spatial points, of which each point is defined by several microstructural state parameters. There is no restriction on the number of state parameters for a representative point. With the larger number of parameters, the more detailed the material is described, and the more extensive the phenomenon is considered, but the more expensive the calculation cost. Typically, a material point can be specified by spatial coordinates, crystallographic orientation and stored energy. The spatial coordinates of points indicate their relative positions to other neighbors. Between nearest neighboring points, the boundary migration rate can be determined as a variant of crystallographic misorientation. The evolution of recrystallization is simulated by state changes of material points, according to energy and boundary criteria. Evaluation and modification of microstructural states at each point is carried on by deterministic or stochastic algorithms. Accordingly, Monte Carlo models, cellular automata and phase field methods are can be used as solvers for recrystallization models.

The main output of the topologically resolved models are microstructural features, including grain shape and grain size distributions. Recrystallization kinetics can also be extracted from these models. Also the recrystallization texture can be captured by large scale simulations. However, in order to obtain reasonable accuracy, a large volume or area of the microstructure needs to be covered, including various features of the deformed state such as e.g. grain boundaries, shear bands and deformation bands. To keep track of the evolution of microstructure during recrystallization



requires long and massive calculations. Therefore, these simulations are usually limited on spatial size and calculation time, because of limited computing resources.

Statistical models for recrystallization also use representative points to describe material states. Opposed to the topologically resolved models, in the statistical models the spatial character of the microstructural state variables are ignored. Recrystallization is considered to be the collective behavior of all grains in an aggregate, rather than the individual evolution of single crystals. A specific crystal orientation may dominate the recrystallization microstructure, because it has energy and boundary mobility advantages to most other crystals in the deformation microstructure, regardless the spatial location of the grain. Specific locations of crystals, therefore, can be neglected, but statistical parameters of microstructure at the initial stage must be known. In crystallographically resolved statistical models, the volume fraction and stored energy of grains are functions of crystallographic orientation. Grain boundaries and migration rate of grain boundaries are variants of grain-grain misorientations. Neighboring crystals, implying relative locations of grains, can be described by orientation correlation function. The evolution of material state variables from the initial deformation state to the final recrystallization state is implemented by probability calculations, according to the stored energy and boundary mobility for each crystal. The more advantage of energy and boundary mobility for a crystal orientation, the better chance for it to be present in the recrystallization texture. Because the spatial coordination of representative points are ignored, geometrical features of the microstructural topology cannot be captured by statistical models. Kinetics of recrystallization is not frequently considered as one of the simulation results. However, recrystallization kinetics can be incorporated in the models by applying a phenomenological function for weight evaluations, for instance via the Johnson-Mehl-Avrami-Kolmogorov (JMAK) equation. The recrystallization texture is the microstructural state variable that is perfectly suited to be simulated by statistical models. Without sophisticate mathematical algorithms, nor long computation durations, a well fitted recrystallization texture to experimental ones could be obtained from such models. The implementation of recrystallization in several statistical models will be reviewed in the following sections.

#### 4.4.1 Bunge-Kohler model

Bunge and Kohler [26] considered recrystallization and the formation of recrystallization texture from atomistic to statistical scales. At the largest scale, the statistical level, all geometrical features of materials are statistically averaged out. Therefore, simulation models at this scale are valid for an entire group of statistically equivalent samples, but not for any particular one. Statistical models for recrystallization texture include two stages: nucleation and growth, both are characterized by distinguished orientation distribution functions. The change of the orientation distribution function, considering the stored energy and grain boundary mobility distributions, accounts for the evolution of texture from deformation to recrystallization. The recrystallization kinetics is incorporated by using a time dependent function for nucleation. The recrystallization texture is calculated by:

$$f^R(g^R, t) = G(n) \cdot f^G(g^R, t) \cdot f^N(g^R, t) \quad (4.15)$$

where  $f^R(g^R, t)$  is the ODF at the time  $t$  during recrystallization;  $G(n)$  is a geometrical factor depending on the dimensionality  $n$  of the growth, which can be 1, 2 or 3D;  $f^N(g^R, t)$  and  $f^G(g^R, t)$  are the nucleation and growth dependent factors.

The nucleation dependent factor  $f^N(g^R, t)$  could be considered as the texture of all nuclei at the time  $t$ . An explicit form of this ODF is given by:

$$f^N(g^R, t) = \int_0^t N(t) \cdot f^N(g^R, t) \cdot t^n \cdot I(x^R(t)) \cdot dt \quad (4.16)$$

in which  $N(t)$  and  $f^N(g^R, t)$  are the total number of recrystallization nuclei and the orientation distribution function of nuclei at the time (t) of recrystallization; respectively, whereby  $t^n \cdot I(x^R(t))$  are time dependent factors of nucleation. These terms account for the kinetics of recrystallization, in which the factor  $I(x^R(t))$  describes the grain impingement. This grain impingement factor is a function of recrystallized volume fraction  $x^R(t)$  which in turn is approximated by the JMAK equation.

Bunge and Kohler [26] proposed two different forms of the growth dependent factor  $f^G(g^R, t)$  for recrystallization texture models. Both are depended on the deformation texture but attributed to distinguished growth mechanisms, and implemented in two different models. In the first case, it is assumed that each nucleus only grows into its own deformed orientation and there are abundance of nuclei during recrystallization. The growth, therefore, occurs in the same way but at very different rates for fast and slow growing grains. For each orientation, the growth rate is proportional to its volume fraction, the stored energy and the boundary mobility. The total growth texture is written as following:

$$f^N(g^R, t) = \int_0^t N(t) \cdot f^N(g^R, t) \cdot t^n \cdot I(x^R(t)) \cdot dt \quad (4.17)$$

in which  $m(\Delta g)$  is the boundary mobility, which depends on the orientation difference between growing grain and deformed matrix grains  $\Delta g = g^R \cdot (g^D)^{-1}$ ;  $P(g^D)$  is the driving force for recrystallization of the deformed orientation  $g^D$ . According to the equation 4.17, the growth texture is simply a linear transformation of deformation texture. The discrete recrystallization texture in fact is a superposition of all individual deformation orientations, which are mapped by mobility and energy operations. The calculation model of the equation 4.15, therefore, is known as the *superposition model*.

Differently, if a nucleus grows simultaneously and successively into many other deformation orientations, its growth rate will be drastically changed both with time and location. While local and instantaneous growth rate of nucleus is not the scope of statistical models, an average growth rate throughout the recrystallization is required for texture calculations. In the *compromise model* [26;27], this average growth rate for each nucleus is determined from growth rates of these nucleus to all orientations in the deformation texture. The time for a boundary sweeping through a specific deformed crystallite is depended on its volume fraction and inversely proportional to the mobility and the stored energy of the grain. The average growth texture is written by:

$$f^G(g^R, t) = \left( \int_{g^D} \frac{f^D(g^D, t)}{m(\Delta g) \cdot P(g^D)} dg^D \right)^{-n} \quad (4.18)$$

Since the growth rate of each nucleus is averaged, the calculated texture of equation 4.18 is the compromised result of the fast and slow growing periods of recrystallization. The compromise model is valid for the case, in which the densities of nuclei are low and each nucleus grows into many different deformation orientations throughout the recrystallization.

The compromise model has been used by Kohler et al. [27-29] to predict the recrystallization textures of both FCC and BCC structured materials. For an FCC structured material, they selected a Brass alloy with a Zn fraction of 30%, exhibiting a conventional rolling texture includes the Brass ( $\{110\}\langle 112\rangle$ ) and the Goss ( $\{110\}\langle 001\rangle$ ) orientations. This *brass-type* texture is very typical for low stacking fault energy FCC metals, in sharp contrast with the *copper-type* (the  $\beta$ -fiber) texture of high stacking fault energy FCC materials. Upon recrystallization, the nucleation is assumed to be random and constant, meaning the nucleation texture  $f^N(g^R, t) = 1$

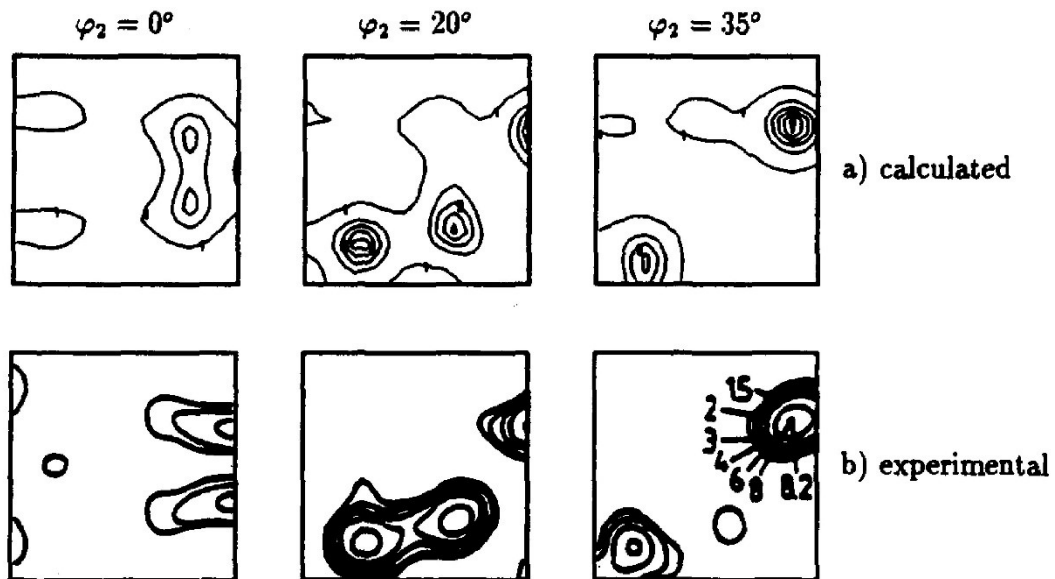


Figure 4.7 The (a) modeled and (b) measured recrystallization texture of a Brass alloy (CuZn30) at section  $\varphi_2 = 0^\circ, 20^\circ$  and  $35^\circ$  of the Euler space [27].

for all orientations. Dependence of growth on boundary mobility is given by the high migration rate for the  $\langle 111 \rangle 40^\circ$  boundary, while the variation of deformation stored

energy is ignored,  $P^D(g^D) = 1$ . The simulation recrystallization texture purely depends on the growth selection of deformation orientations. Nevertheless, the simulation result (Figure 4.7a) shows all features of the measured recrystallization texture (Figure 4.7b). The misfit between simulated and measured ODFs is mainly about texture intensity, particularly at the less favorable orientations. According to Kohler et al. [28], this uncertainty is induced by the simplicity of calculations as oriented nucleation was totally discarded in this simulation. In addition, the homogeneity of the stored energy distribution, which was imposed by  $P^D(g^D) = 1$  is unlikely to be a valid assumption in this situation.

For a BCC structured material, Kohler and Bunge investigated the recrystallization of an ARMCO-Iron [29]. The rolling texture of this material includes the  $\alpha$ -( $\langle 110 \rangle // \text{RD}$ ) and  $\gamma$ -( $\langle 111 \rangle // \text{ND}$ ) fiber textures. This deformation texture is similar to the experimentally observed orientation distribution of nuclei. Therefore, recrystallization texture was predicted by assuming that the texture of nuclei was equal to the deformation texture,  $f^N(g^R) = f^D(g^D)$ . The growth dependent factor was derived from the high growth rate of the  $\langle 110 \rangle 26.5^\circ$  boundary for BCC metals

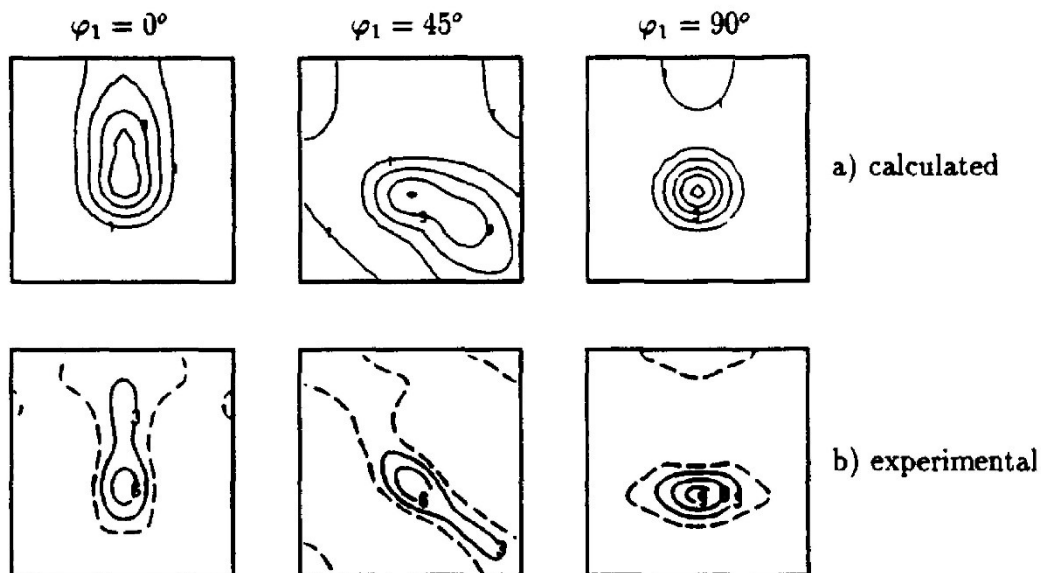


Figure 4.8 The (a) modeled and (b) measured recrystallization texture of ARMCO-Iron at section  $\varphi_1 = 0^\circ, 45^\circ$  and  $90^\circ$  of the Euler space [27].

[25], while the heterogeneity of energy distribution among deformation orientations was suppressed. The calculated and experimental recrystallization texture are given

in Figure 4.8. The two textures are very much similar, although the texture components in the simulated ODF exhibit higher intensities and larger spread than the experimental counterparts.

#### 4.4.2 Kestens-Jonas model

Observing important roles of both oriented nucleation and selective growth on recrystallization, Kestens and Jonas [30] developed a statistical model to simulate the evolution of recrystallization textures. The proposed model includes two separated calculation steps, nucleation and growth. Each of these steps is controlled by separate orientation selective rules.

In the first step of the texture simulation, the probability for each orientation ( $g_i$ ) to nucleate on its own deformed matrix ( $P_N(g_i)$ ) is evaluated. This nucleation probability is assumed to be dependent on the stored energy, which in turn can be estimated by the Taylor factor of crystal plasticity models. The relationship between the plastic stored energy in deformed crystal and the Taylor factor of crystal plasticity models will be discussed in the Chapter 7. In their investigations, Kestens and Jonas [30;31] focused on a specific nucleation mechanism, namely the sub-grain coalescence. This nucleation mechanism is briefly described by the coalescence and rotation of neighboring sub-grains, caused by vacancy or self-diffusion and dislocation climb. During the diffusion, the misorientation between sub-grains is decreased, while the high angle boundary is formed around sub-grain clusters. The sub-grain coalescence is expected to be observed in high stored energy grains of the cold deformation polycrystal, because of the high dislocation density. Therefore, this nucleation mechanism is enhanced in orientations with high Taylor factor, i.e. orientations of which the Taylor factor exceeds a certain value. For orientations which have Taylor factor lower than the threshold value ( $M_o$ ), the probability to nucleate is set to zero. The orientation selection, according to the sub-grain coalescence, is given by:

$$\begin{cases} M(g_i) < M_o \Rightarrow P_N(g_i) = 0 \\ M(g_i) \geq M_o \Rightarrow P_N(g_i) = c_1(M(g_i) - M_o)^m \end{cases} \quad (4.19)$$

Where  $c_1$  is a normalization factor for the nucleation probability function ( $P_N(g_i) \in [0,1]$ ),  $m$  is an exponential factor, which allows the dependence of the nucleation mechanism on Taylor factor distribution to be varied. The orientation distribution function of nuclei is given as following:

$$\begin{cases} M(g_i) < M_0 \Rightarrow f^N(g_i) = 0 \\ M(g_i) \geq M_0 \Rightarrow f^N(g_i) = c_2(M(g_i) - M_0)^m f^D(g_i) \end{cases} \quad (4.20)$$

in which,  $c_2$  is a normalization factor for the total volume of nuclei ( $\int f^N(g)dg = 1$ ).

In the second step of the texture simulation, the probability for a particular nucleus to grow in the deformation matrix ( $P_G(g_i)$ ) is calculated. This probability is an average value from all local growth probabilities of the nucleus to matrix orientations. The weight factor for each local growth probability, contributing to the average growth, is the volume fraction of the disappearing grain in the deformation orientation. The average growth probability is given by:

$$P_G(g_i) = c_3 \sum_{j=1}^Q P_{LG}(g_j \cdot g_i^{-1}) \cdot f^D(g_j) \quad (4.21)$$

where  $c_3$  is the normalization factor for the average growth probability of the orientation  $g_i$  and  $P_{LG}(g_j \cdot g_i^{-1})$  is the local growth probability of the nucleus  $g_i$  into the deformation orientation  $g_j$ .

The local growth probability, in principle, can accept any value from 0 to 1, depending on the misorientation between nucleus and deformed grain  $\Delta g_{ij} = g_j \cdot g_i^{-1}$ . In the simplest form, this probability can be set as an identical value for all possible misorientation, which imposes the randomly growth rule. On the contrary, the local growth probability can be given by a specific function so that some special boundaries exhibit an increased mobility, to account for the selective growth of nuclei. Kestens and Jonas [30] considered a special type of growth rule for BCC structured materials, i.e. the so called the  $\{110\}$  plane matching boundaries. This growth rule attributes an increased mobility to boundaries of which crystallites have a common  $\langle 110 \rangle$  axis, but does not require any specific misorientation angle. In addition, this

special  $\langle 110 \rangle$  axis must be the one perpendicular to the most active slip plane of the deformed grain. This selective growth is accounted for by the stimulated diffusion of solute atoms during recrystallization. During plastic deformation, dislocations are generated in grains, but they are not homogeneously distributed on the whole volume of crystals. The most active slip planes, i.e.  $\{110\}$  planes in BCC materials, should generate and store more dislocations than any other planes. Subsequently, the diffusion of solute atoms along this plane is faster and easier than in the bulk. The migration rate of  $\{110\}$  matching boundaries, therefore, is higher than for normal boundaries. The local growth probability, according to the plane matching boundary theory, is determined by:

$$\begin{cases} \omega < \omega_0 \Rightarrow P_{LG}(\Delta g_{ij}) = 0 \\ \omega \geq \omega_0 \Rightarrow P_{LG}(\Delta g_{ij}) = c_4 \cdot \exp \left[ - \left( \frac{\theta_{ij}}{\theta_0} \right)^n \right] \end{cases} \quad (4.22)$$

in which  $\omega$  is the misorientation angle between the nucleus and deformation orientations;  $\omega_0$  is the critical angle for operation of the local growth rule;  $\theta_{ij}$  is the deviation angle between the misorientation axis and the  $\langle 110 \rangle$  axis. Dependence of local growth probability on the deviation angle is given in the form of a Gaussian probability distribution function, in which the angle  $\theta_0$  controls the spread and the exponential factor  $n$  specifies the sharpness of the probability distribution. In the best situation when the deviation angle vanishes, the local growth probability has its maximum value. In all other situations, this probability has a much lower value.

From calculated nucleation and growth probabilities, the recrystallization texture  $f^R(g_i)$  can be obtained as following:

$$f^R(g_i) = c_5 (P_G(g_i))^p P_N(g_i) f^D(g_i) \quad (4.23)$$

Where  $c_5$  is the normalization factor for the total volume of recrystallization orientations ( $\int f^R(g) dg = 1$ );  $p$  is the amplification factor for growth probability to control the balance between oriented nucleation and selective growth. The volume fraction of a recrystallization orientation is proportional to its fraction in the deformed state with scale factors of nucleation and growth probabilities.



The Kestens-Jonas model was first employed to investigate recrystallization texture of BCC structured materials. A Ti-Nb microalloyed IF steel was used as model material. The material was first cold rolled to reduce the thickness with 85 percent, and then subjected to a recrystallization heat treatment. After the cold rolling, the texture of material contains  $\alpha$ - and  $\gamma$ -fibers. The maximum intensity of this ODF, measured near the  $\{223\}\langle 110\rangle$  orientation, is 12 times the random level, and a local high intensity of 10 times of the random level is observed near the  $\{001\}\langle 110\rangle$  orientation. After the annealing heat treatment, intensities of the  $\gamma$ -fiber texture components are enhanced, while most of the  $\alpha$ -fiber texture components have disappeared. The highest intensity of the ODF is 12 times of random level at the  $\{111\}\langle 112\rangle$  orientation. The texture evolution during recrystallization was simulated with the threshold Taylor factor ( $M_0$ ) of 2.8 and the amplification factor ( $p$ ) for selective growth of 4. The probability function for nucleation is supposed to be linear dependence on the Taylor factor ( $m = 1$ ). Both of the measured and simulated recrystallization texture can be seen in Figure 4.9. There is a good agreement between calculation and experimental results.

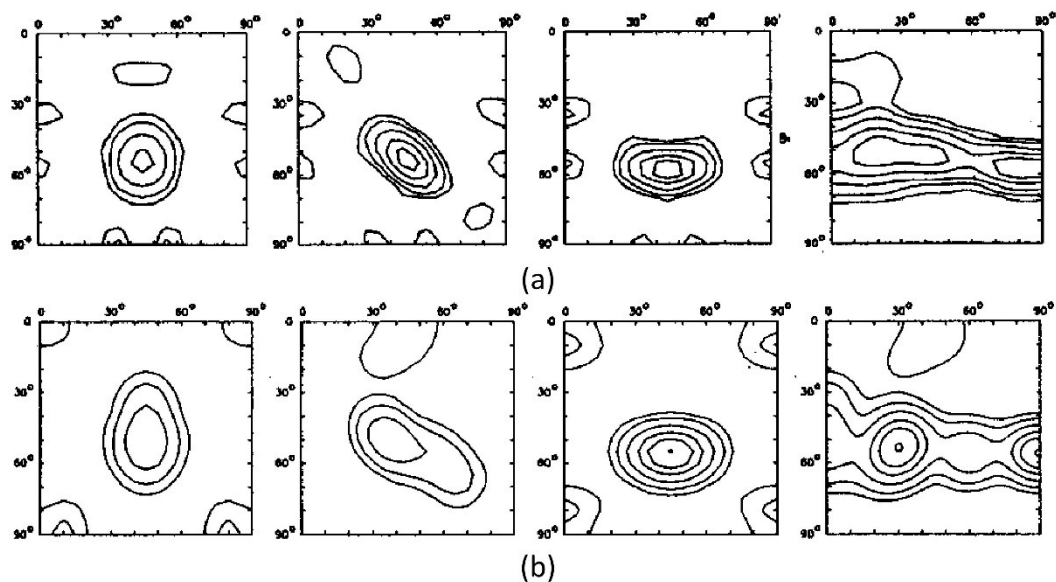
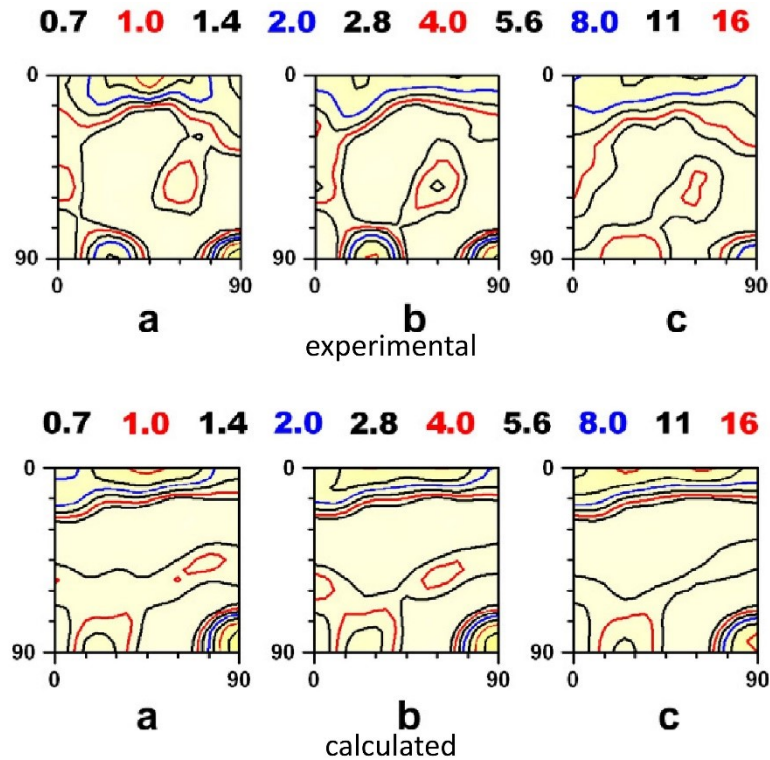


Figure 4.9 ODF sections at  $\varphi_1 = 0, 45$  and  $90$  degrees and  $\varphi_2 = 45$  degrees of the recrystallization textures, measured for an Ti-Nb IF steel (a) and simulated by the Kestens-Jonas model (b) with input parameters of  $p = 4$ ,  $M_0 = 2.8$ ,  $m = 1$  and the initial cold rolling texture [30].

The Kestens-Jonas model was also applied successfully to simulate the recrystallization texture of FCC structured materials. Sidor et al. [32] investigated the texture evolution during recrystallization of an 6016 aluminum alloy. The material was first subjected to three different thermo-mechanical routes, including symmetric or asymmetric hot rolling and annealing, to obtain different microstructures and textures. Conventional cold rolling was then applied to reduce the sheet thickness of 85 to 87%. In the final step, all samples are recrystallization annealed at 550°C for 30s. Although there are differences after hot rolling, microstructures and textures of the materials after the cold rolling are mostly identical, i.e. all samples contain the  $\beta$  fiber texture. Intensities of texture components, however, are slightly different. In two samples of symmetric hot rolling, the maximum intensity of 16 mrd (multiples of random intensity) is measured at the Brass ( $\{110\}\langle 112\rangle$ ) and the S ( $\{123\}\langle 634\rangle$ ) components. In the other one, which was asymmetrically hot rolled, the maximum intensity of the  $\beta$ -fiber is about 9 times of random level. Additionally, a weak Cube ( $\{001\}\langle 100\rangle$ ) texture component is also found in this sample.

After recrystallization, textures of all three samples include the Cube ( $\{001\}\langle 100\rangle$ ), the Goss ( $\{110\}\langle 001\rangle$ ) and the P ( $\{110\}\langle 332\rangle$ ) components. To account for this texture evolution during recrystallization, the texture simulation with the Kestens-Jonas model was employed. The oriented nucleation is assumed to follow the low stored energy rule, which will be discussed more intensively in Chapter 7. The effective range for this oriented nucleation is from 0 to 0.258 of the highest Taylor factor in a specific deformation configuration. The macroscopic deformation configuration for cold rolling is plane strain compression. However, many crystallites are around non-deformation particles are deformed by different deformation modes. Sidor et al. [32] proposed two alternative deformation modes for these crystallites, including uniaxial extension and in-plane shear. These local deformation configurations account for the particle stimulated nucleation (PSN) during recrystallization. In total, the material is expected to exhibit three different and co-existing nucleation mechanisms on the microscopic scale, namely homogeneous nucleation, PSN and the random nucleation. These three nucleation mechanisms operate independently, but they create different nucleation textures, according to



**Figure 4.10** The recrystallization textures of an 6016 aluminum alloy following three different thermo-mechanical routes (a, b and c), which are obtained by measurement (top row) and simulation (bottom row) [32].

their nucleation probability functions. The total nucleation texture is a linear combination of the three local nucleation texture.

The growth of these nuclei, irrespective of the nucleation mechanisms, is supposed to have the same average migration rate. Among all boundaries between nucleus and deformation orientations, only the  $\langle 111 \rangle 40^\circ$  boundary is considered to exhibit a preferred mobility. Therefore, nuclei having the  $\langle 111 \rangle 40^\circ$  orientation relationship to a large fraction of deformation orientations will have higher chance to growth. The recrystallization textures of the material, following three different thermo-mechanical routes are given in the Figure 4.10. The measured textures are shown in the top row, whereas the simulated textures are given in the bottom row of this figure. The excellent fit between experiment and simulation textures illustrates the role of different nucleation mechanisms on the recrystallization texture formation. Specifically, the homogeneous mechanism contributes 0.53, while the random

mechanism brings 0.28 to the total fraction of nucleation. The PSN plays the smallest role on nucleation (0.19 of the total fraction).

#### *4.5 Summary*

In this chapter, plastic deformation and recrystallization in metallic structural materials are reviewed. These physical processes have been systematically analyzed and fully described by mathematical calculation models.

Plasticity of polycrystal materials, in general, are collective behavior of each individual crystal grains. In a single BCC crystal, plasticity is mostly carried on by dislocation glides. These glides are shears of atoms on specific slip planes and along certain slip directions. To fulfill external boundary conditions of crystal plasticity, multi-slips are usually required in which each activated slip systems need to obey the Schmid law of critical resolved shear stress. Accumulation and interaction of dislocation during crystal plasticity increase the critical resolved shear stress for dislocation glides and result in strain hardening during the deformation. The glides of dislocations during plasticity, besides changing crystal geometry, rotate the crystal toward more preferred orientations to deformation condition. To account for the plastic deformation and rotation of crystal, various crystal plasticity models have been developed. From a single to poly-crystal plasticity, assumptions to homogenize deformation condition from micro- to macroscopic scale need to be applied. By considering both stress equilibrium and strain balance near boundaries of crystal pairs, the ALAMEL model could well capture deformation textures of cubic crystal materials after plastic deformation.

Recrystallization is an energy reduction process to regain the lattice-defect free stage in material after plastic deformation. Among other thermal activated processes in material microstructures, recrystallization is evolution of lattice defect free crystals by migrations of high angle grain boundary under the driving force of the plastically stored energy. Stored energy in deformed crystal, induced by the stress field around accumulated dislocations, is an orientation dependence. Migration rate of grain boundary, in general, is a function of grain boundary structure which in turn could be described by the misorientation between a pair of grains. Because of the difference in

stored energy among deformed crystals and the variation of grain boundary mobility, recrystallization texture usually appear in materials after annealing. To predict the evolution of recrystallization texture, statistical calculation models are more suitable and easier to use than microstructure based models. In statistical based models, each stages of the recrystallization (i.e. nucleation and growth) are characterized by specific probability functions. These probability functions are represented for physical rules to select crystallographic orientation during recrystallization. Operation of nucleation and growth function on deformation texture results in the recrystallization texture. The Kestens-Jonas model, in spite of mathematical simple, has been effectively used in prediction of recrystallization texture in both FCC and BCC structured materials.

### *4.6 References*

- [1] Greer JR, De Hosson JTM. Plasticity in small-sized metallic systems: Intrinsic versus extrinsic size effect. *Prog Mater Sci.* 2011;56:654.
- [2] Vitek V, Paidar V. Chapter 87 Non-planar Dislocation Cores: A Ubiquitous Phenomenon Affecting Mechanical Properties of Crystalline Materials, John H, editor in. *Dislocations in Solids*, vol. Volume 14. Elsevier; 2008. p.439.
- [3] Taylor GI, Elam CF. Bakerian Lecture. The Distortion of an Aluminium Crystal during a Tensile Test. *Proceedings of the Royal Society of London. Series A.* 1923;102:643.
- [4] Taylor GI, Elam CF. The Plastic Extension and Fracture of Aluminium Crystals. *Proceedings of the Royal Society of London. Series A.* 1925;108:28.
- [5] Schmid E, Boas W. *Plasticity of crystals: with special reference to metals:* Chapman & Hall; 1968.
- [6] Taylor GI, Elam CF. The Distortion of Iron Crystals. *Proceedings of the Royal Society of London. Series A.* 1926;112:337.
- [7] Taylor GI, Farren WS. The Distortion of Crystals of Aluminium under Compression. Part I. *Proceedings of the Royal Society of London. Series A.* 1926;111:529.

- [8] Taylor GI. The Distortion of Crystals of Aluminium under Compression. Part II. Distortion by Double Slipping and Changes in Orientation of Crystal Axes during Compression. Proceedings of the Royal Society of London. Series A. 1927;116:16.
- [9] Taylor GI. The Distortion of Crystals of Aluminium under Compression. Part III. Measurements of Stress. Proceedings of the Royal Society of London. Series A. 1927;116:39.
- [10] Taylor GI. Plastic Strain in Metals. Journal of the Institute of Metals. 1938;62:307.
- [11] Van Houtte P. A Comprehensive Mathematical Formulation of an Extended Taylor-Bishop-Hill Model Featuring Relaxed Constraints, the Renouard-Wintenberger Theory and a Strain Rate Sensitivity Model. Texture Microstruct. 1988;8:313.
- [12] Kocks UF, Chandra H. Slip geometry in partially constrained deformation. Acta Metallurgica. 1982;30:695.
- [13] Van Houtte P. On the equivalence of the relaxed Taylor theory and the Bishop-Hill theory for partially constrained plastic deformation of crystals. Materials Science and Engineering. 1982;55:69.
- [14] Van Houtte P, Delannay L, Samajdar I. Quantitative Prediction of Cold Rolling Textures in Low-Carbon Steel by Means of the Lamel Model. Texture Microstruct. 1999;31:109.
- [15] Van Houtte P, Li S, Seefeldt M, Delannay L. Deformation texture prediction: From the Taylor model to the advanced Lamel model. Int J Plast. 2005;21:589.
- [16] Van Houtte P. Crystal Plasticity Based Modelling of Deformation Textures, Haldar A, Suwas S, Bhattacharjee D, (eds.) in. Microstructure and Texture in Steels. Springer London; 2009. p.209.
- [17] Doherty RD, Hughes DA, Humphreys FJ, Jonas JJ, Jensen DJ, Kassner ME, King WE, McNelley TR, McQueen HJ, Rollett AD. Current issues in recrystallization: a review. Materials Science and Engineering: A. 1997;238:219.
- [18] Humphreys FJ, Hatherly M. Recrystallization and related annealing phenomena, Second ed. New York: Elsevier Science; 2004.
- [19] Schwartz AJ, Kumar M, Adams BL, Field DP. Electron Backscatter Diffraction in Materials Science: Springer US; 2009.

- [20] Mackenzie JK, Thomson MJ. Some statistics associated with the random disorientation of cubes. *Biometrika*. 1957;44:205.
- [21] Mackenzie JK. Second paper on statistics associated with the random disorientation of cubes. *Biometrika*. 1958;45:229.
- [22] Randle V, Materials Io. *The Role of the Coincidence Site Lattice in Grain Boundary Engineering*; Institute of Materials; 1996.
- [23] Gottstein G, Shvindlerman LS. *Grain Boundary Migration in Metals*; CRC Press; 2009.
- [24] Gangli P, Jonas JJ, Urabe T. A combined model of oriented nucleation and selective growth for the recrystallization of interstitial-free steels. *Metallurgical and Materials Transactions A*. 1995;26:2399.
- [25] Ibe G, Lücke K. Growth selection during recrystallization of single crystals. *Recrystallization, Grain Growth and Textures*. 1966.
- [26] Bunge HJ, Kohler U. Modelling Primary Recrystallization in fcc and bcc Metals by Oriented Nucleation and Growth With the Statistical Compromise Model. *Texture Microstruct*. 1997;28:231.
- [27] Bunge HJ, Köhler U. Model calculations of primary recrystallization textures. *Scr. Metall. Mater*. 1992;27:1539.
- [28] Kohler U, Dahlem-Klein E, Klein H, Bunge HJ. Model Calculations of Recrystallization Texture Formation by Growth Selection. *Texture Microstruct*. 1992;19:125.
- [29] Kohler U, Bunge HJ. Model Calculations of the Recrystallization Texture Formatio in alpha-Iron. *Texture Microstruct*. 1995;23:87.
- [30] Kestens L, Jonas JJ. Modeling texture change during the static recrystallization of interstitial free steels. *Metallurgical and Materials Transactions A*. 1996;27:155.
- [31] Kestens L, Jonas JJ, Van Houtte P, Aernoudt E. Orientation selective recrystallization of nonoriented electrical steels. *Metall Mat Trans A Phys Metall Mat Sci*. 1996;27:2347.
- [32] Sidor JJ, Petrov RH, Kestens LAI. Modeling the crystallographic texture changes in aluminum alloys during recrystallization. *Acta Mater*. 2011;59:5735.

# 5

## *Material and manufacturing*

### *5.1 Introduction*

Microstructure and texture development in polycrystalline materials depend on the processing parameters and the initial condition of the materials. A through-process investigation of microstructure and texture evolution will therefore provide useful information for improved microstructure and texture control during material processing. This investigation will provide an overview of the microstructural and texture changes that occur at different stages of the manufacturing process. Key parameters, affecting texture development after each manufacturing step, will be identified. The physical laws governing texture evolution will also be revealed.

In this chapter, the microstructure and texture of a 1.2 wt.% Si electrical steel in the initial state are measured via EBSD. The chemical composition and processing parameters of the studied material are fully described.



## 5.2 Material

An alloy of iron and 1.2 wt.% Si (see Table 5.1 for chemical composition) is considered in this study. The chemical composition of this material is typical for NO electrical steels. During processing, the material is industrially cast (ingot thickness of 220 mm) and the resulting ingot is then subjected to rough rolling at 1100°C, where the thickness of the material is reduced to 10 mm. Rolling passes of 15 to 50% thickness reduction per pass are applied during this rolling step. After air cooling the material to room temperature, the slabs are de-scaled and divided into groups for further investigation.

**Table 5.1 Chemical composition of the studied material (wt.%).**

Si	C	Mn	Al	Cu	Ti	N	P	S	B	Fe
1.23	0.0025	0.31	0.12	0.014	0.002	0.0023	0.066	0.008	0.0003	bal.

## 5.3 Manufacturing procedures

The production lines, used in this investigation, include hot rolling, continuous annealing, cold rolling, and final annealing. Based on the physical phenomena occurring in the material, these processing steps are divided into two main groups: thermal and mechanical processes. Hot band annealing and final annealing are thermal activation processes, where materials release strain energy (accumulated during rolling) through recovery and recrystallization. Cold rolling refers to the sheet deformation process performed at room temperature. Cold rolling at normal strain rates has negligible thermal effect on crystal behavior and can therefore be considered a purely mechanical process. In contrast, hot rolling is performed at elevated temperatures and is characterized by the occurrence of complex physical phenomena. During hot rolling, materials are constrained by mechanical forces while the influence of thermal forces induced by heat sources and high rolling speeds is non-negligible. Hot rolling is, in general, a mix of thermal and mechanical processes. Depending on the rolling temperature, microstructural and texture evolution during hot rolling is dominated by one of these two processes. In this study, hot rolling is considered a mechanical process, although the thermal process is always deemed crucial for microstructural and texture formation.

Mechanical processes, including hot and cold rolling, are performed via conventional rolling and an innovative process referred to as asymmetrical rolling. *Asymmetrical rolling* is a sheet deformation process where different rolling velocities are applied to the material surfaces. This difference velocities stems from the rolling-mill geometry, roll speed or roll-sheet friction conditions. The difference in the roll diameter, roll speed, and friction of the top and bottom rolls imposes a RD-parallel shear strain on the material sheets. A through-thickness effect of this shear strain, combined with normal strains, is expected. This effect will result in different deformation modes (rather than the plane strain compression associated with the conventional rolling process) and a new type of deformation texture will be generated.

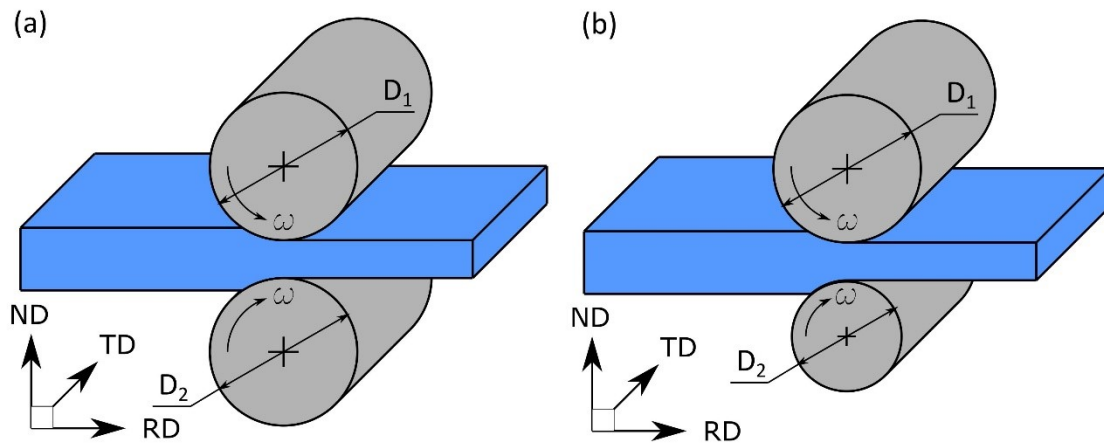


**Figure 5.1 Schematic plots of rolling geometry for the (a) symmetrical and (b) asymmetrical configuration, which are used in this investigation.**

In this study, asymmetrical rolling is performed on a rolling mill, where two motor-driven rolls with different diameters rotate at the same speed. Figure 5.1 shows schematic plots of the symmetrical and asymmetrical rolling configurations used in this study. The use of symmetrical and asymmetrical rolling, at both high and room temperatures, defines four different processing routes of the material.

Differences between the groups of samples produced by various routes indicate the effects of temperature and deformation configuration on the microstructure and texture development of the material. These processing routes are summarized in Figure 5.2.

### 5.3.1 Warm rolling

By high-temperature rolling, the thickness of two groups of as-received samples was reduced to 2 mm. During this process, the samples are heated to 900°C and subjected to three rolling passes yielding 33, 43, and 50% thickness reductions. The first group and second group of samples undergo

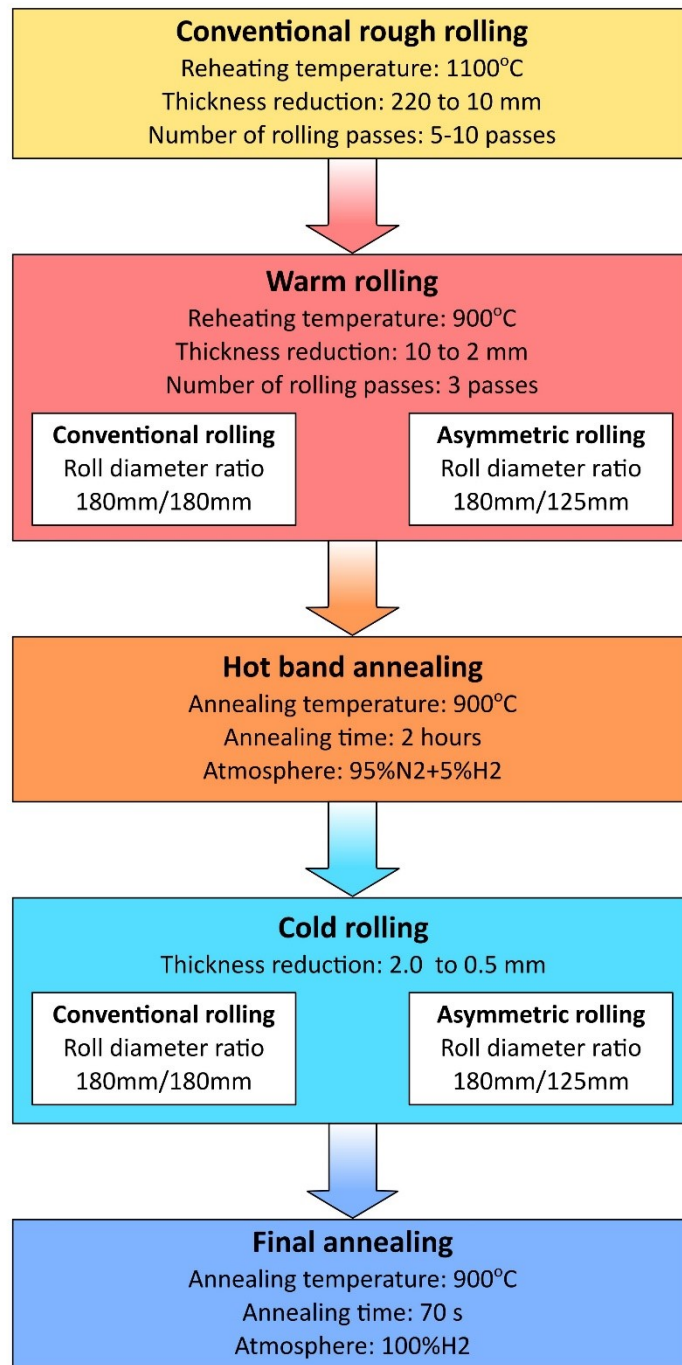


**Figure 5.2 Processing routes of samples considered in this investigation.**

conventional symmetrical rolling and asymmetrical rolling, respectively. The samples are rolled on a 4-high rolling mill equipped with motor-driven rolls. Equal diameter

(i.e., 180 mm) rolls are used for symmetrical rolling, whereas rolls of differing diameters (180 mm: top roll, 125 mm: bottom roll) are used for asymmetrical rolling. During rolling, the temperature is maintained by reheating the samples to 900°C between rolling passes. After warm rolling, the samples are air cooled to room temperature.

### *5.3.2 Hot band annealing*

The warm-rolled samples are subjected to an annealing with the aim of completely recrystallizing the microstructures. During this treatment, samples are heated at a rate of 200 °C/h to 900°C, held at this temperature (i.e., 900°C) for 2 h, and then cooled to room temperature at a rate of 150 °C/h. The samples are protected by a mixed gas of 95 vol.% dry N<sub>2</sub> and 5 vol.% H<sub>2</sub> during annealing. After annealing, the samples are gently sandblasted and pickled.

### *5.3.3 Cold rolling*

Warm rolled and annealed samples are then subjected to different amounts of cold rolling, with the aim of reducing the sample thickness to the final value of 0.5 mm. Symmetrical and asymmetrical rolling configurations are both employed. Furthermore, cold rolling and hot rolling are performed on the same rolling mill. Multi-pass rolling is implemented until the desired thickness is achieved. To improve the flatness and surface quality of each sample, particularly after asymmetrical rolling, the samples are pre-heated for 60 s at 110°C, prior to each rolling pass.

### *5.3.4 Final annealing*

All four different groups of deformation samples undergo the same final heat treatment for recrystallization. In this final annealing, samples are soaked under H<sub>2</sub> protective gas for 70 s in a batch furnace at 900°C.

After each processing step, samples are collected for microstructure and texture investigations.

## *5.4 Initial samples*

In this work, the term as-received refers to samples that have undergone deformation via high-temperature conventional rolling. The microstructure and texture at this stage have rarely been reported. Samples in this condition are usually considered coarse-grained materials with a weak  $\alpha$ - $\gamma$  fiber texture. This microstructure and texture (i) result mainly from deformation and recovery of the material after rolling and during slow cooling to room temperature and (ii) are, in general, unfavorable for magnetic properties. In addition, owing to the large grain size, optical microscopy and X-ray diffraction measurements of these samples is difficult. Nevertheless, in this work, these microstructures are readily investigated by using a scanning electron microscope equipped with an EBSD detector and a fully automated moving stage.

The IPF map (collected via EBSD) in Figure 5.3a shows the microstructure of the initial samples. A total area of  $32000 \times 10000 \mu\text{m}^2$  in the RD-ND plane of the samples is collected at a step-size of  $10 \mu\text{m}$  on a square grid. This initial microstructure consists of equi-axed grains with an average diameter of  $133 \mu\text{m}$ . Although in-grain orientation gradients are absent, slight through-thickness variations in the orientation distribution are observed. Most of the  $\langle 011 \rangle // \text{ND}$ -oriented grains are located in the sub-surface regions and are smaller than the  $\langle 001 \rangle // \text{ND}$ -oriented and  $\langle 111 \rangle // \text{ND}$ -oriented grains, which are located predominantly in the central regions of the samples.

The macroscopic texture of the as-received samples is rather weak (maximum intensity: 3.5 times the random level, see Figure 5.3b). However, large-scale sampling reveals the texture and the statistical symmetry of the samples. This symmetry is imparted to the materials during processing. For conventional rolling, the statistical symmetry of samples results mainly from the deformation geometry. This symmetry, referred to as *mmm* orthorhombic, is characterized by three mirror planes perpendicular to the RD, TD, and ND of the samples. Nevertheless, this orthorhombic sample symmetry was neglected during the calculation of the ODF associated with the as-received samples (see Figure 5.3b). The symmetry corresponding to the  $\varphi_1 = 0^\circ$ ,  $90^\circ$ ,  $180^\circ$ , and  $270^\circ$  positions of the  $\varphi_2 = 45^\circ$  ODF section (c.f. Figure 5.3b) is

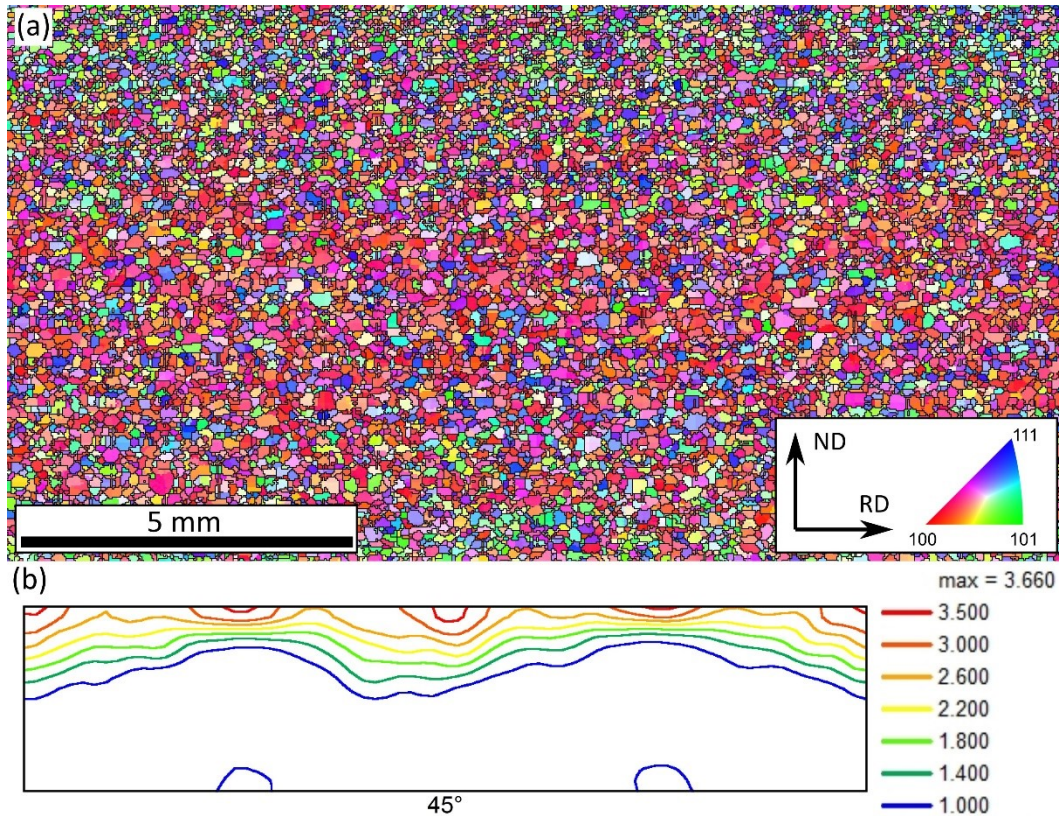


**Figure 5.3(a) Microstructure and (b) texture of the 1.2 wt.% Si electrical steel in the as-received condition.**

characterized by two mirror-planes perpendicular to RD and ND. This symmetry is fully revealed by the orientation sampling of the measurements. The observed symmetry clearly indicates the highly statistical nature of texture measurements.

In contrast to the conventional rolling texture of BCC-structured materials, the macroscopic texture of the as-received material is characterized by a homogeneous Cube ( $\langle 001 \rangle // \text{ND}$ ) fiber and a weak Goss ( $\{110\} \langle 001 \rangle$ ) orientation. The intensities of the orientations along the Cube fiber are all higher than 2.3 times the random level, with the rotated Cube orientation accounting for the highest intensity (i.e., 3.5 times the random level). The Goss orientation occurs with an intensity of 1.2 times the random level. The texture of this initial sample is among the most desirable for NO electrical steels. Nevertheless, the sample thickness (10 mm) is unsuitable for magnetic induction cores, because of the high energy loss stemming from the Eddy current during magnetization.

Although the initial sample was deformed at high temperature, deformation- or recovery-related features are not visible from both the corresponding microstructure and texture. This microstructure and texture associated with high-temperature deformation should form via phase transformation or recrystallization of material during cooling to room temperature.

The Cube fiber texture is rarely observed after conventional processing. However, this texture represents one of the most favorable textures for NO electrical steels and, hence, its occurrence in initial samples will be further discussed in subsequent chapters.

# 6

## *Deformation textures* *of the Fe-1.2 wt.% Si alloy* *after rolling*

To realize the desired thickness (0.2–0.5 mm) for sheet production, samples of electrical steels are usually subjected to various rolling steps. During this deformation, crystal grains in each sample are constrained globally and locally, owing to different geometric conditions. The Fe-1.2 wt.% Si alloy has a body-centered cubic (BCC) lattice structure with high stacking fault energy, and deformation of the grains proceeds mainly via dislocation glide. During this deformation, crystals rotate toward orientations of higher geometrical stabilities, and preferential rotations lead to the formation of deformation textures in materials. In this work, the influence of the



rolling configuration and rolling temperature on the formation of deformation textures is determined. The (i) results of microstructural and EBSD texture investigations and (ii) evolution of deformation textures (evaluated via crystal plasticity simulations) are presented in this chapter.

### *6.1 Hot-rolled samples*

The as-received samples are subjected to hot rolling and an 80% thickness reduction (from 10 to 2 mm) is achieved. Both symmetrical and asymmetrical configurations are employed in this work.

#### *6.1.1 Symmetrically hot-rolled samples*

The microstructure and texture after conventional hot rolling are measured and compared with those formed after asymmetrical rolling. The microstructure of the conventionally hot-rolled samples (see IPF map in Figure 6.1) consists of flat elongated grains, which exhibit significant variations in crystallographic orientation. The grain morphology and orientation spread in this microstructure are consistent with the deformation state of hot-rolled samples. In addition, the occurrence of  $\langle 011 \rangle // \text{ND}$ -oriented grains in the sub-surface layers and  $\langle 001 \rangle // \text{ND}$ - as well as  $\langle 111 \rangle // \text{ND}$ -oriented grains close to the mid-thickness layer reveals the texture variation across the thickness of the sample. This spatial distribution of orientations shows that samples were constrained equally, both on the top and the bottom surfaces. However, the deformation at the surfaces of the sheet differs considerably from that at the center. The friction between the sample and the roll surfaces plays a major role in this texture heterogeneity. In other words, owing to the high friction between the roll and the sample surfaces, samples experience both a shear strain along the rolling direction (RD) and a normal strain. This shear strain is maximum near the surfaces and decreases to a minimum at the mid-thickness layer of the samples. As illustrated in subsequent sections, the RD shear results in grain rotations toward the Goss and the Copper orientations. This shear component is strongest near the sample surface and, hence, shear texture components (i.e., the Goss and Copper

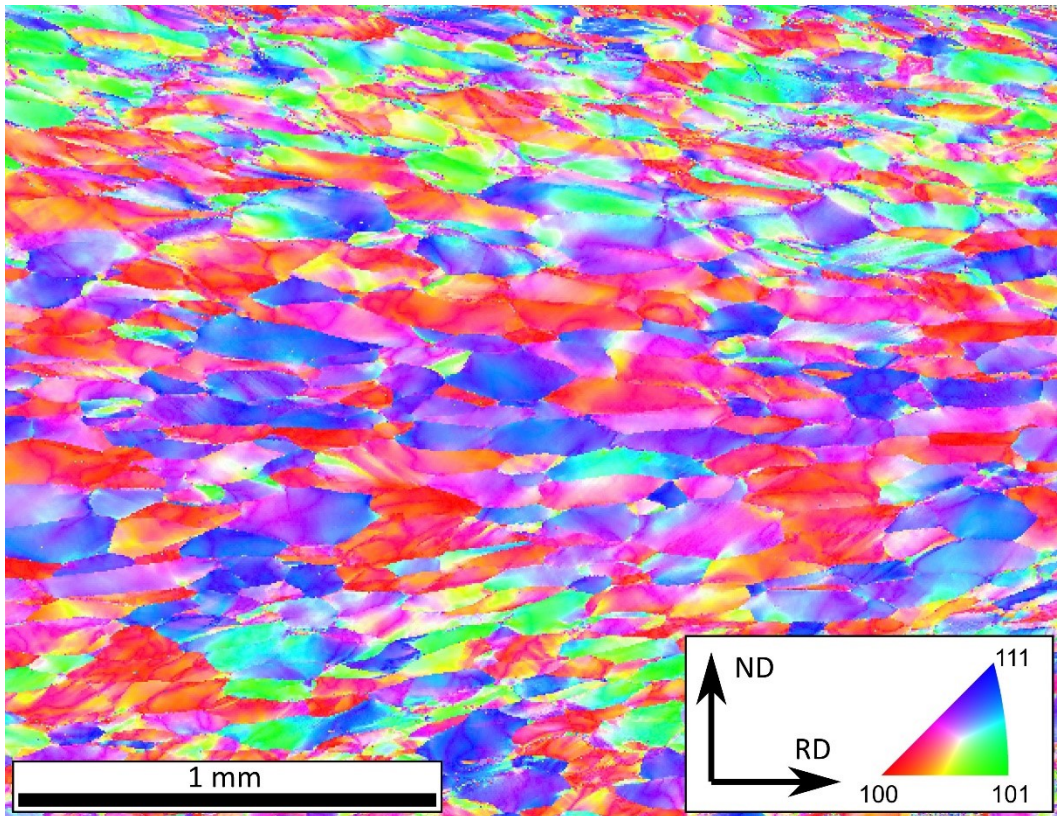


**Figure 6.1** Through-thickness IPF map of the studied material conventionally rolled at 900 °C to a thickness reduction of 80%.

components) are located mainly in the sub-surface regions of the sheet. In contrast, orientations associated with plane strain compression (PSC) are typically concentrated in the mid-thickness layers of the sample.

Although  $\langle 011 \rangle // \text{ND}$ -oriented grains feature prominently in the IPF map of the hot-rolled samples, shear orientations constitute minor fractions of the macroscopic texture (see Figure 6.2). For example, the Copper orientation is absent, and the intensity of the Goss orientation is  $< 1.0$  times the random level. In fact, the highest

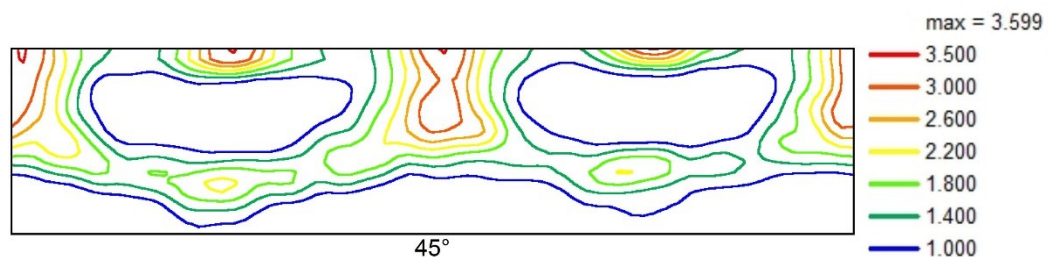


**Figure 6.2** A  $\varphi_2 = 45^\circ$  ODF section showing the macroscopic texture of the studied material conventionally rolled at 900 °C to a sample-thickness reduction of 80%.

intensity (3.7 times the random level) is measured at the  $\{001\}\langle 110\rangle$  and  $\{113\}\langle 110\rangle$  orientations, and a local high intensity (2.0 times the random level) occurs at the  $\{332\}\langle 113\rangle$  orientation.

Although the microstructure of hot symmetrically rolled samples resembles the microstructures of deformed materials, the texture consists of many features that are characteristic of phase transformation textures. The basis of this discrepancy between the microstructure and texture can be determined by examining the microstructure of the hot-rolled material. High spatial resolution EBSD measurements (scan step size: 0.5  $\mu\text{m}$ ) have, therefore, been performed with the aim of resolving the sub-grain structure of this material. Figure 6.3 shows the microstructure of the sub-surface and mid-thickness layers of a hot symmetrically rolled sample. As the IPF maps show (Figure 6.3a and Figure 6.3b), the intra-granular orientation variations in the mid-thickness layers differ from those of the sub-surface regions. Grains in the mid-thickness layer (c.f. Figure 6.3a) are characterized by small, smooth variations whereas grains in the sub-surface region (Figure 6.3b) are characterized by extremely sharp variations. Moreover, small equi-axed islands of well-defined orientations occur near the boundaries of large elongated grains in the sub-surface regions. These small islands suggest that recrystallization nuclei, formed during the subsequent annealing step, can grow into neighboring deformed grains via the movement of high angle boundaries surrounding their parent grains.

The image quality (IQ) maps (see Figure 6.3c and Figure 6.3d) also reveal differences in the sub-grain structures of the sub-surface and mid-thickness layers. Owing to their lower IQ, the grains in the sub-surface layer are, in general, darker than those in the mid-thickness layer. The IQ parameter, which is an indicator of the quality of the electron backscatter diffraction patterns (EBSPs), is calculated from the integrated intensity of all Hough peaks in a diffraction pattern. This parameter depends on the perfection of the diffracting crystal volume. Therefore, lattice distortions, dislocations, and grain boundaries all lead to a decrease in the IQ parameter of a diffraction pattern. The IQ maps shown in Figure 6.3c and Figure 6.3d reveal both the high angle grain boundaries and the sub-grain structures present in the material.

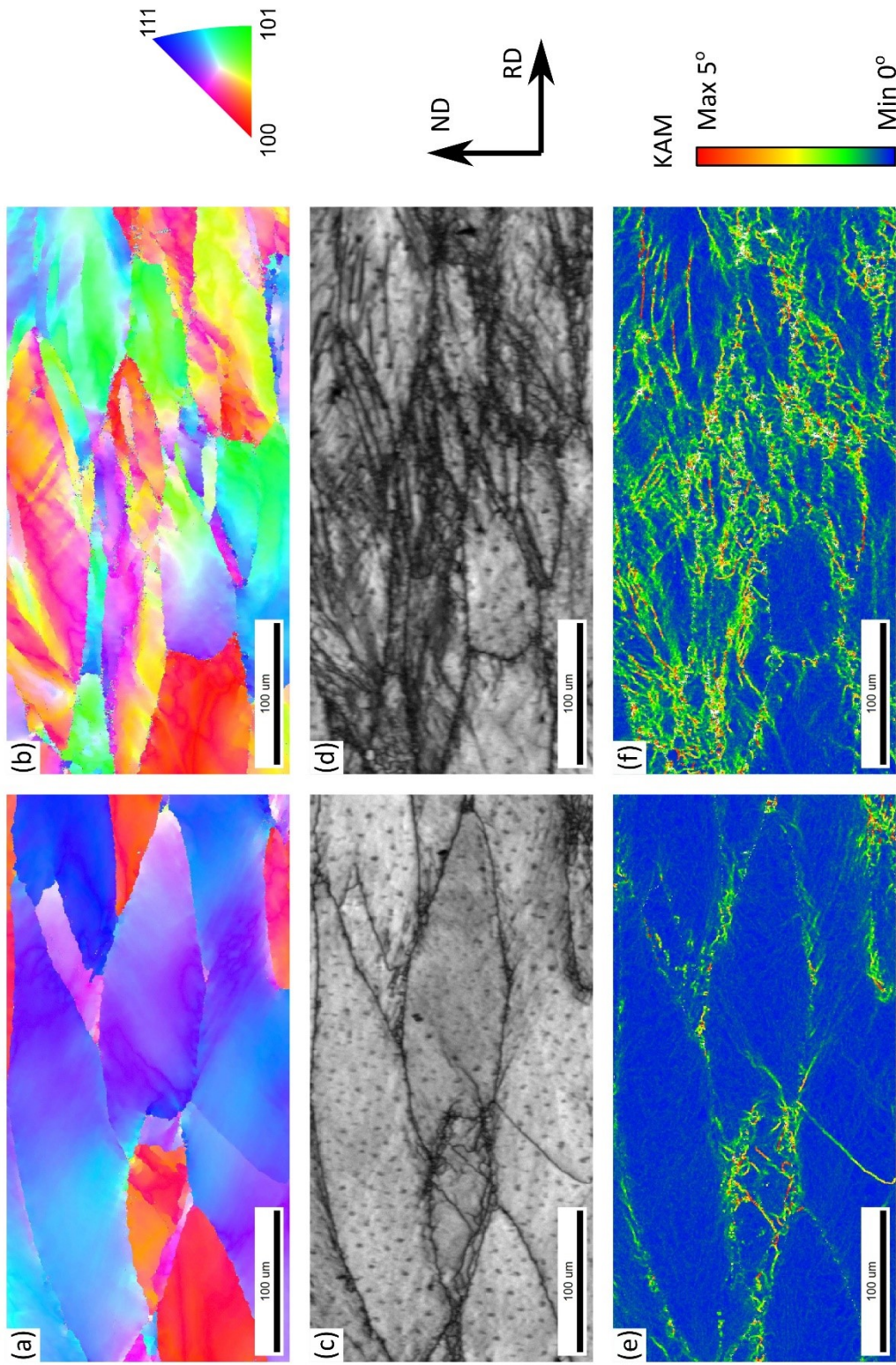


Figure 6.3 (a, b) IPF map, (c, d) IQ map, and (e, f) KAM map of microstructures comprising the mid-thickness (a, c, and e) and sub-surface (b, d, and f) regions of a hot symmetrically rolled sample.

The presence of a sub-grain structure in hot-rolled samples is indicative of the deformation state of the material. However, the occurrence of this structure also depends on crystallographic orientations and non-material factors and, hence, IQ maps are typically combined with kernel average misorientation (KAM) maps for improved resolution of sub-grain structures. The KAM is the average misorientation angle between the point in the center and all points at the perimeter of a kernel in a spatial map of crystallographic orientations. In Figure 6.3e and Figure 6.3f, the KAM (cut-off misorientation angle:  $10^\circ$ ) of a point measured on a square grid is calculated from eight nearest neighbor points. By applying this threshold (cut-off) angle, high angle grain boundaries are excluded, whereas the sub-grain structure and low angle boundaries are highlighted. Regions near high angle grain boundaries have higher KAMs than the grain interiors in both the sub-surface and mid-thickness microstructures. However, the KAM map of the sub-surface microstructure contains more features than the KAM map of the mid-thickness microstructure. These features result from intra-granular orientation variations and are related to geometrically necessary dislocations, a source of stored energy in plastically deformed material. In hot-rolled samples, the presence of this stored energy is indicative of the deformation (rather than the transformation) state of the microstructure and texture.

In summary, the presence of intra-granular orientation gradients, sub-grain features, and KAM patterns indicate the deformation state of hot-rolled samples. Variations in the microstructure across the sample thickness (for example, grain size in sub-surface layers differs from that of the mid-thickness layers) stem from differences in the strain mode. Post-deformation evolution may also lead to through-thickness microstructural differences. In the mid-thickness region, grains are deformed by PSC and then undergo partial recovery, resulting in elongated grain shapes and smooth intra-granular orientation variations. In contrast, the RD shear leads to severe deformation of the grains in the sub-surface regions. The corresponding orientation gradients are sharper and sub-grain structures are more prominent than those of the grains lying in the mid-thickness region. Furthermore, small islands of well-defined orientations occur along the grain boundaries in this

region, consistent with the early state of recrystallization in the sub-surface layer of these samples.

### 6.1.2 Asymmetrically hot-rolled samples

The hot asymmetric-rolling experiments are aimed mainly at changing the microstructure and texture of the conventionally rolled samples. As Figure 6.4 shows, the through-thickness microstructure of an asymmetrically hot-rolled sample differs significantly from that of a conventionally rolled sample (see Figure 6.1). Grains in the microstructure of the asymmetrically rolled samples have mainly the same size and are homogeneously distributed across the sample thickness. Asymmetrically rolled samples and conventionally rolled samples are characterized by significant differences in the crystallographic orientations of the grains across the sample thickness. Orientations with  $\langle 001 \rangle // \text{ND}$  and  $\langle 011 \rangle // \text{ND}$  are present in both of the samples. However, the crystallographic orientation of each grain in the

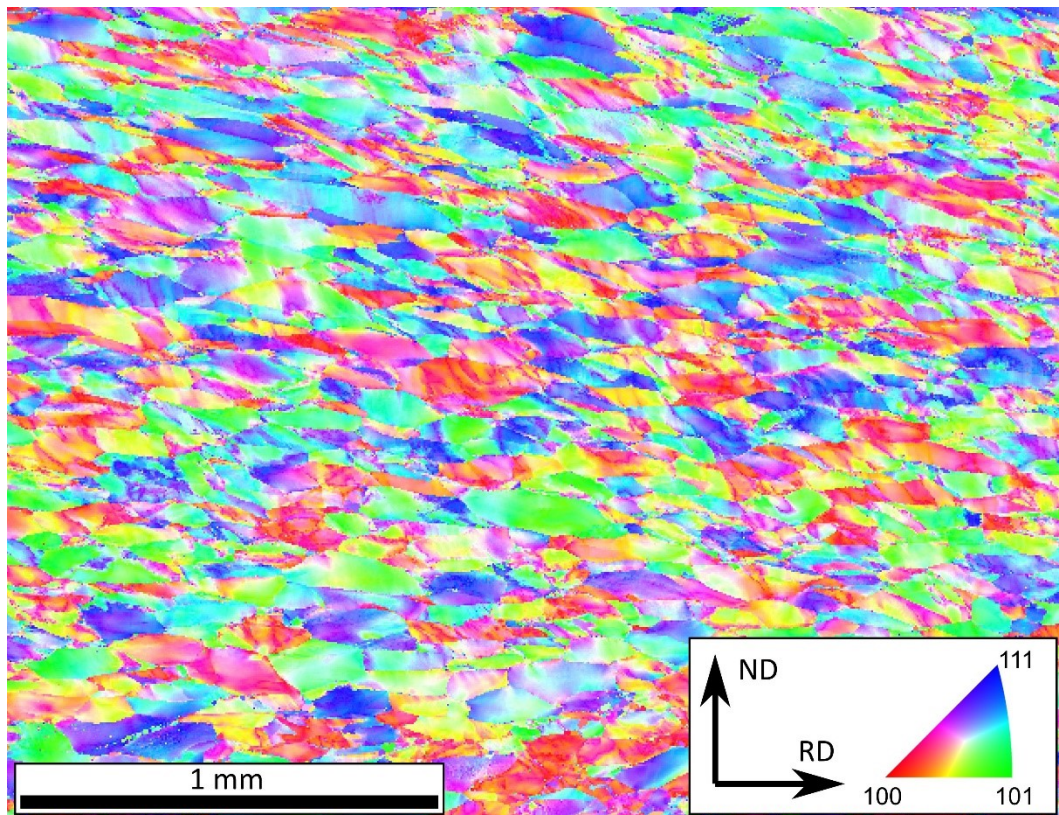


**Figure 6.4** Through-thickness IPF map of the studied material after asymmetrical rolling at 900 °C to a sample-thickness reduction of 80%.

asymmetrically rolled samples is diffused, i.e., these orientations change along the spatial directions and are spread in orientation space.

A comparison of the IPF maps of the mid-thickness and the sub-surface regions in the asymmetrically rolled samples (Figure 6.5a and Figure 6.5b) reveals a homogeneous distribution of crystallographic orientations across the sample thickness. At the high spatial resolution of the EBSD measurements (scan step size: 0.5  $\mu\text{m}$ ), these microstructures appear similar to those comprising the sub-surface regions of conventionally rolled samples. Grains are identified by sharp changes in orientation along spatial directions. Large intra-granular orientation variations, which reveal the deformation state of the asymmetrically rolled samples, are also observed.

Sub-grain structures in asymmetrically rolled samples are clearer resolved by IQ maps and KAM maps (Figure 6.5c–f) than by IPF maps. The IQ maps and KAM maps reveal patterns resulting from intra-granular slip activity during deformation. Features near curvy high angle grain boundaries with many local bulges are also observed. Small circular islands, which are partially or fully surrounded by high angle boundaries, occur at the edges of large grains. These curvy boundaries and round islands are (i) characterized by high KAM values of 5–10° (see Figure 6.5e and Figure 6.5f) and (ii) similar to the nuclei of recrystallization, which are formed during cooling to room temperature after the hot rolling process.

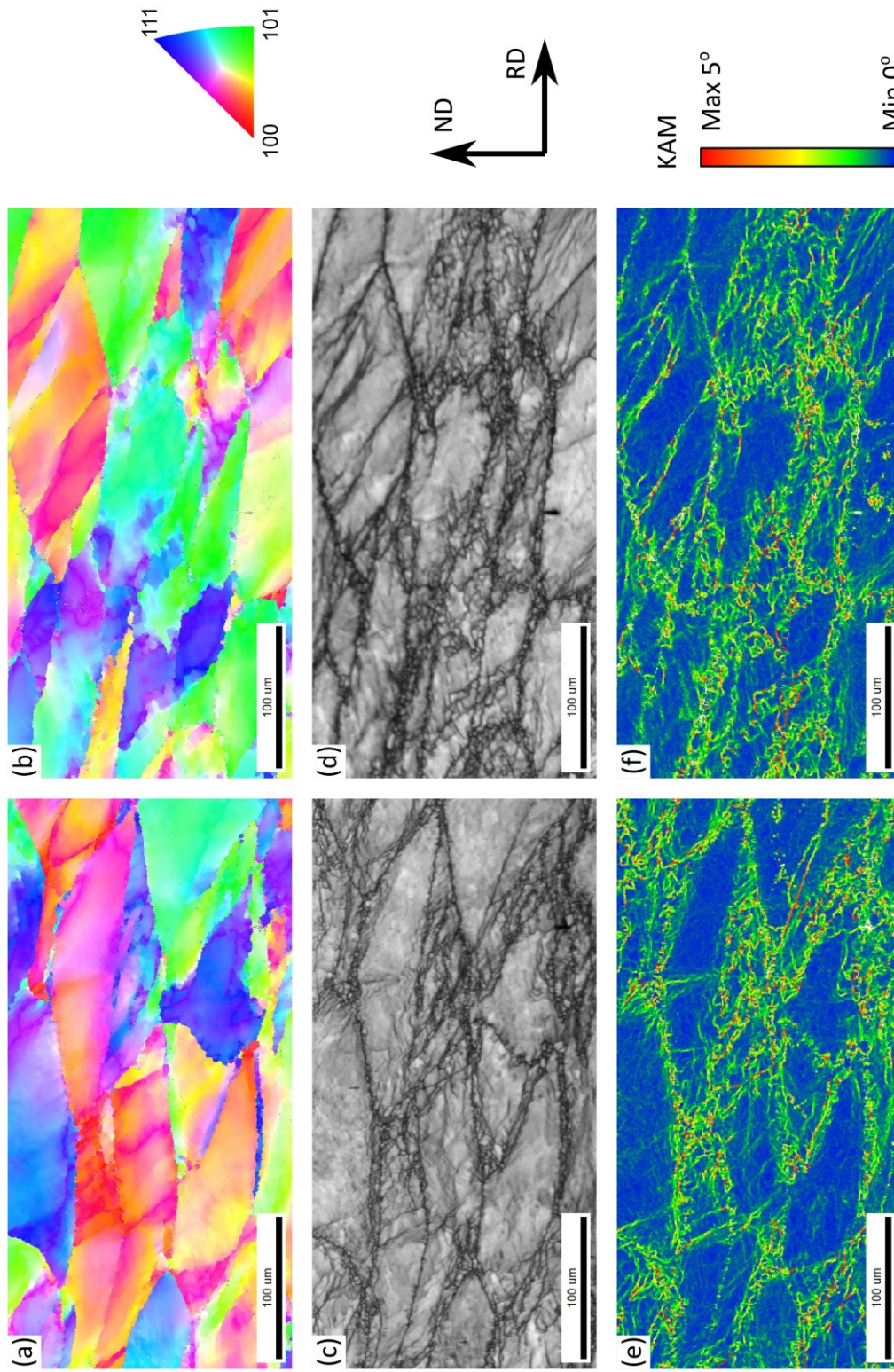
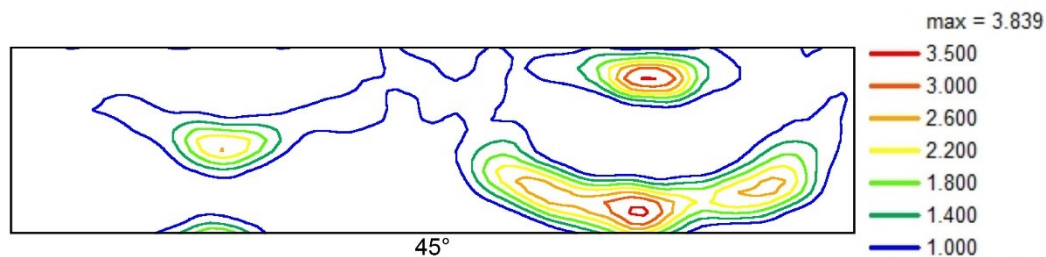


Figure 6.5 (a, b) IPF map, (c, d) IQ map, and (e, f) KAM map of microstructures comprising the mid-thickness (a, c, and e) and sub-surface (b, d, and f) regions of a hot asymmetrically rolled sample.



The macroscopic texture of the studied material also changes, owing to asymmetrical rolling, respectively to conventional rolling. The  $\varphi_2 = 45^\circ$  ODF section in Figure 6.6 shows a typical macroscopic texture of the hot asymmetrically rolled samples. The statistical or sample symmetry of the asymmetrical-rolling texture differs from that of the conventional-rolling texture. For example, the asymmetrical-rolling texture lacks the orthorhombic sample symmetry that is typical of the conventional-rolling textures. The mirror line along the  $\varphi_1 = 90^\circ$  and  $\varphi_1 = 270^\circ$  axes, corresponding to the mirror plane perpendicular to the transverse direction (TD), is apparent in the ODF section (see Figure 6.6). This mirror plane, combined with a two-fold axis parallel to the TD, yields the  $(2/m)$  monoclinic symmetry of the asymmetrically rolled samples.



**Figure 6.6 Macroscopic texture (as shown in the  $\varphi_2 = 45^\circ$  ODF section) of the studied material asymmetrically rolled at 900 °C to a sample-thickness reduction of 80%.**

Secondly, the  $\alpha$ - and  $\gamma$ -fiber orientations, which feature prominently in the macroscopic texture of conventionally rolled samples, are absent from the macroscopic texture of asymmetrically rolled samples. The highest texture intensity (3.6 times the random level) of the asymmetrical-rolling texture is measured for the  $(441)[11-8]$  orientation, which lies along a certain fiber (texture intensity:  $>2.5$  times the random level). This fiber, which occurs at  $\varphi_1$  angles of  $180^\circ$ – $360^\circ$ , is quite similar to the  $\gamma$ -fiber that is a common feature of conventional-rolling textures. However, in the asymmetrical-rolling texture, this fiber is shifted toward higher  $\Phi$ -angle values than those associated with the  $\gamma$ -fiber. This shift is also observed for another high-intensity component, i.e.,  $(116)[33-1]$ , of the asymmetrical-rolling texture. As Figure 6.6 shows, the  $(116)[33-1]$  orientation occurs with the second highest intensity (3.4 times the random level) in the ODF section. This orientation is  $13.26^\circ$ -deviated from the nearest Rotated Cube orientation at  $\varphi_1 = 270^\circ$ ,  $\Phi = 0^\circ$ ,  $\varphi_2 = 45^\circ$ , toward an

orientation with a higher  $\Phi$ -angle value. In contrast, orientations with  $\varphi_1$ -angles ranging from  $0^\circ$  to  $180^\circ$  deviate toward orientations with lower  $\Phi$ -angle values. The (-3-34)[223] orientation, which is a local high-intensity (2.6 times the random level) component of the asymmetrical-rolling texture, is  $18.06^\circ$ -deviated from the (-3-32)[113] orientation of the conventional-rolling texture. In general, for the asymmetrical-rolling texture, high-intensity components with  $\varphi_1 = 180^\circ\text{--}360^\circ$  and  $\varphi_1 = 0^\circ\text{--}180^\circ$  are shifted from the  $\alpha$ - and the  $\gamma$ -fibers toward high  $\Phi$ -angle and low  $\Phi$ -angle orientations, respectively.

The formation of macroscopic texture and the change in statistical symmetry induced by asymmetrical rolling can be attributed to the strain mode or the deformation configuration of asymmetrical rolling. This deformation configuration is investigated exhaustively via simulations. For the sake of simplicity, the deformation imparted during this rolling process is considered a superposition of PSC and RD-ND shear. This deformation configuration is similar to the configuration in the sub-surface regions of conventionally rolled samples. However, in asymmetrically rolled samples, a through-thickness RD-ND shear is expected. This shear strain leads to a shift of the deformation texture from the  $\alpha$ - and  $\gamma$ -fibers to the Goss and the Copper orientations. In conventional rolling, samples are constrained equally on both surfaces and, therefore, RD-ND shears of equal magnitude (but opposite sign) occur in the sub-surface regions. Preferential orientations in these regions undergo opposite but equal-magnitude shifts. As a result, the orthorhombic symmetry is maintained at the macroscopic (through-thickness) scale. However, during asymmetrical rolling, the rolling velocities and, hence the RD-ND shear magnitudes, at the top surfaces differ from those at the bottom surfaces. The preferred orientations developed in the top surface therefore differ from those formed in the bottom surfaces. Mirror planes of RD-TD and TD-ND corresponding to the statistical distribution of crystallographic orientations are absent in the case of asymmetrically rolled samples. Therefore, the asymmetrical-rolling texture is characterized by monoclinic ( $2/m$ ) sample symmetry, rather than orthorhombic ( $mmm$ ) sample symmetry that characterizes the conventionally rolled samples.

The rotation toward the high-intensity Goss and the Copper components in the asymmetrical-rolling texture seems similar to that of a rigid body rotation around the TD of samples with conventional-rolling textures. The rigid body rotation that yields conventional-rolling textures, is uniquely applied to all crystals of the sample, and leads to synchronous motion of high-intensity texture components. In contrast, the crystal rotations in the asymmetrically rolled samples depends on the shear strain absorbed by each crystal, interaction among neighboring grains, and local deformation configurations. This non-synchronous rotation, therefore, results in various deviations of high-intensity components in the asymmetrical-rolling textures from the corresponding positions in the symmetrical-rolling texture. For example, the  $\{332\}<113>$  orientation of the conventional-rolling texture is  $18.06^\circ$ - and  $15.21^\circ$ -separated from the  $\{334\}<223>$  and  $\{441\}<118>$  orientations of the asymmetrical-rolling texture, respectively. In addition, the rotated Cube of the conventional-rolling texture is  $13.26^\circ$ -separated from the  $\{116\}<331>$  orientation of the asymmetrical-rolling texture.

In summary, asymmetrical rolling leads to changes in both the microstructure and macroscopic texture of the studied material. The homogeneous distribution of crystallographic orientations across the sample thickness suggests that grains in the sub-surface and mid-thickness regions in the asymmetrically rolled samples are subjected to a similar strain mode. The large intra-granular spread in orientations is, however, indicative of the complex and non-linear deformation paths of the crystals during this rolling process. In this deformation mode, samples experience a combination of PSC and RD-ND shear, which extends through the sample thickness. Due to the deformation mode, the macroscopic texture of asymmetrically rolled samples is shifted (relative to that of symmetrically rolled samples) toward the Goss and the Copper orientations. These shifts, which vary with the initial orientation of the crystals, depend on the amount of shear, interaction among neighboring crystals, and local deformation configuration. The microstructure and texture of asymmetrically rolled samples indicate the deformation state of the material. For example, high-resolution microscopy reveals bulging regions and small orientation islands along grain boundaries of the asymmetrically rolled sample. These features

are consistent with the initial stages of recrystallization, which may occur during cooling to room temperature after the hot rolling step.

## *6.2 Cold-rolled samples*

To realize the thickness required for commercially electrical steel sheets, hot rolled and annealed samples are subjected to a multi-pass cold rolling, which yields a desired thickness of 0.5 mm. Samples are subjected to both symmetrical and asymmetrical rolling. The same rolling directions and sample surfaces are maintained in all rolling passes, especially in the case of asymmetrical rolling. This ensures that the shear strains imposed by successive rolling passes and the effect of these strains on deformation textures are accumulated, rather than eliminated. The cold-rolled samples are divided into four groups, based on processing path, corresponding to deformation via symmetrical and asymmetrical rolling at both elevated and room temperatures.

The main aim of these cold rolling processes is to determine the influence of different rolling configurations on the microstructure and texture of materials. Therefore, the results of symmetrical rolling will be presented first, as the reference for the results of asymmetrical rolling. Differences in the microstructural and texture evolution, after the same amount of cold rolling, of various hot-rolled and annealed samples are attributed to the effect of initial microstructure and texture.

### *6.2.1 Symmetrically cold-rolled samples*

The microstructure of the sample after symmetrical rolling at high and then at room temperatures is shown in Figure 6.7. A similar microstructure (not shown) is obtained after symmetrical cold rolling of the asymmetrically hot-rolled sample. The highly deformed state persists in the microstructure, as shown in the IPF map (Figure 6.7). The grains in this microstructure are considerably elongated along the RD, yielding a banded microstructure, with intra-band variation in the crystallographic orientations. The  $\langle 001 \rangle // \text{ND}$  bands are characterized by rather smooth orientation variations, whereas  $\langle 110 \rangle$  and  $\langle 111 \rangle // \text{ND}$  bands are characterized by sharp variations. However, these intra-band orientation variations are non-random and, in

fact, form patterns of thin strips inclined to the rolling plane and spread entirely across the ND of the bands. These inclined strips, referred to as shear bands, result from a concentration of shear strain in narrow inclined regions. Shear bands that lie in single-orientation domains and those which traverse several grains as well as the sample thickness are considered microscopic features and macroscopic features, respectively.

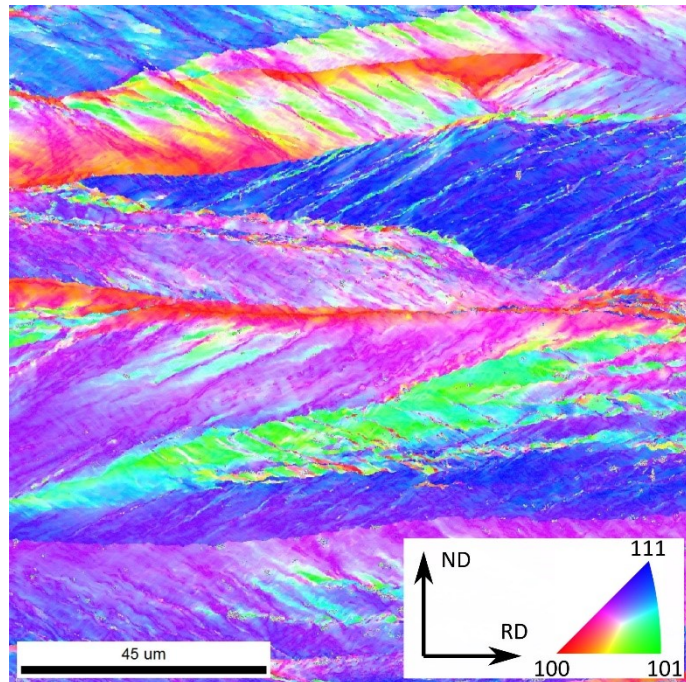


**Figure 6.7** IPF map of the Fe-1.2 wt.% Si after symmetrically hot rolling and symmetrically cold rolling.

The deformation textures of the symmetrically cold-rolled samples (Figure 6.8), although arising from different initial conditions (symmetrical and asymmetrical hot rolling), are mostly identical. The  $\alpha$ - and  $\gamma$ -fibers constitute prominent features of both textures. However, the (maximum) texture intensity of the symmetrically hot-rolled sample is slightly higher

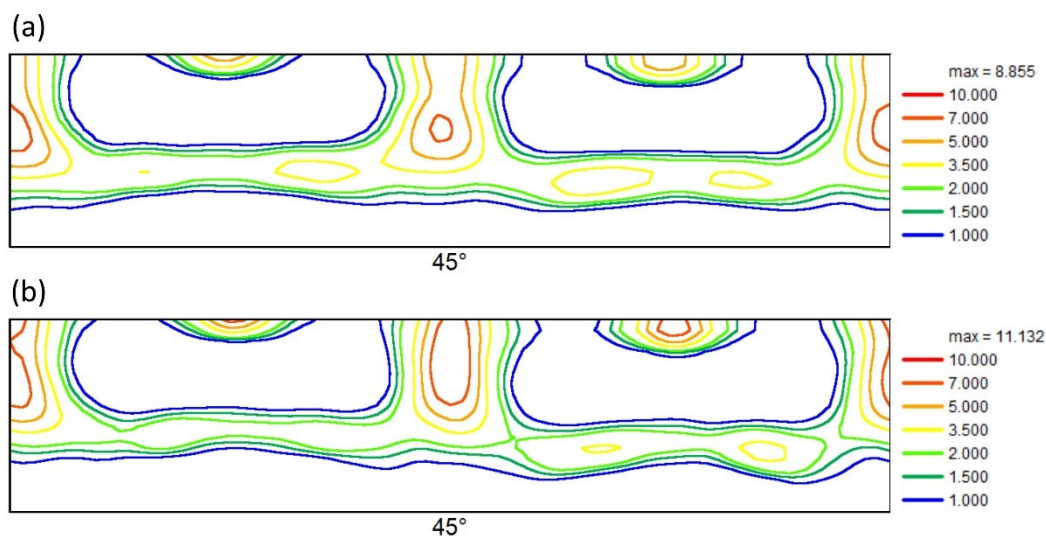


**Figure 6.8** Textures resulting from symmetrical cold rolling of the (a) symmetrically hot-rolled and (b) asymmetrically hot-rolled samples.

(13.0 times the random level vs. 10.8 times the random level) than that of its asymmetrically rolled counterpart. The high-intensity peaks of these textures all occur along the  $\alpha$ -fiber, with the  $\{001\}\langle 110\rangle$  and the  $\{112\}\langle 110\rangle$  orientations exhibiting the strongest intensities. In these textures, the intensity of the  $\gamma$ -fiber is lower than that of the  $\alpha$ -fiber, and the maximum value ( $<5.5$  times the random level) is measured at the  $\{111\}\langle 110\rangle$  orientation.

Since the orthorhombic sample symmetry is omitted from the texture calculations, the ODF sections shown in Figure 6.8 represent the real statistical distribution of orientations in the cold-rolled samples. Regions of the ODF with  $\varphi_1$  ranging from  $0^\circ$  to  $180^\circ$  differ slightly from those with  $\varphi_1$  ranging from  $180^\circ$  to  $360^\circ$ . Specifically, the high-intensity peaks in these ODF regions are shifted  $3^\circ$ – $5^\circ$  in opposite directions along the  $\Phi$ -axes, with respect to the ideal positions of the  $\alpha$ - and the  $\gamma$ -fibers. This deviation is quite similar to the effect of asymmetrical rolling on the hot deformation texture. However, the deviation observed in cold deformation textures suggests that the shear component, if present during symmetrical rolling, is significantly smaller than the dilation part of the total strain. This small shift in the textures may be attributed to a misalignment of the sample RD with respect to the reference axis of the measuring system. The observed deviation in rolling textures can therefore be neglected and the  $\alpha$ - and  $\gamma$ -fibers are still considered the conventional cold rolling textures.

### 6.2.2 *Asymmetrically cold-rolled samples*

Microstructures of the hot-rolled and annealed samples, after asymmetrically cold rolling, are quite similar to those resulting from symmetrically cold rolling. Figure 6.9 shows the microstructure of the asymmetrically hot-rolled and annealed sample after asymmetrically cold rolling. The grains in this sample are all severely deformed in the ND and extended along the RD, thereby forming a banded microstructure characterized by inclined intra-granular shear bands. However, sub-grains in the shear bands are smaller than the current EBSD step size ( $0.1\ \mu\text{m}$ ) and, hence, appear mainly as non-indexed points.

Most of the grains shown in Figure 6.9 have near- $\langle 111 \rangle // \text{ND}$  orientations, and grains with  $\langle 001 \rangle // \text{ND}$  and  $\langle 011 \rangle // \text{ND}$  orientations are less frequently observed than in Figure 6.7. The orientation distributions of the asymmetrically cold-rolled samples differ from those of the symmetrically rolled samples, owing to the shear strain imparted during asymmetrical rolling. Specifically, near-

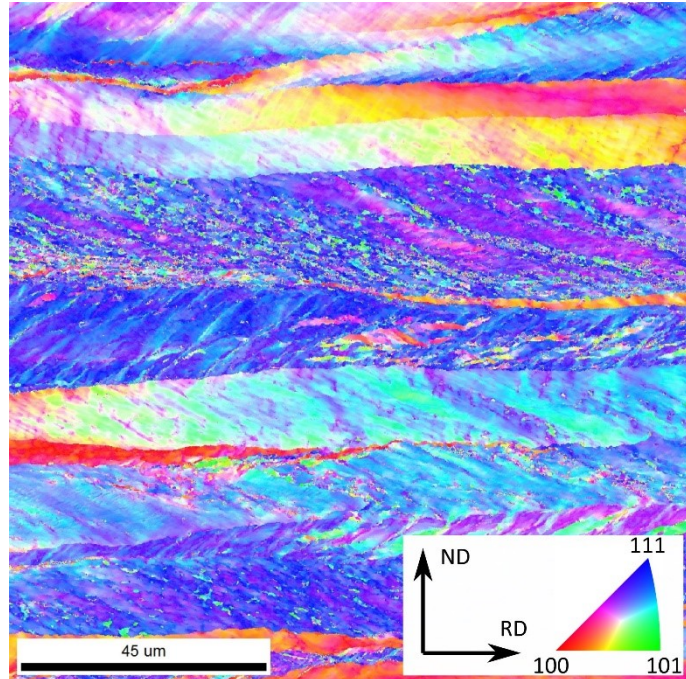


**Figure 6.9** IPF map of the Fe-1.2 wt.% Si after asymmetrical rolling at both high and room temperatures.

$\{116\}\langle 331 \rangle$  orientations exhibit the highest intensities (16.7 and 15.1 times the random level) in the asymmetrically cold rolling textures (see  $\varphi_2 = 45^\circ$  ODF sections in Figure 6.10). These texture intensities are higher than the maximum intensities of the  $\{112\}\langle 110 \rangle$  orientation in the symmetrically cold rolling textures. Nevertheless, the  $\alpha$ -fiber persists in the asymmetrical-rolling textures with a local high-intensity (6.5 times the random level) peak occurring at this orientation. High-intensity peaks along the  $\gamma$ -fiber in asymmetrical-rolling textures occur at the  $\varphi_1 = 0^\circ\text{--}180^\circ$  and  $\varphi_1 = 180^\circ\text{--}360^\circ$  parts of the ODF. These parts correspond to lower  $\Phi$ -angles and higher  $\Phi$ -angles, respectively, than that ( $\Phi = 54.74^\circ$ ) of the ideal position of the  $\gamma$ -fiber. This texture modification (i.e., shift from the ideal  $\gamma$ -fiber position) induced by asymmetrical cold rolling is similar to that induced by hot rolling. The shear, imposed during asymmetrical rolling, results in grain rotations around the sample TD. However, the shift of cold rolling textures from PSC-type is smaller than that observed for hot rolling textures. The magnitude of the shear strain associated with cold asymmetrical rolling is therefore smaller than that of the shear strain associated with hot asymmetrical rolling.

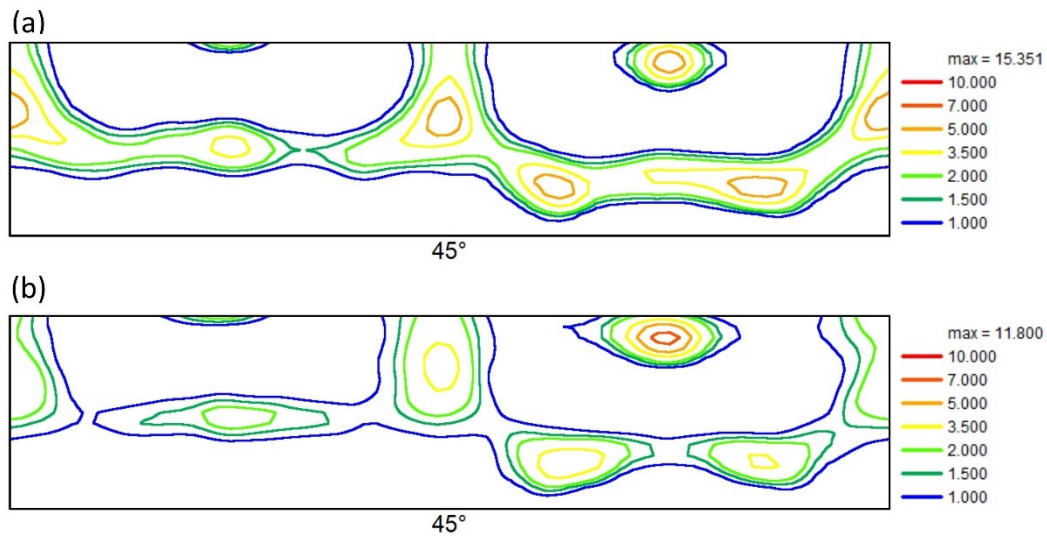


**Figure 6.10 Asymmetrical cold-rolling textures of (a) symmetrically hot-rolled sample and (b) asymmetrically hot-rolled sample.**

### 6.3 Deformation condition of rolling

During plastic deformation, crystals rotate toward more stable orientations, leading to texture development in materials. The deformation conditions of rolling, therefore, form the basis for the development of deformation textures. In this work, deformation conditions (especially those associated with asymmetrical rolling) are investigated through a geometrical approach and finite element (FE) simulations. Using the geometrical approach, the deformation conditions corresponding to symmetrical and asymmetrical rolling are investigated analytically. This method (i) is based on geometrical assumptions of the material in the rolling gap, (ii) calculates the deformation evolution in the material without considering the material response, and (iii) is simple and fast, but provides only a rough estimation of deformation conditions associated with asymmetrical rolling. In contrast, the FE method maintains the relationship between the material and the deformation condition by recording the macroscopic stress-strain constitution law of the material during rolling. Therefore, compared with those of the geometrical method, results of FE simulations provide more details about the rolling condition as well as the correlation between rolling parameters and texture development in materials.



### 6.3.1 Geometrical approach

During conventional rolling, the material typically undergoes PSC, which is usually predicted via numerical calculations and confirmed by strain pattern analyses of the rolled samples. This deformation state is characterized by (i) a contraction along the normal direction (ND) due to the thickness reduction of the sheet during rolling and (ii) an expansion in the RD, in accordance with the law of mass and volume conservation of solid materials. Generally, the material also expands along the TD during rolling. However, owing to the (usually) large width-to-thickness ratio of the sheets, the widening of rolled sheets is typically considered negligible. Symmetrical rolling is characterized by a deformation gradient tensor, which is given as follows:

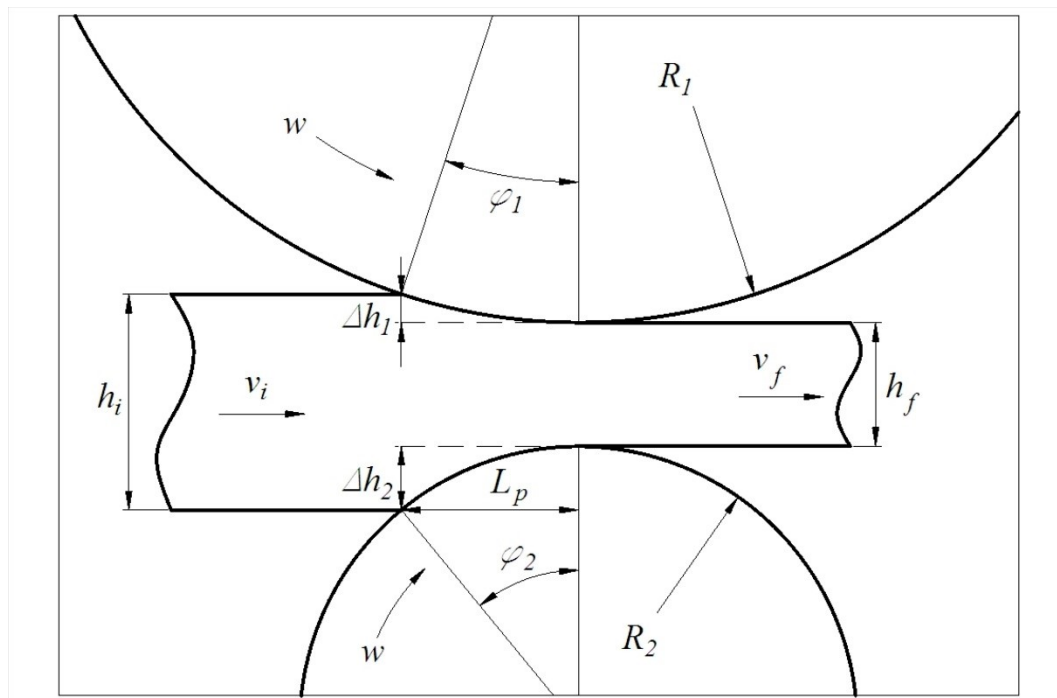


Figure 6.11 Geometry of asymmetric rolling, where material is deformed by a rolling mill with rolls of different diameters, but the same rotation speed.

$$F_{PSC} = \begin{pmatrix} \frac{h_i}{h_f} & 0 & 0 \\ 0 & 1 & 0 \\ 0 & 0 & \frac{h_f}{h_i} \end{pmatrix} \quad (6.1)$$

where,  $h_i$  and  $h_f$  are the initial and final thicknesses, respectively, of the rolled sheet. The corresponding true strain tensor is given as follows:

$$\varepsilon_{PSC} = \begin{pmatrix} \varepsilon_{11} & 0 & 0 \\ 0 & 0 & 0 \\ 0 & 0 & \varepsilon_{33} \end{pmatrix} = \ln\left(\frac{h_i}{h_f}\right) \cdot \begin{pmatrix} 1 & 0 & 0 \\ 0 & 0 & 0 \\ 0 & 0 & -1 \end{pmatrix} \quad (6.2)$$

where,  $\varepsilon_{11}$  and  $\varepsilon_{33}$  are the normal strain components along the RD and ND, respectively, of the sheet. This strain tensor can be separated into scalar and tensor parts, which have different effects on the evolution of deformation textures. For a linear evolution of strain components from the beginning to the end of the rolling gap, the scalar part (unlike the tensor part) of the strain tensor is time-dependent. Therefore, the tensor part defines the persistence features of deformation textures, while the scalar part controls the strength of the textures. A linear estimation of the velocity gradient tensor for symmetrical rolling is given as follows:

$$L_{PSC} = \dot{\varepsilon} \cdot \Delta t = \frac{1}{\Delta t} \cdot \ln\left(\frac{h_i}{h_f}\right) \cdot \begin{pmatrix} 1 & 0 & 0 \\ 0 & 0 & 0 \\ 0 & 0 & -1 \end{pmatrix} \quad (6.3)$$

The deformation gradient tensor, strain tensor, and velocity gradient tensor of asymmetrical rolling can also be derived based on geometric conditions. The geometry of the asymmetrical rolling configuration employed in this investigation is shown schematically in Figure 6.11. Assuming that the initial and final thicknesses of the sample are  $h_i$  and  $h_f$ , respectively (as in the case of symmetrical rolling), the total thickness reduction after an asymmetrical rolling pass is given as:

$$\Delta h = h_i - h_f = \Delta h_1 + \Delta h_2 \quad (6.4)$$

where,  $\Delta h_1$  and  $\Delta h_2$  are nominal reductions of the respective top- and bottom halves of the sample. In the case of conventional rolling,  $\Delta h_1 = \Delta h_2 = \Delta h/2$ . This differs from the case of asymmetric rolling, where  $\Delta h_1 \neq \Delta h_2$ , as the rolling velocity is un-equally distributed across the sample thickness. In addition, owing to the difference in diameters of the rolls used in asymmetrical rolling, the contact angle of the top roll differs from that of the bottom roll. Nevertheless, the projections of the contact lengths ( $L_p$ ) are still identical:

$$L_p = R_1 \sin \varphi_1 = R_2 \sin \varphi_2 \quad (6.5)$$

The dependence of the contact angle on the geometrical parameters of asymmetrical rolling is expressed via  $\varphi_1$  and  $\varphi_2$ , which are given as follows:

$$\begin{aligned}\varphi_1 &= \cos^{-1} \left[ 1 - \frac{\Delta h(2R_2 - \Delta h)}{2R_1(R_1 + R_2 - \Delta h)} \right] \\ \varphi_2 &= \cos^{-1} \left[ 1 - \frac{\Delta h(2R_1 - \Delta h)}{2R_2(R_1 + R_2 - \Delta h)} \right]\end{aligned}\tag{6.6}$$

This condition leads to an unequal distribution of the total thickness reduction between the top and the bottom halves of the sheet. Therefore, the nominal thickness reductions ( $\Delta h_1$  and  $\Delta h_2$ ) are given as:

$$\begin{aligned}\Delta h_1 &= \frac{\Delta h(2R_2 - \Delta h)}{2(R_1 + R_2 - \Delta h)} \\ \Delta h_2 &= \frac{\Delta h(2R_1 - \Delta h)}{2(R_1 + R_2 - \Delta h)}\end{aligned}\tag{6.7}$$

The middle layer of the material sheet moves away from the center plane of the rolling gap during rolling. At the entrance of the rolling gap, the distance between the middle point of the material sheet and the center line of the rolling gap is determined from:

$$\Delta s = \Delta h_2 - \Delta h_1 = \frac{\Delta h(R_1 - R_2)}{R_1 + R_2 - \Delta h}\tag{6.8}$$

This distance is relatively small compared with other parameters of asymmetrical rolling, but, nevertheless, controls the entrance angle of the sheet, thereby influencing the shear strain imposed by the rolling. Specifically, if this distance is ignored during the formulation of FE models for asymmetrical rolling, the computation time of the simulations will increase, but the accuracy will decrease.

Assume that the deformation resulting from asymmetrical rolling is composed of two components, namely PSC and simple shear, which are associated with the

thickness reduction and differences in the roll tangent velocities, respectively. The deformation gradient tensor of asymmetrical rolling is then given as:

$$F = F_{SS} \cdot F_{PSC} = \begin{pmatrix} 1 & 0 & \gamma \\ 0 & 1 & 0 \\ 0 & 0 & 1 \end{pmatrix} \cdot \begin{pmatrix} \alpha^{-1} & 0 & 0 \\ 0 & 1 & 0 \\ 0 & 0 & \alpha \end{pmatrix} = \begin{pmatrix} \alpha^{-1} & 0 & \alpha\gamma \\ 0 & 1 & 0 \\ 0 & 0 & \alpha \end{pmatrix} \quad (6.9)$$

where,  $\alpha$  is the ratio of the thickness reduction and  $\gamma$  is the shear deformation induced by asymmetrical rolling. Accordingly, the true strain tensor of samples subjected to asymmetrical rolling is given as follows:

$$\varepsilon = \begin{pmatrix} \varepsilon_{11} & 0 & \varepsilon_{13} \\ 0 & 0 & 0 \\ \varepsilon_{31} & 0 & \varepsilon_{33} \end{pmatrix} = \|\varepsilon\| \cdot \begin{pmatrix} 1 & 0 & \kappa \\ 0 & 0 & 0 \\ \kappa & 0 & -1 \end{pmatrix} \quad (6.10)$$

where,  $\varepsilon_{11}$  and  $\varepsilon_{33}$ : normal components,  $\varepsilon_{13}$  and  $\varepsilon_{31}$ : shear components of the strain tensor,  $\|\varepsilon\|$ : magnitude of the normal strain components, and  $\kappa$  (i.e., the shear factor): ratio of the shear and normal strain components ( $\kappa = \varepsilon_{13} / \varepsilon_{11}$ ). The normal components of the strain tensor are calculated in the same manner for both asymmetrical and symmetrical rolling. In addition, as proposed by Kang et al. [1], the shear strain components are estimated as averaged differences of the roll contact lengths across the sheet thickness:

$$\varepsilon_{13} = \varepsilon_{31} = \frac{1}{h_i + h_f} \cdot \left[ R_1 \cos^{-1} \left( 1 - \frac{\Delta h}{2R_1} \right) - R_2 \cos^{-1} \left( 1 - \frac{\Delta h}{2R_2} \right) \right] \quad (6.11)$$

The strain tensor of asymmetrical rolling, as in the case of symmetrical rolling, is composed of scalar and tensor parts. The shear components (as represented by the shear factor ( $\kappa$ )) associated with the strain tensor of asymmetrical rolling lead to more variations in the texture, compared with those resulting from symmetrical rolling. Persistence features of asymmetrical-rolling textures, therefore, change with the value of  $\kappa$ . In fact, when  $\kappa$  increases from 0 to  $\infty$ , the orientations of the deformation textures will shift from the PSC-type to the shear-type. The linear development of the velocity gradient tensor in asymmetrically rolled samples is described by:

$$L = \frac{\|\varepsilon\|}{\Delta t} \cdot \begin{pmatrix} 1 & 0 & 2\kappa \\ 0 & 0 & 0 \\ 0 & 0 & -1 \end{pmatrix} \quad (6.12)$$

In the last asymmetrical hot-rolling pass, the thickness of the material sheet is reduced by 50% (from 4 mm to 2 mm). The rolling mill consists of two rolls (diameter roll one: 180 mm, diameter roll two: 125 mm), driven by separate motors operating at the same speed. The values of the strain components are as follows:

$\varepsilon_{11} = -\varepsilon_{33}$	0.69
$\varepsilon_{13} = \varepsilon_{31}$	0.38
$\kappa$	0.54

**Table 6.1** Magnitudes of normal and shear strain components associated with the last asymmetrical hot-rolling pass.

### 6.3.2 Finite element (FE) simulation

The deformation state of samples during symmetric and asymmetric rolling can also be evaluated via FE simulation, where a rolled sheet is discretized into many representative elements. The behavior of each element depends on the element-element interactions and the boundary conditions applied to the entire system. In addition, the response of each element varies with the mechanical constitution of the materials. The response of individual elements is tracked at each calculation time step during the rolling. Therefore, the development of strain in rolled samples can be assessed both with respect to the rolling time and the sheet thickness.

For the rolling simulations in this study, the initial conditions of the models include the: geometry of the rolling gap, roll diameters, contact condition between the rolls and the sheet, rolling speed, and thickness reduction of the sheet (see Table 6.2 for the parameters associated with both symmetric and asymmetric hot rolling). In addition, the plastic behavior of an Fe-1.2 wt.% Si alloy has been determined via PSC tests performed at 900 °C and various strain rates on a Gleebe™ machine. Experimental data after noise reduction and separation from the elastic part, are presented as effective stress-strain curves (see Figure 6.12).

Thickness reduction	50%
Initial thickness	4 mm
Rolling speed	2.09 rad/s
Rolling temperature	900 °C
Simulation mode	Isothermal; Rigid-plastic deformation
Roll diameter ratio	Asymmetric mode: 180 mm/125 mm Symmetric mode: 180 mm/180 mm
Coulomb friction	$\mu = 0.3$
Time step	0.005 s

**Table 6.2 Set-up parameters for FE models of symmetric and asymmetric hot rolling.**

Models of symmetric and asymmetric hot rolling at 900°C (see Figure 6.13) have been formulated in the DEFORM2D™ software. In each model, the rolling sheets are discretized into square-shaped elements. The size of the FEs is chosen so that there

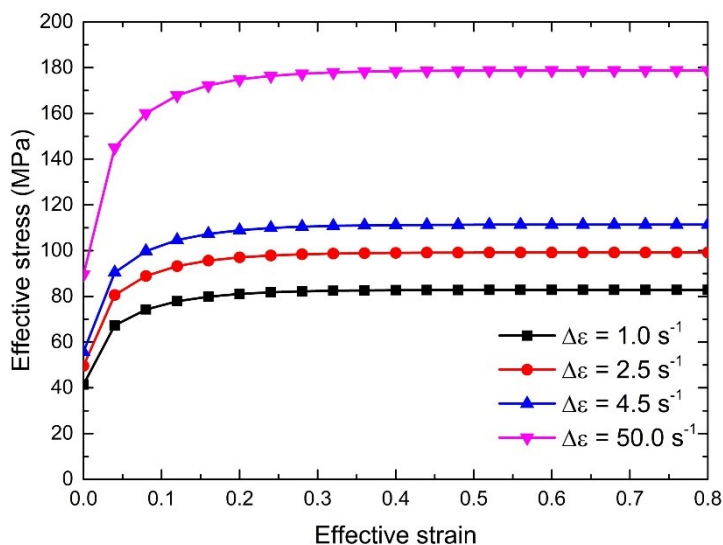


**Figure 6.12 Stress-strain curves of the Fe-1.2 wt.% Si determined via PSC tests at 900 °C and strain rates of 1.0, 2.5, 4.5, and 50 s<sup>-1</sup>.**

are 12 elements spanning along the sheet thickness. Each model is successfully run (for ~15 min) on a general purpose personal computer. Subsequently, for the duration of rolling, components of the strain tensor and velocity gradient tensor at 21 tracking points across the sheet thickness are exported for use in texture simulations.

Figure 6.14 shows distributions of the normal and the shear strain components ( $\epsilon_{11}$  and  $\epsilon_{13}$ ) across the thickness of symmetrically and asymmetrically hot-rolled samples. In the symmetrically hot-rolled sample, the normal strain ( $\epsilon_{11}$ ) is more homogeneously distributed than the shear strain ( $\epsilon_{13}$ ). A value of 0.15 is obtained for

the largest difference between normal strains calculated at the sub-surface layer and mid-thickness layers. In contrast, the shear strain ( $\epsilon_{13}$ ) at the sub-surface layer differs significantly from that at the mid-thickness region of the same sample. For example, values of 0.51 and  $\sim 0.08$  are obtained for  $\epsilon_{13}$  at sub-surface layer and  $\epsilon_{13}$  at mid-thickness layer, respectively. In the symmetrical rolled sample, the shear strain is mainly localized near the surfaces. For the 2-mm-thick symmetrically rolled sample, more than 54% of the total shear strain is distributed in the sub-surface layers with the thickness of 0.3 mm. For the through-thickness average of the normal strain and the average shear strain of this sample, values of 0.64 and 0.34 are calculated, respectively. The average normal strain obtained via the FE-method (0.64) is comparable to the normal strain (0.69) calculated via the geometrical method. Additionally, the FE-model predicts that a significant amount of shear strain is generated by the friction between the rolls and the material sheet. Therefore, the total strain calculated by the FE-method is higher than that obtained from the geometrical model.

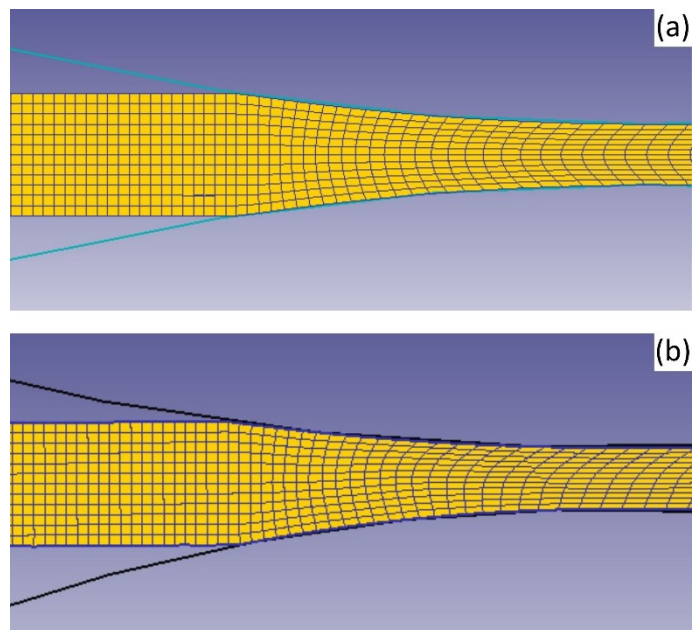


**Figure 6.13 Warm deformation of the Fe-1.2 wt.% Si steel samples simulated by FE model for (a) symmetric and (b) asymmetric rolling at 900°C to reduce the sample thickness from 4 to 2 mm.**

The FE model also predicts that the normal and the shear strains will both change considerably across the thickness of the asymmetrically rolled sample. As Figure 6.14b shows, the most homogeneous region of this sample occurs in a 0.3-mm-thick layer near the surface that is in contact with the smaller of the two rolls. In this region, values of the normal and the shear strain are calculated as 0.67 and 0.18, respectively. From this layer toward the surface contacting the larger of the two rolls, the shear

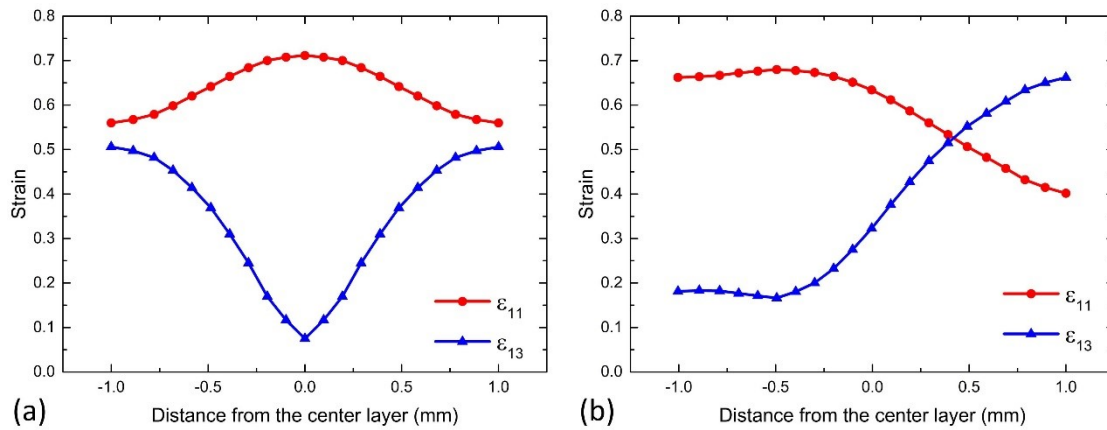


**Figure 6.14** Distribution of strain components across the sheet thickness of the (a) symmetrically and (b) asymmetrically rolled samples.

strain increases monotonically from 0.18 to 0.66, whereas the normal strain decreases (monotonically) from 0.67 to 0.40. Total shear strains, generated in the symmetrically rolled and the asymmetrically rolled samples are similar, but the strain is more widely distributed across the sheet thickness in the asymmetrically rolled samples. This is indicative of the deeper penetration of shear strain across the thickness of the asymmetrically rolled samples, compared with that occurring across the symmetrically rolled samples. According to the predictions, the grains across the thickness of the asymmetrically rolled samples will all undergo a mixed-mode of deformation characterized by a combination of compressive and shear strains. This shear strain plays a significant role in the re-orientation of the crystals.

In addition to the strain distribution across the sample thickness, FE-simulations also predict the evolution of the deformation during rolling of the samples. Figure 6.15 shows the evolution of displacement gradient components ( $u_{ij} = (F - I)_{ij}$ ) at the top-surface, mid-thickness, and bottom-surface of the symmetrically and the asymmetrically rolled samples. Owing to the geometry of the rolling gap, the normal displacement gradient components ( $u_{11}$  and  $u_{33}$ ) of both samples increase continuously during the rolling. However, depending on the rolling velocities and the friction between the rolls and the material sheet, these normal components and, hence, the evolution rates vary with spatial location in the samples. The most stable evolution of  $u_{11}$  and  $u_{33}$  occurs in the mid-thickness regions of both samples. The total evolution of these components during rolling can be described in terms of one or two



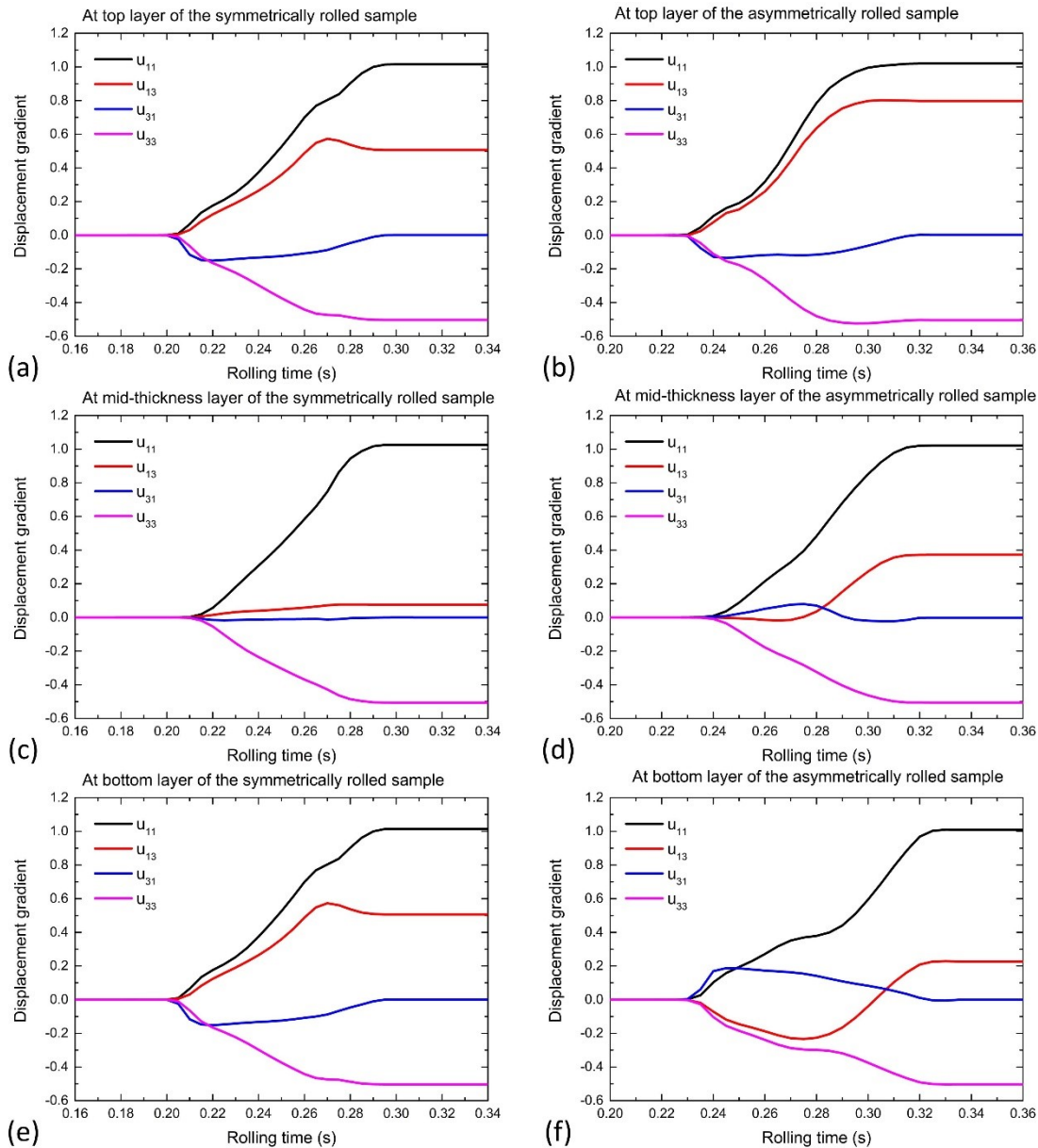


**Figure 6.15** Evolution of displacement gradient components at the top (a, b), mid-thickness (c, d), and bottom (e, f) regions of the symmetrically (a, c, and e) and the asymmetrically (b, d, and f) rolled samples.

linear deformation-gradient segments. In contrast, the evolution rates of the normal displacement gradient varies at the sub-surface regions. A least three linear segments are required to describe the evolution of the normal displacement gradient in the sub-surface regions of the symmetrically and the asymmetrically rolled samples.

The shear displacement gradient ( $u_{13}$  and  $u_{31}$ ) of both sets of samples develops in a quite similar manner during rolling. In both cases,  $u_{31}$  increases rapidly to a

maximum value at the beginning of rolling, and then decreases to zero at the end of rolling. However, the model predicts that  $u_{13}$  in most of the regions across the thickness of both sets of samples will increase continuously during rolling. The maximum (calculated) values of  $u_{13}$  are significantly larger than those of  $u_{31}$ . The shear strain imparted during symmetric and asymmetric rolling may therefore be attributed only to the shear displacement gradient  $u_{13}$ .

However, owing to contact with rolls of unequal diameters, the development of  $u_{13}$  predicted for the sub-surface region of the asymmetrically rolled sample differs from that predicted for the symmetrically rolled sample. The most significant difference is observed from the development of  $u_{13}$  at sub-surface regions of symmetrically and asymmetrically rolled samples. For the asymmetrically rolled sample, during the first half of the rolling, the  $u_{13}$  in this region develops in the direction opposing the RD, whereas in the second half  $u_{13}$  decreases and evolves along the RD. This complex evolution of  $u_{13}$  suggests that the corresponding development of the deformation textures differs from that associated with monotonic deformation paths.

#### *6.4 Simulation of deformation textures*

In general, deformation-texture development in materials results from various material and process parameters. The crystallographic structure (BCC/FCC), deformation mechanism (slip/twin), hardening behavior, and interaction among grains in the materials all contribute to the evolution of the deformation texture. This evolution is also sensitive to changes in the process parameters. Although many process parameters affect this evolution, these effects are limited mainly to changes in the strain magnitude and the strain configuration. In this work, the evolution of deformation textures after symmetric and asymmetric rolling is evaluated. The development of the asymmetric rolling texture is considered in detail, and compared with the evolution of the symmetric rolling texture.

##### *6.4.1 Persistent features*

Although deformation and rotation of crystal grains are influenced by many material and process parameters, the deformation textures of certain materials are

generally invariant. This is especially true of high-intensity texture components, which occur in the ODF plots of the deformed materials. The locations of these features in the ODF plots are relatively independent to the initial texture, hardening behavior, grain interaction, and the magnitude of the strain applied to the materials. These locations depend only on the plastic deformation mechanism of the crystal and the configuration of the applied strain. In crystal plasticity theory, these locations are referred to as *persistence features* of deformation textures. Persistence features are directly linked to the stability of crystallographic orientations that are associated with a certain deformation configuration. These features are derived from the crystal plasticity theory by calculating the lattice spin ( $\mathbf{\Omega}$ ) of crystals from the skew-symmetric part of Equation 4.13. Assuming that the elastic stretch ( $\mathbf{U}^{el}$ ) of the crystals is negligible,  $\mathbf{\Omega}$  is given as follows:

$$\mathbf{\Omega} = \dot{\mathbf{R}}\mathbf{R}^T = skew(\mathbf{L}) - \mathbf{R} \cdot skew\left(\sum_{\alpha} \mathbf{M}^{\alpha}\dot{\gamma}^{\alpha}\right) \cdot \mathbf{R}^T \quad (6.13)$$

The lattice spin ( $\mathbf{\Omega}$ ) is a skew-symmetric tensor with diagonal elements equal to zero, and may be expressed as follows:

$$\mathbf{\Omega} = \begin{pmatrix} 0 & \Omega_{12} & -\Omega_{31} \\ -\Omega_{12} & 0 & \Omega_{23} \\ \Omega_{31} & -\Omega_{23} & 0 \end{pmatrix} \quad (6.14)$$

Accordingly, the rotation rates in the Bunge Euler angles ( $\dot{\varphi}_1, \dot{\Phi}, \dot{\varphi}_2$ ) are related to  $\mathbf{\Omega}$  as follows [2]:

$$\begin{aligned} \dot{\varphi}_1 &= \frac{\sin \varphi_2}{\sin \Phi} \Omega_{23} + \frac{\cos \varphi_2}{\sin \Phi} \Omega_{31} \\ \dot{\Phi} &= \cos \varphi_2 \Omega_{23} - \sin \varphi_2 \Omega_{31} \end{aligned} \quad (6.15)$$

$$\dot{\varphi}_2 = \Omega_{12} - \dot{\varphi}_1 \cos \Phi$$

The lattice spin of a crystal depends on three parameters ( $\Omega_{23}, \Omega_{31}, \Omega_{12}$ ) and can therefore be treated as a vector lying in the three-dimensional (3D) space. The magnitude of this vector is determined from:

$$\|\Omega\| = \sqrt{\Omega_{23}^2 + \Omega_{31}^2 + \Omega_{12}^2} \quad (6.16)$$

For a given crystal deformation, the stability of the crystals decreases with increasing magnitude of  $\Omega$ , resulting in a decrease in the texture intensity of the crystallographic orientation. Compared with all other possible orientations, those having lower  $\Omega$  will rotate more slowly away from their initial orientations and have a higher likelihood of occurring in the deformation texture. Some orientations of zero spin are called zero-orientations. In fact, a zero rotation rate constitutes only one of the two attributes that characterize a stable orientation. According to Bunge [2], zero orientations can be classified into three categories, depending on orientation flows in their vicinity. If neighboring orientations all flow toward, all flow away from, and flow both toward and away from the zero-orientation, then the zero-orientation, is considered stable, unstable, and metastable, respectively. Therefore, the magnitude and the direction of the lattice spin vectors around zero-orientations are both required to identify stable orientations.

### Persistence features of symmetrical-rolling textures

The calculated rotation rate and rotation field around zero-orientations associated with symmetric rolling are used to validate set-up parameters and compare rotation rates of crystals subjected to different deformation modes. Figure 6.16 shows the rotation rate map, as a  $\phi_2 = 45^\circ$  section of Bunge Euler space, of orientations subjected to PSC. These rotation rates are normalized to the largest rotation rate of all possible

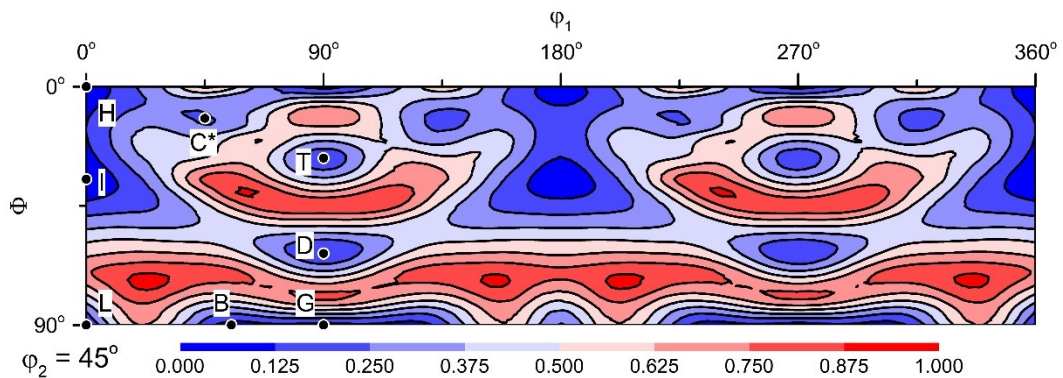


**Figure 6.16**  $\phi_2 = 45^\circ$  Euler angle section showing the rotation rate map of BCC-structured materials subjected to plane strain compression (PSC).

orientations of BCC-structured crystals and, hence, have values ranging from zero to one. The rotation rate map (Figure 6.16) consists of eight zero-orientations and their symmetrically equivalent orientations. Among them, the H- $\{001\}\langle 110\rangle$ , I- $\{112\}\langle 110\rangle$ , and D- $\{111\}\langle 111\bar{2}\rangle$  orientations are typical high-intensity symmetrical-rolling texture components. These three orientations are stable, according to the rotation flow criterion defined by Bunge. For example, consider the rotation field around the I- $\{112\}\langle 110\rangle$  orientation, which is shown in the  $(\varphi_1-\Phi)$  and  $(\varphi_2-\Phi)$  Euler sections in Figure 6.17a and Figure 6.17d. The orientations in the vicinity of the  $\{112\}\langle 110\rangle$  orientation flow toward this zero-orientation, leading to its stability during PSC. In addition to stable orientations, orientations with zero rotation rates (for example, the G- $\{110\}\langle 001\rangle$  and the C\*- $\{016\}\langle 061\rangle$  orientations) are also defined. Neighboring orientations flow completely away from these orientations (Figure 6.17b and Figure 6.17e) and, hence, the G- and the C\*-orientations are considered unstable. These two orientations rarely occur in the deformation texture of conventionally rolled BCC-structured materials. Other zero-orientations, including the T- $\{442\}\langle 111\bar{2}\rangle$ , Br- $\{110\}\langle 112\rangle$ , and L- $\{110\}\langle 110\rangle$ , experience both inward and outward orientation flow and are therefore considered meta-stable. Meta-stable orientations rarely occur with measurable intensities in the macroscopic texture of symmetrically rolled materials. However, a small number of grains with meta-stable orientations may be retained in the deformation microstructures of BCC-structured materials.

In summary, locations in Euler space, symbols, Miller indices, and stability of all zero-orientations associated with PSC are listed in Table 6.3.

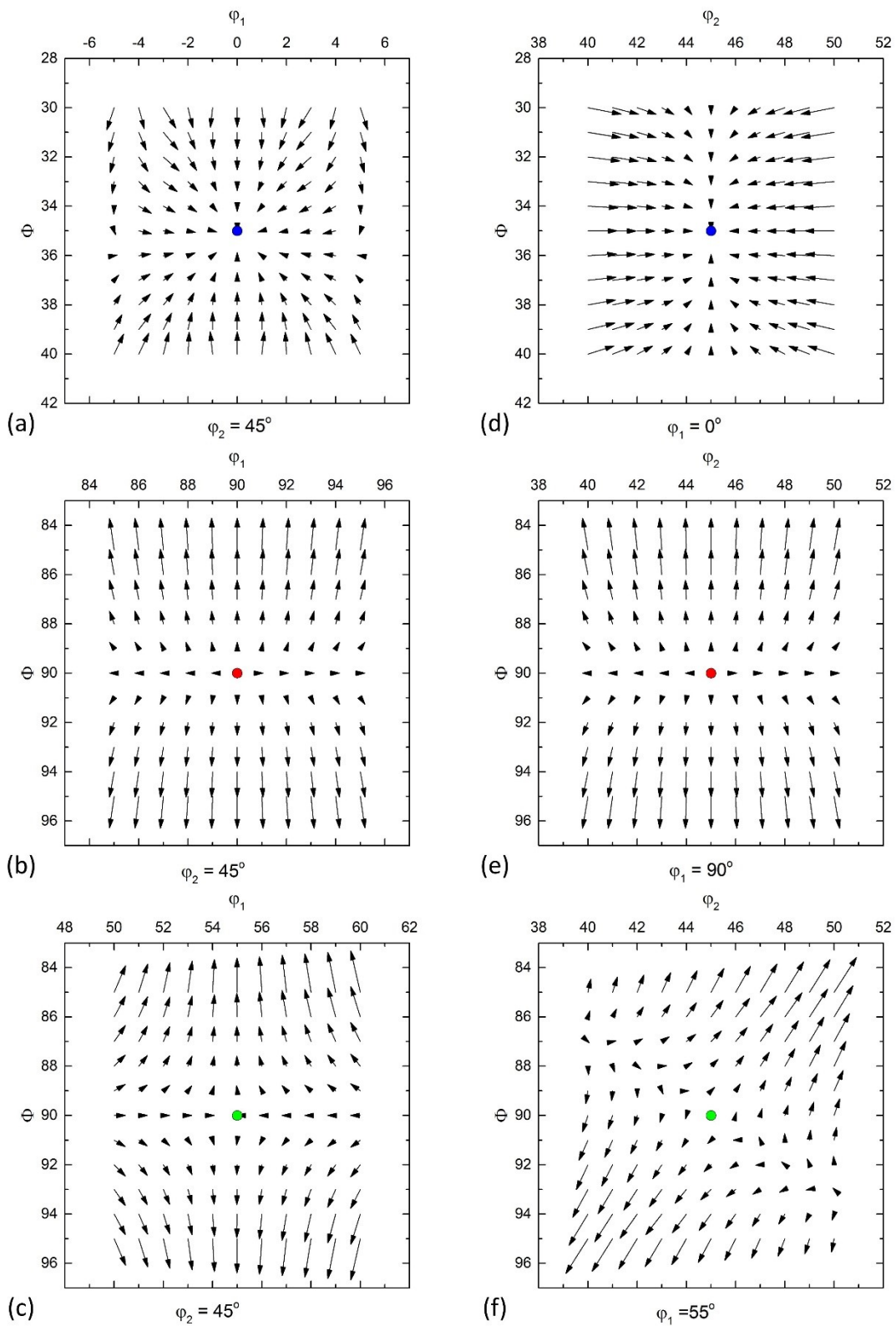


Figure 6.17 Rotation fields around different types of zero-orientations associated with PSC. Rotation field around the (a) and (d) stable orientation  $\{112\}\langle 110\rangle$ , (b) and (e) unstable orientation  $\{110\}\langle 001\rangle$ , (c) and (f) meta-stable orientation  $\{110\}\langle 112\rangle$ .

Symbol	Euler Angles ( $\varphi_1, \Phi, \varphi_2$ )	Miller Indices	Stability
H	(0.00°, 0.00°, 45.00°)	{001}<110>	Meta-stable
I	(0.00°, 35.26°, 45.00°)	{112}<110>	Stable
L	(0.00°, 90.00°, 45.00°)	{110}<110>	Meta-stable
C*	(90.00°, 9.22°, 0.00°)	{016}<061>	Unstable
Br	(54.74°, 90.00°, 45.00°)	{110}<112>	Meta-stable
T	(90.00°, 27.37°, 45.00°)	{4 4 11}<11 11 8>	Meta-stable
D	(90.00°, 62.63°, 45.00°)	{11 11 8}<4 4 11>	Stable
G	(90.00°, 90.00°, 45.00°)	{110}<001>	Unstable

**Table 6.3 Orientations of zero rotation rate in conventionally rolled BCC-structured materials.**

### Persistence features of asymmetrical-rolling textures

As discussed in the previous section, the deformation resulting from asymmetric rolling can be considered a combination of PSC and simple shear. Persistence features of asymmetrical-rolling textures can be derived from the rotation rate and rotation field, as in the case of symmetrical-rolling textures. The rotation rate map of BCC-structured materials subjected to asymmetric rolling ( $\kappa = 0.5$ ) is plotted in the  $\varphi_2 = 45^\circ$  Euler section (see Figure 6.18).

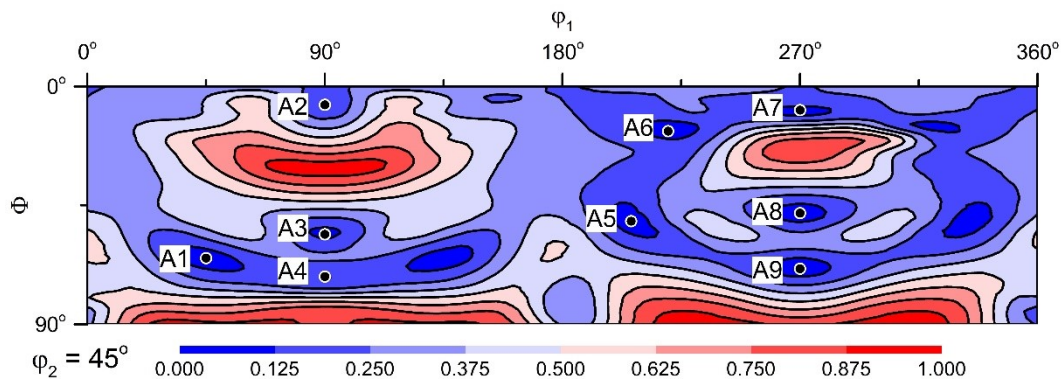


**Figure 6.18 A  $\varphi_2 = 45^\circ$  Euler angle section showing the rotation rate map of BCC-structured materials subjected to a combination of PSC and simple shear (shear factor  $\kappa = 0.5$ ).**

Nine zero-orientations, referred to as A1 to A9, occur in this rotation rate map. Orientation representation via Miller indices is complicated and requires several digits. Therefore, in this work, the positions of zero-orientations associated with asymmetric rolling are described by Euler angles. The A3-, A5-, A7-, and A9-

orientations are stable zero-orientations; see Figure 6.19a and Figure 6.19d for the rotation field around the A5-(209°, 54°, 47°) orientation, as plotted in the ( $\varphi_1$ - $\Phi$ ) and ( $\varphi_2$ - $\Phi$ ) sections of Euler space. The  $\langle 110 \rangle$  crystallographic axes of stable orientations, such as the A3, A7, and A9, are parallel to the TD. These orientations lie between the meta-stable or unstable zero-orientations along the  $\langle 110 \rangle$ //TD fiber. The stable A9-(270°, 68°, 45°) and A3-(90°, 57°, 45°) orientations lie next to the unstable A8-(270°, 48°, 45°) and the meta-stable A4-(90°, 72°, 45°) orientations, respectively (see Figure 6.19b-f for the corresponding rotation fields). In addition to the zero-orientations lying along the  $\langle 110 \rangle$ //TD fiber, the rotation rate map (Figure 6.18) also includes two other zero-orientations, i.e., the unstable A1 and the A6-orientations. Owing to their instability, the absence of these orientations from the deformation texture of asymmetrically rolled BCC-structured materials is expected. The symbols, angular positions in Euler space, and stability of all the zero-orientations associated with asymmetric rolling are listed in Table 6.4.

Symbol	Euler Angles ( $\varphi_1, \Phi, \varphi_2$ )	Stability
A1	(41.21°, 64.15°, 43.60°)	Unstable
A2	(90.00°, 6.60°, 45.00°)	Meta-stable
A3	(90.00°, 56.83°, 45.00°)	Stable
A4	(90.00°, 72.43°, 45.00°)	Meta-stable
A5	(208.68°, 53.71°, 47.25°)	Stable
A6	(233.46°, 12.79°, 35.00°)	Unstable
A7	(270.00°, 8.99°, 45.00°)	Stable
A8	(270.00°, 48.13°, 45.00°)	Unstable
A9	(270.00°, 68.43°, 45.00°)	Stable

**Table 6.4 Orientations of zero-rotation rates in asymmetrically rolled ( $\kappa$ : 0.5) BCC-structured materials.**



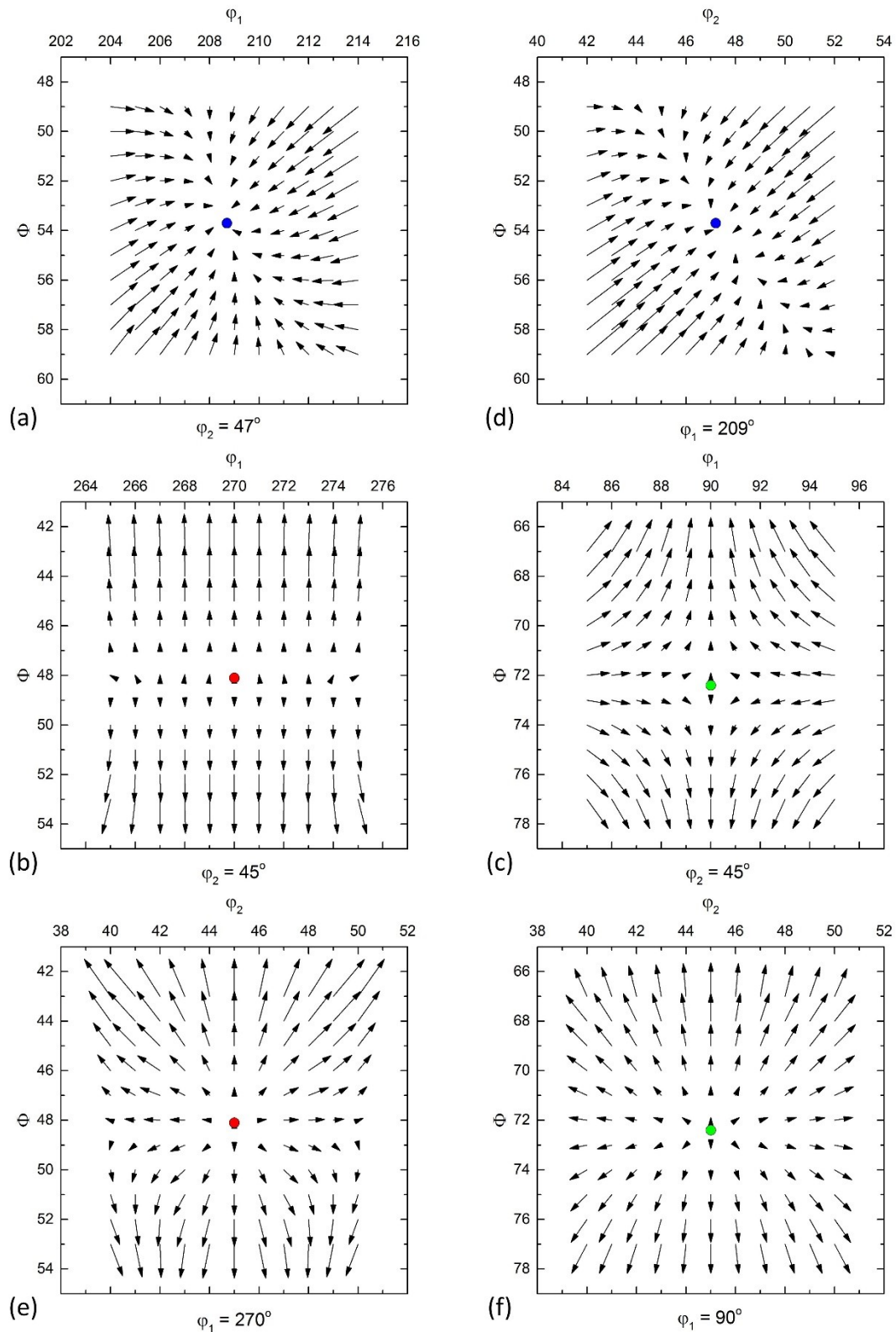


**Figure 6.19** Rotation fields around different zero-orientations undergoing a combination of PSC and simple shear ( $\kappa$ : 0.5). Field around the (a) and (d) stable A5-orientation, (b) and (e) unstable A8-orientation, (c) and (f) meta-stable A4-orientation.

### Correlation between persistence features of symmetrical- and asymmetrical-rolling textures

The rotation rate maps of BCC-structured materials subjected to symmetrical and asymmetrical rolling exhibit similar features, with zero-orientations lying along the  $\langle 110 \rangle // \text{TD}$  orientation fiber in both cases. In the case of symmetrical rolling, these zero-orientations are the H- $(\{001\} \langle 110 \rangle)$ , T- $(\{4\ 4\ 11\} \langle 11\ 11\ 8 \rangle)$ , D- $(\{11\ 11\ 8\} \langle 4\ 4\ 11 \rangle)$ , and G- $(\{110\} \langle 001 \rangle)$  orientations. The H- and the D-orientations are stable, whereas the T-orientation and the G-orientation are meta-stable and unstable, respectively. In the case of asymmetrical rolling, six zero-orientations lie along the  $\langle 110 \rangle // \text{TD}$  fiber. The A2-, A3-, and A4-orientations occur at  $\varphi_1 = 90^\circ$  in the  $\varphi_2 = 45^\circ$  section of Euler angle space, whereas the A7-, A8-, and A9-orientations occur at  $\varphi_1 = 270^\circ$ . For asymmetrical rolling, the (i) A4-, A7-, and A9-orientations and (ii) A2-, A3-, and A8-orientations constitute (i) stable and (ii) meta-stable or unstable orientations, respectively, that lie along the  $\langle 110 \rangle // \text{TD}$  fiber.

Orientations along the  $\langle 110 \rangle // \text{TD}$  fiber of symmetrical- and asymmetrical-rolling textures constitute zero-orientations in the rotation rate maps and have a unique rotation axis (i.e., the  $\langle 110 \rangle // \text{TD}$ ) during deformation. In Euler coordinates, the rotations around the TD are represented by rotation rate vectors with non-zero values of the  $\Phi$ -angle coordinate ( $\dot{\varphi}_1 = 0$ ;  $\dot{\Phi} \neq 0$ ;  $\dot{\varphi}_2 = 0$ ). The rotation rate vectors

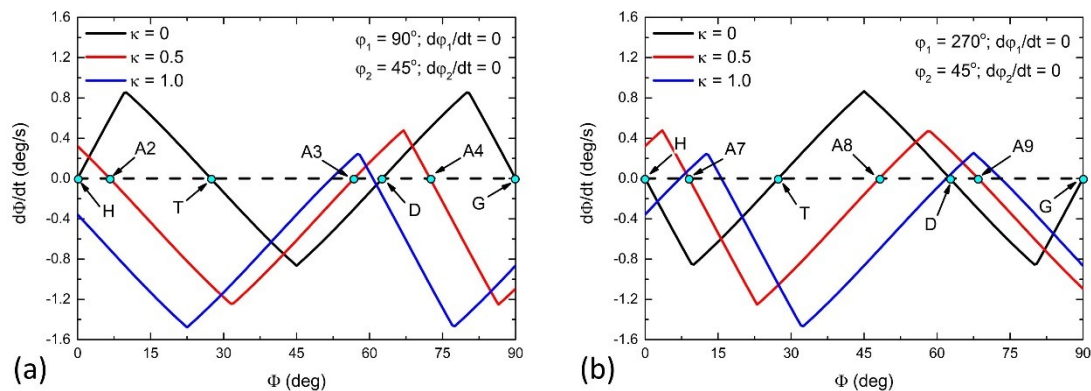


**Figure 6.20** Rotation rate components of all orientations along the  $\langle 110 \rangle // \text{TD}$  fiber. Rates for orientations lying in the (a)  $\varphi_1 = 90^\circ$  and (b)  $\varphi_1 = 270^\circ$  sections of Euler space. The orientations are subjected to a combination of planar compressive and simple shear strains (shear factor  $\kappa$ : 0, 0.5, 1.0).

associated with three different deformation modes have been calculated for all orientations along the  $\langle 110 \rangle // \text{TD}$  fiber. These deformation modes represent various combinations of PSC and simple shear, where shear factors ( $\kappa$ ) of 0, 0.5, and 1.0 are considered. Figure 6.20 shows the results of these calculations for crystals with  $\varphi_1 = 90^\circ$  and  $\varphi_1 = 270^\circ$  that lie in the positive part and negative part of the  $\langle 110 \rangle // \text{TD}$  orientation fiber, respectively. For each deformation mode, the rotation rates of the  $\langle 110 \rangle // \text{TD}$ -oriented crystals change linearly with the magnitude of the  $\Phi$ -angle. In the case of symmetrical rolling ( $\kappa = 0$ ), the rotation rates vary from -0.87 to 0.87. Negative values of the rotation rate correspond to opposing rotations around the common axis, and null values indicate the positions of zero-orientations. All four zero-orientations of symmetrical rolling are clearly visible in Figure 6.20a and Figure 6.20b. The rotation rates change when the shear factor is increased from 0 to 0.5 and 1.0. In the positive part of the  $\langle 110 \rangle // \text{TD}$  fiber, the maximum value of the rotation rate decreases, whereas the minimum value increases. Positions of the zero-rotation points are shifted to  $\Phi$ -angles smaller than the original values. Specifically, for asymmetrical rolling ( $\kappa = 0.5$ ), (i) the stable A3-orientation is deviated by  $5.8^\circ$  from the stable D-orientation and (ii) the meta-stable A2-orientation is shifted  $20.8^\circ$  from the meta-stable T-orientation associated with symmetrical rolling. By the same strain configuration, zero-orientations in the negative part of the  $\langle 110 \rangle // \text{TD}$  fiber also change positions, albeit in a different direction. The  $\Phi$ -angle of the stable A7-orientation resulting from asymmetrical rolling is  $9.0^\circ$  larger than that of the stable H-orientation associated with symmetrical rolling. Similarly, the stable A9-orientation is  $5.8^\circ$  deviated from the stable D-orientation. The shift of zero-orientations is attributed to the shear strain that is characteristic of the deformation mode. Therefore, for both symmetrical and asymmetrical rolling, the locations of stable orientations depend on the value of the shear factor. Conversely, the contribution of the shear component to the total deformation of crystals can be estimated by measuring the deviation angle between the stable orientations associated with symmetrical rolling and those associated with asymmetrical rolling.

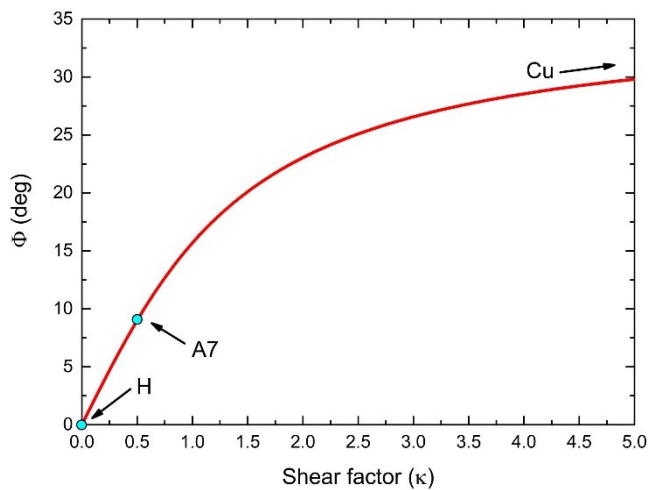


**Figure 6.21** Location of stable orientations along the  $\Phi$ -angle axis as a function of the shear factor.

The correlation between the shear factor ( $\kappa$ ) and persistent features of rolling textures is illustrated by plotting the locations of stable orientations as a function of  $\kappa$ . For example, at a  $\kappa$  of zero, a stable orientation occurs at the position of the H-orientation, associated with symmetrical rolling (see Figure 6.21). When  $\kappa$  is increased, the stable orientation associated with asymmetrical rolling is shifted along the  $\langle 110 \rangle // \text{TD}$  fiber toward orientations with larger  $\Phi$ -angle values. As  $\kappa$  approaches infinity, crystals experience mainly simple shear strain and the stable orientation will approach the Cu ( $\{112\} \langle 111 \rangle$ ) orientation. This simple shear strain is not expected for rolling deformation, neither symmetrical nor asymmetrical. However, to keep the generality of the current study, Figure 6.21 shows a smooth transition of deformation textures from the PSC type to the simple shear type. The deformation texture associated with asymmetrical rolling, therefore, is a specific results of a mixed deformation mode characterized by PSC and simple shear.

#### 6.4.2 Homogeneous development of deformation textures

If the origin of the persistence features is known, the development of deformation texture after symmetric and asymmetric hot rolling can be simulated in a relatively straight-forward manner. Texture development after conventional rolling has been extensively investigated and, hence, this work mainly considers deformation texture development after asymmetric rolling.

First-order estimation of the deformation texture after hot asymmetric rolling, is performed by using a geometrical model to calculate the strain mode and the strain magnitude (Section 6.3.1). This model is based on the assumption that the

deformation imparted during asymmetrical rolling is homogeneously distributed across the sheet thickness. In addition, all strain components change linearly from the beginning to the end of the rolling gap. This deformation evolution is considerably simpler than that obtained via the FE method. Moreover, the relatively short time required for strain calculation renders the geometric model suitable for the quantitative prediction of macroscopic texture development after asymmetrical rolling.

The texture evolution after asymmetrical rolling is simulated with the grain interaction crystal plasticity advanced LAMEL (ALAMEL) model developed by Van Houtte et al. [3]. The initial texture for this simulation is taken as the one measured after the rough rolling step. To minimize the calculation time and the computer resources used, the initial ODF is discretized into 2000 individual orientations using the method proposed by Toth & Van Houtte [4]. The total deformation imparted during the hot asymmetrical rolling process is applied to the polycrystal in 200 strain steps (see Figure 6.22 for the corresponding simulation result).

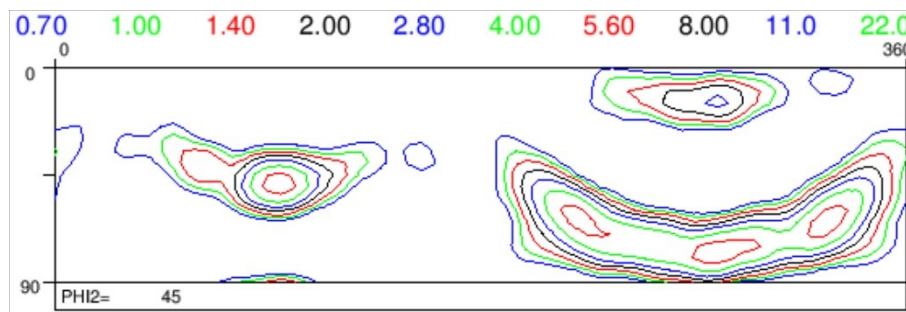


**Figure 6.22 Simulated macroscopic texture of the Fe-1.2 wt.% Si alloy after the last asymmetrical hot rolling pass, determined via the ALAMEL model with the strain mode derived from the geometrical method.**

The simulated texture (Figure 6.22) and measured texture (Figure 6.6) exhibit similar features. Stable orientations, including the A3-, A5-, A7-, and A9-orientations, occur with high intensity in both cases. In the simulated texture (Figure 6.22), the A3-, A5- and A9-orientations occur with intensities more than 6.4 times the random level. The A7-orientation in this simulated texture has the intensity of 3.0 times the random level. Texture intensities characterizing the simulated texture are, in general, two times higher than those of the measured texture. This over-estimation of the

intensities (by the simulation) may stem from (over)simplification (by the geometric method) of the strain condition associated with asymmetrical rolling. Improved texture prediction, therefore, is expected with use of the strain condition calculated by the FE method.

To quantitatively compare the simulated and measured textures, the normalized texture index of the ODF difference ( $TI_{ODF}$ ), which is mathematically expressed as following, can be used:

$$TI_{ODF} = \frac{\int_{\forall g \in \Gamma} (f_{ex}(g) - f_{mo}(g))^2 dg}{\int_{\forall g \in \Gamma} (f_{ex}(g))^2 dg} \quad (6.17)$$

where,  $f_{ex}(g)$  and  $f_{mo}(g)$  are values of the experimental and simulated ODFs, respectively. The integrals in the numerator and denominator are applied to all orientations in the orientation space. The value of  $TI_{ODF}$  ranges from zero to infinity, and decreases with decreasing difference between the measured and the simulated ODFs. Therefore, a low  $TI_{ODF}$  value is indicative of a good fit between the simulated and the experimental textures.

A  $TI_{ODF}$  of 0.74 is obtained for the simulated texture associated with asymmetrical rolling under the strain condition calculated by the geometrical method.

#### 6.4.3 Heterogeneity of the deformation textures

Prediction of the deformation-texture evolution after asymmetrical rolling can be improved if the strain development during rolling is described in more detail, compared with the description provided by the geometrical method. The development of the macroscopic texture after hot asymmetrical rolling is accurately predicted by assuming (in the geometrical method) that the strain components evolve in a linear and homogeneous manner during deformation. However, the intensities of the preferred orientations in the simulated texture are all higher than those of the corresponding orientations in the measured texture. The texture prediction can be improved by considering the fact that, during asymmetrical rolling, the strain components (i) are heterogeneously distributed across the sheet thickness and (ii)

evolve in a non-linear manner. Different strain evolutions will produce various local textures across the thickness of the asymmetrically rolled sample. The weighted average of these local textures can be considered the macroscopic texture of the entire sample. Compared with the previously predicted texture, this texture is expected to be a better fit to the measured texture. The strain evolution associated with local and macroscopic textures of the asymmetrically rolled sample can also be determined via the FE method.

Local textures, in principle, can be calculated for each discrete element of the FE grid and at each time-step of the simulation. Nevertheless, these textures must be consistent with the physical features of the materials. The FE method is applied on the continuum scale with element-to-element strain discrepancy across the sheet thickness. In contrast, the CP model is applied at the grain scale and the local texture is defined for a polycrystalline aggregate. Strain compatibility between the FE model and the CP model is realized if each finite element is larger than the crystal grains. The initial material (prior to hot asymmetrical rolling) has an average grain diameter of  $\sim 100 \mu\text{m}$ . In the FE model, the thickness (4 mm) of the sample is discretized into 12 elements and, hence, each element contains a maximum of three crystal grains across the thickness. Compared with a smaller number of elements, a larger number of FEs across the sheet thickness yields a smoother variation of the strain components. A small number of crystal grains across an element thickness, however, leads to ambiguity in the texture prediction. Therefore, for the CP-model texture simulation performed in this study, elements across the sample thickness are merged into layers, thereby increasing the number of grains across the thickness. Strain components in a layer are calculated from the average value of the strain components in the elements. This calculation assumes that these components are homogeneously distributed within layers of elements, but also allows inter-layer strain variation. In this study, FEs across the sample thickness are merged into one, three, and five homogeneous layers.

In addition to the strain heterogeneity across the sheet thickness, FE simulation also predicts a non-monotonic development of strain components during

asymmetrical rolling. This development is described by multi-linear segments of finite deformations. In each segment of the 0.005-s time interval, constant velocity gradients are applied to the FEs, yielding linear development of the components during the time interval. The strain evolution during asymmetrical rolling is characterized by the occurrence of many consecutive segments with almost identical velocity gradient (see Figure 6.15). Therefore, rather than 10 to 20 segments, the total deformation in the asymmetrically rolled sample can be described by considerably fewer linear segments. In the CP model employed in the current study, the strain development in each homogeneous layer of FEs is linearized by one, two, and three segments.

The local textures of the homogeneous strain layers and linear deformation segments used to describe asymmetrical hot rolling are first simulated by the ALAMEL model. The macroscopic textures are then represented by the weighted average of these local textures. In addition, the fit between the simulated and the measured textures is evaluated via the  $TI_{ODF}$  parameter. Figure 6.23 shows the simulated local textures at the top, middle, and bottom layers of the asymmetrically rolled samples where the strain evolutions in each layer are described by three linear segments. These textures are all characterized by similar high-intensity texture components, which are stable orientations associated with asymmetrical rolling. However, the intensities of these components vary across the sample thickness. For example, in the local textures, the highest and lowest intensities of the (i) A3-orientation (4.5 times and 3.0 times the random level) occur for the mid-thickness and the bottom layers, respectively, and (ii) A7-orientation (2.5 times and 1.5 times the random level) occur for the top/mid-thickness layers and the bottom layer, respectively.

The weaker texture intensities of the stable orientations in the bottom layer, compared with those in the top/mid-thickness layers, result from different strain evolutions in the various homogeneous layers. As Figure 6.15b, d, and f show, the FE simulation predicts that the shear strain imparted during asymmetrical rolling consists of two displacement gradient components namely,  $u_{13}$  and  $u_{31}$ . The  $u_{13}$  values in all three homogeneous layers are larger than those of  $u_{31}$ ; therefore,  $u_{13}$  plays a greater role in the deformation of the sample, and the  $u_{13}$  component associated with



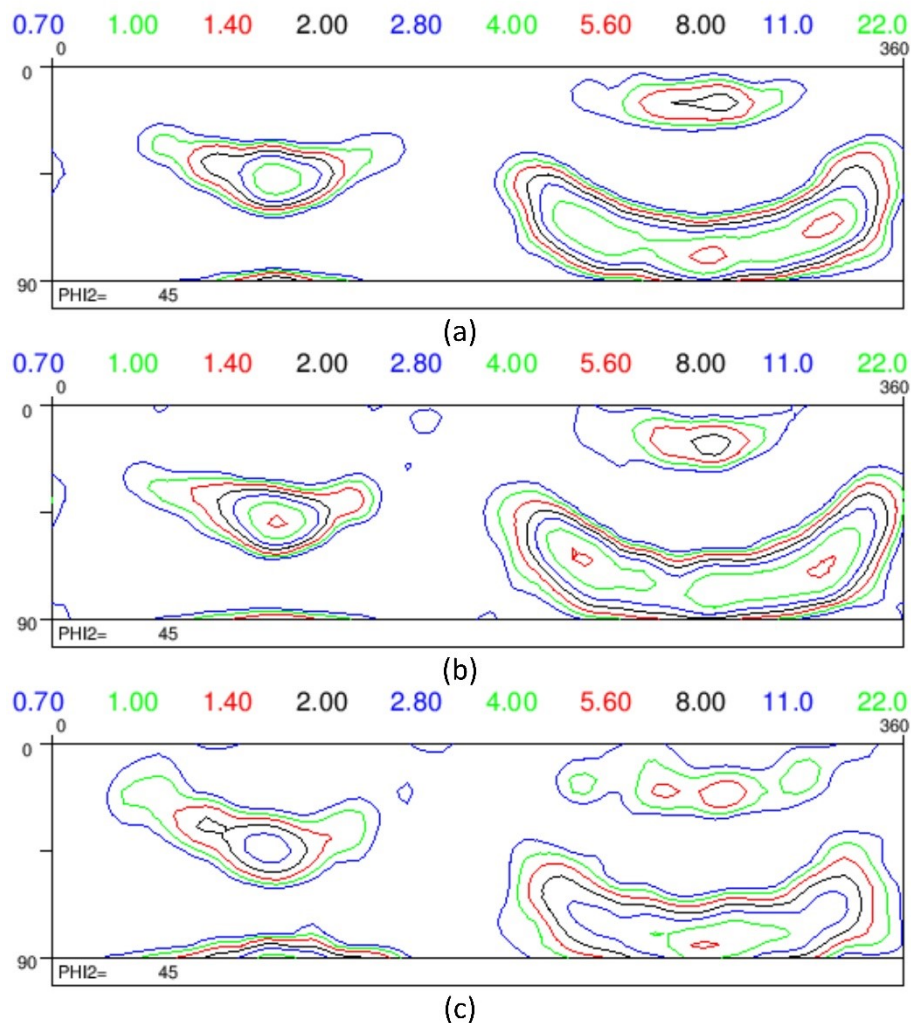


**Figure 6.23** Local textures at the (a) top, (b) middle, and (c) bottom layers of the hot asymmetrically rolled sample. These textures are simulated by the ALAMEL crystal plasticity (CP) model with the strain evolutions in each layer represented by three linear deformation segments.

the bottom layer of the asymmetrically rolled sample lack a unique direction of evolution, in contrast to those associated with the top and the middle layers. During the first half of the deformation, the  $u_{13}$  component in the bottom layer develops in the direction opposing the RD, but, in the second half, decreases and evolves along the RD. This non-monotonic development of  $u_{13}$  results in complex local-texture evolution in the bottom layer of the asymmetrically rolled sample. Therefore, crystal grains in the bottom layer rotate along various (rather than unique) directions. The

rotation of crystal grains first forward and then backward produces a weak texture in the bottom layer of the asymmetrically rolled sample.

Weak local textures are obtained, via FE simulation, by taking into account the strain heterogeneity across the sheet thickness and the non-monotonic development of strain components during asymmetrical rolling. However, the effect of this description (i.e., the strain evolution in the asymmetrically rolled sample) on the macroscopic texture remains unknown. Therefore, in this work, the influence of the strain-evolution description on the accuracy of texture prediction is investigated. This influence is revealed by comparing the simulated macroscopic textures, associated with each strain-homogeneous layer and linear segment, with the experimental texture.

Figure 6.24 shows the  $TI_{ODF}$  values for different simulation textures corresponding to various descriptions of the strain evolution in asymmetrical rolling. As the figure shows, these values decrease with increasing number of homogeneous layers and linear strain segments. This indicates that the fit of the simulation texture improves when a more detailed description of the strain evolution (compared with that provided by the geometric method) in asymmetric rolling is provided. Specifically,  $TI_{ODF}$  values of the simulation textures decrease by 10–30% when the number of homogeneous layers is increased from one to three and five. This decrease occurs, however, without a corresponding improvement in the simulated textures obtained for three and five homogeneous layers. In fact, the  $TI_{ODF}$  values corresponding to the macroscopic textures of five homogeneous layers are all slightly higher than those of the textures obtained for three layers.

The  $TI_{ODF}$  value of the simulated textures decreases by 50–60% when the non-monotonic strain evolution during asymmetrical rolling is considered. However, the value changes only slightly when the number of linear strain segments is increased from two to three. This results from the fact that, by increasing the number of segments, local variations in the velocity gradient components are added to the CP model (ALAMEL). These variations are small and have neither a negative effect on the quality of the predicted textures, nor a positive effect on the simulation results.

The influence of the non-monotonic evolution of strain components on the simulated textures is also revealed by comparing the  $Tl_{ODF}$  values corresponding to the FE-determined and geometric-method-determined strain evolutions. In Figure 6.24, the  $Tl_{ODF} = 0.74$  value (obtained for the strain evolution estimated by the geometrical method) is denoted by a horizontal dashed

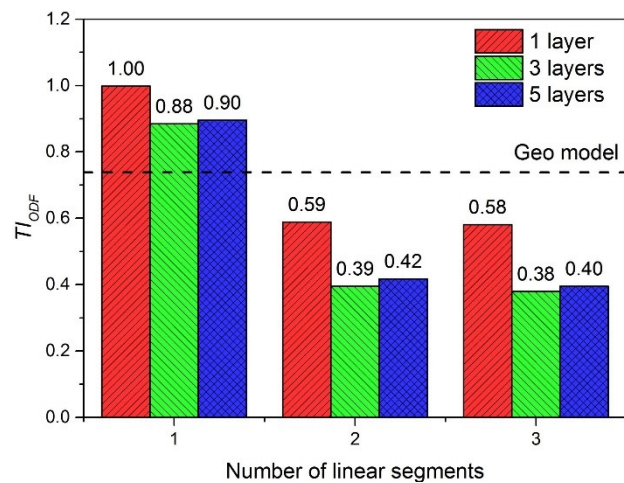


**Figure 6.24 Comparison of experimental and simulated textures. The simulated textures are calculated for various descriptions of the strain evolution in asymmetrical rolling.**

line. The  $Tl_{ODF}$  value of the geometric model is higher than the values obtained for two and three linear segments and, hence, the corresponding simulated texture is less accurate. However, if non-monotonic evolutions of the strain components are neglected by the FE method, the simulation results obtained are worse than those of the geometric model, regardless of the number of homogeneous layers considered.

### 6.5 Conclusions

The evolution of the deformation texture of Fe-1.2 wt.%Si alloy is investigated for samples asymmetrically rolled at both elevated and room temperatures. The results are compared with those of the samples conventionally rolled at the same temperatures.

Deformation textures resulting from conventional rolling at both high and room temperatures consist mainly of the  $\alpha$ - and the  $\gamma$ -fiber texture components. This is typical of BCC-structured materials subjected to PSC. However, a different deformation texture is obtained when the material is deformed via asymmetrical rolling. The development of deformation texture after asymmetrical rolling is explained by evaluating (via the geometrical model and the FE method) the deformation mode of this rolling process. These strain analyses indicate that the

deformation occurring during asymmetrical rolling consists mainly of two components: the compressive strain along the ND and the shear strain along the RD. Samples subjected to this mixed mode of deformation experience PSC (associated with conventional rolling) and a simple shear strain along the RD. The deformation texture resulting from asymmetrical rolling constitutes, therefore, an intermediate between PSC and simple shear-type textures. The deviation of stable orientations associated with asymmetrical rolling, from those associated with conventional rolling, can be calculated from the ratio between the compressive strain and the shear strain. Accordingly, the deformation texture of asymmetrical rolling is accurately predicted, using the simple strain estimation of the geometrical model. Nevertheless, more accurate texture prediction (than that of the geometrical model) is realized by using a FE method to perform the strain analysis. The FE method predicts a non-monotonic evolution and a heterogeneous distribution of strain components across the thickness of asymmetrically rolled samples. Consideration of both these effects, particularly the non-linear development of strain components during asymmetrical rolling, yields the best fit between the simulated and the experimental textures.

## **6.6 References**

- [1] Kang S-B, Min B-K, Kim H-W, Wilkinson D, Kang J. Effect of asymmetric rolling on the texture and mechanical properties of AA6111-aluminum sheet. *Metallurgical and Materials Transactions A*. 2005;36:3141.
- [2] Bunge HJ. Some applications of the Taylor theory of polycrystal plasticity. *Krist. Tech.* 1970;5:145.
- [3] Van Houtte P, Li S, Seefeldt M, Delannay L. Deformation texture prediction: From the Taylor model to the advanced Lamel model. *Int J Plast.* 2005;21:589.
- [4] Tóth LS, Van Houtte P. Discretization Techniques for Orientation Distribution Functions. *Texture Microstruct.* 1992;19:229.



# 7

## Recrystallization textures of the Fe-1.2 wt.% Si alloy after annealing

To regain the lattice defect free state of materials after plastic deformation, recrystallization annealing has been applied to the Fe-1.2 wt.% Si alloy. After hot rolling, samples of both symmetric and asymmetric rolling were annealed at 900 °C in 2 hours under the dry nitrogen protective atmosphere. After cold rolling, samples were annealed in a batch furnace at 900 °C during 70 seconds under the pure hydrogen atmosphere. During these annealing steps, stored energy in deformed crystals are released, defect-free crystals “nucleate” and grow into the deformation matrix, leading to the changes of microstructure and texture in materials. Orientation

dependences of recrystallization “nucleation” and growth occur differently at various annealing temperatures, resulting in different recrystallization textures. Deformation microstructures and textures in conventionally and asymmetrically rolled samples are different. Therefore, evolution of recrystallization textures after conventional and asymmetric rolling will not be the same.

In this chapter, developments of recrystallization textures and microstructures in symmetrically and asymmetrically rolled samples after warm and cold rolling are investigated by the EBSD technique. Developments of recrystallization textures are simulated by the Kestens-Jonas model [1]. Differences in recrystallization textures are revealed and analyzed by comparing measured and simulated textures.

### *7.1 Evolutions of recrystallization textures*

#### *7.1.1 Hot band annealing textures*

After both conventional and asymmetric rolling, samples of the Fe-1.2 wt.% Si alloy were annealed at 900 °C during 2 hours in a protective atmosphere for full recrystallization. Details of these annealing experiments and the sample preparation procedures for EBSD measurements are given in Chapter 5.

Microstructures of symmetrically and asymmetrically rolled samples (see Figure 7.2a and Figure 7.1a) after the annealing are rather similar. Across the sample thickness, grains of various orientations are distributed homogeneously. Each grains in these microstructures have individually sharp orientations. Most of the grains have equi-axed shapes, although some grains in the mid-thickness region of the symmetrically rolled sample have a somewhat extended dimension in the RD. The average grain-size diameter of symmetrically rolled and annealed sample is 130  $\mu\text{m}$ , which is slightly larger than the value of 110  $\mu\text{m}$  of asymmetrically rolled and annealed sample. The grain-size distribution in the former sample (c.f. Figure 7.2b) is broader than in the latter one (c.f. Figure 7.1b). These microstructure features account for the fully recrystallized state of the materials.

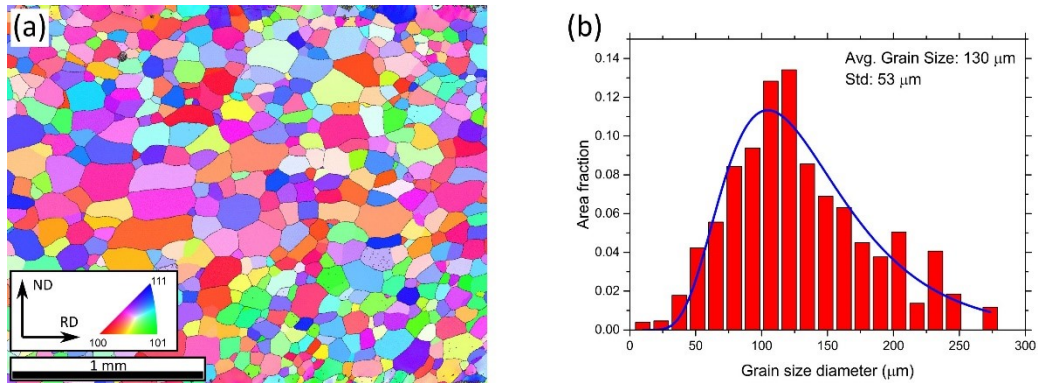


**Figure 7.1** The microstructure across the thickness (a) and the grain-size diameter distribution (b) of a warm conventionally rolled and annealed sample.

Variances in recrystallization microstructures of conventionally and asymmetrically rolled samples, though small, are due to differences in deformation conditions of the two rolling configurations. Warm rolling conditions and their impacts on microstructure and texture of the material have been analyzed in the Chapter 6. Main features of the deformation microstructures, however, are briefly summarized here for better understanding of the formation of recrystallization texture and microstructure.

In warm conventionally rolled sample, grains of different preferred orientations from the mid-thickness to the sub-surface regions are observed (c.f. Figure 6.1a). The grains in the mid-thickness region mostly have the  $\alpha$ - and the  $\gamma$ -fiber orientations, while grains in the sub-surface region are dominated by the Goss and Copper orientations. A sub-structure is more frequently observed in grains of the sub-surface regions than in the ones of the mid-thickness region (c.f. Figure 6.3). Density of

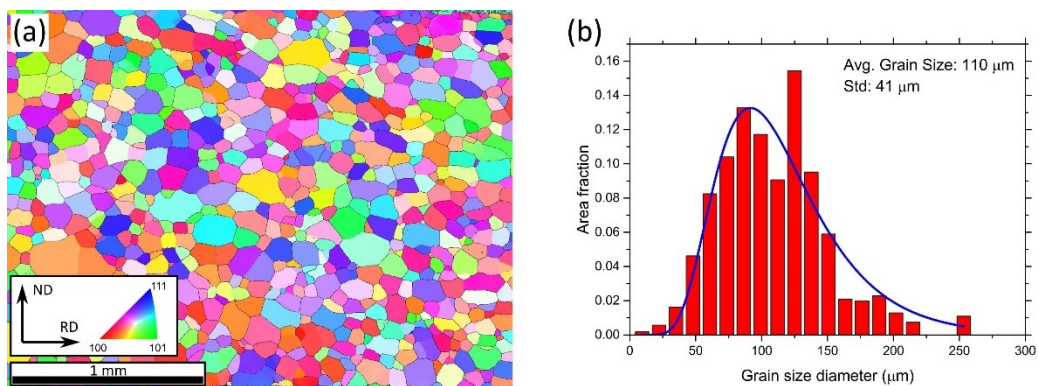


**Figure 7.2** (a) the microstructure across the thickness and (b) the grain-size diameter distribution of a warm asymmetrically rolled and annealed sample.



recrystallization nucleation sites in sub-surface regions could be higher and progress of recrystallization in these regions will be faster than those in the mid thickness region. Therefore, grain impingement will occur earlier and the recrystallized grains in the sub-surface regions will have smaller size than the ones in the mid-thickness region (cf. Figure 7.2a). For asymmetrically rolled sample, because no difference in deformation microstructures of the sub-surface and the mid-thickness regions is observed, evolution of recrystallization is expected to be homogeneous across the sample thickness.

After the annealing, weak recrystallization textures are present in both conventionally and asymmetrically warm rolled samples. In Figure 7.3, the highest intensity peak of the recrystallization texture in a conventionally rolled and annealed sample is observed near the  $\{001\}\langle 110 \rangle$  orientation with the intensity of 2.8 mrd. Texture components of the  $\alpha$ -fiber from the  $\{001\}\langle 110 \rangle$  to the  $\{114\}\langle 110 \rangle$  orientations are present in this ODF with the intensities of 2.0 mrd. A locally intensity peak of 1.7 mrd is also measured near the  $\{332\}\langle 113 \rangle$  orientation in the same ODF section. This annealing texture is quite similar to the one of symmetric hot rolling (cf. Figure 6.2). Nevertheless, orientations of the  $\gamma$ -fiber texture which were observed in the deformation texture are not present in this recrystallization texture. The absence of the  $\gamma$ -fiber texture components in the recrystallization texture suggests these are not preferred orientations during the recrystallization annealing.

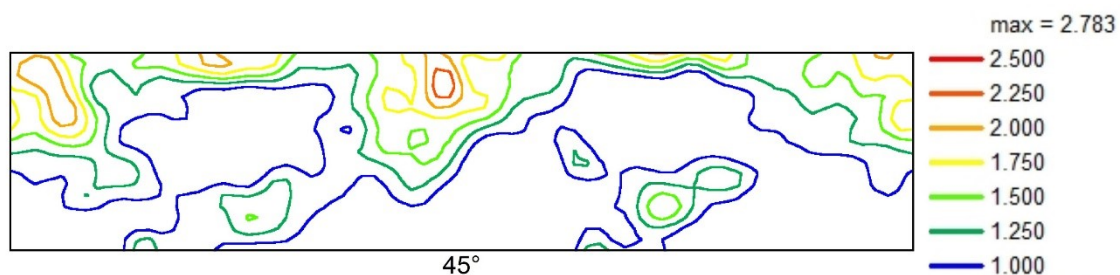


**Figure 7.3** The  $\varphi_2 = 45^\circ$  ODF section of a warm conventionally rolled and annealed sample.

Figure 7.4 shows the  $\varphi_2 = 45^\circ$  ODF section of the asymmetrically warm rolled and annealed sample. Such a type of recrystallization texture has never been captured before. Additionally, formation of the recrystallization texture components are completely unknown. Therefore, deformation texture and persistent features of

asymmetric rolling, which have been analyzed in Chapter 6, will be referred to during analysis of this recrystallization texture. The highest intensity peak in the ODF of asymmetrically warm rolled and annealed sample is found near the A7-(270.00°, 8.99°, 45.00°) orientation with the texture intensity of 2.9 mrd. The A6-(233.46°, 12.79°, 35.00°) orientation, which was not observed in the deformation texture because of its high instability in the asymmetric rolling, is present in the recrystallization texture with the texture intensity of 2.4 mrd. The A5-(208.68°, 53.71°, 47.25°) component in the asymmetric rolling texture is still visible in this recrystallization texture as a local high intensity peak of 1.7 mrd. In the same recrystallization texture, intensity of the A3-(90.00°, 56.83°, 45.00°) texture component is measured as 1.7 mrd. All other persistent orientations of the asymmetric rolling, irrespective to their stabilities, are not observed in the recrystallization texture.

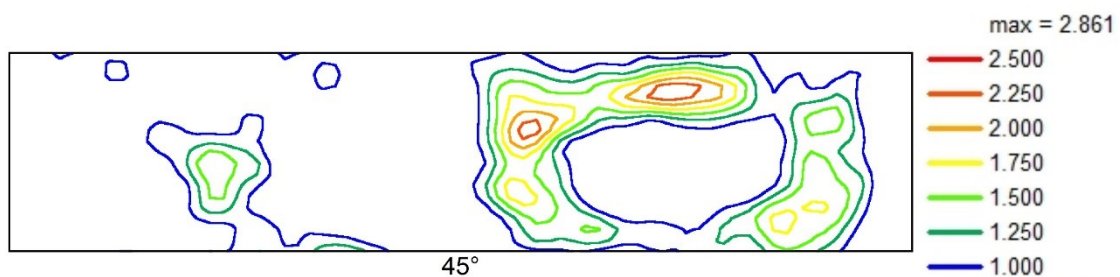


**Figure 7.4** The  $\phi_2 = 45^\circ$  ODF section of a warm asymmetrically rolled and annealed sample.

Formations of recrystallization texture components, particularly in the asymmetrically rolled and annealed sample, are not fully understood. Orientations of the  $\alpha$ -fiber and the  $\{332\}\langle 113 \rangle$  orientations, which are high intensity texture components in the conventional rolling texture, are still visible in corresponding recrystallization texture. The  $\gamma$ -fiber texture, which is a main part of the deformation texture after conventional rolling, is not really observed in this recrystallization texture. Similarly, the high intensity components of asymmetric rolling texture near the A3-(90.00°, 56.83°, 45.00°), the A5-(208.68°, 53.71°, 47.25°) and the A7-(270.00°, 8.99°, 45.00°) orientations are still visible in the recrystallization texture. On the contrary, other stable orientations of the asymmetric rolling texture (e.g. the A9-

( $270.00^\circ$ ,  $68.43^\circ$ ,  $45.00^\circ$ ) orientation) are absent from the recrystallization texture. The A6-( $233.46^\circ$ ,  $12.79^\circ$ ,  $35.00^\circ$ ) orientation, although being un-preferred component in asymmetric rolling texture, appears in the recrystallization texture as one of the main components. Formation of recrystallization oriented grains in warm rolled samples, although involving in their orientation stability in rolling condition, is not completely defined by their orientation densities in deformation textures. In the section 7.2, the formation of recrystallization texture components will be further analyzed from the view of plastically stored energy in crystals after the warm rolling.

### 7.1.2 Annealing textures after cold rolling and annealing

All different groups of cold rolled samples are subjected to a similar recrystallization heat treatment. The annealing schedule includes a fast heating of samples to  $900^\circ\text{C}$ , holding at this temperature during 70 seconds and finally slow cooling to room temperature in furnace. During the annealing, samples are protected from high temperature oxidation by pure hydrogen gas.

The recrystallization microstructures of symmetrically and asymmetrically rolled samples are given in Figure 7.6 and Figure 7.5. Both of these microstructures are composed by equiaxial grains, distributed homogeneously across the sample thickness. Grains in these microstructures are distinguished by sharp orientation regions, enclosed by high angle boundaries. A large number of grains in the recrystallization microstructures have orientations near  $\langle 111 \rangle // \text{ND}$  and

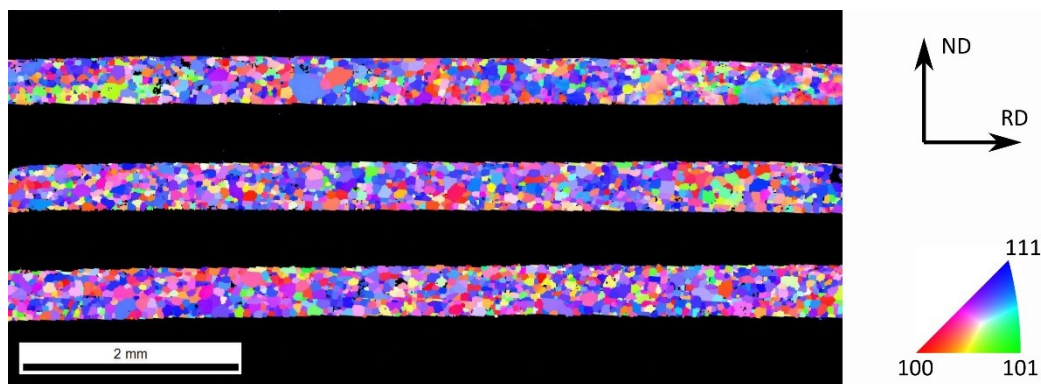


**Figure 7.5** Microstructures of the Fe-1.2 wt.% Si after conventional cold rolling and annealing, measured on the RD-ND section.

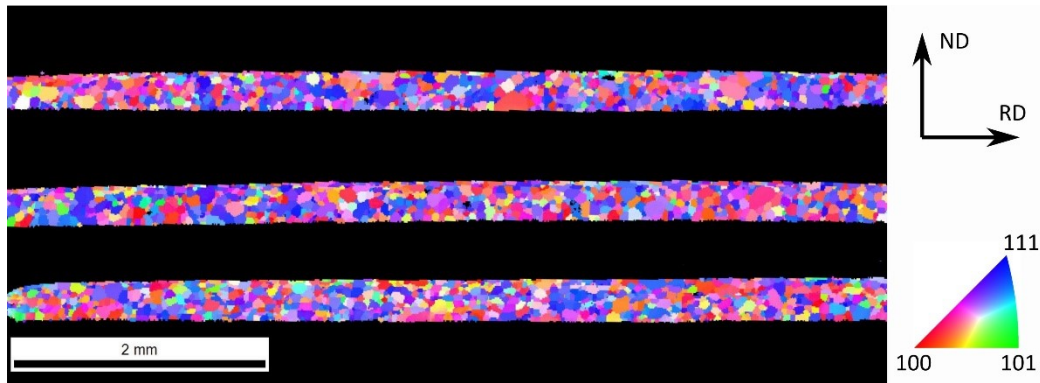


**Figure 7.6** Microstructures of the Fe-1.2 wt.% Si after asymmetric cold rolling and annealing, measured on the RD-ND section.

$\langle 001 \rangle // \text{ND}$ , while some grains of the  $\langle 011 \rangle // \text{ND}$  orientation are also observed in the same microstructures.

Because of the large grain-size in the recrystallization microstructures, wide field EBSD measurements were carried to obtain statistically representative orientation data for texture calculations. Specifically, crystallographic orientations from each annealed samples were collected in an area of  $6,350 \times 2,550 \mu\text{m}^2$  of the RD-TD plane. Recrystallization textures of different samples are similar, and thus only two ODFs of symmetric and asymmetric cold rolled samples are shown in Figure 7.8. These recrystallization textures are both composed by the  $\{111\}\langle 112 \rangle$  orientation and a fiber texture which is parallel to the  $\alpha$ -fiber of the conventional rolling texture.

In the recrystallization textures, the  $\{111\}\langle 112 \rangle$  component has the highest texture intensity. The intensity of this orientation in the recrystallization texture of the conventionally rolled sample is 7.3 mrd, whereas in the asymmetric rolled sample, the intensity of the same component is 8.2 mrd. The  $\{111\}\langle 112 \rangle$  orientation is well-known as one of the most preferential components in recrystallization textures of BCC structured materials after the conventional cold rolling. The formation of this texture component is accounted for by the nucleation and growth of crystal orientations in fragmented bands of the  $\langle 111 \rangle // \text{ND}$  orientations.

The second part in recrystallization textures of cold rolled samples is the fiber texture, which is apparently parallel to the  $\alpha$ -fiber of the conventional rolling texture. In the  $\varphi_2 = 45^\circ$  ODF section, this fiber, denominated here as the shifted  $\alpha$ -fiber, is

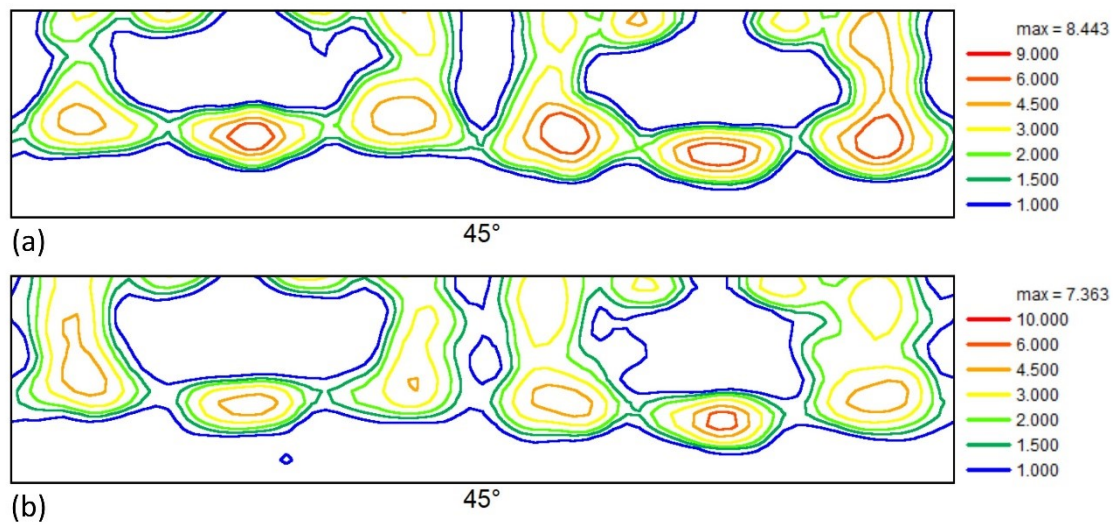


**Figure 7.8** Recrystallization textures of (a) symmetrically and (b) asymmetrically cold rolled samples after conventional warm rolling.

observed from  $23^\circ < \varphi_1 < 30^\circ$  with  $\Phi$  ranging from  $0^\circ$  to  $54.7^\circ$ . The skeleton line of this fiber is commonly observed on  $\{h h 1\} < 2 1 h \rangle$  orientations, with the  $h$ -value ranging from 0 to 1. Between this shifted  $\alpha$ -fiber and the conventional  $\alpha$ -fiber, there are common features. For each orientations in the  $\alpha$ -fiber, there is an equivalent one on the shifted  $\alpha$ -fiber, and the more interesting feature is they share the same crystallographic plane which is normal to the ND. For instance, the  $\{001\} < 110 \rangle$  orientation of the  $\alpha$ -fiber and the  $\{001\} < 210 \rangle$  orientation of the shifted  $\alpha$ -fiber share the  $\{001\}$  plane which is perpendicular to the ND. Between the  $\{113\} < 110 \rangle$

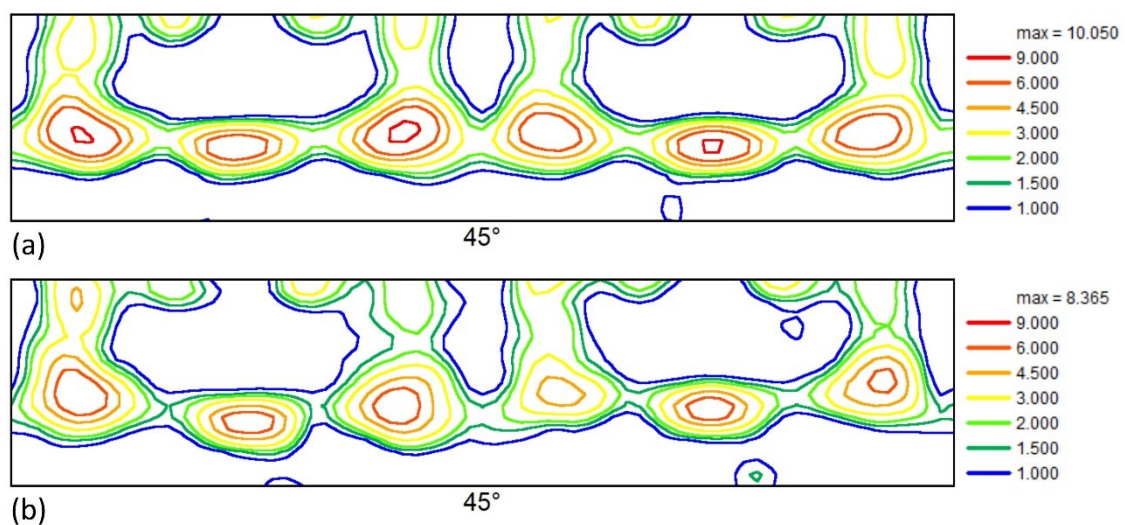


**Figure 7.7** Recrystallization textures of (a) symmetrically and (b) asymmetrically cold rolled samples after conventional warm rolling.

orientation of the  $\alpha$ -fiber and the  $\{113\}\langle 631 \rangle$  orientation of the shifted  $\alpha$ -fiber, there is a common  $\{113\}$  crystallographic plane. However, orientations along the shifted  $\alpha$ -fiber do not have any common axis, as compared to the ones of the  $\alpha$ -fiber. From the  $\{001\}\langle 210 \rangle$  orientation to the  $\{111\}\langle 211 \rangle$  orientation, there is an orientation of  $22.5^\circ$  to  $30.0^\circ$  shifted from the corresponding orientations on the shifted  $\alpha$ -fiber. The shifted  $\alpha$ -fiber, in fact, is not parallel to the ideal  $\alpha$ -fiber of the conventional rolling texture. The formation origin of the shifted  $\alpha$ -fiber in the recrystallization texture is not well understood. Nevertheless, the common features between this fiber and the  $\alpha$ -fiber of the conventional rolling texture reveal an intricate relation between them. The formation of the shifted  $\alpha$ -fiber during recrystallization is probably correlated to the presence of ideal  $\alpha$ -fiber orientations. In Chapter 8, the origin of the shifted  $\alpha$ -fiber in the recrystallization texture will be investigated by simulations, considering local micromechanics in the  $\alpha$ -fiber texture components upon cold rolling.

## *7.2 Simulations of recrystallization textures*

### *7.2.1 The stored energy of deformed crystals*

During plastic deformation, dislocations are generated and accumulated in deformed crystals. The presence of dislocations in crystals creates stress fields around these lattice defects and thus rises the internal energy of the crystals. The amount of energy, accumulated in crystals during plastic deformation, is called the plastically stored energy.

The plastically stored energy, as compared to the total amount of energy spent to deform a crystal, is very small. According to Humphreys and Hatherly [2], this stored energy is only about 5 to 10 % of the total amount of mechanical work applied to deform a crystal. The major part of the mechanical work is dissipated as heat. Additionally, the plastically stored energy is negligible to the amount of energy released during phase transformation. For deformed crystals of common metals and alloys, the stored energy is in the range of 20-200 J/mol, whereas the energy change during the ferrite to austenite transformation of iron alloys is typically of 900-1,000 J/mol.

In spite of its small value, the plastically stored energy has an important role on the recovery and recrystallization of deformed crystals because it is the driving force for these thermal activation processes in deformed materials. Depending on the amount of energy stored in each grain during plastic deformation, oriented crystals should have high or low stability during thermal treatments. During annealing, the stored energy in the deformed crystals is first released by rearrangement and annihilation of dislocations. Crystals that have the higher stored energy are more energetically unstable and the driving energy for these crystals to regain lattice defect free state will be larger. This recrystallization mechanism is called the high stored energy driven process. Recrystallization of the high stored energy crystals is commonly observed in BCC structured materials after cold deformation. A typical example for this recrystallization mechanism is the development of the  $\gamma$ -fiber texture in low carbon steel after cold rolling and annealing. Opposing to the recrystallization of high stored energy crystals, development of the low stored energy grains during annealing are also reported. The low stored energy recrystallization mechanism frequently occurs in FCC structured materials (e.g. Al alloys) after cold deformation and in BCC structured materials after warm deformation. Recrystallization of low stored energy crystals will be further analyzed later, since it involves in formation of recrystallization textures after warm rolling. Nevertheless, it is worth to mention that irrespective to the high or low stored energy mechanism, recrystallization always evolves to reduce the total energy of a microstructure system. Differences between the high and the low stored energy mechanisms are due to energy states of various dislocation structures in deformed crystals.

In a deformed microstructure, the plastically stored energy is different from grain to grain, whereby this variation of stored energy is accounted for by two observations. Firstly, the accommodation to the deformation boundary condition is different from crystal to crystal. Secondly, during deformation, all grains in the microstructure rotate toward higher stability orientations. Depending on the initial orientation and the deformation mode, the number of active slip systems and the slip activities for each slip systems in the deformed crystals are different, and thus the dislocation structures in deformed crystals are not similar.

If all deformed crystals store the same amount of energy, there will be no orientation preference in the nucleation stage and the recrystallization texture is mostly dependent on the grain boundary mobility. The grain boundary mobility in the case of uniform stored energy among all deformed crystals is not driven by plastically stored energy but by energy of boundary structure and their interfacial areas. The energy differences among various boundary structures and interfacial areas, in general, are much smaller than the absolute value of the plastically stored energy in crystals. Moreover, grain boundary migrations to minimize energy of boundary structures and interfacial areas are not considered as primary recrystallization but grain growth. Formation of recrystallization texture could not be accounted for by grain boundary migrations among crystals of the same stored energy level. Different stored energy in various oriented crystals, therefore, is a necessary argument for the evolution of recrystallization textures.

Although its importance on recovery and recrystallization have been recognized since long, precise values of the plastically stored energy in each deformed crystals remain difficult to be captured by experiments and simulations. Soon after the first crystal plasticity models appeared, G.I. Taylor and his co-workers have concentrated on studying the energy storage and releasing in cold worked metals [3]. For various metals, they observed about 5-10 % of the mechanical energy first absorbing during deformation and then releasing during heating in the cold work samples. However, because of technical limitations for instruments, this amount of energy was determined for the whole sample of the polycrystalline aggregate, but not for each individual oriented crystals in a microstructure. Recently, thanks to developments of electron microscopy methods, materials characterization can be carried out at the sub-grain scale with very high precision. Dislocation density has been measured for several thousand of crystals in deformed samples of pure Copper by high resolution EBSD technique [4]. The average dislocation density is observed to increase with the level of plastic strain. Higher dislocation density is measured near grain boundaries rather than at grain interior. Nevertheless, as the method is based on the cross-correlation of EBSD patterns, only the excessive part of the total dislocation density, namely the geometrically necessary dislocation (GND) density is measured. The



density of dislocations which are mutually trapped as dipoles and multipoles in crystals, known as the statistically stored dislocations (SSD), has not been captured.

In the course of time, many efforts to evaluate the plastically stored energy in deformed crystals by crystal plasticity simulations have been carried out. Most recently, Anand et al propose a theory of strain gradient single crystal plasticity to investigate the dislocation accumulation during plastic deformation, as well as the reduction of dislocation density upon subsequent thermal annealing [5]. This theory is developed on the principles of micro force and energy balance, in which effects of both glide and geometrically necessary dislocations are taken into consideration. This theory is able to predict the fraction of mechanical work expended to heat during deformation and the total amount of stored energy from both statistically stored and geometrically necessary dislocation densities. As micro-mechanical and thermal phenomena are coupled in this theory, it leads to a complicated mathematical description. The numerical formulation of the theory, therefore, is not popular and difficult to implement.

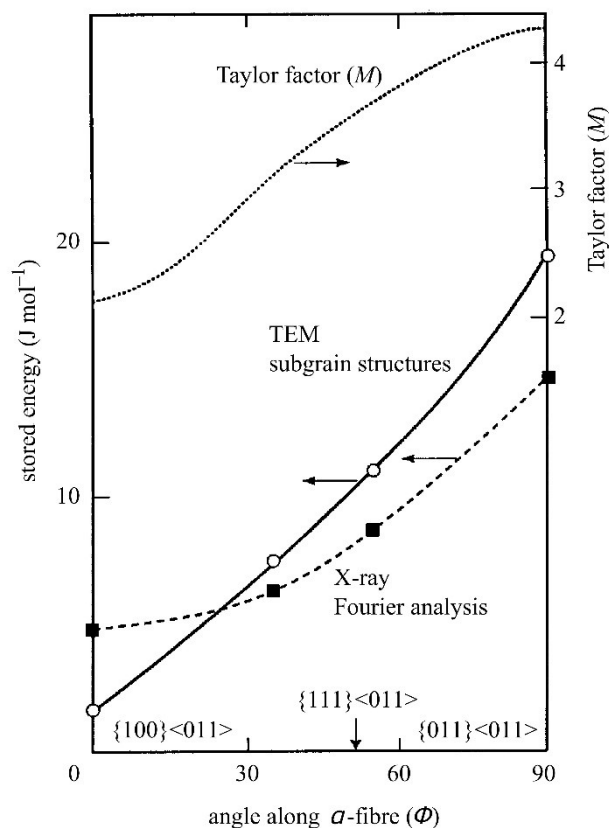


**Figure 7.9** The variation of stored energy, calculated from TEM and X-ray diffraction result, and the Taylor factor on several orientations along the  $\alpha$ -fiber of cold rolled iron and steel [6].

Conventionally, the stored energy in deformed crystals is represented by the Taylor factor of crystal plasticity models. The correlation between the Taylor factor and the plastically stored energy in deformed crystals is not fully proved. The Taylor factor of crystal plasticity theory is a scaled parameter for plastic energy dissipation to dislocation slips in a deformed crystals. In fact, it does not measure the plastic

stored energy in deformed crystals. Nevertheless, the Taylor factor links to the plastic stored energy when the total dislocation density in a deformed crystal is assumed to be proportional to slip distances of activated dislocation systems. For crystallographic orientations of typical deformation modes, the correlation between the Taylor factor and the plastically stored energy is regularly reported. For instance, Figure 7.9 shows the proportionality of the Taylor factor and the stored energy in various orientations along the  $\alpha$ -fiber texture of cold rolled iron and steel [6]. In this work, Hutchinson compared the Taylor factor and the stored energy, calculated by TEM and X-ray diffraction results. Although the analytical formulation between the Taylor factor and the stored energy could not be derived, the strong correspondence between these two parameters is clearly observed.

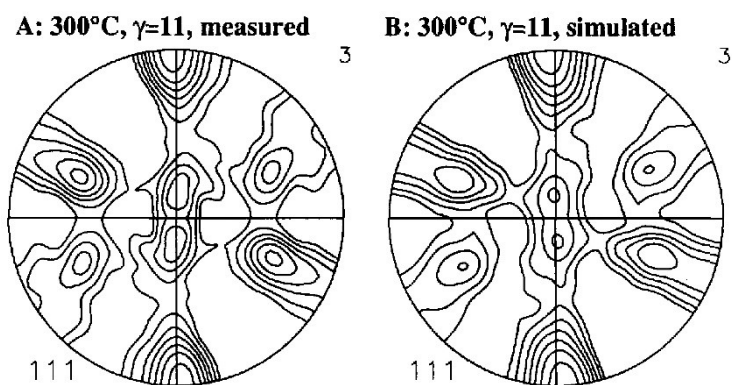


**Figure 7.10** Measured and simulated textures in Copper bars after torsion deformation at 300°C [7].

The correlation between the Taylor factor and the plastically stored energy is also validated by using this factor in calculation models to predict recrystallization textures. Toth and Jonas [7] used the Taylor factor to simulate the texture

development during the hot torsion of copper bars. Texture evolution in this study is rather complicated, because of the high shear strain and dynamic recrystallization. However, all features of the measured texture are well predicted by the simulated one (Figure 7.10). Remarkably, the fit between simulated and measured textures is only achieved when the Taylor factor is considered as the criteria for oriented nucleation during dynamic recrystallization.

In 1996 and 1997, Kestens et al applied the Taylor factor as a nucleation criteria in simulation of static recrystallization textures [1;8;9]. For both low and high stored energy nucleation mechanisms, the authors obtained well fitted recrystallization textures. More recently, Sidor et al [10] used the Taylor factor, calculated for various

deformation modes, to simulate the evolution of recrystallization textures in particle included aluminum alloys. Although the deformation around these particles is non-homogeneous and difficult to quantify, authors successfully predicted the orientation preference during particle stimulated nucleation (PSN).

The Taylor factor of crystal plasticity, by its definition, is a dimensionless parameter quantifying the instantaneous dissipation of energy to activate slip in a unit crystal volume, under the basic assumption of the Taylor theory:

$$M = \frac{\sum_s \tau_s^c |\dot{\gamma}_s|}{\tau^c \dot{\epsilon}_{vM}} \quad (7.1)$$

in which  $\tau_s^c$  and  $\dot{\gamma}_s$  are the critical resolved shear stress and the slip rate the active dislocation system  $s$ ,  $\tau^c$  is a scaling parameter of the macroscopic stress and involving the macroscopic work hardening,  $\dot{\epsilon}_{vM}$  is the von Mises equivalent strain rate. In the equation 7.1, the numerator is representing the dissipated energy on the microscopic crystal scale, while the denominator represents the macroscopic plastic work applied to the crystal. For plastic deformation in which the critical resolved shear stresses of all slip systems are nearly identical, the Taylor factor is linearly proportional to the total slip rates. By accumulating the total slip rates during deformation, the total dislocation density and thus the stored energy are able to be estimated. In addition, if the same amount of plastic energy is applied to different crystals, the Taylor factor measures the stored energy in deformed crystals of various orientations for a certain deformation mode. Obviously, this derivation of the stored energy from the Taylor factor is rather simple. The stored energy of deformed crystals, in principle, is a function of the strain history and the specific activities of slip systems. Configuration of dislocation structure in deformed crystals is not considered in the Taylor factor. This full description of plastically stored energy is beyond the scope of this study as it necessitates a fully-fledged work hardening model based on dislocation dynamics. In this study, the Taylor factor is assumed to linearly scale with the stored energy and it will be used to account for the formation of recrystallization texture by oriented nucleation.

### 7.2.2 Recrystallization textures of rough rolled samples

Assuming the correlation between the Taylor factor and the plastically stored energy, the distribution of the stored energy among crystals of various orientations for the same deformation mode can be observed from the change of the Taylor factor in the orientation space. For the PSC of conventional rolling, the Taylor factor map of BCC structured materials has been calculated by the full constraint Taylor model, c.f. Figure 7.11.

This Taylor factor map is rather familiar, since it has been used for a long time to represent the stored energy in of BCC crystals after the conventional rolling. Only minor features of Figure 7.11 are different from Taylor factor maps reported in the literature [1;11]: (i) the range of the  $\varphi_1$  Euler angle is different from the more conventional  $0^\circ$ - $90^\circ$  range and (ii) the scale of the Taylor factor varies between 1.8 and 3.7 instead of the usual range between 2.0 and 4.2. The Taylor factor map for conventional rolling is usually given in the range of  $0^\circ$  to  $90^\circ$  of the  $\varphi_1$  Euler angle. That is due to the reduction of the Euler space by the orthorhombic sample symmetry. In this study, to emphasis on the difference of the Taylor factor maps for symmetric and asymmetric rolling, the range of the  $\varphi_1$  Euler angle in the Taylor factor map is set from  $0^\circ$  to  $360^\circ$ . Nevertheless, the orthorhombic sample symmetry of the conventional rolling is still visible in Figure 7.11. The Taylor factor map of the asymmetric rolling, cf. infra, will exhibit the monoclinic sample symmetry.

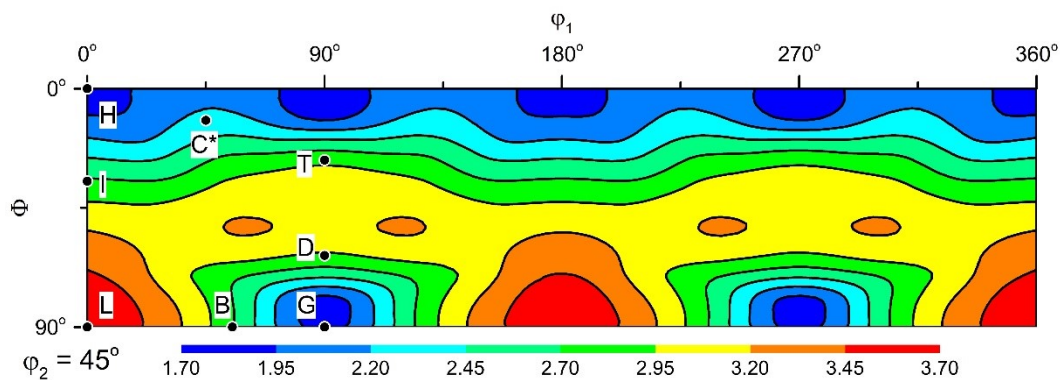


**Figure 7.11 The Taylor factor map in the  $\varphi_2 = 45^\circ$  Euler section of BCC structured materials in plane strain compression, calculated by the full constraint Taylor model.**

The Taylor factor map in Figure 7.11 is calculated for an unit of equivalent strain rate ( $\dot{\epsilon}_{vM} = 1$ ) but not for a unit of the strain rate tensor components ( $\dot{\epsilon}_{11} = -\dot{\epsilon}_{33} = 1$ ). Therefore, the Taylor factors in this study are a factor 1.15 times smaller than the ones conventionally reported in the literature [1;11]. Since oriented nucleation is accounted for by differences of the stored energy among various crystallographic orientations, absolute values of the Taylor factor are less important than the ratio between the Taylor factors. In addition, by using the same equivalent strain rate, Taylor factors of any orientation in various deformation modes can be directly compared. Therefore, in this study, the Taylor factor calculated for unit equivalent strain rate is more convenient than the one calculated for the unit strain rate tensor components.

In the Taylor factor map of conventional rolling (Figure 7.11), the highest Taylor factor is calculated for the  $\{110\}\langle 110 \rangle$  orientation. This highest Taylor factor value of 3.7 indicates that the  $\{110\}\langle 110 \rangle$  oriented crystals are the least well oriented to accommodate PSC. The stored energy in these crystals, therefore, is expected to be the highest among all orientations of the BCC structured materials after conventional rolling. Accordingly, the  $\{110\}\langle 110 \rangle$  oriented crystals have the least chances to develop as recrystallization grains by the law of low stored energy nucleation. On the contrary, crystals of the  $\{110\}\langle 001 \rangle$  and  $\{001\}\langle 110 \rangle$  orientations have the smallest Taylor factor of 1.8. All orientations of the Cube fiber texture have the Taylor factor smaller than 2.2, which is among the 20% lowest Taylor factor of all possible orientations in the BCC structured material under the PSC. The Cube fiber and the  $\{110\}\langle 001 \rangle$  orientation therefore are the most preferred ones for recrystallization grains according to the low stored energy nucleation mechanism.

The prediction of recrystallization texture in BCC structured materials after the conventional rolling would select Cube fiber and Goss orientations for nucleation, based on a low-stored energy criterion. Nevertheless, recrystallization textures dominated by the Cube fiber and the Goss orientation are not frequently observed in BCC structured materials after conventional rolling and annealing. In fact, cold rolling and annealing textures of BCC structured materials are mostly composed by the  $\alpha$ - and the  $\gamma$ -fiber texture components. Orientations of the  $\alpha$ - and the  $\gamma$ -fibers are among

the most stable orientations under the PSC of conventional rolling. The stored energy in oriented crystals of these fibers is relatively high, particularly for grains of the  $\gamma$ -fiber orientations. Energetically, nucleation of the  $\alpha$ - and the  $\gamma$ -fiber oriented crystals is more favored than that of the Cube-fiber and the Goss oriented crystals. The high stored energy mechanism of recrystallization actually occurs in materials which are deformed at low temperatures (see section 7.2.4).

Deformation temperature, therefore, should be a key factor to define different recrystallization texture evolutions in cold rolled and warm rolled samples. Temperature, in fact, could affect the stored energy of plastically deformed crystals. At low temperatures, the larger amount of plastic energy is dissipated to dislocation slips, the higher density of dislocation is accumulated in deformed crystals and the faster recrystallization kinetics of oriented crystals. On the contrary, at high temperatures, activation and interaction of dislocations are not just driven by mechanical plastic work but more importantly by thermal energy. Density and structure of dislocations in the same crystal but deformed at high temperature will be much different from the ones at low temperature. The density of dislocation in the crystal is lower as it is deformed at higher temperature, and the arrangement of dislocations is more homogeneous.

Smooth changes of crystallographic orientations are indeed observed in grains of the  $\alpha$ -fiber orientations, particularly of the rotated Cube orientation, after cold rolling. On the contrary, fragmentation into tiny but sharply oriented crystals usually occurs to grains of the  $\gamma$ -fiber orientations, for instance of the  $\{111\}\langle 112 \rangle$  orientation after cold rolling. Grain fragmentation assists to the development of high angle grain boundaries which can fast migrate toward deformation matrix to form a recrystallized grain. Nevertheless, grain fragmentation is not a general microstructure evolution during warm deformations.

Homogeneous changes of crystallographic orientations in grains of both the  $\alpha$ - and the  $\gamma$ -fiber texture are more frequently observed in warm rolled samples. During crystal plasticity at high temperatures, accumulation of dislocations are presence near grain boundaries rather grain interiors. During annealing, migration of pre-exist grain

boundaries toward neighbor deformed grains should be faster than re-arrangement of dislocation structures and formation of new high angle grain boundaries inside the grains. Growth potential of each oriented crystals is dependent on its high angle misorientation to all available crystals in the deformation matrix. The plastically stored energy in deformed crystals have higher impacts to the formation of recrystallization texture than the grain boundary migration. Different recrystallization texture evolutions in the same material but plastically deformed at various temperatures are partially accounted for by above arguments. Nevertheless, dislocation structures in crystals deformed at room and high temperatures have not yet completely measured and analyzed. Recrystallization mechanism of the lower Taylor factor crystals during annealing after warm deformation has not yet exhaustively explained.

Orientation selection of the high and the low stored energy crystals for recrystallization texture simulation is still an open question and it is far beyond the scope of this study. In this chapter, it has been assumed that the high and low stored energy recrystallization mechanisms are both existence. The preference of one mechanism to the other is dependent on deformation temperatures. Orientation selection according to these rules in the simplest cases is just picking or removing crystallographic orientations from the deformation ODF based on their Taylor factor values. Critical value for this selection is not sharply defined, but it could be understood as an energy criteria for recrystallization nucleation. This critical value, therefore, is tuned to match the simulated texture to the experimental one. The growth potential of recrystallization nucleus is considered to be equal. Because of the abundance of high angle grain boundaries, all oriented nucleus are allowed to develop as recrystallized grains. Recrystallization texture, as a result, is identical to the nucleation one.

To illustrate for the low stored energy nucleation on recrystallization texture, simulations have been carried out with the Kestens-Jonas model. Oriented nucleation accounts for the difference in probabilities to nucleate individual crystal orientations, which in turn depend on the Taylor factor of the orientations. Assuming the co-

existence of the high and the low stored energy mechanisms, the nucleation probability is calculated by a logistic function:

$$P_N(g) = 1/(1 + \exp\left(k \cdot \frac{M(g) - M_0}{M_{\max} - M_{\min}}\right)) \quad (7.2)$$

in which  $M(g)$ ,  $M_{\max}$ ,  $M_{\min}$  are the current, the maximum and the minimum Taylor factor for oriented crystals in a certain deformation mode.  $M_0$  is the critical Taylor factor, at which the nucleation probability is equal to 0.5. The  $k$  parameter is a factor controlling the sharpness of nucleation selection. The larger the  $|k|$  value, the stronger the effects of nucleation mechanisms. Values of the  $k$ -parameter, theoretically, are in the range from  $-\infty$  to  $+\infty$ , but in reality the  $k$ -values of 500 to 1000 are enough to form a step probability function for nucleation. For  $k > 0$ , the low stored energy nucleation mechanism is dominant, whereas the high stored energy nucleation mechanism is accounted for by  $k < 0$ . At  $k = 0$ , all orientations, irrespective of the stored energy, have the same nucleation probability, and the nucleation mechanism of recrystallization is completely random. Figure 7.12 illustrates the dependence of nucleation probability on various nucleation mechanism steepness ( $k$ ) combined with the fixed critical Taylor factor ( $M_0 = 0.5 (M_{\max} + M_{\min})$ ).

As the first case in this study, the texture evolution after rough rolling and annealing of the Fe – 1.2 wt.% Si alloy is simulated. The rough rolled samples were

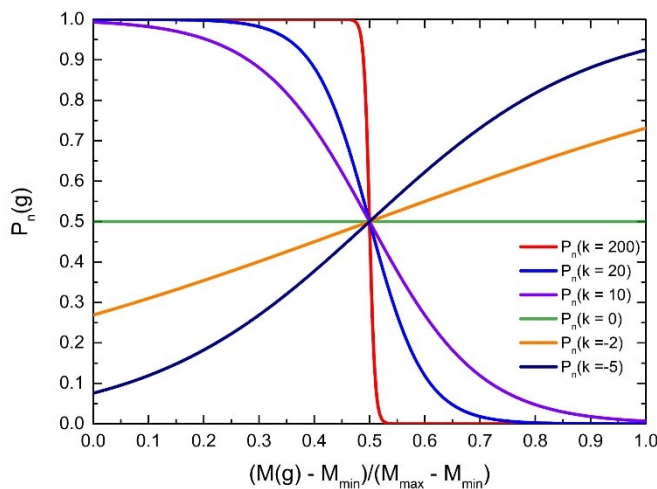


**Figure 7.12** Dependence of recrystallization nucleation probability on the Taylor factor value of oriented crystals for various combination of the critical Taylor factor ( $M_0$ ) and the nucleation mechanism steepness ( $k$ ), in which  $M_0 = (M_{\max} + M_{\min})/2$ ,  $k > 0$  is the low stored energy nucleation;  $k = 0$  is the random nucleation and  $k < 0$  is the high stored energy nucleation.



obtained after the conventional rolling at high temperature with the thickness reduction of 15-50% per pass. Samples were reheated to initial rolling temperature between rolling passes. The deformation texture for the rough rolled samples was not captured experimentally, but it can be assumed to be random or weakly textured composed of the  $\alpha$ - and the  $\gamma$ -fiber. Specifically, both random texture and rolling texture of 20% thickness reduction, c.f. Figure 7.13a and Figure 7.13b, are discretized into 10,000 individual orientations and used as initial textures for recrystallization simulations. The probability of individual orientations to develop as recrystallization grains was evaluated by oriented nucleation. The oriented nucleation is set by a strong dominance of the low stored energy nucleation ( $k=200$ ) with the critical Taylor factor ( $M_0$ ) of 2.2. The probability for nucleation of crystals with the 20% lowest stored energy in the total energy range of deformed crystals is equal to one, while for all the rest it is set to zero.

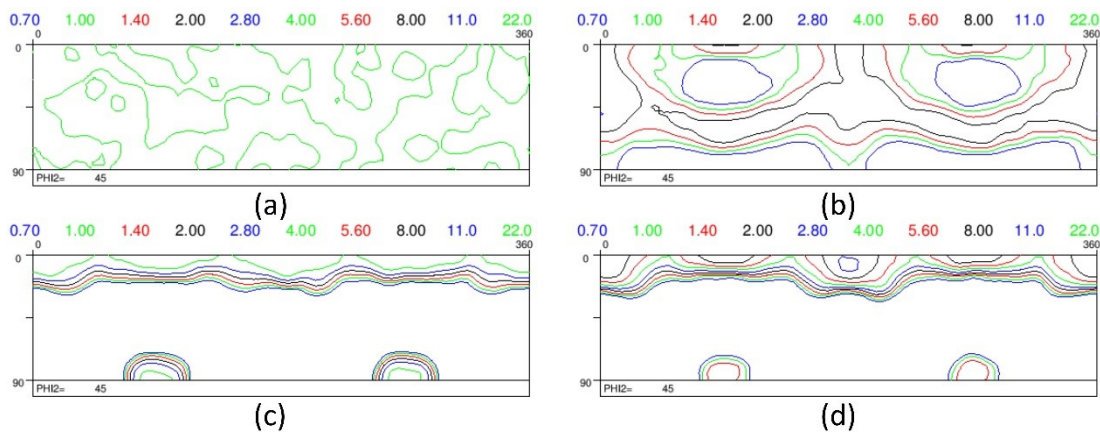


**Figure 7.13 Initial (a and b) and simulated recrystallization textures (c and d) in the rough rolled and annealed sample predicted by the Kestens-Jonas model with the low stored energy nucleation.**

The simulated recrystallization textures for different initial rough rolling textures are given in Figure 7.13c and Figure 7.13d. These simulated textures are quite similar to the measured counterpart shown in Figure 5.3b. High texture intensities in the simulated textures are observed near the Cube fiber and the Goss orientation. The rotated Cube ( $\{001\}\langle 110\rangle$ ) orientation is the most preferred orientation in both the simulated textures with intensities 5.0 and 10.0 rmd, respectively, for the random and  $\alpha/\gamma$  fiber initial textures. The difference in intensities of the rotated Cube orientation

between simulated textures is related to the presence of this orientation in the initial textures. In the  $\alpha/\gamma$  fiber deformation texture (Figure 7.13b) the intensity of the rotated Cube orientation is 2.0 times higher than in the random texture (Figure 7.13a). In addition, there is no significant fraction of the Goss orientation in the deformation texture, while in the random texture this orientation has the same fraction as the rotated Cube orientation. This difference in the initial volume fraction is also the reason for the variation of the Goss orientation in the recrystallization textures. In the simulated recrystallization texture of  $\alpha$ - and  $\gamma$ -fiber textured rolled material, the ratio between the rotated Cube and the Goss orientations is 5.0, while of the random oriented sample is 1.0. In the measured texture, intensity ratio between these two orientations is 3.0.

### 7.2.3 Recrystallization textures of warm rolled samples

#### **Recrystallization textures of symmetrically warm rolled samples**

Before the hot band annealing, half of the samples were conventionally rolled. Deformation texture of these samples haven been measured and the results are shown in Figure 6.2. As for the previous recrystallization simulation, the measured texture was discretized in 10,000 individual orientations and used as initial rolling texture for simulation of the recrystallization texture. The stored energy distribution on the crystallographic orientation space of these samples are expected to be similar to the ones after rough rolling. Therefore, the Taylor factor map of Figure 7.11 is also valid in this case.

To illustrate for the dependence of recrystallization textures on the energy criteria of nucleation, simulations of recrystallization textures have been carried on with two critical Taylor factors,  $M_0 = 2.2$  and  $M_0 = 2.7$ . These Taylor factors, in combination to the low stored energy nucleation rule ( $k = 200$ ), correspond to selecting grains having 20% and 50% of the lowest stored energy among all deformed crystallites. Recrystallization textures have been obtained and given in Figure 7.14.

The simulated recrystallization textures for conventionally hot rolled samples as shown in Figure 7.14 are not similar to each other. In the case of the more stringent

criterion  $M_0 = 2.2$ , the simulated recrystallization texture contains the Cube fiber with the maximum intensity near the rotated Cube orientation. This texture very much resembles the one of the rough rolled sample, although there is no trace of the Goss orientation in the current texture. The absence of the Goss orientation in the current texture is due to the scarcity of the same orientation in the deformed sample, although it has the same energy preference to nucleate as Cube orientations. However, the simulated texture with  $M_0 = 2.2$  is not similar to the measured texture after the hot band annealing (c.f. Figure 7.3).

On the contrary, the simulated recrystallization texture with the critical Taylor factor  $M_0 = 2.7$  is more resemble to the measured one (c.f. Figure 7.3). As observed in the Figure 7.14b, the hot band annealing texture is predicted to contain the upper part of the  $\alpha$ -fiber and a weak texture intensity near the  $\{332\}\langle 113 \rangle$  orientation.

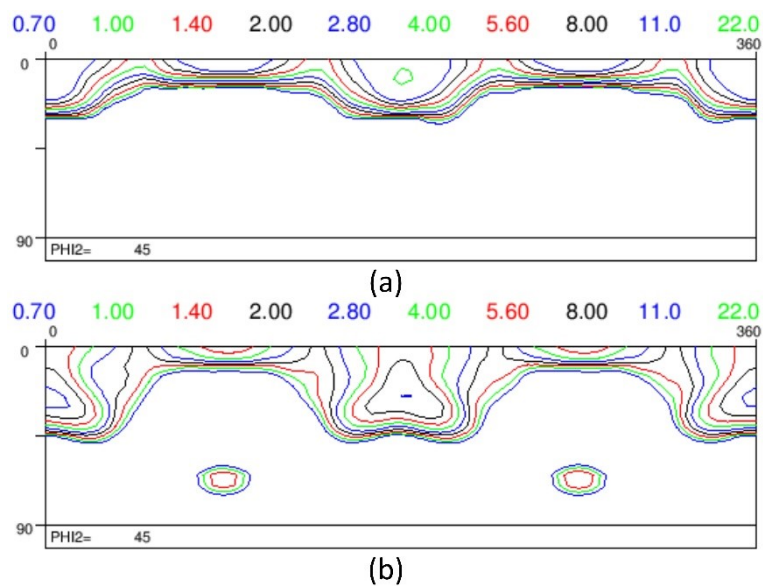


**Figure 7.14** Simulated recrystallization textures of conventionally hot rolled samples, predicted with the critical Taylor factor of (a)  $M_0 = 2.2$  and (b)  $M_0 = 2.7$ .

Both of these texture components are present in the hot band annealing texture. Nevertheless, intensities of texture components in the measured texture are about 5 times weaker than the corresponding ones in the simulated texture. These weak intensities in the measured texture suggest that in reality not only low stored energy crystals have chances to nucleate and recrystallize. High stored energy crystals, in spite of their low probability to nucleate, are also present in the recrystallization texture. From the simulation point of view, the low stored energy nucleation law is valid after hot rolled samples, but a wider range of orientation for nucleation needs to be taken into account. In the current recrystallization model, the range of nucleating

orientations can be adjusted by changing the critical Taylor factor ( $M_0$ ) and/or the steepness factor of the nucleation law ( $k$ ). Since the purpose of current simulations is to demonstrate the effect of nucleation energy criteria on the formation of recrystallization, only the critical Taylor factor ( $M_0$ ) for nucleation is changed from 2.2 to 2.7, while the nucleation steepness factor was kept constant at  $k = 200$ , which assumes a step-type nucleation probability (cf. Figure 7.11). Because of this change in the critical Taylor factor, the simulated recrystallization texture with  $M_0 = 2.7$  better corresponds to the measured texture of the hot band annealed sample. The effect of reducing nucleation steepness factor to an order of magnitude, though did not given here, is similar to the increasing of the critical Taylor factor. The co-existence of low and high stored energy nucleation mechanisms, although could be captured by tuning the nucleation steepness factor ( $k$ ), is not the main aim of this study. Without any change of the nucleation steepness, a small adjustment of the critical Taylor factor in recrystallization texture model already brings better prediction result. The correspondence between the Taylor factor and preferred orientations of recrystallization texture, in this case, is rather strong in spite of the plain meaning of the factor and its application in the calculation model as compared to the recrystallization itself.

### **Recrystallization textures of asymmetrically warm rolled samples**

For a half of the rough rolled samples, asymmetric warm rolling was applied to reduce the thickness from 10 to 2 mm. The deformation mode and the texture development in these asymmetrically rolled samples have been analyzed in Chapter 6. The deformation mode of asymmetric rolling, as reported in Section 6.3.1 by the geometric model, includes both normal and shear strain components. The shear strain during asymmetric rolling is in the rolling plane and parallel to the rolling direction (so called “13” shear) and it has the magnitude of half of the normal strain component. Since the deformation mode is different from PSC (conventional rolling), a new Taylor factor map corresponding to deformation of asymmetric rolling has been calculated by the FCT model. This Taylor factor map is represented by the  $\varphi_2 = 45^\circ$  Euler section in Figure 7.15.

Similar to the one of conventional rolling, the Taylor factor map of asymmetric rolling has the highest value at the rotated Goss ( $\{110\}\langle 110\rangle$ ) orientation. However, the rotated Cube ( $\{001\}\langle 110\rangle$ ) and the Goss ( $\{110\}\langle 001\rangle$ ) orientations are not among the lowest Taylor factor components in asymmetric rolling. In general, there is a shift of the lowest Taylor factor orientations when the deformation mode is changed from the conventional to asymmetric rolling. For the  $\varphi_1$  Euler angle from  $0^\circ$  to  $180^\circ$ , the shift towards lower  $\Phi$ -Euler angles changes the orientation of the lowest Taylor factor from the Goss orientation of the conventional rolling to the meta-stable A4- $(90.00^\circ, 72.43^\circ, 45.00^\circ)$  orientation of asymmetric rolling. In addition, the shift in opposite direction for the  $\varphi_1$  Euler angle from  $180^\circ$  to  $360^\circ$  produces low Taylor

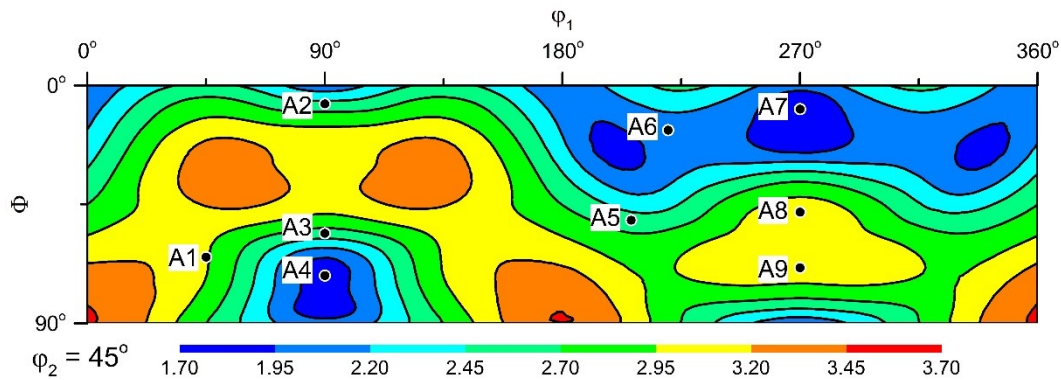


**Figure 7.15** The Taylor factor map in the  $\varphi_2 = 45^\circ$  Euler section of BCC structured materials in asymmetric rolling which includes a shear strain component on the rolling plane and along the rolling direction with the magnitude of the half of the normal strain component.

factor regions near the unstable A6- and the stable A7-orientations of the asymmetric rolling, instead of the rotated Cube orientation of conventional rolling. These shifts break the mirror symmetry in the Taylor Factor map with respect to  $\varphi_1 = 180^\circ$ , and thus the Taylor factor map of asymmetric rolling has the monoclinic sample symmetry but not the orthorhombic symmetry of conventional rolling.

These differences in the Taylor factor map of asymmetric rolling, as compared to the one of conventional rolling, account for the evolution of the recrystallization textures in various rolling samples. Except for differences in deformation, samples of both symmetric and asymmetric rolling were manufactured by the same procedure. In the conventionally rolled samples, the formation of the recrystallization texture is

attributed to the nucleation of low stored energy crystals and the normal growth of these nuclei into deformed grains, which exhibit high angle boundaries with respect to the growing nuclei. By applying these rules, the recrystallization textures in asymmetrically rolled samples can be predicted from the deformation textures. The deformation texture of asymmetrically rolled samples, cf. Figure 6.6, is discretized in 10,000 individual orientations. The low stored energy nucleation is modelled with two different values of the critical Taylor factor threshold, being  $M_0 = 2.2$  and  $2.7$ , respectively. Deformed crystals which have high nucleation probabilities contribute to the formation of recrystallization textures.

The simulated recrystallization textures of asymmetrically rolled samples are given in Figure 7.16. Both of the two simulated textures are composed by weak texture components. The highest intensity components in these textures are 5.6 and 4.2 mrd. In the first recrystallization texture, calculated with the critical Taylor factor  $M_0 = 2.2$ , the high intensity texture components are present near the A4-(90.00°, 72.53°, 45.00°), the A6-(233.46°, 12.79°, 35.00°) and the A7-(270.00°, 8.99°, 45.00°) orientations of the asymmetric rolling. All of these texture components are observed in the measured texture. However, a local high intensity component near the A5-(208.68°, 53.71°, 47.25°) orientation in the measured texture did not appear in the

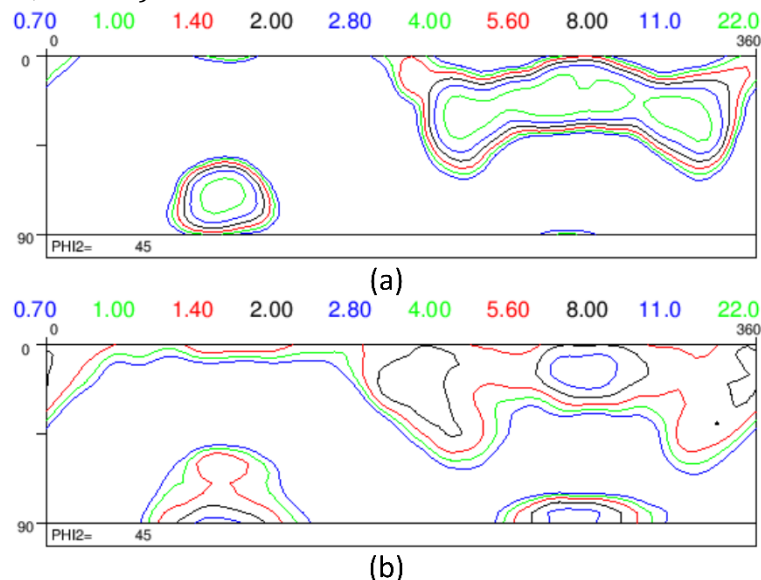


**Figure 7.16 Simulated recrystallization texture of asymmetrically hot rolled samples, predicted with the critical Taylor factor ( $M_0$ ) of (a) 2.2 and (b) 2.7.**

simulated texture. The absence of the A5-(208.68°, 53.71°, 47.25°) orientation in the simulated texture could be due to its stored energy. According to crystal plasticity calculation, the A5-(208.68°, 53.71°, 47.25°) orientation of asymmetric rolling has the Taylor factor of 2.8. In the first recrystallization simulation, the critical Taylor factor of the low stored energy nucleation is set as 2.2 and the steepness factor of the nucleation rule ( $k$ ) is 200. It implies that there is no chance for orientations having Taylor factors higher than 2.2 to nucleate. By relaxing the critical Taylor factor to 2.7 in the second recrystallization simulation, many more orientations of asymmetrically rolled samples, indeed, have chances to nucleate and grow. Local high intensity regions in the simulated texture expand to higher Taylor factor orientations and the maximum intensity of the simulated texture is reduced to 4.2.

However, by increasing the critical Taylor factor, orientations that were not observed in the measured textures, neither in the deformation nor in the recrystallization samples are present in the simulated texture. For example, the Goss orientation, which has an in-significant intensity in the deformation texture of asymmetric rolling (c.f. Figure 6.6), becomes one of the most preferred components in the simulated recrystallization texture. This orientation is predicted to have the highest intensity, equal to the A7-orientation in the simulated texture of Figure 7.16b. The presence of the Goss orientation is due to the low Taylor factor of this orientation. In the Taylor factor map of asymmetric rolling, the Goss orientation has the Taylor factor of 2.0. However, other orientations in vicinity of the Goss orientation have much higher Taylor factor values. Most of them have the Taylor factor values in the range of 2.4 to 2.8. (c.f. Figure 7.15). A small change in the critical Taylor factor, therefore, could promote or prohibit the nucleation and growth of the Goss and neighboring orientations. The presence of the Goss orientation in the simulated recrystallization texture, though was not observed in the measured texture, indicating that the critical Taylor factor of 2.7 in the second simulation was chosen too large. It also implies that by further increasing the critical Taylor factor, the A5-(208.68°, 53.71°, 47.25°) orientation could appear in the simulated texture, but the simulated texture will be dominant by the Goss orientation, which does not correspond to the experimental observation.

The misfit between simulated and measured recrystallization in asymmetrically rolled samples, therefore, cannot be solved simply by the theory of the low stored energy nucleation. Other phenomena occurring during recrystallization of asymmetrically rolled samples need to be considered as well. A relaxation of the low stored energy nucleation law by allowing some high stored energy crystals to nucleate may promote the A5-orientation while prohibit the Goss orientation in recrystallization texture. This relaxation can be implemented in the recrystallization texture model by reducing the nucleation steepness factor ( $k$ ). In addition, there may have been an effect of high migration rate boundaries between the A5-orientation and deformed matrix rather than the Goss orientation. Effects of boundary mobility on the formation of recrystallization texture can be included in the model by applying a special growth rule. Nevertheless, these extensions of the recrystallization model are beyond the main purpose to illustrate influences of the stored energy on formations of recrystallization textures. The refinements of simulated textures will not be considered in the current study. The recrystallization texture, calculated with the critical Taylor factor  $M_0 = 2.2$ , therefore is considered the best fit to the measured texture.

#### *7.2.4 Final annealing textures*

Dependences of recrystallization textures on the stored energy of deformed crystals can also be observed after annealing of the cold rolled samples, which will be analyzed by texture simulation in this section. It is intended that the fit or misfit between simulated and experimentally observed textures will contribute to an improved insight in the recrystallization mechanisms of cold rolled samples.

Samples of warm rolling and hot band annealing are subjected to both symmetric and asymmetric cold rolling before final annealing. The total thickness reduction of the cold rolling is 75%, corresponding to a thickness reduction from 2.0 mm to 0.5 mm. Although different deformation modes of symmetric and asymmetric rolling were applied to the cold rolling, the deformation textures in all samples are quite similar. This can be ascribed to the negligible amount of shear strain imposed by cold asymmetric rolling, as compared to the hot asymmetric rolling. The impact of



asymmetric rolling to recrystallization textures is even smaller than to deformation textures. As observed in Figure 7.8 and Figure 7.7, there is no difference in recrystallization textures of symmetrically and asymmetrically cold rolled samples. To simplify the analysis, only the development of recrystallization textures in symmetrically cold rolled samples is considered.

Because the deformation mode of cold symmetric rolling is plane strain compression, the Taylor factor map, which is given in Figure 7.11, can be considered as representative for the distribution of stored energy among oriented crystals. The nucleation behavior for cold rolled samples, however, is definitely not the low stored energy nucleation as was observed in the warm rolled samples. Previous experimental observations [12;13] showed that during the recrystallization in cold rolled low carbon steels, intensities of the  $\gamma$ -fiber components are enhanced, while intensities of the  $\alpha$ -fiber components are weakened. In the full recrystallized stage, there is no trace of  $\alpha$ -fiber orientations, while high intensities of the  $\gamma$ -fiber components from the  $\{111\}\langle 110 \rangle$  to the  $\{111\}\langle 112 \rangle$  orientation are observed.

This observation, indeed, suggests the preferred nucleation of medium and high Taylor factor orientations, rather than the lower ones. In the present simulations, the high stored energy nucleation is implemented by setting the steepness factor of the nucleation law  $k = -200$  and different critical Taylor factors ( $M_0$ ) of 2.49, 2.72 and 2.95. This high stored energy nucleation is combined to two different growth rules. In the first case, the normal growth rule of high angle grain boundaries is applied. This growth rule is similar to the one applied in texture simulations of warm rolled and annealed samples. All nuclei exhibiting misorientation angles to deformed crystals larger than  $15^\circ$  allowed to grow. The normal growth rule is schematically given in Figure 7.17a. In the second case, high mobility is assumed for the special boundary of  $\langle 110 \rangle 26.5^\circ$  misorientation between nucleus and deformed crystals. Among all nuclei of recrystallization, only the ones which have less than  $5^\circ$  deviation from the  $\langle 110 \rangle 26.5^\circ$  misorientation to a deformed crystal are counted as recrystallized grains. This special growth rule has been well reported in literatures [8;9;14;15] to explain for the formation of the  $\{111\}\langle 112 \rangle$  oriented crystals in cold rolled and annealed steels. According to previous studies, the enhancement of the  $\{111\}\langle 112 \rangle$  component

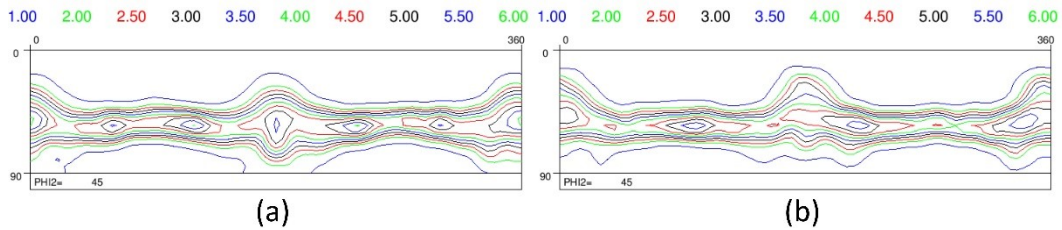


**Figure 7.17** The growth probabilities for recrystallized nuclei in a cold rolled sample with a normal growth rule of  $10^\circ$  misorientation boundaries (a) and a special growth rule of high mobility  $\langle 110 \rangle 26.5^\circ$  boundaries (b).

in recrystallization texture, instead of the  $\{111\}\langle 110 \rangle$  component, is attributed to the high mobility of the  $\langle 110 \rangle 26.5^\circ$  grain boundaries. Nucleus of  $\langle 111 \rangle // ND$  orientations, besides the energy advantage, will grow faster when the boundary between the nucleus and deformed crystals is nearer to the  $\langle 110 \rangle 26.5^\circ$  misorientation. The  $\{111\}\langle 112 \rangle$  oriented crystals have the orientation relationship near to the  $\langle 110 \rangle 26.5^\circ$  misorientation with the  $\{112\}\langle 110 \rangle$  deformed grains. The formation of the  $\{111\}\langle 112 \rangle$  orientation in recrystallization texture is further enhanced by high volume fraction of the  $\{112\}\langle 110 \rangle$  component in the deformation texture. The special growth rule of the high mobility  $\langle 110 \rangle 26.5^\circ$  boundary is represented by a growth probability as given in Figure 7.17b. To simulate recrystallization texture in cold rolled samples, the measured texture is discretized to 10,000 individual orientations and used as the input data.

Figure 7.18 shows simulated recrystallization textures of cold rolled and annealed samples. By applying the high stored energy nucleation, orientations of the  $\gamma$ -fiber indeed appear in the simulated recrystallization textures. However, the preference on different orientations of the  $\gamma$ -fiber can be observed among various simulated recrystallization textures. Without considering the high mobility of special grain boundaries, simulated recrystallization textures are only different by values of the critical Taylor factor. Because of the sharp steepness of nucleation law ( $k = -200$ ), the critical Taylor factor can be considered as the threshold value for recrystallization nucleation. Crystals with Taylor factor values below the critical value have no chance to nucleate. On the contrary, the ones having Taylor factor values higher than the critical value are certain to nucleate. In the Taylor factor map of Figure 7.11, most of the orientations along the  $\gamma$ -fiber show the Taylor factor values higher than 2.7, and

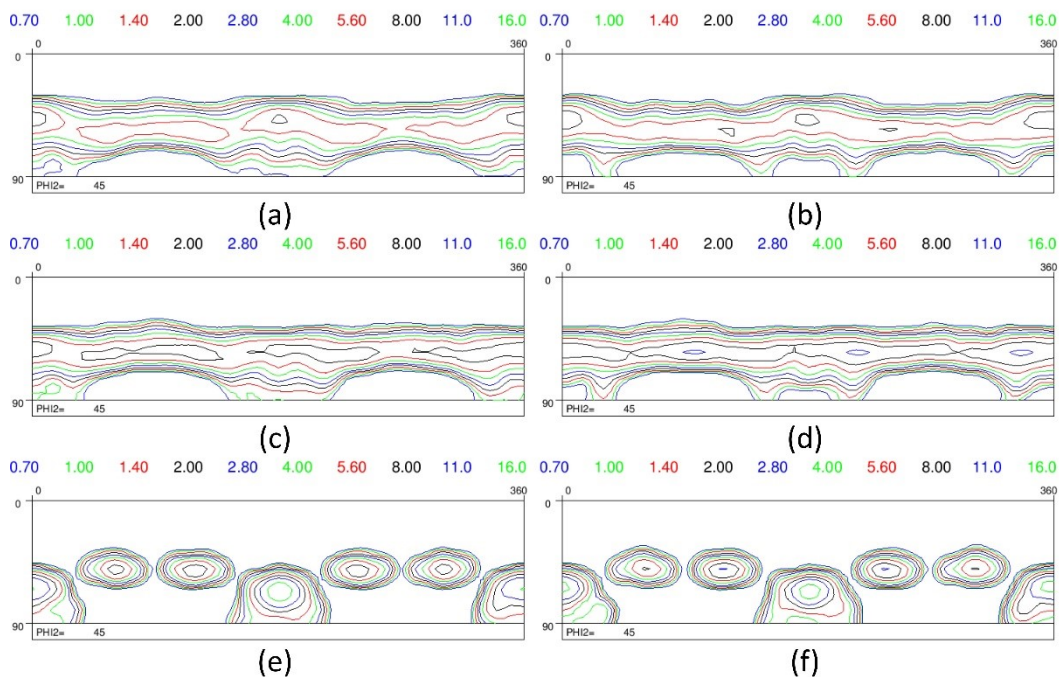


**Figure 7.18 Simulated recrystallization textures of cold rolled and annealed samples, obtained by the high stored energy nucleation with  $k = -200$  and  $M_0 = 2.49$  (a and b),  $M_0 = 2.72$  (c and d) and  $M_0 = 2.95$  (e and f). Different growth rules include: the normal growth of high angle grain boundaries (a, c and e) and the high migration rate of the  $\langle 110 \rangle 26.5^\circ$  boundaries (b, d and f).**

thus have high probabilities to nucleate in all recrystallization simulations. When the critical Taylor factor is increased from 2.49 to 2.72 and 2.95, not all orientations of the  $\gamma$ -fiber are selected for nucleation. Among the components of the  $\gamma$ -fiber, the  $\{111\}\langle 110 \rangle$  component has the highest Taylor factor of 3.23, while the  $\{111\}\langle 112 \rangle$  component exhibits the lowest Taylor factor of 3.05. In the simulation with  $M_0 = 3.05$ , although the  $\{111\}\langle 112 \rangle$  orientation still has high probability to nucleate, the density of nuclei for this oriented crystal, on the contrary, is much smaller than the nuclei density of the  $\{111\}\langle 110 \rangle$  oriented crystals. As a result, the simulated recrystallization texture, which is strongly affected by the oriented nucleation criterion contains the highest intensity peak at the  $\{111\}\langle 110 \rangle$  component.

The growth of recrystallization nuclei, in fact, also affects the formation of recrystallization textures. In the first series of recrystallization simulations, the normal growth rule of high angle boundaries is applied. This growth rule implies a random growth of nuclei, in which all nuclei have the same migration rate to deformed

crystals, only taking into account the limited mobility of low angle grain boundaries with misorientation angles lower than  $15^\circ$ . This implies that the normal growth rule only excludes the self-growth of oriented crystals, and thus just changes texture intensities of the same components between nucleation and recrystallization textures. Intensities of highly favorable orientations in the nucleation texture are weakened, while intensities of less preferred orientations are enhanced.

In the second series of simulations (c.f. Figure 7.18b, d and f), the high migration rate is attributed to the special boundary of  $\langle 110 \rangle 26.5^\circ$  misorientation. This special growth rule strongly selects nuclei exhibiting the  $\langle 110 \rangle 26.5^\circ$  misorientation for enhanced growth during recrystallization. Simulation results of the selective growth, therefore, are different from predicted recrystallization textures of the normal growth rule. Specifically, Figure 7.18c and Figure 7.18d illustrate the differences in recrystallization textures for the same nucleation criteria but different growth rules. In both of the two textures, because of the high stored energy nucleation with the same Taylor factor criteria, the  $\gamma$ -fiber texture components are present. However, the highest intensity peaks in these two textures are located at different orientations. In the recrystallization texture simulated by the normal growth rule, the highest intensity peak is observed at the  $\{111\}\langle 110 \rangle$  component. This orientation is the most preferred in the nucleation texture, because of its highest Taylor factor among all orientations of the  $\gamma$ -fiber. During the growth of nuclei, the normal growth rule reduces intensity of the  $\{111\}\langle 110 \rangle$  component, but could not change the preference of recrystallization texture from this orientation. In the recrystallization texture simulated by the special growth rule, the same nucleation rule also results in the selection of the  $\{111\}\langle 110 \rangle$  orientation, although the selective growth of the  $\langle 110 \rangle 26.5^\circ$  misorientation boundaries effectively changes the highest intensity peak to the  $\{111\}\langle 112 \rangle$  orientations (c.f. Figure 7.18d)

Comparing the simulated and the measured recrystallization textures, similar features between the two textures can be found. The measured recrystallization textures, which are shown in Figure 7.8, have the highest intensity peak on the  $\{111\}\langle 112 \rangle$  component. Among simulated recrystallization textures, the highest intensity peak at the  $\{111\}\langle 112 \rangle$  orientation is observed in the texture, which is

simulated with the critical Taylor factor of 2.72 and the selective growth of the  $\langle 110 \rangle 26.5^\circ$  misorientation boundaries, c.f. Figure 7.18d. Similarities between simulated and measured textures reveal the formation mechanism of recrystallization texture in cold rolled samples. During the nucleation stage of recrystallization, deformed crystals with the higher stored energy are more preferred to nucleate. Among oriented crystals in a cold rolled sample, the ones of the  $\gamma$ -fiber texture components have higher chance to nucleate, and the  $\{111\}\langle 110 \rangle$  orientation is the most preferred component in the nucleation texture. In the growth stage of recrystallization, the selective growth enhances texture intensities of nuclei which have the  $\langle 110 \rangle 26.5^\circ$  misorientation boundaries to a larger number of deformed crystals. Result of this selective growth is the formation of the  $\{111\}\langle 112 \rangle$  orientation in recrystallization texture (c.f. Figure 7.8b).

Although the main component of recrystallization texture can be modelled by high stored energy oriented nucleation and the selective growth of deformed crystals, some important features of the measured texture could not be reproduced in the simulated texture. Specifically, the shifted  $\alpha$ -fiber, which is an important component of the measured recrystallization texture, is not present in the simulated one. The maximum intensity peak in the measured texture is located exactly at the  $\{111\}\langle 112 \rangle$  orientation, while the simulated texture still contains other components of the  $\gamma$ -fiber texture. The formation of the shifted  $\alpha$ -fiber in recrystallization textures has not been captured by the recrystallization mechanism that was considered in this chapter. Origins of this fiber texture should be related to the micromechanics of crystal plasticity and thus will be further investigated in the Chapter 8.

### 7.3 Conclusions

In this chapter, the formation of recrystallization textures in symmetrically and asymmetrically rolled samples of Fe-1.2% Si has been investigated. These samples are both rolled at room and elevated (900°C) temperatures before recrystallization annealing at the same temperature (900°C). Different recrystallization textures have been observed between samples of symmetric and asymmetric rolling at high temperature. However, for the samples rolled at room temperature, no significant

differences in developments of recrystallization textures after symmetric and asymmetric rolling has been found, which could be attributed to the negligible effect of the shear component in the displacement field.

The formation of different recrystallization textures has been argued by various recrystallization rules. For hot rolled samples, nucleation and growth of oriented crystals at grain boundaries produce recrystallization textures of low stored energy orientations. In simulations, these texture developments are reasonably well reproduced by the Kestens-Jonas model with the orientation selection of low Taylor factor orientation during nucleation and random growth of these nuclei in the deformation matrix. It was demonstrated that this low-energy nucleation was valid both after symmetrically and asymmetrically rolling, leading to widely different recrystallization textures, but could be explained with one single selection criterion.

Contrary to the development in hot rolled samples, the evolution of recrystallization textures in cold rolled samples has been attributed to nucleation of high stored energy crystals and increased growth rate of boundaries between nuclei and deformation matrix which, are closed to the  $\langle 110 \rangle 26.5^\circ$  misorientation. Among all preferred orientations in plane strain compression condition, the  $\{111\}$ //ND oriented crystals have the higher Taylor factors. Therefore, these crystals are more preferred to fully develop as grains of the recrystallization microstructures. The similarity in stored energy distribution among grains of different orientations accounts for identical development of recrystallization textures in cold rolled samples. However, not all recrystallization texture components in the cold rolled samples can be predicted by simulations based on the high stored energy nucleation rule added with  $\langle 110 \rangle 26.5^\circ$  selective growth. The shifted  $\alpha$ -fiber, which is observed in recrystallization textures of cold rolled samples, is completely absent in the simulation textures. This misfit between experiment and simulation textures suggests a different recrystallization mechanism for the shifted  $\alpha$ -fiber texture. The origin of the shifted  $\alpha$ -fiber oriented grains in the recrystallization texture will be addressed in the next chapter.

## ***7.4 References***

- [1] Kestens L, Jonas JJ. Modeling texture change during the static recrystallization of interstitial free steels. *Metallurgical and Materials Transactions A*. 1996;27:155.
- [2] Humphreys FJ, Hatherly M. *Recrystallization and related annealing phenomena*, Second ed. New York: Elsevier Science; 2004.
- [3] Quinney H, Taylor GI. The Emission of the Latent Energy due to Previous Cold Working When a Metal is Heated. *Proceedings of the Royal Society of London. Series A - Mathematical and Physical Sciences*. 1937;163:157.
- [4] Jiang J, Britton TB, Wilkinson AJ. Evolution of dislocation density distributions in copper during tensile deformation. *Acta Mater*. 2013;61:7227.
- [5] Anand L, Gurtin ME, Reddy BD. The stored energy of cold work, thermal annealing, and other thermodynamic issues in single crystal plasticity at small length scales. *Int J Plast*. 2015;64:1.
- [6] Hutchinson B. Deformation microstructures and textures in steels. *Philos. Trans. R. Soc. A Math. Phys. Eng. Sci*. 1999;357:1471.
- [7] Tóth LS, Jonas JJ. Modelling the texture changes produced by dynamic recrystallization. *Scr. Metall. Mater*. 1992;27:359.
- [8] Kestens L, Jonas JJ. Modelling Texture Change during the Static Recrystallization of a Cold Rolled and Annealed Ultra Low Carbon Steel Previously Warm Rolled in the Ferrite Region. *ISIJ Int*. 1997;37:807.
- [9] Kestens L, Jonas JJ, Van Houtte P, Aernoudt E. Orientation selective recrystallization of nonoriented electrical steels. *Metall Mat Trans A Phys Metall Mat Sci*. 1996;27:2347.
- [10] Sidor JJ, Petrov RH, Kestens LAI. Modeling the crystallographic texture changes in aluminum alloys during recrystallization. *Acta Mater*. 2011;59:5735.
- [11] Bunge HJ. Some applications of the Taylor theory of polycrystal plasticity. *Krist. Tech*. 1970;5:145.
- [12] Hutchinson B. Practical aspects of texture control in low carbon steels. *Mater Sci Forum*. 1994;157-6:1917.
- [13] Ray RK, Jonas JJ, Hook RE. Cold rolling and annealing textures in low carbon and extra low carbon steels. *International Materials Reviews*. 1994;39:129.
- [14] Ibe G, Lücke K. Growth selection during recrystallization of single crystals. *Recrystallization, Grain Growth and Textures*. 1966.

[15] Kohler U, Bunge HJ. Model Calculations of the Recrystallization Texture Formatio in alpha-Iron. *Texture Microstruct.* 1995;23:87.





# 8

## *Locally oriented crystals* *in cold rolled samples*

### *8.1 The roles of local orientations in deformed samples on developments of recrystallization texture*

In chapter 6 and 7, formations of crystallographic textures after rolling and annealing in the Fe-1.2 wt.% Si alloy have been investigated. Evolution of deformation textures both at high and room temperatures have been accounted for by rotations of oriented grains toward preferred orientation(s) to prescribed straining conditions. To both conventional and asymmetric rolling, oriented grains which are higher orientation stability, are more frequently observed in the deformation microstructures. Volume fraction of the highly stable orientations in the deformation texture is also larger than that of the others orientation. During

recrystallization annealing, deformed crystals of the higher volume fraction have more chances to develop as recrystallized grains. Formations of the recrystallization textures in warm and cold rolled samples are essentially followed different mechanisms. In warm rolled samples, the development of recrystallization textures is attributed to low stored energy nucleation of deformed crystals and the normal growth of recrystallization nuclei. In cold rolled samples, the dominance of the  $\{111\}\langle 112 \rangle$  component in the recrystallization texture is accounted for by the high stored energy nucleation and the selective growth of nuclei, which exhibit the  $\langle 110 \rangle 26.5^\circ$  misorientation boundaries to the surrounding deformed crystals. Although the development of low stored energy oriented crystals during recrystallization of the warm rolled sample has not been fully understood, recrystallization textures in the same samples are reasonably captured by recrystallization calculation models (c.f. section 7.2.3). Evolutions of recrystallization texture in cold rolled samples of BCC structured materials are frequently accounted for by developments of high stored energy crystals in deformed samples. However, various combinations of high stored energy nucleation and selective growth of the  $\langle 110 \rangle 26.5^\circ$  high angle grain boundary are not able to explain for the presence of the shifted  $\alpha$ -fiber components in recrystallization textures of the cold rolled samples (c.f. section 7.2.4).

The absence of the shifted  $\alpha$ -fiber components in simulated textures of cold rolled and annealed samples is just one among various examples of the same problem. Another well-known example is the retention and development of the Goss oriented grains in iron – silicon alloys during primary and secondary recrystallization. As compared to the shifted  $\alpha$ -fiber texture, the Goss orientation develops in recrystallization texture of the iron – silicon alloys at much later stage, until the secondary recrystallization. The dominance of the Goss oriented crystals in microstructure of the material is attributed to the abnormal growth of these crystals on the primarily recrystallized grain matrix. Formation of the Goss crystals in conventional rolling and retention of these oriented grains during primary recrystallization are not the main subjects for macroscopic texture simulations in rolling and annealing. However, origin of the Goss orientation and the shifted  $\alpha$ -fiber

texture in rolling deformation is one of the most important features to account for the developments of these components in recrystallization textures.

Macroscopic rolling deformation of the PSC, apparently, is not favorable for the development of the Goss and the shifted  $\alpha$ -fiber oriented crystals in cold rolled samples (see section 6.4). Local deformation, in which various components of the strain tensor are activated, might enhance the stability of these oriented crystals during rolling deformation. Local deformation could be assumed for small crystal regions but not for a whole microstructure. Besides the condition of small effective crystal volume, local deformation need to be confined within the macroscopic PSC of the rolling deformation.

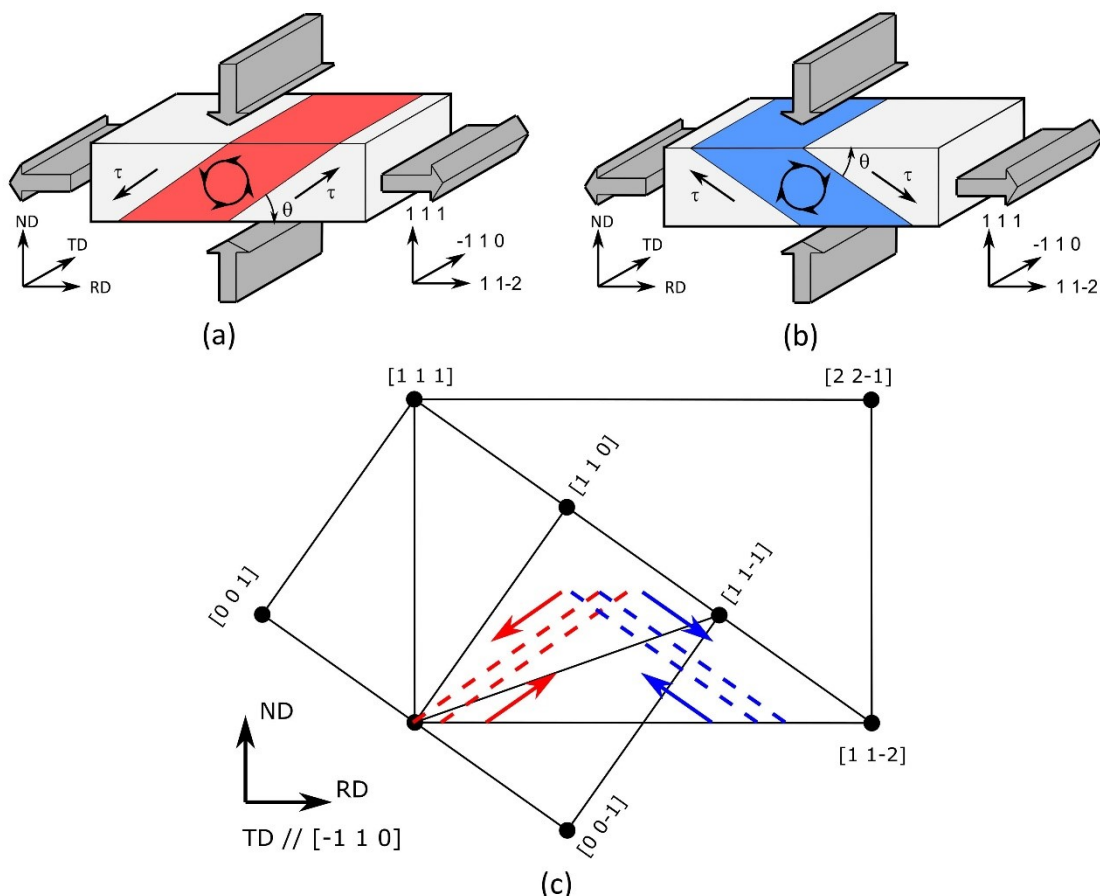


**Figure 8.1** Shear banding in the  $(111)[1\ 1-2]$  oriented crystals with (a) positive inclination angle, (b) negative inclination angle to the sample coordinate system (RD-TD-ND) and (c) to the crystal reference system.

For the Goss oriented crystals, local deformation condition for shear banding in the  $\{111\}\langle 112\rangle$  grains is frequently applied. Shear strain on inclined plane to the RD has been used successfully to account for the presence of shear bands in the  $\{111\}\langle 112\rangle$  oriented grains. Among all crystals of the shear bands, the Goss oriented crystals have the highest energetic advantage while the lattice curvature around these crystals is at the maximum. Shear banding in the  $\{111\}\langle 112\rangle$  oriented grains and formation of the Goss ( $\{110\}\langle 001\rangle$ ) oriented crystal in shear bands, therefore, will be reproduced in this chapter by crystal plasticity calculations with the full constraint Taylor model. Geometric softening theory to account for the formation of microscopic shear bands in oriented grains, afterward, will be applied to the rotated Goss ( $\{110\}\langle 110\rangle$ ) oriented grains. The presence of shear bands in the hardest oriented grains of the rotated Goss orientation, therefore, will validate for the local deformation of shear banding.

For the shifted  $\alpha$ -fiber oriented crystals, although their origins are closely linked to the  $\alpha$ -fiber oriented grains [1], local deformation condition for these crystals in polycrystalline microstructure has not yet known. A number of microstructure investigations to illustrate for the relationship between the  $\alpha$ -fiber in rolling texture and the shifted  $\alpha$ -fiber in recrystallization texture has been carried out [1;2]. However, under which local deformation the shifted  $\alpha$ -fiber texture components are enhanced is still an open question. Therefore, in this study, the main focus is spent on local plasticity of the  $\alpha$ -fiber oriented grains. The study is carried on by crystal plasticity simulations, in which influences of strain tensor components to the stability of the  $\alpha$ -fiber oriented crystals are analyzed. Results of the study will account for the development of the shifted  $\alpha$ -fiber oriented crystals in the  $\alpha$ -fiber grains. Location and microstructure features of the shifted  $\alpha$ -fiber oriented crystals in the  $\alpha$ -fiber grains are also suggested. Crystal plasticity calculation is first implemented with the rotated Cube ( $\{001\}\langle 110\rangle$ ) orientation. Development of the local texture from the  $\alpha$ -fiber to the shifted one, is then illustrated by simulation results of the full constrain Taylor model.

## *8.2 Local texture developments in microscopic shear bands of the {111}<112> and the {110}<110> oriented crystals*

In conventional rolling microstructures, grain fragmentation is more frequently observed in the  $\gamma$ -fiber oriented crystals, rather than in the  $\alpha$ -fiber oriented crystals. Fragmentation in the  $\gamma$ -fiber oriented crystals commonly occurs by the appearance of in-grain shear bands. Shear banding, a common type of plastic instability in rolled metals, has been studied for many years [3-5]. Shear banding can be considered as a microscopic equivalent of necking instability in a tensile test. In the microstructure of a heavily rolled metal sheet, shear bands appear as narrow planar regions, parallel to the TD and  $20^\circ$  to  $35^\circ$  inclined to the RD. The presence of shear bands is independent of the grain structure and irrespective of the grain orientation. However, depending on the number of grains in a microstructure and the magnitude of plastic strain applied to the material, shear bands in deformed microstructures are categorized as microscopic or macroscopic types. Macroscopic shear bands, as mentioned previously, are results of local plastic deformation, appearing through-out the sample thickness and do not depend on grain orientations. They are frequently observed just before the necking strain during a tensile experiment or near the fracture region of a heavily cold deformed sample. On the contrary, microscopic shear bands are regularly confined in individual grains. Their occurrences link to specific grain orientations after a certain straining magnitude, while they are not present in other grains of the same microstructures. Dillamore et al [5] studied the deformation of crystals in shear bands with particular attention to crystallographic orientation mechanisms. The origin of the plastic instability ( $d\sigma/d\varepsilon \leq 0$ ) was attributed to the geometric softening of crystal grains ( $dM/d\varepsilon \leq 0$ ). During a progressive deformation, the resistance to plane strain compressive deformation of crystallographic grains increases due to contributions of both geometric hardening ( $dM/d\varepsilon > 0$ ) and work hardening ( $d\tau_c/d\varepsilon > 0$ , with  $\tau_c$  being the critical resolved shear stress of dislocation glide). At some points, strain localization may occur as the homogeneous deformation of the crystal is energetically less favorable. The imposed boundary conditions, in these situations, are accommodated by locally increased strain. A concentration of imposed strain on inclined bands changes the deformation geometry of the crystal locally.

Because of this change, the deformation resistance to the rotated shear deformation, as compared to the PSC, leads to deformation and rotation of in-band crystal volumes, while the crystal volume outside these region remain unchanged.

Liked other types of grain fragmentations, shear bands are of particular interest, not only because they represent a characteristic feature of the heavily rolled metal structure, but also due to the potential impact of in-band crystallographic orientations on the formation of recrystallization textures [6]. Ridha and Hutchinson [7] observed the influence of shear bands on texture evolution of annealed copper sheets. With the presence of shear bands in the deformed structure, a sharp Cube ( $\{001\}\langle 100\rangle$ ) texture, commonly observed after recrystallization of FCC structured metals, is almost eliminated. Alternatively, there is a random development of orientations in shear bands. In BCC structured materials, shear banding is most frequently observed in the  $\{111\}\langle 112\rangle$  oriented grains. A shear concentration on  $\pm 35^\circ$  inclined bands causes a rotation of in-band crystal volume around the  $\langle 110\rangle$  crystal axis, which is parallel to the TD. The rotated orientation exhibits a reduced Taylor factor compared to the original  $\{111\}\langle 112\rangle$  orientation, i.e. geometric softening occurs. Preferred orientations in shear bands are dependent on the inclination of the applied strain [3]. Particularly, in  $\{111\}\langle 112\rangle$ -oriented grains, shear bands are associated with the appearance of the Goss texture component ( $\{110\}\langle 001\rangle$ ) after recrystallization [3;4;8]. The formation mechanism of the latter texture component was attributed to its advantage in sharp lattice curvature [3] and locally low dislocation density [9], among other orientations in shear bands after conventional cold rolling.

### *8.2.1 Crystal plasticity simulations for shear banding in the $\{111\}\langle 112\rangle$ oriented grains*

To illustrate for the occurrence of shear banding in the  $\{111\}\langle 112\rangle$  oriented grains, crystal plasticity simulations could be employed. Results of these simulations also elucidate for the formation the Goss ( $\{110\}\langle 001\rangle$ ) oriented crystals in shear bands of the  $\{111\}\langle 112\rangle$  oriented grains. Occurrence of shear banding and orientation evolution in shear bands of the  $\{111\}\langle 112\rangle$  oriented grains, indeed, have been predicted by crystal plasticity calculations and reported by Ushioda and Hutchinson [3;4]. Because of its importance, shear banding of the  $\{111\}\langle 112\rangle$

oriented grains are reproduced in the current study by crystal plasticity simulations with the full constraints Taylor model. The aim of these calculations is firstly to identify the inclination angles, which are preferred for the occurrence of shear banding. The second purpose of these calculations is to account for the origin of the Goss ( $\{110\} \langle 001 \rangle$ ) oriented crystals in shear bands of the  $\{111\} \langle 112 \rangle$  oriented grains. The Goss orientation is one of the most important components in recrystallization textures of Fe-Si electrical steels. Abnormal growth of Goss oriented grains in the secondary recrystallization must be a result of the formation and retaining of Goss oriented crystals after deformation and primary recrystallization.

General investigation on shear banding requires a re-formulation of the geometric softening condition. To identify the preferred inclination angle for shear banding, Taylor factor and rotation rate of the  $\{111\} \langle 112 \rangle$  oriented crystals in shear bands of various deformation conditions are calculated. Conventionally, shear bands are assumed to be parallel to the TD but inclined to the RD. Deformations of crystal regions in shear bands are schematically described by the simple shear in different inclined planes. The total range of shear band inclination angles  $\theta$  is changed from  $-90^\circ$  to  $+90^\circ$ , in which the  $\theta = 0^\circ$  corresponds to the simple shear on the rolling plane and parallel to the RD. Figure 8.2 shows the change of Taylor factor and rotation rate for the  $\{111\} \langle 112 \rangle$  oriented crystal in shear bands of various inclination angles.

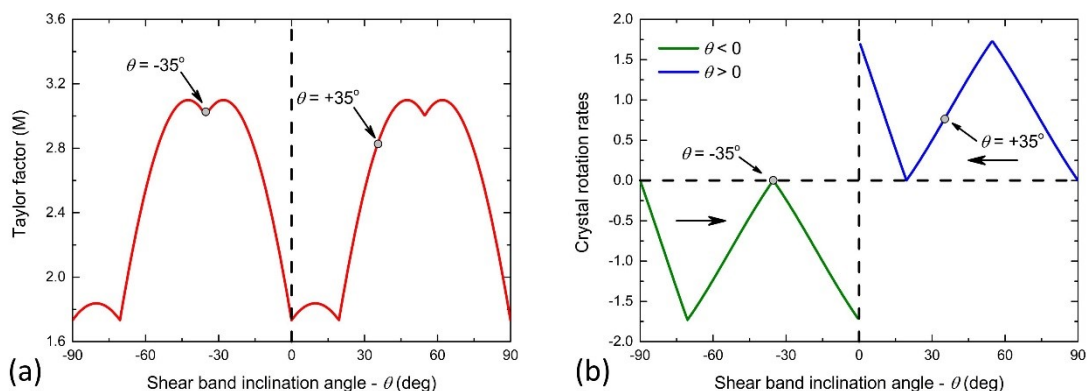


**Figure 8.2 Variations of (a) Taylor factor and (b) rotation rate of the  $\{111\} \langle 112 \rangle$  oriented crystal in deformation conditions of shear bands, which have different inclination angles to the RD.**



For a grain of specific orientation, various Taylor factors in different strain modes indicate a non-similar resistance of the crystal to plastic deformations. In addition, for the  $\{111\}\langle 112\rangle$  oriented crystal, simple shear strain in an inclined band produce rotations of the crystal around the  $\langle 110\rangle//TD$  axis. In the crystal reference system, these rotations are equivalent to the change of shear band inclination angles, while the orientation of crystal is fixed. Therefore, the change of Taylor factor as observed in Figure 8.2a shows two important features for shear banding in the  $\{111\}\langle 112\rangle$  oriented grains. First, it indicates the initial resistance to deformation of crystal regions in shear bands. Second, the change of Taylor factor with shear banding inclination angle shows the evolution of geometric resistance for crystals in shear bands during progressive shearing. For shear banding at inclination angles  $\theta$  of  $\pm 90^\circ$  and  $0^\circ$ , the Taylor factor of the  $\{111\}\langle 112\rangle$  oriented crystal is at the lowest value of 1.75. Shear banding in the  $\{111\}\langle 112\rangle$  oriented crystals are expected to occur immediately when cutting shear and in-plane shear strain are applied with the minimum crystallographic orientation resistance. However, the occurrence of these shear banding at inclination angles  $\theta = \pm 90^\circ$  and  $0^\circ$  do not bring any benefit to the strain energy. To maintain these shear banding, more energy is required during the deformation. It means that the shear banding at inclination angles  $\theta = \pm 90^\circ$  and  $0^\circ$  occurs under the condition of geometrical hardening but not the geometric softening. Additionally, both of these shear strains (cutting and in-plane shears) are not compatible to the PSC of the rolling deformation. Inclined shear strains with inclination angles higher than  $45.0^\circ$  to the RD, in fact, could not occur in the conventional rolling deformation. Shear bands with inclination angles higher than  $45.0^\circ$ , therefore, may never appear in conventionally rolled samples.

Among all shear banding with inclination angles lower than  $45.0^\circ$ , the ones with inclination angles of  $-42.5^\circ$  and  $-28.0^\circ$  have the highest orientation resistance. In Figure 8.2a, the highest orientation resistance for shear banding is measured by the maximum Taylor factor of 3.1. Shear banding with these inclination angles (i.e.  $-42.5^\circ$  and  $-28.0^\circ$ ) and the one with the inclination angle of  $+45.0^\circ$  therefore benefit the most from the strain energy reduction by geometric softening. Shear banding with other inclination angles in the range of  $-42.5^\circ$  to  $+45.0^\circ$ , although exhibit the geometric

softening, are less energetically advantage than the ones with  $-42.5^\circ$ ,  $-28.0^\circ$  and  $+45.0^\circ$ . Particularly, because of the weak or non-geometric softening effect, shear bandings with inclination angle from  $0.0^\circ$  to  $+19.0^\circ$  are not expected to occur in the  $\{111\}\langle 112 \rangle$  oriented crystals.

Besides energy criteria, it is also suggested by Hutchinson and Ushioda [3;4] that shear banding also depends on rotation rates of the crystals in shear bands. Geometric softening only occur when crystal volume during deformation rotates toward lower energy states and hence the rotation rate to softer orientations can be considered as the driving force for shear band formation. Shear banding will be stopped under condition of zero rotation rate of the crystal insides shear bands. In Figure 8.2b, the rotation rates of the  $\{111\}\langle 112 \rangle$  oriented grains are zero at shear band inclination angles of  $\pm 90^\circ$ ,  $-35^\circ$  and  $+19.5^\circ$ . Geometric softening, therefore, is completely impossible for shear banding at  $\pm 90^\circ$  and  $+19.5^\circ$  inclination angles, because of both energetically un-favorable and zero rotation of crystals in these shear bands. On the contrary, geometric softening may occur in shear bands of  $-42.5^\circ$  to  $-28.0^\circ$  inclination angles, although crystal rotation rates in these shear bands are rather small. The largest rotation of the  $\{111\}\langle 112 \rangle$  oriented crystals in the shear band of  $-42.5^\circ$  inclination angle is about  $0.5^\circ$  per strain step. The maximum rotation of the  $\{111\}\langle 112 \rangle$  crystal in the shear band of  $-42.5^\circ$  inclination angle is  $7.5^\circ$  around the  $\langle 110 \rangle // \text{TD}$  axis. This small rotation of crystal regions in shear bands of  $-42.5^\circ$  inclination angle limits further development of the shear band during deformation. Shear banding with the inclination angles of  $-42.5^\circ$ , therefore, is predicted to occur just at the beginning of deformation. As the crystal region in shear bands approach its stable orientation, strain energy will not be further reduced and the shear banding with inclination angle of  $-42.5^\circ$  will stop to develop. For the same reason, shear bandings with inclination angles from  $+19.5^\circ$  to  $+45.0^\circ$  cease to develop when the crystal regions in shear bands reach their zero-rotation rate at the softest orientation. Shear banding with inclination angle of  $+45.0^\circ$  is fully developed when crystals in shear bands rotate  $25.5^\circ$  around the  $\langle 110 \rangle // \text{TD}$  toward the Goss ( $\{110\}\langle 001 \rangle$ ) orientation. In Figure 8.2, this rotation corresponding to the change of strain energy

and rotation rate for crystal regions in the shear band from  $45^\circ$  to  $19.5^\circ$  inclination angle.

Although shear banding at inclination angles of  $-42.5^\circ$ ,  $-28.0^\circ$  and  $+45.0^\circ$  are predicted to be the most preferred, microstructural investigations usually report a wide spread of inclination angles. Microstructural characterization of shear bands in the  $\{111\}\langle 112 \rangle$  oriented grains, as shown in Figure 8.3, exhibit a large variation of inclination angles, from  $20^\circ$  to  $45^\circ$ . The Goss ( $\{110\}\langle 001 \rangle$ ) orientation is commonly reported to be present in crystal regions of the sharpest lattice curvature in shear band of  $35^\circ$  inclination angle. To verify this observation, shear banding at  $\pm 35^\circ$  inclination angles in the  $\{111\}\langle 112 \rangle$  oriented grains are specifically simulated. As can be observed in Figure 8.2 positive and negative inclination angles produce different evolutions of the Taylor factor and the rotation path. These different evolutions are better observed from Figure 8.4, showing the change with equivalent strain of Taylor factor and crystallographic orientation for crystal regions in both negatively and positively inclined shear bands of  $-35^\circ$  and  $+35^\circ$ , respectively.

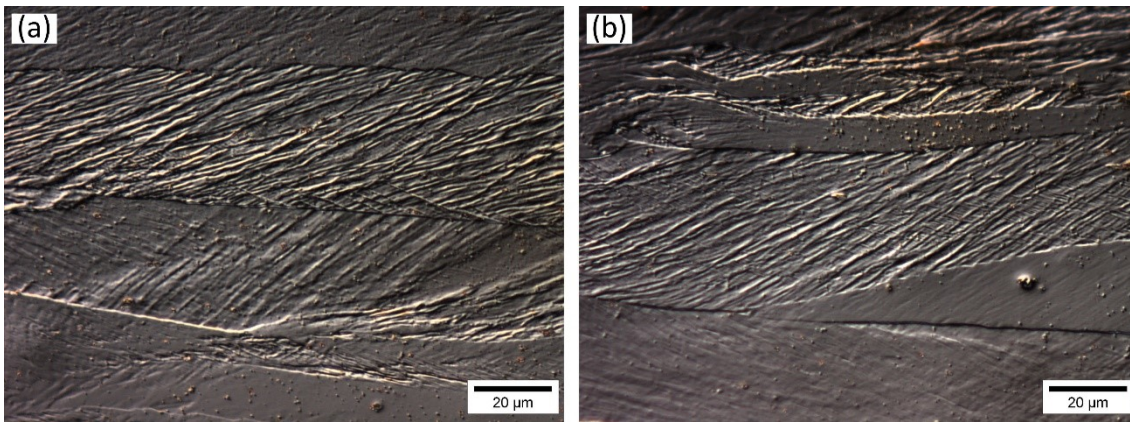


**Figure 8.3** Microstructures in RD-ND sections of the  $\{111\}\langle 112 \rangle$  oriented grains, in which microscopic shear banding occurs.

In shear bands of  $-35^\circ$  inclination angle,  $\{111\}\langle 112 \rangle$  orientations have the initial Taylor factor of 3.02. During progressive shear strain from 0 to 1.25, the Taylor factor of in-band crystals is first increased to 3.07. Rotation of in-band crystals in the same strain domain is very limited, because of the small rotation rate. However, when the applied strain exceeds the value of 1.25, the crystal rotation rate increases and the Taylor factor decreases quickly. The steep reduction of Taylor factor exhibits a strong

effect of geometric softening for shear banding. At the equivalent strain of 1.71, the Taylor factor of in-band crystals is at the lowest value of 1.75 at which point the geometric softening effect of shear banding at  $-35^\circ$  inclination angle is expected to be exhausted. In addition, the rotation rate of in-band crystals reaches the highest speed at the  $\{110\}\langle 001\rangle$  orientation. At this point the orientation gradient is maximum and indeed, the Goss oriented crystals are predicted in the region of the sharpest lattice curvature. Beyond the equivalent strain of 1.71, the development of in-band crystals is still possible, although requiring a larger amount of strain energy and with diminishing rotation rates. The orientation evolution of crystal volume in shear band of  $-35^\circ$  inclination angle has fully stopped, when the rotation rate of the crystal is equal to zero at an orientation that is  $19.5^\circ$  away from the ideal Goss orientation.

Alternatively, the shear strain occurring in bands at  $+35^\circ$  inclination angle exhibits geometric softening immediately right from that activation of simple shear. The Taylor factor of in-band crystal reduces continuously from 2.81 to 1.75 as strain increases from 0 to 2.00, c.f. Figure 8.4b. However, the energy advantage of geometric softening is mostly exhausted in the first period of deformation, during straining from 0 to 0.75. This change of Taylor factor is accompanied by a fast rotation rate of in-band crystals at the first period of deformation. Since the crystal rotation rate reduces to zero as the in-band crystals approach their stable orientation, the orientation evolution and geometric softening are both terminated at the  $\{221\}\langle 114\rangle$  orientation.

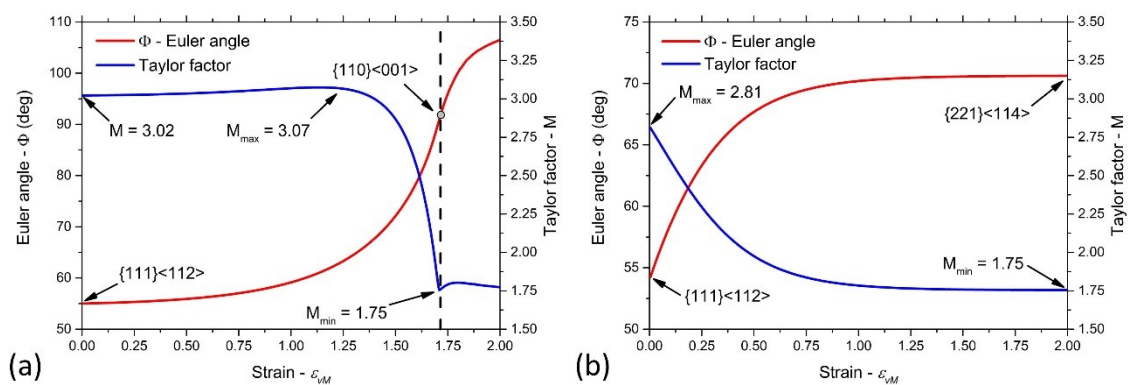


**Figure 8.4** The change with strain of Taylor factor and crystallographic orientation for crystal regions in shear bands of (a)  $-35^\circ$  and (b)  $+35^\circ$  inclination angles. Crystallographic orientations are given by  $(\varphi_1, \Phi, \varphi_2)$  Euler angles, in which  $\varphi_1 = 90^\circ$  and  $\varphi_2 = 45^\circ$  do not change their values in all considered strain range.

The stable orientation for in-band crystals of  $+35^\circ$  inclination angle is  $15.8^\circ$  away from the Goss orientation.

In summary, by crystal plasticity simulations, shear banding at  $\pm 35^\circ$  inclination angles are both confirmed to enhance geometric softening.  $\{111\}\langle 112\rangle$  oriented crystals in shear bands of positive and negative inclination angles both rotate toward the Goss orientation. The rotation rates of in-band crystals, however, are not similar. Differences in rotation rates and developments of Taylor factor lead to various stable orientations for crystal regions in shear bands of positive and negative inclination angle. These stable orientations are deviated  $15.8^\circ$  and  $19.5^\circ$  from the ideal Goss orientation. Goss oriented crystals are predicted to present in shear bands of  $-35^\circ$  inclination angle as the ones with the sharpest lattice curvature regions. The same feature is not expected to appear in shear bands off the  $+35^\circ$  inclination angle.

### *8.2.2 Shear banding in the $\{110\}\langle 110\rangle$ oriented grains*

#### **Crystal plasticity predictions**

In the previous section, microscopic shear banding has been shown to be closely related to deformation resistance of oriented grains. The initial resistance to plane strain compression of various oriented crystals in BCC structured materials are able to be observed from the Taylor factor map, as given in Figure 7.10. The  $\{111\}\langle 112\rangle$  orientation is in the high Taylor factor region as the Taylor factor of this orientation is equal to 3.1 in the total range from 1.75 to 3.75 for all possible orientations in Euler space. In addition, it is easy to recognize that the rotated Goss ( $\{110\}\langle 110\rangle$ ) orientation has the highest Taylor factor (= 3.75) among all crystallographic orientations of BCC structured materials, considering  $\{110\}$  and  $\{211\}$  slip, which implies that this orientation exhibits the highest resistance to plasticity. Consequently, it entails the largest impact of geometric softening, if shear banding occurs in these rotated Goss oriented crystals.

It is assumed that at the start of polycrystal plasticity, strain energy is mostly accommodated by neighboring grains, rather than by the rotated Goss grains. Progressive deformation, however, increases deformation resistances of these

neighboring grains, because of the strain hardening. After a certain level of deformation, the system may energetically benefit from a local strain instability, very similar to the in-grain shear bands observed in  $\{111\}\langle 112 \rangle$  orientations, i.e. a strain localization in small and inclined bands of simple shear. Resistance of crystals to shear strain, in general, is smaller than the one against plane strain compression.

Shear banding in rotated Goss oriented grains, if it occurs, should be even more prominent than in the  $\{111\}\langle 112 \rangle$  oriented grains. However, shear bands in rotated Goss oriented grains of BCC structured material after plane strain compression have not been reported yet. The main aim of this study, therefore, is to predict the formation of shear bands in rotated Goss oriented grains and to provide experimental evidence. Orientation development of in-band crystal regions in rotated Goss grains could be useful for future texture control and improvement of material properties.

To investigate shear banding in rotated Goss oriented grains, the same simulation method as applied to  $\{111\}\langle 112 \rangle$  oriented grains has been used. Shear bands in the rotated Goss oriented grains are supposed to be parallel to the TD and inclined to the RD. Deformations of in-band crystal regions are described by simple shear on an inclined plane to the TD. The primary requirement of shear banding in rotated Goss grains is the condition of geometric softening. Nevertheless, in order to know the preferred conditions for shear band formation, the potential for shear banding at various inclination angles has been calculated. The change of Taylor factor and rotation rate for crystal regions with shear band inclination angles from  $-90^\circ$  to  $+90^\circ$  are given in Figure 8.5.

As compared to shear banding in  $\{111\}\langle 112 \rangle$  oriented grains, formation of shear bands in the  $\{110\}\langle 110 \rangle$  oriented grains is simpler to be predicted because in the  $\{110\}\langle 110 \rangle$  oriented crystals there is a mirror symmetry parallel to the rolling plane. The changes of Taylor factor and rotation rate for crystal regions in shear bands of negative inclination angles are similar to the ones of positive inclination angles. Orientation evolutions of crystal regions in shear bands of positive and negative inclination angles are equal, but in opposite directions. Moreover, constant rotation rates of in-band crystals in the entire range of shear band inclination angles, as

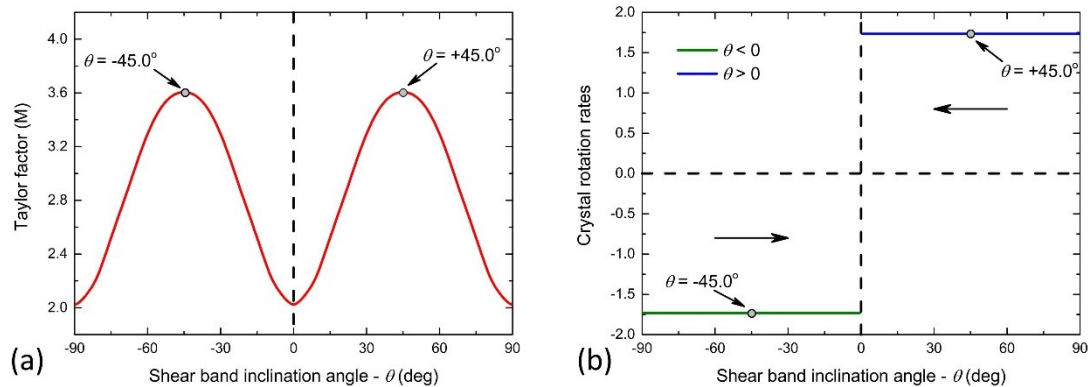


**Figure 8.5** Variations of (a) Taylor factor and (b) rotation rate of the  $\{110\}\langle 110 \rangle$  oriented crystal in deformation conditions of shear bands, which have different inclination angles to the RD.

observed in Figure 8.5b, produce continuous and linear rotation of in-band crystals during shearing. Shear banding in the  $\{110\}\langle 110 \rangle$  oriented crystals at different inclination angles are just constrained by the energy criterion, but not dependent on rotation rates.

The energy criterion for shear banding, in general, includes two factors: (i) the initial resistance to plasticity in rotated shear and (ii) energy gain (potential for geometric softening) during progressive deformation. Both of these two factors depend on the initial dislocation structure and the development of this structure during shearing. In this study, both factor are simply represented by the initial value and the gradient of the Taylor factor, but it can be quantified by other parameters such as e.g. the progressive dislocation densities in different crystal orientations. The physical origin of shear banding, however, is expected not to be changed by the choice of characteristic parameters.

The initial resistance to deformation of the  $\{110\}\langle 110 \rangle$  oriented crystals in shear bands are able of different inclination angles to observed in Figure 8.5a. The  $\{110\}\langle 110 \rangle$  oriented crystals have the smallest initial resistance to shear strains of  $0^\circ$  and  $90^\circ$  inclination angles because the Taylor factor for crystal in such shear bands is as low as 2.02. Plasticity of the  $\{110\}\langle 110 \rangle$  oriented crystals by cutting shear and in-plane shear is predicted to be the easiest to initialize. However, to maintain these modes, increasing amounts of strain energy are required because of the geometric

hardening under these conditions. Moreover, cutting shear and in-plane shear are not compatible to the macroscopic deformation of plane strain compression. Shear bandings on the  $\{110\}\langle 110\rangle$  oriented grains at  $0^\circ$  and  $90^\circ$  inclination angles, therefore, are not possible to occur in rolled samples.

Shear bands at inclination angles of  $45^\circ$  to  $90^\circ$  require more energy to initialize as compared to the ones at  $0^\circ$  and  $90^\circ$ . Additionally, they exhibit geometric hardening instead of softening. There is no energy advantage for shear bandings at inclination angles higher than  $45^\circ$ . On the contrary, formations of shear bands at inclination angles less than  $45^\circ$  are more energetically favored. The initial resistance of crystal regions in shear bands of  $\pm 45^\circ$  inclination angles is the highest among all possible inclined shear conditions as the Taylor factor = 3.60 (Figure 8.5a). Assuming that the lowest resistance of crystal regions in shear bands is equal to the one of in-plane shear, shear bands with inclination angles less than  $45^\circ$  all exhibit geometric softening effect. The amount of strain energy reduced by geometric softening, however, is inversely proportional to shear banding inclination angle. During the deformation of crystal regions in shear bands inclined at  $45^\circ$ , the Taylor factor is able to sharply reduce, from 3.60 to 2.02 and thus, the development of the  $\pm 45^\circ$  inclined shear band is energetically most favorable. In this shear band, the  $\{110\}\langle 110\rangle$  oriented crystal regions are predicted to rotate around the  $\langle 100\rangle//TD$  axis. These rotations of crystal regions in shear band, when considered from crystal reference system, are equivalent to a counter rotations of shear band around the TD. The rotations are maintained at the constant rate as shown by Figure 8.5b, until in-band crystal regions reach the lowest energy state at the Taylor factor of 2.02. The orientation at this lowest energy state is predicted to be the Cube ( $\{001\}\langle 100\rangle$ ) orientation.

To illustrate for the geometric softening, associated with the  $45^\circ$  inclined shear banding in the  $\{110\}\langle 110\rangle$  oriented grains, developments of Taylor factor and orientation of in-band crystal regions with strain have been simulated. Figure 8.6 shows the change of Taylor factor and orientation of in-band crystal regions with increasing equivalent shear strain from 0 to 1.05. During shearing on  $45^\circ$  inclined bands of the  $\{110\}\langle 110\rangle$  oriented grains, in-band crystallites are predicted to reduce the Taylor factor continuously from 3.60 to 2.02, as the shear strain increases from 0



to 0.85. Geometric softening by shear banding in the  $\{110\}\langle 110\rangle$  oriented grains, with  $45^\circ$  inclination angle occurs immediately when the shear strain is applied. The rate of geometric softening, however, is not linear. The highest softening rate is expected at the strain of 0.43, while the lowest rate is calculated at the initial strain and at the strain of 0.85. Shear banding at  $45^\circ$  inclination angle in the  $\{110\}\langle 110\rangle$  oriented grains will occur slowly at the beginning and stagnate toward the end of the geometric softening domain at  $\varepsilon_{VM} = 0.85$ . Beyond the shear strain of 0.85 shear banding is no longer energetically favorable.

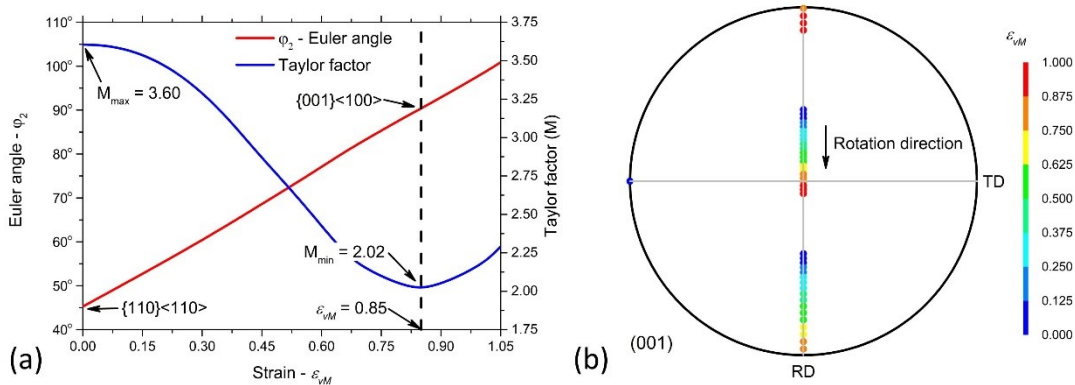


**Figure 8.6 Developments of Taylor factor and orientation of in-band crystal regions during shear banding at  $45^\circ$  inclination angle of the  $\{110\}\langle 110\rangle$  oriented grains. Orientation of in-band crystal regions during shear banding is represented by (a) three Euler angles ( $\varphi_1$ ,  $\Phi$ ,  $\varphi_2$ ) and (b) coordinates of the  $\langle 100\rangle$  crystallographic axis in the pole figure.**

During the shear banding at  $45^\circ$  inclination angle in the  $\{110\}\langle 110\rangle$  oriented grains, in-band crystal regions are predicted to rotate around the  $\langle 001\rangle//TD$  axis. These rotations of in-band crystal regions are shown in Figure 8.6. In Figure 8.6a, orientations are represented by three Euler angles ( $\varphi_1$ ,  $\Phi$ ,  $\varphi_2$ ). The initial orientation of in-band crystal regions in rotated Goss grains is assumed to be  $(\varphi_1, \Phi, \varphi_2) = (0^\circ, 90^\circ, 45^\circ)$ . During shearing, two Euler angle coordinates  $\varphi_1$  and  $\Phi$  do not change their values, while the Euler angle  $\varphi_2$  linearly increases. Figure 8.6a equally shows that the minimum Taylor factor value of 2.02 is reached for  $\varphi_2 = 45^\circ$ , which corresponds to the cube component. In Figure 8.6b, the orientation evolution with strain of in-band crystallites is shown by the rotation path of a crystal on the (001) pole figure. Rotation of the  $\{110\}\langle 110\rangle$  oriented crystals around the  $\langle 001\rangle//TD$  axis toward the Cube

orientation is illustrated by the  $\langle 001 \rangle$  polar coordinates. The Cube orientation is visible in this pole figure, after rotating the  $\{110\}\langle 110 \rangle$  orientation  $45^\circ$  around the  $\langle 001 \rangle$ //TD crystallographic axis, at the equivalent strain of 0.85.

### **Microstructure observations**

Shear banding in rotated Goss oriented grains need to be confirmed experimentally by microstructural investigation. For this investigation, conventionally cold rolled samples of the Fe – 1.2 wt.% Si alloy have been employed. These samples are among the most suitable for microstructure investigations on rotated Goss oriented grains, although the microstructural investigations on rotated Goss oriented grains are limited by the scarcity of these grains in the overall sample texture.

Although shear banding in rotated Goss oriented grains is predicted to be more prominent than in the  $\{111\}\langle 112 \rangle$  oriented grains, the rotated Goss orientation is not a preferred component of the conventional rolling textures of BCC structured materials. The origin of rotated Goss oriented grains is mostly related to the ferrite transformation product of austenite at high temperatures. With a high temperature austenite parent texture, either a rolling or a recrystallization texture, the phase transformation of austenite to ferrite produces a certain fraction of rotated Goss oriented grains, though the volume fraction of the  $\{110\}\langle 110 \rangle$  orientation in transformation textures, in general, is smaller than other components (e.g.  $\{001\}\langle 110 \rangle$ ,  $\{112\}\langle 110 \rangle$  or  $\{554\}\langle 225 \rangle$  orientations). That is due to the fact that the  $\{110\}\langle 110 \rangle$  oriented grains are not preferred variants among all transformation products of the parent austenite grains. Moreover, according to Bunge [10], rotated Goss oriented grains are meta-stable under the plane strain compression condition. Crystal plasticity calculations [11] showed orientation flows toward the rotated Goss orientation from neighboring orientations, which have the common  $\langle 110 \rangle$ //ND axis. Nevertheless, there is a flow from the rotated Goss orientation toward the  $\{111\}\langle 110 \rangle$  orientation. Therefore, rotated Goss only is a minor component in the deformation texture. Additionally, because of its meta-stable condition in plane strain plastic flow, the orientation scatter of rotated Goss grains is expected to be large,

particularly toward the  $\langle 111 \rangle // \text{ND}$  fiber texture. Microstructural tracking of rotated Goss oriented grains, therefore, requires large scanning areas of several square millimeters. On the other hand, to resolve in-grain structures, particularly crystallographic orientations inside shear bands, high resolution EBSD measurements are necessary. To compromise between these two extreme boundary conditions, microstructure investigations have been carried out in two steps. In the first step, a rough EBSD scan in an area of  $2,500 \times 2,000 \mu\text{m}^2$  in the RD-ND plane is measured with a step size of  $10 \mu\text{m}$ . Potential locations for rotated Goss oriented grains are identified with the maximum orientation deviation between measured EBSD points and the  $\{110\} \langle 110 \rangle$  orientation of  $5.0$  degrees. In the second step, EBSD measurements are carried out on areas of  $60 \times 20 \mu\text{m}^2$  at such potential Rotated Goss locations with a step size of  $100 \text{ nm}$ .

Figure 8.7 shows the microstructure and texture of three different rotated Goss oriented grains. In all measurements, rotated Goss oriented grains can be distinguished from neighboring grains, because of their high degree of fragmentation. In-grain orientation gradients of the rotated Goss grains are much sharper than in neighboring crystals. Rotated Goss grains, therefore, can be identified in the microstructures by defining regions with an orientation gradient  $> 10.0$  degrees. In the IPF maps of Figure 8.7a, c and e, neighbors of rotated Goss grains are colored black, whereas the ideal rotated Goss orientations ( $< 5^\circ$  from the ideal component) are colored green. Although the average orientations of these regions is located in the vicinity of the rotated Goss orientation, many regions in these grains exhibit different orientations because of orientation spread of rotated Goss oriented crystals. The spread of the rotated Goss grains toward the  $\{111\} \langle 110 \rangle$  orientation is due to rotations of the rotated Goss crystal around its  $\langle 110 \rangle // \text{RD}$  axis after plane strain compression. Moreover, interactions with neighboring grains also lead to local rotations of the rotated Goss grains in the vicinity of grain boundaries. Orientation scatter around the  $\{110\} \langle 110 \rangle$  orientation can be observed in the local textures, shown in Figure 8.7b, d and f. In all three textures, the peak at the rotated Goss orientation has the highest intensity of 10 to 14 mrd. The spread toward the

$\langle 111 \rangle // \text{ND}$  fiber at the rotated Goss orientation is recognized by the non-spherical shape of this texture component in the  $\varphi_2 = 45^\circ$  section of the ODF.

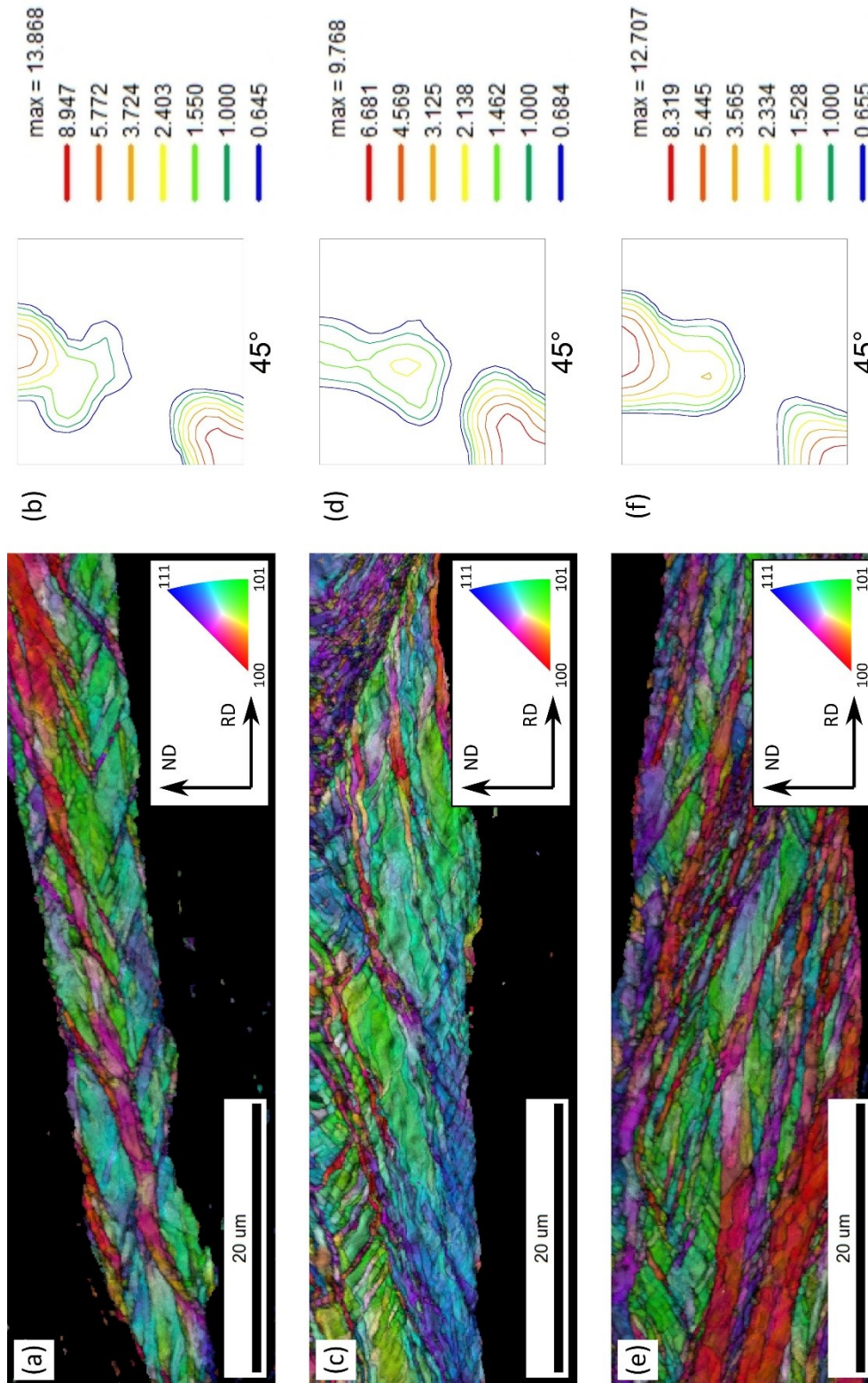


Figure 8.7 IPF maps (a, c, e) and  $\varphi_2 = 45^\circ$  ODF sections (b, d, f) of three rotated Goss oriented grains in RD-ND section.

In addition to local orientation variations in rotated Goss grains, inclined bands of sharply different orientations are also visible in IPF maps of Figure 8.7a, c and e. These bands are predicted by the crystal plasticity simulations in the previous sub-section. Micro shear bands in rotated Goss grains are distinguished from the ones in the  $\{111\}\langle 112\rangle$  oriented grains by the arrangements of these features. The presence of both positive and negative inclined shear bands in the same rotated Goss grains produces “fish-bone” structures [12]. This fish-bone structure originates from the mirror symmetry of the rotated Goss crystals with respect to the rolling plane. Shear bands with both positive and negative inclination angles in the same grain of the  $\{111\}\langle 112\rangle$  orientation are also possible to occur. However, since the  $\{111\}\langle 112\rangle$  oriented crystals do not have the mirror symmetry with respect to the rolling plane, for each individual  $\{111\}\langle 112\rangle$  grains, one of the two types of shear bands is always dominant.

Although shear bands in rotated Goss grains are predicted to be the most preferred at  $\pm 45^\circ$  inclination angle, the measurements indicate that most of the shear bands exhibit an inclination angle from  $25^\circ$  to  $35^\circ$ . Shear banding at inclination angles lower than  $45^\circ$  could occur in the rotated Goss oriented grains, since they also exhibit geometric softening effect as indicated in the previous sub-section. Geometric softening of these shear banding, however, is weaker than the one of the  $45^\circ$  inclination angle. Additionally, as the deformation progresses, thickness of rotated Goss oriented grains is reduced, inclination angle for shear bands become smaller. Accommodation of inclined shear strain to PSC will be less energetically advantage than activation of new shear bands at  $45^\circ$  inclination angle. Therefore, shear bands with  $25^\circ$  to  $35^\circ$  inclination angles, as observed in the rotated Goss oriented grains, could be results of the shear banding at initial  $45^\circ$  inclination angle. Afterward, because of the thickness reduction during rolling, shear band inclination angle is decrease but the accommodation of inclined shear strain to PSC is less favorable. Shear banding at initial  $45^\circ$  inclination angle ceases to develop at  $25^\circ$  to  $35^\circ$  inclination angles.

As can be seen in Figure 8.7a, c and e, orientations of crystal regions in shear bands are sharply distinguished from the ones outside the SB volume. In-band crystal

regions are recognized by their  $\langle 001 \rangle // ND$  orientations, on the contrary to the  $\langle 110 \rangle // ND$  orientation of rotated Goss grains. In Figure 8.7b, d and f, besides the peak at the  $\{110\} \langle 110 \rangle$  orientation, a high texture intensity peak is observed near the  $\{001\} \langle 100 \rangle$  orientation, which correspond precisely to the orientations that have been predicted by crystal plasticity simulations. During shear banding at initial  $45^\circ$  inclination angle, the  $\{001\} \langle 100 \rangle$  oriented crystals are calculated to be the most energetic stable. It is due to further straining of crystal regions in shear bands do not exhibit the geometric softening. The high intensity peak near the  $\{001 \langle 100 \rangle$  orientation is due to energy stable of the corresponding crystals in shear bands of the rotated Goss oriented grains. Microstructure observations in this sub-section indeed prove for the occurrence of the shear banding in the rotated Goss oriented grains. In shear bands of initial  $45^\circ$  inclination angle, the Cube ( $\{001\} \langle 100 \rangle$ ) orientation is present as the most preferred orientation.

### *8.3 The development of the $\alpha$ -fiber texture by local deformations*

The presence of the shifted  $\alpha$ -fiber, instead of the ideal  $\alpha$ -fiber, in recrystallization textures of electrical steels rises a question about the possible relation between these two fibers. By observing evolution of recrystallization textures in various BCC structured materials (e.g. electrical steels and IF steels) after severe plastic deformations (i.e. cross rolling and accumulated roll bonding), Kestens et al [2;13;14] clearly confirmed the close link between the ideal and the shifted  $\alpha$ -fiber textures. Developments of the shifted fiber components during recrystallization originate from components of the ideal  $\alpha$ -fiber. Successful development of the shifted  $\alpha$ -fiber orientations during recrystallization is partially contributed by the high migration rate of the special  $\langle 110 \rangle 26.5^\circ$  boundaries between nuclei and deformation matrix [15]. The presence of the shifted  $\alpha$ -fiber texture components in deformation textures of conventional rolling is indeed observed experimentally [2]. Deformation condition which brings orientation stability to the shifted  $\alpha$ -fiber oriented crystals in cold rolled samples, nevertheless, has not yet known.

None of the components of the shifted  $\alpha$ -fiber texture, in fact, are stable orientations in the deformation condition of plane strain compression. Crystal plasticity simulation for rolling texture of BCC structured materials does not show any preference to the shifted  $\alpha$ -fiber. On the contrary, because of their high stability, components of the  $\alpha$ -fiber are always among the most preferred ones in conventional rolling texture. Along the  $\alpha$ -fiber, the  $\{112\}\langle 110\rangle$  orientation and the rotated Cube ( $\{001\}\langle 110\rangle$ ) orientation are zero rotation orientations, i.e. the rotation rate of these orientations in plane strain compression display zero magnitude. The  $\{112\}\langle 110\rangle$  orientation is one of the most stable in conventional rolling textures (Figure 6.17). Orientation flow in vicinity of the  $\{112\}\langle 110\rangle$  orientation is convergence. Intensity of this component is usually predicted among the highest values for conventional rolling textures. Conversely, the rotated Cube ( $\{001\}\langle 110\rangle$ ) orientation is predicted as a metastable orientation. A strong orientation flow from the Cube ( $\{001\}\langle 100\rangle$ ) orientation toward the rotated Cube orientation can be observed, c.f. Figure 8.8. However, a flow of increasing rate from the rotated Cube orientation toward the  $\{112\}\langle 110\rangle$  orientation is also observed in the same figure. Generally, in the deformation condition of plane strain compression, orientations flow of the neighboring orientations toward the  $\alpha$ -fiber texture components, leaving almost no chance for components of the shifted  $\alpha$ -fiber to be retained.

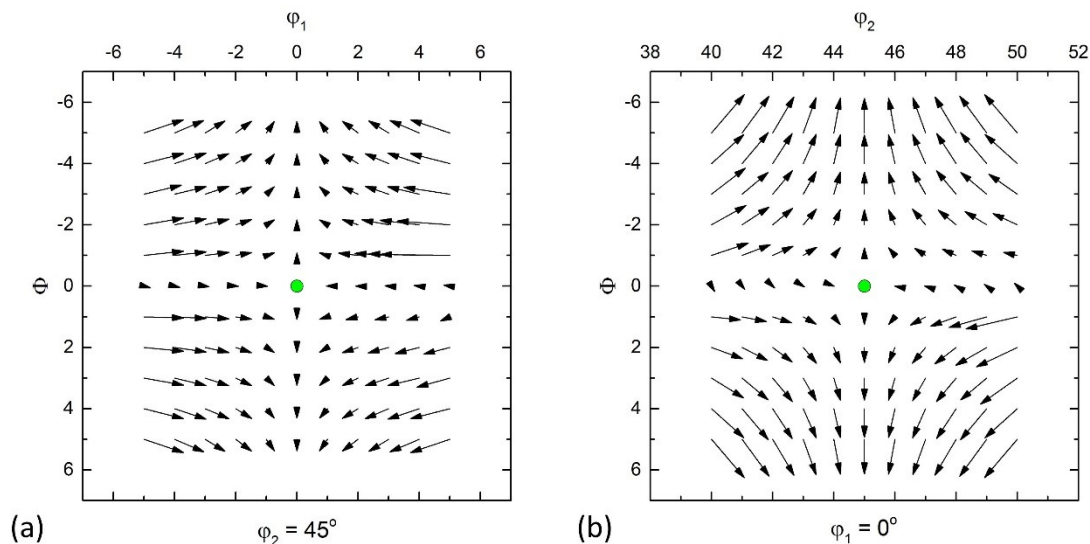


**Figure 8.8** Rotation field in vicinity of the rotated Cube ( $\{001\}\langle 110\rangle$ ) orientation under the plane strain compression of conventional rolling.

On the contrary to texture predictions by crystal plasticity models, orientations of the shifted  $\alpha$ -fiber are indeed observed in deformation microstructures of the conventional cold rolling [2;14]. The existence of the shifted  $\alpha$ -fiber oriented crystals is also evidently demonstrated by their successful development during recrystallization (c.f. section 7.1.2). The presence of the shifted  $\alpha$ -fiber oriented crystals in cold rolled samples, therefore, can only be argued by stability enhancement of these orientations under local deformation conditions. These local deformations should have influences on the steady flow toward the  $\alpha$ -fiber during conventional rolling of neighboring orientations. Moreover, a local deformation which could reverse the orientation flows toward the  $\alpha$ -fiber induced by plane strain compression and enhance the stability of the shifted  $\alpha$ -fiber texture components is the most desirable for this study.

To identify the local deformation condition(s), which can reverse the rotation flow toward the  $\alpha$ -fiber and increase the stability of the shifted  $\alpha$ -fiber, the response of the rotated Cube oriented crystal to different deformation conditions are first investigated. Orientation evolutions of other crystals belonging to the  $\alpha$ -fiber are then assumed to be similar to the ones of the rotated Cube oriented crystals. Crystal plasticity simulation to all crystals of the  $\alpha$ -fiber is finally implemented to demonstrate for the orientation evolution of the  $\alpha$ -fiber under the same local deformation condition.

Because the deformation condition of conventional rolling is approximated by plane strain compression, local deformations of the rotated Cube orientation could be reasonably assumed to be microscopic deviations from the macroscopic one. In addition to normal strain components along the RD ( $\epsilon_{11}$ ) and the ND ( $\epsilon_{33}$ ) of the PSC, local deformations may also contain different shear components ( $\epsilon_{ij}$ ). For each shear strain of  $\epsilon_{ij}$ , the shear vector is parallel to the direction (i) and perpendicular to the direction (j). To understand their effects on orientation evolution of the rotated Cube oriented crystal, these shear strains are separately combined to normal strains ( $\epsilon_{11}$  and  $\epsilon_{33}$ ) forming different sets of local deformations. To account for deviations of local deformations from the macroscopic one, ratios between shear and normal



components of the local velocity gradient ( $\kappa = L_{ij}/2L_{11}$  with  $i \neq j$ ) have been used. For all local deformation sets of various shear components ( $L_{12}$ ,  $L_{13}$ ,  $L_{21}$ ,  $L_{23}$ ,  $L_{31}$  and  $L_{32}$ ), the shear ratio ( $\kappa$ ) is chosen in the range from 0 to 0.25. The rotation rate vector components ( $\Omega_{23}, \Omega_{31}, \Omega_{12}$ ) of a rotated Cube oriented crystal with Euler angles ( $45^\circ$ ,  $90^\circ$ ,  $0^\circ$ ) are calculated by the full constraint Taylor crystal plasticity model under these local deformation conditions. The results of these calculations are given in Figure 8.9.

Among all deformation conditions applied to the rotated Cube crystal, different responses have been observed. As the most inert deformation conditions, local deformations containing the  $L_{12}$  and  $L_{32}$  shear components do not have any influence on the orientation of the rotated Cube oriented crystals. In the total range of the shear ratio from 0 to 0.25, the rotation rates of the rotated Cube orientation (Figure 8.9a and Figure 8.9f) are all equal to zero. In these deformation conditions, rotated Cube oriented crystals are deformed without re-orientation. Crystals of the  $\{001\}\langle 210 \rangle$  orientation as well as others orientations of the shifted  $\alpha$ -fiber, therefore, are not able to be present as a result of a velocity field containing  $L_{12}$  and  $L_{31}$  shear components.

For local velocity fields with  $L_{13}$  and  $L_{31}$  shear components, a similar responses of the rotated Cube can be observed from Figure 8.9b and Figure 8.9e. Two rotation rate vector components ( $\Omega_{23}, \Omega_{12}$ ) of the rotated Cube orientation in these local deformation conditions are different from zero. These rotation rate components have equal magnitude but opposite signs, while the other component ( $\Omega_{31}$ ) of the rotation rate vector does not change its zero value in the entire range of the considered shear ratio. The developments of the rotation rate vector to the shear ratio implies rotations of the rotated Cube oriented crystals around one of the  $\langle 110 \rangle$  crystallographic axes. Specifically, for the rotated Cube ( $(0\ 1\ 0)[1\ 0\ 1]$ ) orientation represented by ( $45^\circ$ ,  $90^\circ$ ,  $0^\circ$ ) Euler angles, this is the rotation at a constant rate around the  $[-101]$  crystallographic axis, which is parallel to the TD axis. In the reference coordinate system (RD, TD, ND), deformation conditions with  $L_{13}$  and  $L_{31}$  shear components  $\neq 0$  result in rotations of the rotated Cube oriented crystals around TD, which is parallel to the  $\langle 110 \rangle$  crystallographic axes. Hence, under these deformation conditions (i.e.

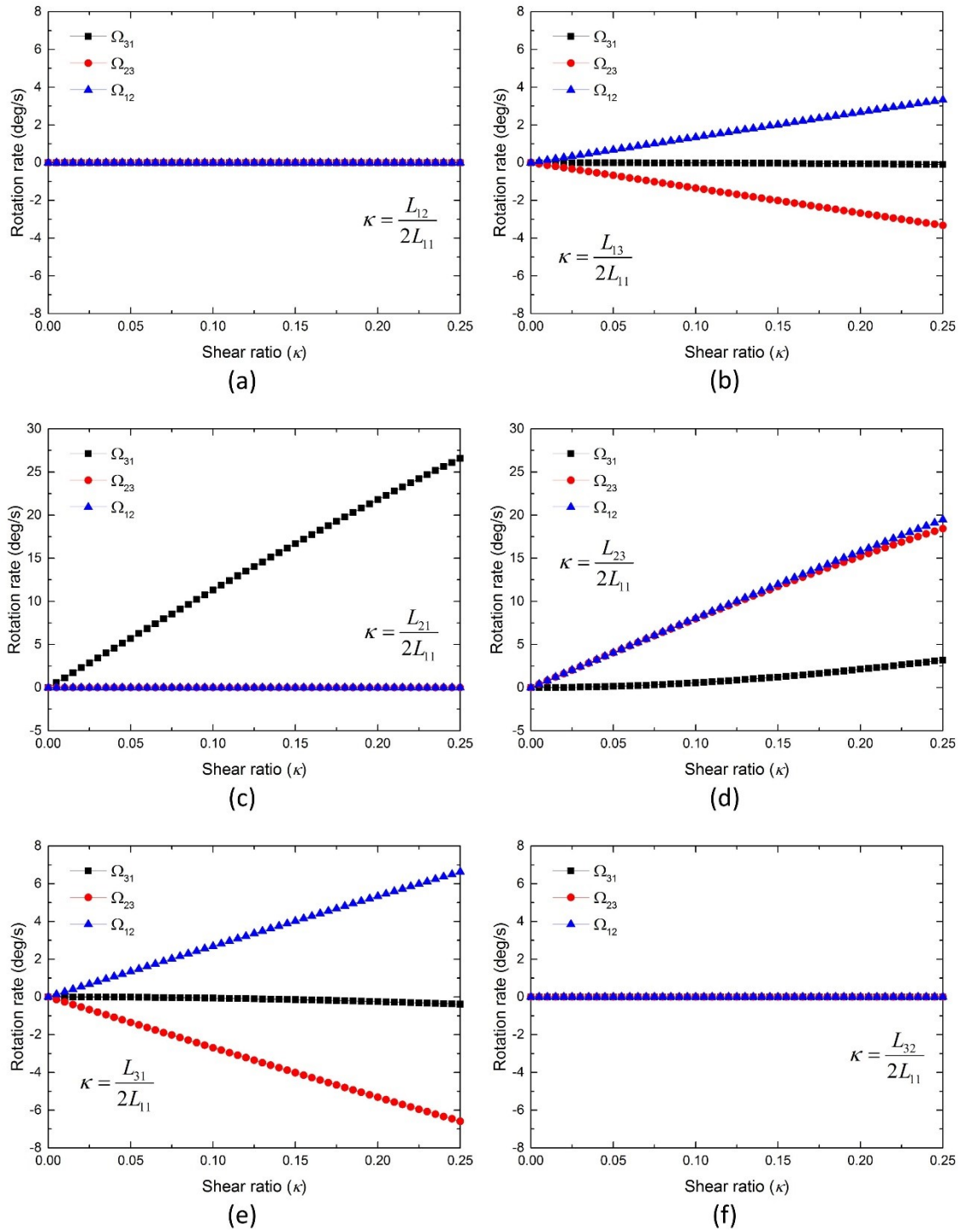


**Figure 8.9** Rotation rates ( $\Omega_{23}, \Omega_{31}, \Omega_{12}$ ) of a rotated Cube orientation at the  $(45^\circ, 90^\circ, 0^\circ)$  Euler angles in local deformation conditions, which are combinations of normal deformation components ( $L_{11}$  and  $L_{33}$ ) and various shear deformation components (a)  $L_{12}$ , (b)  $L_{13}$ , (c)  $L_{21}$ , (d)  $L_{23}$ , (e)  $L_{31}$  and (f)  $L_{32}$ . Ratios of shear components to normal components ( $\kappa = L_{ij}/2L_{kk}$ ) in local deformations are given in the range of 0.0 to 0.25.

$L_{13}$  or  $L_{31} \neq 0$ ) the rotated Cube orientation does not rotate toward the shifted  $\alpha$ -fiber orientations.

The response of the rotated Cube orientation to deformations with  $L_{23} \neq 0$  shear component are rather complicated (Figure 8.9d). Numerically, the values of all three components of the rotation rate vector increase proportionally to the shear ratio. However, the increments for various rotation rate vector components are different. The  $\Omega_{23}$  and  $\Omega_{12}$  components are nearly identical and both a factor  $\sim 7.0$  times higher than the  $\Omega_{31}$  component. At the highest considered shear ratio ( $\kappa = 0.25$ ), values of the  $\Omega_{23}$  and  $\Omega_{12}$  rotation rate components are 18.4 and 19.5 deg/s, while the value of the  $\Omega_{31}$  component is 3.2 deg/s. The non-linear development of all rotation rate vector components results in a complicated rotation history of the rotated Cube oriented crystals. The rotation rates of the crystals are not constant and the rotation axes are not fixed. By neglecting the small evolution of the  $\Omega_{31}$  component as compared to the other two rotation rate components, the response of the rotated Cube orientation to deformations of  $L_{23}$  shear component are easier to be analyzed. In this simplified situations, rotation axes of the rotated Cube orientation are closed to the  $\langle 110 \rangle$  crystallographic axis which is parallel to the RD. The rotation of the rotated Cube oriented crystals in deformation conditions containing the  $L_{23}$  shear component is toward the  $\{111\}\langle 110 \rangle$  orientation, like in plane strain compression. Therefore, for all considered local deformations containing the  $L_{23}$  shear components, the main flow of orientation is toward the  $\{112\}\langle 110 \rangle$  orientation, but not toward the  $\{001\}\langle 210 \rangle$  orientation.

In the last set of local deformations, the  $L_{21}$  shear component is combined with the  $L_{11}$  and  $L_{33}$  normal components. Effects of these local deformations on the rotation rate vector of the rotated Cube orientation can be observed in Figure 8.9c. The evolution of the  $\Omega_{31}$  rotation rate component is linear to the shear ratio ( $\kappa$ ), while there is no response of the other two rotation rate components ( $\Omega_{23}, \Omega_{12}$ ) in the entire range of considered shear ratios. The response of the rotation rate components to the shear ratio indicates rotations of the rotated Cube orientation around the  $\langle 001 \rangle$  crystallographic axis which is parallel to the ND. In addition, the magnitude of these

rotations is linearly proportional to the shear ratio ( $\kappa = L_{21}/2L_{11}$ ). Local deformations containing the  $L_{21}$  shear component, therefore, are the only deformation conditions promoting the formation of the  $\{001\}\langle 210 \rangle$  orientations from the  $\{001\}\langle 110 \rangle$  oriented crystals.

By rotations around the  $\langle 001 \rangle // ND$  axis, the rotated Cube oriented crystals are able to re-orient toward the  $\{001\}\langle 210 \rangle$  orientation and even to the  $\{001\}\langle 100 \rangle$  orientation. These rotations are uniquely defined by deformation conditions with  $L_{21}$  shear velocity gradient different from zero. Nevertheless, because the rotation rate of the rotated Cube orientation is linearly dependent on the ratio between the  $L_{21}$  and the  $L_{11}$  velocity gradients, any components of the Cube fiber from the rotated Cube ( $\{001\}\langle 110 \rangle$ ) to the Cube ( $\{001\}\langle 100 \rangle$ ) orientations could be a stable orientation.

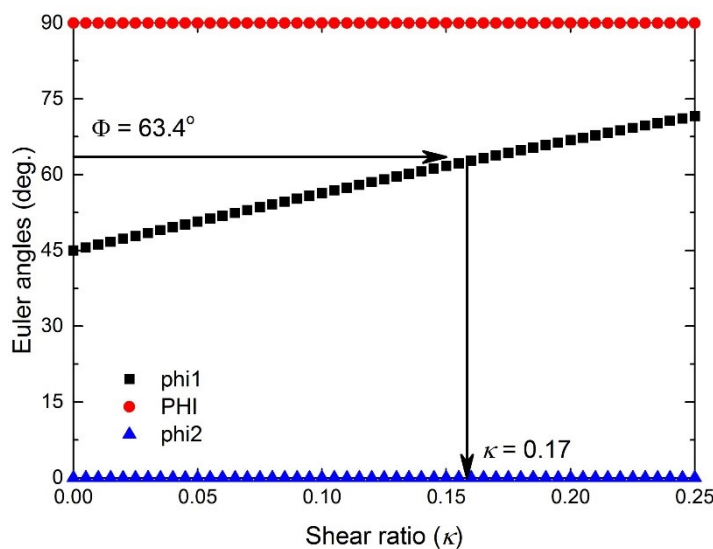


**Figure 8.10** The change of zero orientations along the Cube ( $\langle 001 \rangle // ND$ ) fiber with shear ratio ( $\kappa$ ) of the  $L_{21}$  and the  $L_{11}$  velocity gradient components.

To identify specifically the shear ratio and thus the deformation condition, which produces a stable shifted  $\alpha$ -fiber, the zero rotations along the Cube fiber for various shear ratios have been calculated. In these calculations, the shear ratio ( $\kappa$ ) is changed from 0 to 0.25 and zero rotation components (i.e.

$$\Omega_{23} = \Omega_{31} = \Omega_{12} = 0)$$

along the Cube fiber texture

are identified for each individual value the shear ratio. Figure 8.10 shows the position of the zero rotation orientations along the Cube fiber as a function of shear ratios ( $\kappa = L_{21}/2L_{11}$ ) from 0 to 0.25. As expected, at the shear ratio of zero, corresponding to the plane strain compression, the rotated Cube ( $\{001\}\langle 110 \rangle$ ) orientation is defined as the meta-stable component along the Cube ( $\langle 001 \rangle // ND$ ) fiber. When the shear ratio is increased from 0 to 0.25, the zero rotation orientation along the Cube fiber linearly

shifts from the rotated Cube toward the Cube ( $\{001\}\langle 100\rangle$ ) orientation by rotating around the  $\langle 001\rangle//ND$  axis. Remarkably, at the shear ratio of 0.17, the  $\{001\}\langle 210\rangle$  orientation of the shifted  $\alpha$ -fiber texture which is represented by the three Euler angles of  $(63.4^\circ, 90^\circ, 0^\circ)$  is predicted to be a zero rotation component of the Cube fiber texture. The presence of the  $\{001\}\langle 210\rangle$  orientation at the shear ratio of  $\kappa = 0.17$  in the deformation condition with  $L_{21} \neq 0$  suggests the highest stability of this orientation as well as other components of the shifted  $\alpha$ -fiber texture.

Local velocity fields containing the  $L_{21}$  shear velocity gradient are able to reverse orientation flows induced by macroscopic PSC and enhance the stability of the shifted  $\alpha$ -fiber orientations. However, the  $L_{21}$  shear velocity gradient is not compatible to the macroscopic deformation condition of conventional cold rolling. In theory, the  $L_{21}$  shear velocity gradient is produced by differences of in TD displacement along the RD. In reality, widening of rolling sheets are usually negligible, because the homogeneous gradient of TD displacement along the RD is zero. The  $L_{21}$  shear velocity, therefore, can only be present as a local deformation at grain-scales, but not at the sample scale. Moreover, it is easy to recognize imbalance effects of the  $L_{21}$  shear velocity gradient on grain orientations. Regardless of the orthorhombic sample symmetry, rotations of the rotated Cube ( $\{001\}\langle 110\rangle$ ) oriented crystals toward the  $(001)[210]$  orientation and the  $(001)[120]$  orientation must be the same, based on symmetry arguments and experimental observation. Nevertheless, by applying the local deformation containing the  $L_{21}$  shear component at a shear ratio  $\kappa = 0.17$ , the rotated Cube crystals only rotate toward the  $(001)[210]$  orientation, called the positive direction. The negative rotation toward the  $(001)[120]$  orientation of the rotated Cube oriented crystals is only possible by imposing the  $L_{21}$  velocity gradient along the opposite direction.

The conditions for macroscopic deformation compatibility and balance effects of crystallographic rotations require a *dual* deformation condition, with both positive and negative  $L_{21}$  shear, for the formation of the shifted  $\alpha$ -fiber. Thanks to the cancelation of the  $L_{21}$  velocity gradients locally, the composite parts of this local deformation mode are fully compatible with the boundary conditions of plane strain compression. The net effect of this co-deformation condition on the initial rotated

cube orientation is the splitting and rotating toward two equivalent branches of the shifted  $\alpha$ -fiber.

Texture evolution of the  $\alpha$ -fiber oriented crystals in the co-deformation condition can be simulated by crystal plasticity models and will be given later. In addition, the microstructure locations that are suitable for the formation of the shifted  $\alpha$ -fiber orientations can be predicted from the co-deformation condition. Figure 8.11 schematically shows two possible geometrical configurations in which co-deformation occurs and the shifted  $\alpha$ -fiber orientations are able to be formed. In the first configuration, c.f. Figure 8.11a, the  $L_{21}$  shear velocity gradient is supposed to

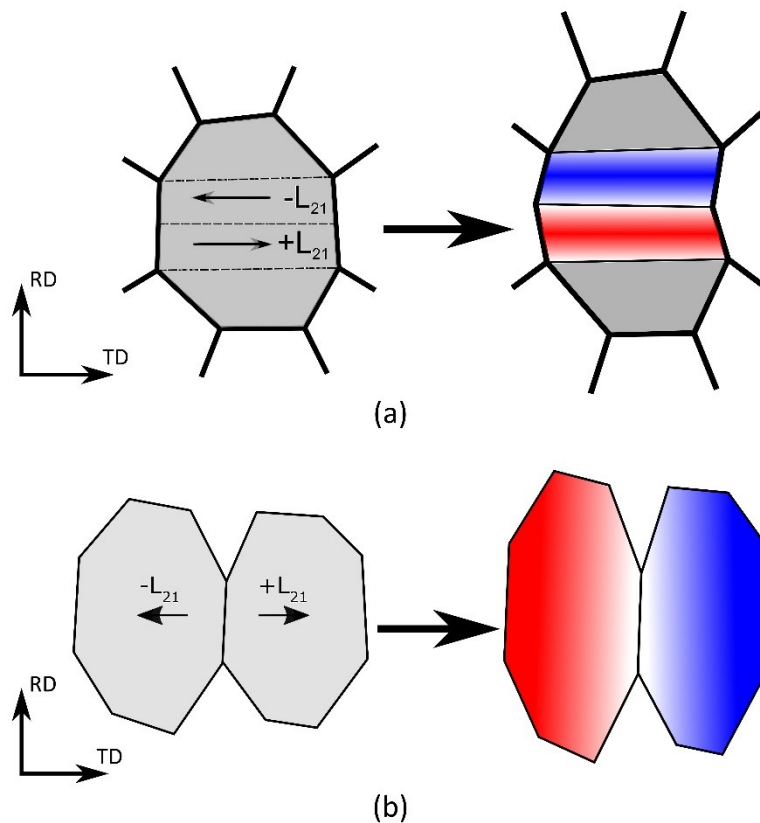


**Figure 8.11 Schematic representations for microstructures which are preferred by crystals of the shifted  $\alpha$ -fiber textures. Deformation conditions at these microstructures are similar, but arrangements of the  $L_{21}$  shear velocity gradient are different: (a) in a single grain and (b) in a pair of grains.**

appear in individual grains. The variation of the  $L_{21}$  velocity gradient in both positive and negative directions produces alternative deformation bands across the RD inside each crystals. Preferred orientations of alternative bands are components from different branches of the shifted  $\alpha$ -fiber. The variation of  $L_{21}$  velocity gradient among different bands may produce wavy grain boundaries along the RD.

Instead of appearing in individual grains, the  $L_{21}$  shear velocity gradient could also appear in couples of neighboring crystals. In the second case (c.f. Figure 8.11b), each grain in a local microstructure is deformed by a single deformation condition, with  $L_{21}$

either positive or negative. Because of the single deformation condition, all preferred orientations in an individual grain rotate toward the same branch of the shifted  $\alpha$ -fiber. Alternatively, orientations from the other branch of the shifted  $\alpha$ -fiber appear in the neighboring crystals, which are deformed under the flow condition with the  $L_{21}$  velocity gradient of the opposite direction.

In addition to the local deformation condition, the development of shifted  $\alpha$ -fiber orientations from  $\alpha$ -fiber oriented crystals is also affected by the strain magnitude and the stored energy in the deformed crystals. The development of the  $\{001\}\langle 210 \rangle$  orientation in the  $\{001\}\langle 110 \rangle$  oriented crystals during straining from  $\varepsilon_{VM}$  varying from 0 to 2.5, therefore, is investigated by simulations with the full constraints Taylor model. The orientation evolution with strain of a crystal initially having the rotated Cube orientation is shown by the change of the three Euler angles. The developments of the stored energy increments in this crystal during deformation is represented by a function of the Taylor factor as a function of applied strain. Figure 8.12 shows the evolutions of the crystallographic orientation and the Taylor factor of the rotated Cube oriented crystal after a  $\varepsilon_{VM}$  strain, increasing from 0 to 2.5 with strain increments in steps of 0.005. The applied deformation condition is characterized by a velocity field with  $L_{21}$ ,  $L_{11}$  and  $L_{33} \neq 0$ , in which the shear ratio ( $\kappa = L_{21}/2L_{11} = 0.17$ ).

As can be seen in Figure 8.12, the evolutions with strain of both crystallographic orientation and Taylor factor of the crystal are non-linear. With increasing strain, the rotated Cube oriented crystal is rotated around its  $\langle 001 \rangle // ND$  crystallographic axis with decreasing rates. This rotation produces changes in the crystallographic orientation, from the  $\{001\}\langle 110 \rangle$  initial orientation to the  $\{001\}\langle 210 \rangle$  final orientation. The rate of these rotation, however, becomes smaller when the crystal approaches its stable end orientation at  $\{001\}\langle 210 \rangle$  after a the strain of 2.5.

Different from the orientation evolution, the change of the Taylor factor with strain can be divided into two consecutive parts. In the first part of the crystal plasticity, the Taylor factor of deformed crystals quickly increases from 1.750 to 1.795 as the strain increases from 0 to 0.5. On the contrary, in the second part, corresponding to the strain from 0.5 to 2.5, the Taylor factor gradually decreases from

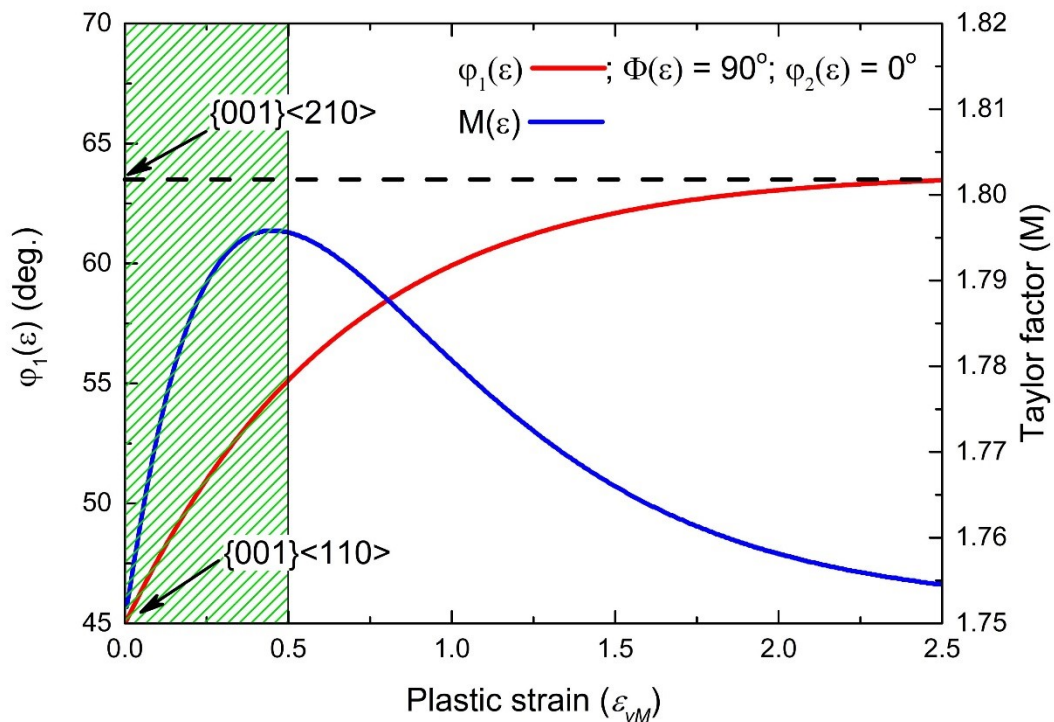


**Figure 8.12** Evolutions with strain of crystallographic orientation and Taylor factor in a rotated Cube oriented crystal having the initial orientation at  $(45^\circ, 90^\circ, 0^\circ)$  Euler angles. The applied deformation is composed by the shear  $L_{21}$  and the normal  $L_{11}$  and  $L_{33}$  velocity gradients, in which the shear ratio  $\kappa = L_{21}/2L_{11} = 0.17$ . The von Mises equivalent strain ( $\varepsilon_{vM}$ ) applied to crystals is increase from 0 to 2.5.

1.795 to 1.750. The evolution of the Taylor factor during crystal plasticity can give some insight in the development of dislocation structures and changes of dislocation density in deformed crystals.

It is assumed that the Taylor factor is a scaled measure of the stored energy in deformed crystals. The crystal plasticity model of the Taylor factor, c.f. Figure 8.12, shows that with  $\varepsilon_{vM} < 0.5$  the increase in Taylor factor can be interpreted as a phase of generation and accumulation of dislocations. The stored energy in deformed crystals during this period increases after each deformation steps and the latter deformation steps will require higher stresses than the previous ones, which corresponds to a stage of geometric hardening (i.e. rotation toward higher Taylor factor orientations). In the second part of straining with  $\varepsilon_{vM} > 0.5$  the crystal plasticity calculation reveals a reduction of the Taylor factor corresponds to an energy



advantage of geometric softening. Dislocation density in deformed crystals is still increase, but rotation toward “softer” orientation helps to limit the increase of plastic stress. Local deformation of the rotated Cube oriented crystals is difficult to occur at the initial, rather than later period during straining.

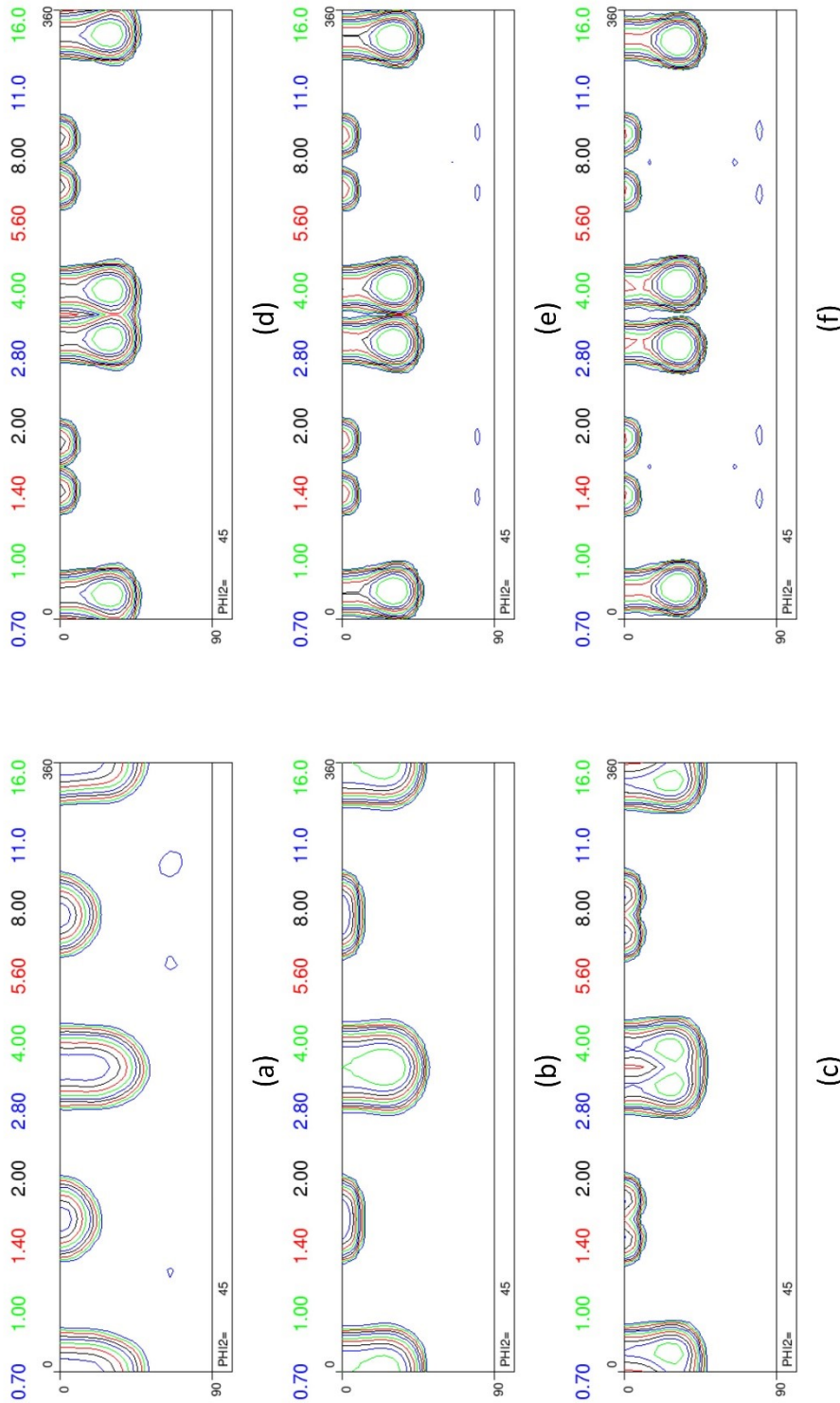


Figure 8.13 Orientation evolution of the  $\alpha$ -fiber texture after straining ( $\epsilon_{yM}$ ) from 0 to 2.5 by the deformation condition containing the  $L_{21}$  velocity gradient of the shear ratio  $\kappa = \pm 0.17$ . Local textures are given at the strain of (a) 0, (b) 0.5 (c) 1.0, (d) 1.5, (e) 2.0 and (f) 2.5.

The rotation toward the  $\{001\}\langle 210 \rangle$  orientation of the  $\{001\}\langle 110 \rangle$  initial oriented crystals would not occur immediately during straining. However, as the plastic strain for the rotated Cube oriented crystal passes a critical value (e.g.  $\sim \varepsilon_{VM} = 0.5$ ), development of the  $\{001\}\langle 210 \rangle$  oriented crystals becomes energetically favorable. Formation of the shifted  $\alpha$ -fiber oriented crystals in grains of the  $\alpha$ -fiber orientation, therefore, will be more prominent after high plastic deformation. This simulation result could be an argument for the observation of the shifted  $\alpha$ -fiber oriented crystals in the  $\alpha$ -fiber oriented grains. Experimentally, the shifted  $\alpha$ -fiber orientations are frequently reported to be present in recrystallization textures of heavily deformed samples, rather than of lightly deformed ones [1;14].

To complete the investigation on the formation of the shifted  $\alpha$ -fiber texture, texture development after straining under co-deformation conditions with  $L_{21} \neq 0$ , is calculated by the FCT crystal plasticity model. The deformation condition used in these simulations contains the  $L_{21}$  velocity gradient with the shear ratio  $\kappa = \pm 0.17$  and an  $\alpha$ -fiber initial texture, which is represented by 10,000 individual orientations homogeneously distributed from the  $\{001\}\langle 110 \rangle$  orientation to the  $\{112\}\langle 110 \rangle$  orientation and observing orthorhombic sample symmetry. Texture evolutions after each strain increments of 0.5 from 0 to 2.5 are given in Figure 8.13.

Compared to the initial  $\alpha$ -fiber texture, local deformation texture after straining to  $\varepsilon_{VM} = 0.5$  has no significant evolution (c.f. Figure 8.13a and Figure 8.13b). Most of the oriented crystals are rotated toward the  $\{112\}\langle 110 \rangle$  orientation. Rotation rates, however, are not similar as the higher rotation rates are observed for the crystals with orientations closer to the  $\{114\}\langle 110 \rangle$  orientation. The most intense peaks in this deformation texture after straining to 0.5 is observed near the  $\{113\}\langle 110 \rangle$  orientation with 18 mrd. However, this deformation texture is not as sharp as the initial one. A wide scatter of orientations around the  $\alpha$ -fiber in the deformation texture are due to the presence of the  $L_{21}$  velocity gradient in the imposed velocity condition. This  $L_{21}$  component changes the reverses the orientation flow toward the shifted  $\alpha$ -fiber components. Nevertheless, the strain energy is not sufficient to support

these rotations, and thus the result is the widening of the  $\alpha$ -fiber as observed in Figure 8.13b.

When the equivalent strain is increased from 0.5 to 1.0 and 1.5, the splitting of the  $\alpha$ -fiber becomes more favorable, due to the geometric softening. After a value of  $\varepsilon_{VM} = 1.0$  (Figure 8.13c), the splitting of the  $\alpha$ -fiber is identified by the presence of two intensity peaks near the  $\{113\}\langle 110 \rangle$  component. These two peaks are variants of the same crystallographic orientations which are connected by a rotation of 10deg around the ND axis. After increasing the strain  $\varepsilon_{VM}$  to 1.5, these two peaks are further shifted apart (Figure 8.13d). The shift, however, becomes smaller as the equivalent strain is increased to 2.0 and 2.5 (Figure 8.13e and Figure 8.13f). The smaller texture evolution in the strain range from 1.5 to 2.5, as compared to the ones in the previous range, is due to the reduction of rotation rates when crystals approach their stable end orientations.

### *8.4 Conclusions*

Local orientation evolutions, in general, do not show any significant influence on formation of macroscopic deformation textures. Local texture components are usually not visible in the macroscopic texture. However, they have been shown to play a very important role in the formation of recrystallization textures. In this chapter, orientation developments in deformation bands and shear bands of some specific crystallographic orientations were investigated.

Contrary to deformations at elevated temperatures, plastic deformations at low temperatures are not homogenous among grains of various orientations. Depending on the applied strain and resistance to deformation for specific orientations, different sub-grain structures as well as various micro textures may develop locally. In rolled samples of BCC structured materials, the  $\langle 110 \rangle // RD$  oriented grains are considered to have the lower deformation resistances compared to the grains of the  $\langle 111 \rangle // ND$  fiber. The  $\langle 110 \rangle // RD$  oriented grains, therefore, are more homogeneously deformed than the  $\langle 111 \rangle // ND$  oriented grains.

In spite of their easy susceptibility to plastic deformation, oriented grains of the  $\langle 110 \rangle // \text{RD}$  fiber texture will fragment after certain level of straining. Fragmentation of the  $\alpha$ -fiber oriented grains is at the origin for the development of the shifted  $\alpha$ -fiber oriented grains in recrystallization textures. Grain fragmentation, in general, depends on local deformation conditions rather than on the macroscopic boundary conditions. Among all possible local deformation conditions for the  $\langle 110 \rangle // \text{RD}$  oriented grains, only the one with the  $L_{21}$  shear component  $\neq 0$  could increase the stability of the shifted  $\alpha$ -fiber oriented grains and reverse the orientation flow around the  $\alpha$ -fiber oriented grains. The presence of the  $L_{21}$  shear components of opposite sign along the RD produces deformation bands in grains of the  $\alpha$ -fiber oriented grains. In such bands, the most preferred orientations are predicted as components of the shifted  $\alpha$ -fiber texture.

Because they have exhibit the higher deformation resistance than the  $\alpha$ -fiber oriented grains, grains of the  $\gamma$ -fiber texture are more fragmented during plastic deformation. The most prominent fragmentation mode for  $\gamma$ -fiber oriented grains is shear banding. Microscopic shear banding in oriented crystals is known as a result of geometric softening, i.e. in-band crystallites rotate toward lower Taylor factor orientations. Shear banding emerging in the  $\{111\}\langle 112 \rangle$  oriented grains will rotated toward the Goss orientation, which is one of the most important recrystallization texture components for electrical steels. By crystal plasticity simulations, shear banding in the  $\{111\}\langle 112 \rangle$  oriented grains at  $35^\circ$  inclination angles have been shown to exhibit geometric softening. It was shown that Goss oriented grains exhibit the lowest Taylor factor under  $35^\circ$  inclined simple shear, together with the largest lattice curvature, i.e. the highest rotation gradient among all possible orientations appearing in the SB.

With the highest deformation resistance under boundary conditions of plane strain compression, the rotated Goss ( $\{110\}\langle 110 \rangle$ ) oriented grains are expected to show the strongest geometric softening induced by shear banding among all orientations of BCC structured materials. Because of the mirror symmetry with respect to the rolling plane, shear banding in rotated Goss oriented grains are

identical for positive and negative inclination angles. Shear banding in rotated Goss oriented grains at inclination angles lower than  $|45^\circ|$  is dependent on energy criteria, but not on rotation rates of in-band crystal regions as the rotation rate is independent of the SB inclination angle in the domain of  $-45^\circ$  to  $+45^\circ$ . The highest energy gain by geometric softening is calculated for shear banding under a  $\pm 45^\circ$  inclination angle. Geometric softening of such shear bands is exhausted after in-band crystal regions rotations  $45^\circ$  around the  $\langle 100 \rangle // \text{TD}$  axis, which rotates the initial rotated Goss orientation to the ideal Cube ( $\{001\} \langle 100 \rangle$ ) component. Shear banding in the rotated Goss oriented grains and the presence of the Cube oriented crystal regions in shear bands were both observed in EBSD microstructural investigations of Fe-Si steels.

### 8.5 References

- [1] Homma H, Nakamura S, Yoshinaga N. On  $\{h,1,1\} \langle 1/h,1,2 \rangle$ , the recrystallisation texture of heavily cold rolled BCC steel. Mater Sci Forum, vol. 467-470, 2004. p.269.
- [2] Gobernado P, Petrov RH, Kestens LAI. Recrystallized  $\{3\ 1\ 1\} \langle 1\ 3\ 6 \rangle$  orientation in ferrite steels. Scripta Materialia. 2012;66:623.
- [3] Haratani T, Hutchinson WB, Dillamore IL, Bate P. Contribution of shear banding to origin of Goss texture in Silicon Iron. Met Sci. 1984;18:57.
- [4] Ushioda K, Hutchinson WB. Role of shear bands in annealing texture formation in 3%Si-Fe  $(111)[112]$  single crystals. ISIJ Int. 1989;29:862.
- [5] Dillamore IL, Roberts JG, Bush AC. Occurrence of shear bands in heavily rolled cubic metals. Met Sci. 1979;13:73.
- [6] Hatherly M, Malin AS. Shear bands in deformed metals. Scripta Metallurgica. 1984;18:449.
- [7] Ridha AA, Hutchinson WB. Recrystallisation mechanisms and the origin of cube texture in copper. Acta Metallurgica. 1982;30:1929.
- [8] Barnett MR. Role of in-grain shear bands in the nucleation of  $\langle 111 \rangle // \text{ND}$  recrystallization textures in warm rolled steel. ISIJ Int. 1998;38:78.
- [9] Murakami K, Morishige N, Ushioda K. The effect of cold rolling reduction on shear band and texture formation in Fe-3%Si alloy. Mater Sci Forum. 2012;715-716:158.

- [10] Bunge HJ, Esling C, Dahlem E, Klein H. The Development of Deformation Textures Described by an Orientation Flow Field. *Texture Microstruct.* 1986;6:181.
- [11] Tóth LS, Jonas JJ, Daniel D, Ray RK. Development of ferrite rolling textures in low- and extra low-carbon steels. *Metallurgical Transactions A.* 1990;21:2985.
- [12] Vanderschueren D, Yoshinaga N, Koyama K. Recrystallisation of Ti if steel investigated with electron back-scattering pattern (EBSP). *ISIJ Int.* 1996;36:1046.
- [13] Kestens L, Jonas JJ, Van Houtte P, Aernoudt E. Orientation selection during static recrystallization of cross rolled nonoriented electrical steels. *Texture Stress Microstruct.* 1996;26-27:321.
- [14] Gobernado P, Petrov R, Ruiz D, Leunis E, Kestens LAI. Texture evolution in Si-alloyed ultra low-carbon steels after severe plastic deformation. *Adv Eng Mater.* 2010;12:1077.
- [15] Verbeken K, Kestens L, Nave MD. Re-evaluation of the Ibe-Lücke growth selection experiment in a Fe-Si single crystal. *Acta Mater.* 2005;53:2675.



# 9

## *General conclusions*

Polycrystalline materials are, in general, anisotropic. This anisotropy arises from crystallographic structures and the non-random arrangements of crystalline grains in aggregates. During material processing, anisotropy is intensified by axial boundary conditions. In polycrystalline materials, grains which better accommodate to external constraints will constitute higher fractions of the aggregates than the other grains. Crystallographic texture of a material results from the orientation preference of grains, is induced by material processing, and affect the performance of materials in applications.

In this study, the relationship between crystallographic texture and the behavior of an electrical steel during material processing is investigated. Electrical steels are conventional steel products. However, to remain competitive with other soft magnetic materials, their properties and performance must be improved. From this viewpoint,



the texture evolution during deformation and recrystallization of a Fe-1.2 wt.% Si alloy are investigated via experimental measurements and theoretical simulations. The overall conclusions of this work are summarized as follows:

Texture development in polycrystals during plastic deformation depends on the crystallographic-orientation stability under specific deformation conditions. The glide of multi-dislocation systems is required for satisfying the geometric constraints of the deformation conditions and, in most cases, this glide is accompanied by crystal re-orientation. Nevertheless, in some special cases, dislocation glide is symmetrical and crystals are then plastically deformed without changing in their orientations. Crystals with invariant orientations during plastic deformation are referred to as zero-rotation crystals, and are classified as stable, meta-stable or un-stable, depending on the vicinal flow fields. For example, stable orientations are zero-rotation crystals with convergent vicinal flow fields. Stable orientations occur with the highest intensities in the measured deformation textures of conventionally and asymmetrically rolled materials. However, the crystal-orientation stabilities under deformation conditions of conventional rolling and, hence, the resulting textures differ from the stabilities and textures associated with asymmetrical rolling. The deformation condition of (i) symmetrical rolling is referred to as plane strain compression (PSC), which is characterized by two normal strain components ( $\epsilon_{11}$  and  $\epsilon_{33}$ ) and (ii) asymmetrical rolling (as calculated in this study) includes these normal components and the shear strain ( $\epsilon_{13}$ ) component. For asymmetrical rolling, the orientation stability depends on the normal components and the shear strain component. Depending on the ratio  $\kappa$  of the shear strain ( $\epsilon_{13}$ ) and the normal strain ( $\epsilon_{11}$ ) components, the deformation textures resulting from asymmetrical rolling can be considered combinations of PSC textures and simple shear textures.

Different rolling modes are characterized by differing deformation conditions, which yield inter-sample differences in the deformation textures and, in some cases, intra-sample through-thickness texture variations. Samples rolled at high temperature experience large amounts of shear strain, owing to the friction between the rolls and the material surfaces. In conventionally hot-rolled samples, the shear strains are mainly concentrated in the sub-surface layers, which constitute ~15% of

the total sample thickness. These strains lead to the formation of shear deformation textures, consisting of the Brass ( $\{110\}\langle 112\rangle$ ), Copper ( $\{112\}\langle 111\rangle$ ), and Goss ( $\{110\}\langle 001\rangle$ ) components, in the sub-surface regions of the material. However, the mid-thickness regions of the sample are characterized by a deformation texture consisting mainly of  $\alpha$ -( $\langle 110\rangle//RD$ ) and  $\gamma$ -( $\langle 111\rangle//ND$ ) fiber components. In the asymmetrically hot-rolled samples, shear strains penetrate on the sample thickness (rather than being concentrated mainly in the sub-surface regions). A monotonic increment in these strains across 75% of the total sample thickness leads to smooth changes in the deformation textures associated with the asymmetrically rolled samples.

The symmetrically and asymmetrically cold-rolled samples both exhibit through-thickness texture homogeneity. Owing to the low friction between the rolls and the sample surfaces, the deformation conditions at the sub-surface regions of the material differ only modestly from those at the mid-thickness. Additionally, the shear strain of asymmetrical rolling is dissipated via slip between the sample and the rolls, resulting in only small differences between the asymmetrical-cold-rolling texture and the PSC texture.

Recrystallization refers to the restoration of structural perfection in plastically deformed grains, through the release of plastically stored energy. Moreover, the recrystallization microstructure and texture are formed with growth of the recrystallization nuclei into the deformed matrix.

In this study, the development of recrystallization texture components in both hot- and cold-rolled samples is strongly influenced by the orientation preference of nucleation. The growth of oriented nuclei in the cold-rolled samples is enhanced by high migration rates of the  $\langle 110\rangle 26.5^\circ$  special boundary. However, this selective growth has negligible effect on the recrystallization textures of the hot-rolled samples.

An orientation preference of nucleation refers to the ability of some deformed crystals to become viable nuclei of recrystallization. The stored energy varies with the crystal orientation and oriented nucleation arises from differences in this energy.

During plastic deformation, dislocations are generated and accumulated in deformed crystals. The stress fields surrounding these lattice defects (i.e., the dislocations) lead to an increase in the internal energy of the crystals. The plastically stored energy represents, therefore, the amount of energy accumulated in the crystals during plastic deformation. Considering the grains in a sample, those with higher dislocation densities store a larger amount of mechanical energy than those with lower densities (and vice-versa). In crystal plasticity theory, the stored energy in crystals is represented by the Taylor factor. This factor is a dimensionless parameter that is used as a measure of energy dissipation, via slip, in a unit crystal volume subjected to a specific deformation condition.

In hot-rolled and annealed samples, high-intensity peaks of the recrystallization textures are all measured at low Taylor factor orientations. The formation of recrystallization textures in hot-rolled samples is attributed to low-stored-energy nucleation and the random growth of these nuclei into the deformation matrix. Symmetrical and asymmetrical hot rolling are characterized by different deformation conditions. Therefore, for the same material, the deformation textures and the distribution of plastically stored energy among the grains differ between these rolling conditions. Furthermore, owing to the difference in the deformation conditions, the recrystallization textures of symmetrically hot-rolled samples differ significantly from those of their asymmetrically hot-rolled counterparts.

Samples subjected to symmetrical and asymmetrical cold rolling exhibit almost the same recrystallization textures. For example, in both cases, the highest-intensity and second-highest intensity peaks occur at the  $\{111\}\langle 112 \rangle$  orientation and components along the shifted  $\alpha$ -fiber, respectively. The occurrence of similar features in the recrystallization textures indicates that recrystallization in these two sets of samples is governed by the same mechanism. However, owing to the small difference in the deformation conditions, the deformation textures of the symmetrically cold-rolled samples differ slightly from those of their asymmetrically rolled counterparts. Therefore, the cold rolling mode has a smaller effect on the recrystallization texture than on the deformation texture.

The occurrence of the  $\{111\}\langle 112 \rangle$  orientation in the recrystallization textures of cold-rolled samples is attributed to high-stored-energy nucleation. This orientation develops preferentially, compared with the other  $\gamma$ -fiber components, owing to the high migration rate of the  $\langle 110 \rangle 26.5^\circ$  boundaries lying between these crystals and the deformed  $\alpha$ -fiber grains.

However, orientations of the shifted  $\alpha$ -fiber are not described by either high- or low-stored-energy nucleation mechanisms. Calculations performed by the full constraint Taylor crystal plasticity model indicate that these orientations are not zero rotation orientations during symmetrical rolling. Components of the shifted  $\alpha$ -fiber texture are only retained in the corresponding  $\alpha$ -fiber-oriented grains via in-grain deformation. Among all possible deformation conditions for the  $\alpha$ -fiber-oriented grains, the condition including the  $L_{21}$  shear velocity gradient is the only criterion that allows high stability at the shifted  $\alpha$ -fiber orientations. Moreover, for consistency with the macroscopic deformation condition of symmetrical rolling, the  $L_{21}$  shear velocity must occur in both the positive and the negative directions. This local deformation condition suggests that deformation bands and the vicinities of grain boundaries in the  $\alpha$ -fiber-oriented grains are suitable locations for the shifted  $\alpha$ -fiber orientations. The microstructures of the  $\alpha$ -fiber-oriented grains are then experimentally verified. Subsequently, the evolution of the shifted  $\alpha$ -fiber orientations during recrystallization is (i) discussed in terms of the underlying mechanisms and (ii) is then attributed to low-stored-energy nucleation and special growth, owing to migration of the  $\langle 110 \rangle 26.5^\circ$  boundaries separating the shifted and ideal  $\alpha$ -fiber-oriented crystals.

Local deformation conditions and the consequent microstructural features are more important for evolution of recrystallization textures in cold-rolled samples than for the evolution in hot-rolled samples. Therefore, the occurrence of microscopic shear bands in cold-rolled samples is investigated. In-grain microscopic shear banding in strongly oriented grains is accounted for by implementing the geometric softening of crystal plasticity proposed by Dillamore et al. Progressive deformation via PSC yields strongly oriented grains with high densities of dislocations. However, further homogeneous deformation via PSC becomes less energetically feasible than

locally rotated shear strain. Concentration of strain energy into inclined shear bands results in rotations of in-band crystal regions toward lower energy orientations, whereas the crystal regions outside the bands remain un-deformed.

Geometric softening via shear banding in the  $\{111\}\langle 112 \rangle$ -oriented grains is replicated with particular attention on the orientation evolution in shear bands. Crystal plasticity simulations reveal the energy decrease accompanying geometric softening via shear banding at both positive and negative inclination angles (in this case,  $+35^\circ$  and  $-35^\circ$ ). However, rotations of in-band crystal are limited, to different extents, by the crystal rotation rates. The lowest energy state for in-band crystal regions in (i) positive shear bands is reached with a  $16^\circ$  rotation of  $\{111\}\langle 112 \rangle$ -oriented crystals around their  $\langle 110 \rangle // \text{TD}$  axis and (ii) negative shear bands is reached at the Goss ( $\{110\}\langle 001 \rangle$ ) orientation. The highest rotation rate calculated at the Goss orientation indicates that Goss-oriented crystals lie in regions characterized by sharp lattice curvature. The Goss orientation although absent from the recrystallization textures of cold-rolled samples, represents one of the most important texture components for electrical steels that have undergone secondary recrystallization.

In accordance with geometric softening, microscopic shear banding depends on the initial deformation resistance of oriented grains to the macroscopic deformation condition. Among all oriented crystals of a BCC-structured material, those with the rotated Goss ( $\{110\}\langle 110 \rangle$ ) orientation have the highest resistance to PSC. Rotated-Goss-oriented grains are, therefore, more susceptible to shear banding than any other deformation condition. During deformation in  $45^\circ$  inclined shear bands, in-band crystal regions of the rotated-Goss oriented grains rotate around the  $\langle 100 \rangle // \text{TD}$  axis, thereby reaching the lowest energy state of the Cube ( $\{001\}\langle 100 \rangle$ ) orientation. Although the rotated Goss occurs only rarely in deformation textures, a small fraction of rotated-Goss-oriented grains is observed after cold rolling of the Fe-1.2 wt.% Si alloy. These grains are retained from the austenite-to-ferrite phase transformation. In addition, Cube-oriented crystals occur in shear bands of the rotated-Goss-oriented grains.

## Summary

Texture and anisotropy are persistent characteristics of polycrystal. Because of the ordered and periodic arrangement of atoms in crystal lattices, responses of each oriented crystals in a polycrystal to the same external forces are not similar. Crystal grains which are better accommodated to boundary conditions because of their energetically orientation stable, should have higher volume fractions. The dependence of crystal behaviors on their relative orientations to applied field vector(s) result in anisotropy. To enhance or reduce anisotropy, crystallographic texture in materials need to be controlled and improved.

For quantitative analyses on crystallographic orientations and textures, mathematic representation for orientation and parameterization of rotation space are the first demands. Among others, Miller indices of crystallographic orientations and pole figures of crystal plane normal vectors are the best known representations to metallurgists. The Miller index has the advantage on human perception of crystallographic plane and direction, while pole densities of crystal planes could be measured directly by high energy radiation (X-ray, neutron ...) diffraction. However, to describe general orientations which do not have low Miller indexed plane and/or direction parallel to reference axes, rotation matrix and triple Euler angles are more practically used. Because of its tensorial properties, rotation matrix is the unique orientation representation in micromechanics and crystal plasticity models. Thanks to the works by H.J. Bunge on mathematical description of orientation distribution functions, the triple Euler angles nowadays has been the most common orientation representation in texture studies. Beyond the above mentioned representations, crystallographic orientations could also be described by axis-angle pair, Rodrigues-Frank vector and unit quaternion. These parameters, particularly the unit quaternion, are very useful in analyses of grain boundaries and misorientation distribution functions. Nevertheless, none of the orientation representations is perfect for all applications. In this study, orientation coordinates in Euler space are applied for

---

texture analysis, rotation matrix is calculated by crystal plasticity models and Miller indices of orientations are used whenever convenience is possible.

To demonstrate for the texture control in industrially produced materials, evolutions of crystallographic texture in an Fe-1.2 wt.% Si alloy after rolling and annealing are investigated. The alloys of iron with 1.0-6.5 wt.% silicon, so called electrical steels, are well-known as magnetic flux carrying cores in electrical machines (e.g. transformers, electrical motors ...). They have a long history since the early 20<sup>th</sup> century, but still among the most important materials for highly efficient electrical conversions. To reduce the energy loss but maintain the high flux density of iron cores, electrical steels are commonly produced as thin sheets of 0.2-0.5 mm. Crystallographic textures of the materials are designed to obtain the maximum volume fraction of grains having the easiest magnetization directions (i.e. the  $\langle 100 \rangle$  crystallographic direction) parallel to the external magnetic field vectors of the stacked sheet cores. As a consequence, depending on their applications, the materials are divided into two groups; grain oriented and non-oriented grades. For uni-axial variation of magnetic field in transformers, thanks to the manufacturing process proposed by N.P. Goss in 1934, the Goss ( $\{110\}\langle 001 \rangle$ ) texture is the most feasible to obtain in grain oriented grades. For rotating magnetic fields in motors and generators, isotropic distribution of the  $\langle 100 \rangle$  crystallographic axes (i.e. the Cube fiber) on the sheet plane is the most desirable texture in non-oriented electrical steels. To produce non oriented electrical steels with the Cube fiber texture, various manufacturing processes have been proposed recently, but none of them is applied at the industrial scale. Moreover, formations of crystallographic textures in electrical steels, particularly in non-oriented grades, have not been completely understood.

Except on few special cases, rolling and annealing are still among the most common processes in manufacturing of electrical steels. Evolution of crystallographic textures after plastic deformation and recrystallization, therefore, have important roles on final properties of the materials. To account for the development of deformation textures, crystal plasticity theory is employed. Under mechanical boundary conditions, plastic deformation of crystal grains in electrical steels is carried on by multi-slips of various dislocation systems. The pencil glide in body

centered cubic structured materials is considered by potential activities of all three slip systems, including  $\{110\}\langle 111\rangle$ ,  $\{112\}\langle 111\rangle$  and  $\{123\}\langle 111\rangle$ , during warm deformations. For deformations at room temperature, only glides of the first two ( $\{110\}\langle 111\rangle$  and  $\{112\}\langle 111\rangle$ ) slip systems are taken into account. During crystal plasticity, besides geometric shape change, dislocation glides result in each oriented crystals a preferential rotation. Orientation preference of polycrystal during plasticity, however, is not just a function of applied strain mode as in single crystals, but also affected by grain interactions among neighboring crystals. The Advanced Lamel model, therefore, is chosen for prediction of rolling textures.

To explore the possibility to change deformation texture of the conventional rolling, asymmetric rolling has been implemented. The presence of the RD-ND shear strain ( $\epsilon_{13}$ ) on the rolling plane and parallel to the rolling direction in the strain tensor results in asymmetrically rolled sample a different deformation texture, rather than the one of conventional rolling. Impacts of the shear strain on asymmetric rolling texture could be estimated by rotations of the conventional rolling texture around the sample transverse direction. The higher ratio of the shear to the normal strain component, the larger deviation of the asymmetric rolling texture to the one of the conventional rolling. In reality, because of the variation of the shear strain across the sample thickness, deformation of the asymmetric rolling sample is better simulated by a linear finite element model than estimated by a geometric model. The consideration of inhomogeneous strain distribution across the sample thickness and non-linear development of the strain path during rolling in the finite element model improves the texture prediction result. Deformation texture simulated with the strain tensor from the finite element model exhibits a better fit to the measure texture than the one calculated with the strain tensor of the geometry model.

To reduce the plastically stored energy in deformed crystals, rolling samples were annealed in a box furnace under the protective atmosphere for fully recrystallization. Recrystallization textures in warm and cold rolled samples, however, exhibit different evolutions. Evolutions of recrystallization textures, therefore, are analyzed by texture predictions with a mean-field statistical recrystallization model. Formation of crystallographic texture in this model is accounted for by oriented nucleation of



---

deformed crystals and selective growth of high angle grain boundaries. Being the driving force for recrystallization, the plastically stored energy of deformed crystals is estimated by the Taylor factor of crystal plasticity theory in this study. The Taylor factor, by definition, is a scaled parameter representing for the plastic energy dissipation to activated slip systems in a deformed crystal. Assuming a linear relationship between glide and accumulation of slip systems, the Taylor factor could be used as a scaled measurement for the dislocation density in deformed crystals. The application of the low Taylor factor nucleation mechanism in the recrystallization model results a good fit between simulated and measured recrystallization textures in warm rolled samples. Recrystallization textures in rough rolled and particularly in asymmetrically warm rolled samples which have never been reported before, are well reproduced by simulations. On the contrary, development of the recrystallization texture in conventionally cold rolled samples, although has been well reported, is not completely captured by simulations. Evolution of recrystallization texture in cold rolled samples exhibits the orientation preference to high Taylor factor grains. Relative intensities among various components of the recrystallization texture indicate the important role of the high mobility grain boundary  $\langle 110 \rangle 26.5^\circ$  on growth of recrystallized grains. Moreover, the presence of the shifted  $\alpha$ -fiber recrystallization texture which is parallel to the  $\alpha$ -fiber of the conventional rolling texture in the  $\varphi_2 = 45^\circ$  Euler section could not be captured by the current recrystallization model.

One of the reasons for the absence of the shifted  $\alpha$ -fiber in predicted recrystallization texture is due to the homogeneous deformation condition assumed by polycrystal plasticity simulations. In reality, local strain variations particularly at low temperatures, although do not affect macroscopic deformation textures, result different microstructures in cold rolled than in warm rolled samples. A local concentration of strain to inclined shear bands within specific oriented crystals is known as micro shear banding. Occurrence of micro shear bands in deformed crystals is argued by the geometric softening effect. During progressive deformation, locally inclined shear becomes more energetically favorable than homogeneous strain of grains. Oriented crystals inside shear regions although have minor contributions to the macroscopic deformation texture, are potential nuclei of recrystallization

microstructures. An illustration for the geometric softening effect in electrical steels is the presence of the Goss ( $\{110\}\langle 001\rangle$ ) oriented crystals in shear bands of the  $\{111\}\langle 112\rangle$  oriented grains. In this study, the geometric softening effect also accounts for the formation of the Cube ( $\{001\}\langle 100\rangle$ ) oriented crystals in shear bands of the rotated Goss ( $\{110\}\langle 110\rangle$ ) grains which are the “hardest” oriented crystals of body centered cubic materials under the plane strain compression. The geometric softening effect, on the contrary, may not be a reason for the presence of the shifted  $\alpha$ -fiber oriented crystals in deformation microstructures. The relationship between this fiber and the  $\alpha$ -fiber of deformation texture, although is confirmed by previous studies, has not been captured by any crystal plasticity simulations. Therefore, crystal plasticity of the  $\alpha$ -fiber oriented crystals (e.g. the rotated Cube  $\{001\}\langle 110\rangle$  oriented crystal) by different deformation modes are simulated in this study. Assuming deformation of the  $\alpha$ -fiber oriented crystals is locally deviated from the plane strain compression of the conventional rolling, shear components are individually added to the velocity gradient tensor for crystal plasticity simulations. Among all six components, only the velocity gradient vector ( $L_{21}$ ) which is parallel to the transverse direction and perpendicular to the normal direction of the sample produces in the  $\alpha$ -fiber oriented grains, crystals of the shifted  $\alpha$ -fiber orientation. To be confined within the macroscopic plane strain compression, the shear velocity gradient vector is required to exist in both positive and negative directions. This net zero effect of the shear velocity gradient tensor, therefore, suggests for the presence of the shifted  $\alpha$ -fiber oriented crystals in deformation bands of the  $\alpha$ -fiber oriented grains.



# Samenvatting

Textuur en anisotropie zijn hardnekkige kenmerken van polykristal. Door de geordende en periodieke rangschikking van de atomen in kristalroosters zijn de reacties van elk georiënteerd kristal in een polykristal op dezelfde externe krachten niet gelijk. Kristalkorrels die beter geschikt zijn voor grenscondities vanwege hun energetisch stabiele oriëntatie, zouden hogere volumefracties moeten hebben. De afhankelijkheid van het gedrag van de kristallen van hun relatieve oriëntatie ten opzichte van de toegepaste veldvector(en) resulteert in anisotropie. Om de anisotropie te verbeteren of te verminderen, moet de kristallografische textuur in materialen worden gecontroleerd en verbeterd.

Voor kwantitatieve analyses op kristallografische oriëntaties en texturen zijn mathematische representatie voor oriëntatie en parametrisering van de rotatieruimte de eerste eisen. Onder andere Miller-indices van kristallografische oriëntaties en poolcijfers van kristalvlakke normaalvectoren zijn de bekendste representaties voor metallurgen. De Miller-index heeft het voordeel op de menselijke perceptie van kristallografisch vlak en richting, terwijl pooldichtheden van kristalvlakken direct gemeten kunnen worden door hoge energiestraling (röntgenstraling, neutronen...) diffractie. Echter, om algemene oriëntaties te beschrijven die geen laag Miller geïndexeerd vlak en/of richting parallel aan referentie-assen hebben, worden de rotatiematrix en drievoudige Euler hoeken meer praktisch gebruikt. Door zijn tensoriële eigenschappen is de rotatiematrix de unieke oriëntatieweergave in micromechanica en kristalplasticiteitsmodellen. Dankzij de werken van H.J. Bunge over de wiskundige beschrijving van oriëntatieverspreidingsfuncties is de drievoudige Euler-hoek tegenwoordig de meest voorkomende oriëntatieweergave in textuurstudies. Naast de bovengenoemde representaties konden kristallografische oriëntaties ook worden beschreven met behulp van ashoekpaar, Rodrigues-Frank vector en eenheidsquaternion. Deze parameters, in het bijzonder de eenheidsquaternion, zijn zeer nuttig bij analyses van

---

korrelgrenzen en misoriëntatie-verdelingsfuncties. Toch is geen enkele van de oriënteringsvoorstellingen perfect voor alle toepassingen. In deze studie worden oriëntatiecoördinaten in de Euler ruimte toegepast voor textuuranalyse, wordt de rotatiematrix berekend met behulp van kristalplasticiteitsmodellen en worden Miller-indices van oriëntaties gebruikt wanneer dat mogelijk is.

Om de textuurcontrole in industrieel geproduceerde materialen aan te tonen, worden evoluties van de kristallografische textuur in een Fe-1,2 wt.% Si legering na het walsen en gloeien onderzocht. De legeringen van ijzer met 1,0-6,5 wt.% silicium, zogenaamde elektrische staalsoorten, zijn bekend als magnetische fluxdragende kernen in elektrische machines (bijv. transformatoren, elektromotoren ...). Ze hebben een lange geschiedenis sinds het begin van de 20e eeuw, maar behoren nog steeds tot de belangrijkste materialen voor zeer efficiënte elektrische conversies. Om het energieverlies te beperken, maar de hoge fluxdichtheid van ijzeren kernen te behouden, worden elektrische staalsoorten meestal geproduceerd als dunne platen van 0,2-0,5 mm. De kristallografische texturen van de materialen zijn ontworpen om de maximale volumefractie van de korrels te verkrijgen met de gemakkelijkste magnetisatierichtingen (d.w.z. de  $\langle 100 \rangle$  kristallografische richting) parallel aan de externe magnetische veldvectoren van de gestapelde plaatkernen. Als gevolg hiervan zijn de materialen, afhankelijk van hun toepassingen, verdeeld in twee groepen; korrelgerichte en niet-georiënteerde kwaliteiten. Voor uni-axiale variatie van het magnetisch veld in transformatoren, dankzij het fabricageproces voorgesteld door N.P. Goss in 1934, is de Goss ( $\{110\}\langle 001 \rangle$ ) textuur de meest haalbare om te verkrijgen in korrelgerichte kwaliteiten. Voor roterende magnetische velden in motoren en generatoren is de isotrope verdeling van de  $\langle 100 \rangle$  kristallografische assen (d.w.z. de Kubusvezel) op het plaatvlak de meest wenselijke textuur in niet-georiënteerde elektrische staalsoorten. Voor de productie van niet-georiënteerde elektrische staalsoorten met de Kubusvezeltextuur zijn onlangs verschillende productieprocessen voorgesteld, maar geen van hen wordt toegepast op de industriële schaal. Bovendien zijn formaties van kristallografische texturen in elektrische staalsoorten, met name in niet-georiënteerde kwaliteiten, niet volledig begrepen.

Behalve in enkele speciale gevallen behoren walsen en gloeien nog steeds tot de meest voorkomende processen bij de productie van elektrische staalsoorten. Evolutie van kristallografische texturen na plastische vervorming en herkristallisatie spelen daarom een belangrijke rol bij de uiteindelijke eigenschappen van de materialen. Om rekening te houden met de ontwikkeling van de deformatietexturen wordt de theorie van de kristalplasticiteit gebruikt. Onder mechanische grenscondities wordt de plastische vervorming van kristalkorrels in elektrisch staal voortgezet door multislips van verschillende dislocatiesystemen. De potloodglijbaan in lichaamsgecentreerde kubisch gestructureerde materialen wordt beschouwd door potentiële activiteiten van alle drie de slipsystemen, inclusief  $\{110\}\langle 111\rangle$ ,  $\{112\}\langle 111\rangle$  en  $\{123\}\langle 111\rangle$ , tijdens warme vervormingen. Bij vervormingen bij kamertemperatuur wordt alleen rekening gehouden met de glijders van de eerste twee ( $\{110\}\langle 111\rangle$  en  $\{112\}\langle 111\rangle$ ) slipsystemen. Tijdens kristalplasticiteit, naast de geometrische vormverandering, resulteren dislocatieglijbanen in elke georiënteerde kristallijn een voorkeursrotatie. De oriëntatievoorkeur van het polykristal tijdens de plasticiteit is echter niet alleen een functie van de toegepaste rekmodus zoals bij enkelvoudige kristallen, maar wordt ook beïnvloed door de korrelerinteracties tussen naburige kristallen. Het Advanced Lamel-model wordt daarom gekozen voor de voorspelling van de rolstructuren.

Om de mogelijkheid te onderzoeken om de deformatiestructuur van het conventionele walsen te veranderen, is asymmetrisch walsen toegepast. De aanwezigheid van de RD-ND afschuifspanning ( $\epsilon_{13}$ ) op het walsvlak en parallel aan de walsrichting in de reksensor resulteert in een asymmetrisch gewalst monster met een andere deformatiestructuur dan bij conventionele walsen. De effecten van de afschuifspanning op de asymmetrische walstextuur kunnen worden geschat door rotaties van de conventionele walstextuur rond de dwarsrichting van het monster. De hogere verhouding van de afschuiving ten opzichte van de normale vervormingscomponent, de grotere afwijking van de asymmetrische walsstructuur ten opzichte van de conventionele walsstructuur. In werkelijkheid, vanwege de variatie van de afschuifspanning over de dikte van het proefstuk, wordt de vervorming van het asymmetrische walsmonster beter gesimuleerd door een lineair

---

eindige-elementenmodel dan geschat door een geometrisch model. Het rekening houden met inhomogene vervormingsverdeling over de dikte van het proefstuk en de niet-lineaire ontwikkeling van het vervormingspad tijdens het walsen in het eindige-elementenmodel verbetert het resultaat van de textuurvoorspelling. De deformatietextuur die gesimuleerd wordt met de reksensor van het eindige-elementenmodel past beter bij de meetstructuur dan die berekend wordt met de reksensor van het geometriemodel.

Om de plastisch opgeslagen energie in vervormde kristallen te verminderen, werden de rollende monsters in een doosoven onder de beschermende atmosfeer gegloeid voor volledige herkristallisatie. Herkristallisatiestructuren in warme en koudgewalste monsters vertonen echter verschillende evoluties. Evoluties van de herkristallisatietexturen worden daarom geanalyseerd door textuurvoorspellingen met een gemiddeld veld statistisch herkristallisatiemodel. De vorming van de kristallografische textuur in dit model wordt verantwoord door georiënteerde nucleatie van vervormde kristallen en selectieve groei van de korrelgrenzen onder een hoge hoek. Als drijvende kracht voor herkristallisatie wordt de plastisch opgeslagen energie van vervormde kristallen geschat door de Taylor-factor van de kristalplasticiteitstheorie in deze studie. De Taylor-factor is per definitie een geschaalde parameter die de plastische energiedissipatie aan geactiveerde slipsystemen in een vervormd kristal vertegenwoordigt. Uitgaande van een lineair verband tussen glijden en accumulatie van slipsystemen, zou de Taylorfactor kunnen worden gebruikt als een geschaalde meting voor de dislocatiedichtheid in vervormde kristallen. De toepassing van het nucleatiemechanisme met lage Taylorfactor in het herkristallisatiemodel resulteert in een goede aansluiting tussen gesimuleerde en gemeten herkristallisatietexturen in warmgewalste monsters. Herkristallisatiestructuren in ruw gewalste en in het bijzonder in asymmetrisch warm gewalste monsters die nooit eerder zijn gerapporteerd, worden goed gereproduceerd door simulaties. Integendeel, de ontwikkeling van de herkristallisatietextuur in conventioneel koudgewalste monsters, hoewel goed gerapporteerd, is niet volledig vastgelegd door simulaties. Evolutie van de herkristallisatietextuur in koudgewalste monsters vertoont de oriëntatievoorkeur

---

voor korrels met een hoge Taylorfactor. Relatieve intensiteiten tussen verschillende componenten van de herkristallisatietextuur geven de belangrijke rol aan van de hoge beweeglijkheid van de korrelgrens  $\langle 110 \rangle 26,5^\circ$  bij de groei van geherkristalliseerde korrels. Bovendien kon de aanwezigheid van de verschoven  $\alpha$ -vezelherkristallisatiestructuur die parallel loopt aan de  $\alpha$ -vezel van de conventionele walstechnologie in de  $\varphi_2 = 45^\circ$  Euler-sectie niet worden opgevangen door het huidige herkristallisatiemodel.

Een van de redenen voor de afwezigheid van de verschoven  $\alpha$ -vezel in de voorspelde herkristallisatietextuur is te wijten aan de homogene vervormingstoestand die wordt verondersteld door polykristallijne plasticiteitssimulaties. In werkelijkheid hebben lokale vervormingsvariëaties, vooral bij lage temperaturen, weliswaar geen invloed op de macroscopische vervormingstexturen, maar resulteren ze in andere microstructuren in koudgewalste monsters dan in warmgewalste monsters. Een lokale concentratie van de vervorming tot hellende afschuivingsbanden binnen specifieke georiënteerde kristallen staat bekend als microschiivingsband. Het optreden van microafschuivingsbanden in vervormde kristallen wordt beargumenteerd door het geometrische verzachtende effect. Tijdens de progressieve vervorming wordt de lokaal geneigde afschuiving energetisch gunstiger dan de homogene stam van de korrels. De georiënteerde kristallen in afschuivingsgebieden hebben weliswaar een kleine bijdrage aan de macroscopische deformatietextuur, maar zijn potentiële kernen van herkristallisatiemicrostructuren. Een illustratie voor het geometrische verzachtende effect in elektrisch staal is de aanwezigheid van de Goss ( $\{110\}\langle 001 \rangle$ ) georiënteerde kristallen in afschuivingsbanden van de  $\{111\}\langle 112 \rangle$  georiënteerde korrels. In deze studie is het geometrische verzachtendseffect ook verantwoordelijk voor de vorming van de Kubus ( $\{001\}\langle 100 \rangle$ ) georiënteerde kristallen in schuifbanden van de gedraaide Goss ( $\{110\}\langle 110 \rangle$ ) korrels die de "hardste" georiënteerde kristallen zijn van de kubusvormige materialen in het lichaam onder de vlakke rekcompressie. Het geometrische verzachtende effect daarentegen mag geen reden zijn voor de aanwezigheid van de verschoven  $\alpha$ -vezel georiënteerde kristallen in vervormingsmicrostructuren. Het verband tussen deze vezel en de  $\alpha$ -vezel van de



---

deformatietextuur is weliswaar bevestigd door eerdere studies, maar is niet opgevangen door enige kristalplasticiteitssimulaties. Daarom wordt kristalplasticiteit van de  $\alpha$ -vezel georiënteerde kristallen (bv. het geroteerde Kubus  $\{001\}\langle 110 \rangle$  georiënteerde kristal) door verschillende vervormingsmodi gesimuleerd in deze studie. Ervan uitgaande dat de deformatie van de  $\alpha$ -vezel georiënteerde kristallen lokaal wordt afgeweken van de vlakke rekcompressie van de conventionele walsen, worden afschuivingscomponenten individueel toegevoegd aan de snelheidsgradiënttensor voor kristalplasticiteitssimulaties. Van alle zes componenten produceert alleen de snelheidsgradiëntvector (L21) die evenwijdig is aan de dwarsrichting en loodrecht staat op de normale richting van het monster, in de  $\alpha$ -vezel georiënteerde korrels, kristallen van de verschoven  $\alpha$ -vezel oriëntatie. Om binnen de macroscopische vlakstrepressie te blijven, moet de afschuifnelheidsgradiëntvector zowel in positieve als in negatieve richting bestaan. Dit netto nulpunt van de afschuifnelheidsgradiënttensor suggereert dus de aanwezigheid van de verschoven  $\alpha$ -vezel georiënteerde kristallen in vervormingsbanden van de  $\alpha$ -vezel georiënteerde korrels.

## *List of publications*

- [1] Nguyen-Minh T, Sidor J, Petrov R, Kestens LAI. Texture evolution during asymmetrical warm rolling and subsequent annealing of electrical steel. Mater Sci Forum, vol. 702-703, 2012. p.758.
- [2] Nguyen-Minh T, Sidor JJ, Petrov RH, Kestens LAI. Occurrence of shear bands in rotated Goss ( $\{110\}\langle 110\rangle$ ) orientations of metals with bcc crystal structure. Scripta Materialia. 2012;67:935.
- [3] Nguyen-Minh T, Sidor JJ, Petrov RH, Kestens LAI. Shear banding and its contribution to texture evolution in rotated Goss orientations of BCC structured materials. IOP Conference Series: Materials Science and Engineering. 2015;82:012023.
- [4] Santofimia MJ, Nguyen-Minh T, Zhao L, Petrov R, Sabirov I, Sietsma J. New low carbon Q&P steels containing film-like intercritical ferrite. Mater. Sci. Eng. A. 2010;527:6429.
- [5] Kestens L, Sidor J, Petrov R, Nguyen-Minh T. Texture control in steel and aluminium alloys by rolling and recrystallization in non-conventional sheet manufacturing. Mater Sci Forum, vol. 715-716, 2012. p.89.
- [6] De Knijf D, Nguyen-Minh T, Petrov RH, Kestens LAI, Jonas JJ. Orientation dependence of the martensite transformation in a quenched and partitioned steel subjected to uniaxial tension. J Appl Crystallogr. 2014;47:1261.
- [7] Aranas C, Jr., Nguyen-Minh T, Grewal R, Jonas JJ. Flow softening-based formation of Widmanstätten ferrite in a 0.06%C steel deformed above the Ae3. ISIJ Int. 2015;55:300.

---

[8] Castro Cerda FM, Vercruysse F, Nguyen-Minh T, Kestens L, Monsalve A, Petrov R. The Effect of Heating Rate on the Recrystallization Behavior in Cold Rolled Ultra Low Carbon Steel. *Steel Res Int.* 2017;88.

[9] Lutz A, Lapeire L, Nguyen-Minh T, Verbeken K, Terryn H, De Graeve I. Effect of the shear layer on the etching behavior of 6060 aluminum extrusion alloys. *Surface and Interface Analysis.* 2019;51:1251.

# Acknowledgements

As a scientific work, this study would never be completed if I did not receive invaluable help, support and encouragement of many people to whom I owe a debt of gratitude.

I would like to thank Prof. Leo A.I. Kestens and Prof. Roumen H. Petrov, my PhD promoters, for inspiring me with scientific problems, guiding me through the issues, and never losing their expectation on my ability.

Thanks to Prof. Jilt Sietsma and Prof. Maria J. Santofimia-Navarro for their great knowledge and experiences of which I had chances to learn as a Master student. Their kind helps for the time as I was at the Microstructure research group (TU Delft) up to now are very much appreciated.

My gratefulness to Prof. Jurij Sidor for his introduction to crystal plasticity and texture analysis. My special thanks to Vitaliy Bliznuk, Roger Van Hecke and Ilse Vercruysse (UGent) for their valuable assistance on microstructure characterization, computer issues as well as administrative procedures.

My appreciation to friends and colleagues from Delft and from Gent (Jai Gautam, Patricia Governado, Orlando Leon-Garcia, Tricia Bennett, Alexis Miroux, Hemant Sharma, Andrea Bojack, Lie Zhao, Ron van Tol, Peter van Liempt, Kirk Ofei, Richard Huizenga, Pina Mecozzi, Jesus Galan-Lopez, Victor Carretero Olalla, Elisabete Pinto da Silva, Dorien De Knijf, An Verdiere, Linsey Lapeire, Athina Puype, Soroosh Naghdy, Felipe Castro-Cerda, Edgar Gomes, Harish Lanjewar, Edwin Lopez, Florian Vercruysse, Hadi Pirgazi) for their help and fruitful discussion.

Lastly, I would like to express my deep gratitude to my parents for their unconditional support and care to my every steps on life. My heartfelt thanks to my wife, Thao Vu, for her love, understanding and patience. Thanks to Tommy and Benny, my two little boys, for bringing joys, motivation and a lot encouragement to my work.



# Curriculum Vitae

Tuan NGUYEN MINH

Born on 6<sup>th</sup> of June 1982 in Hanoi, Vietnam

2018-now	Center for Research in Metallurgy (CRM Group), Ghent, Belgium Project Leader in Metal Processing and Product Metallurgy
2017-2018	Delft University of Technology, Delft, the Netherlands Researcher in Materials Science and Engineering
2013-2016	Ghent University, Ghent, Belgium Scientific fellow in Metal Science and Technology
2009-2013	Delft University of Technology, Delft, the Netherlands PhD Researcher in Materials Science and Engineering
2006-2008	Delft University of Technology, Delft, the Netherlands Master of Science in Materials Science and Engineering
2005-2006	Hanoi University of Technology, Hanoi, Vietnam Lecturer of Materials Science and Heat Treatment
2000-2005	Hanoi University of Technology, Hanoi, Vietnam Bachelor of Metallurgy and Materials Technology
1997-2000	Hanoi – Amsterdam High school, Hanoi, Vietnam